UNIVERSITY OF NOTTINGHAM

SCHOOL OF MECHANICAL, MATERIALS, MANUFACTURING ENGINEERING AND MANAGEMENT

ANALYSIS OF THE VACUUM INFUSION MOULDING PROCESS

by

Eng.º Nuno André Curado Mateus Correia

Thesis submitted to the University of Nottingham for the degree of Doctor of Philosophy

April 2004

CONTENTS

ACKNOWLEDGEMENTS

Dedico esta tese à Célia: por todo o amor, confianca e apoio, por aceitar aquilo que sou e apoiar os meus sonhos; aos meus pais, a quem devo tudo (principalmente as minhas poucas virtudes); aos meus irmãos Be__, Nana e Toninho, sobrinha Isabelinha, e ao Ivar e à Inês; por me recordarem de quem eu sou na realidade.

I dedicate this thesis to Célia: for all her love, confidence and support, for accepting who I am and embracing my dreams; to my parents, to whom I owe all that I am (especially my few virtues); to my siblings Be__, Nana e Toninho, my niece Isabelinha, and to Ivar and Inês; for reminding me of whom I am.

Aos meus avós, que estarão sempre comigo.

To my grandparents who are and always will be with me.

I would also like to thank the support of all those whom I was privileged to work with: the supervisors who made this thesis possible: Professors Rudd, Long and Advani and Doctors Robitaille and Šimáček; my friends and colleagues whose help I was never denied and who made my time here meaningful (and immensely fun): Phil, Rafael, Agnès, François (all of them), Dhiren, Barbara, Jon, Nuno, AD, Brendon, Sophie, James, Graham, Miguel, Catarina, Chris, Yuuki, Olga, Pearl, Maria, Tiziana and Cláudia. Thanks also to Roger, Paul, Dave, Geoff and both Brians (Foster and Webster) for their support, humour and generosity. I must also express my gratitude to the Head of the School of Mechanical, Material, Manufacturing Engineering and Management of the University of Nottingham for the use of facilities and to the RoadLite project partners: VT Group, Europrojects, and Southfields; and funding entities: EPSRC and DfT. Finally, I would like also to add an acknowledgement to all friends and supervisors in INEGI who helped me get here in the first place.

ABSTRACT

This thesis focuses on flow through compliant porous media with applications to the manufacturing of composites by vacuum infusion (VI). The context of this work is the need for reliability in environmentally friendly composite processing methods for composite materials. Commercial reality and the prospective application to low cost structures for the transportation industry dictate that appropriate emphasis should be put on obtaining robust simulations, ensuring reliability and progressing toward efficient means of process control. In this context, the open mould manufacturing processes which have been used to produce large composite structures, and are not conducive to quality nor environmental responsibility, must be replaced. Hence, establishing composites as a viable alternative requires closed moulding techniques, of which VI is the most practical for large structures, but where reliability is required for economic survival.

This work addresses many aspects of this problem, by making innovative use of fluid mechanics and developing, implementing and proposing new analysis and modelling tools for VI. Main results include a validated analytical model for flow through compliant media, a study of the compliance of textile reinforcements, a finite element model for VI and novel stochastic techniques for the analysis of reliability in liquid composite moulding processes.

The work discussed herein stems from a thorough evaluation of published models and leads to novel flow modelling tools for VI including a unique and general formalism for textile compliance. Using these tools it was possible to study, for the first time, the effect of different parameters on VI manufacturing. The reliability issue was addressed by integrating stochastic models for compliance and permeability, and the ability to model complex geometries was demonstrated by adapting a commercial finite element flow code (LIMS).

NOMENCLATURE

UPPER CASE SYMBOLS

A	Finite difference coef. matrix	-
A	*A*rea	m^2
As	Compaction spring constant	Pa
B	Compaction stiffening index	-
C_α	Flow front fluid pressure gradient ratio P_{VI}/P_{RTM}	-
C	Compaction fitting parameter (Wyk and Chen *et al*)	-
C	Master curve coefficients (Chapter 3)	-
E	Young's bulk modulus of reinforcement	Pa
H	Total thickness	m
K	Scalar permeability	m^2
K	Permeability tensor	m^2
L	Flow front position	m
P	Pressure	Pa
Q	Volume flow rate	m^3 / s
R^2	Correlation coefficient	-
S	Surface	m^2
V	Volume	m^3

LOWER CASE SYMBOLS

a	Parameter used in fluid pressure field solution	Pa
a	Dimension of RVE (Figure 2.3)	m
b	Parameter used in fluid pressure field solution	Pa
c	Parameter used in fluid pressure field solution	Pa
c	Vector of constants in numerical solutions	Pa
c_1, c_2	Gebart permeability constants	m^2
h	Laminate thickness	m
k	Kozeny constant	m^2
m	Mass	kg
n	Number of nodes	-

$\hat{\mathbf{n}}$	Vector normal to a surface (normalized)	-
$\vec{n}$	Normal vector	-
p	Fluid pressure vector	Pa
t	Time	s
u	Superficial velocity	m / s
u	Superficial velocity vector	m / s
v	Filter velocity	m / s
v	Filter velocity vector	m / s
v_f	Fibre volume fraction	-
v_0	Fibre vf at zero compaction	-
v_{f0}	Fibre vf at a Pcomp = 1 Pa	-
v_{fa}	Theoretical maximum fibre vf	-
x, y, z	Rectangular coordinates	m

SUBSCRIPTS AND SUPERSCRIPTS

0	Initial
1,2,3	Principal directions
atm	Atmospheric
b	Chen's compaction coefficient index
bulk	Bulk value
comp	Compaction
eq	Equivalent
f	Relative to the reinforcement
h	Hydraulic
i	Iteration number / In
n	Node number
o	Out
RTM	Resin transfer moulding
sup	Superficial [density]
t	Instant t
t	Transverse direction
VI	Related to vacuum infusion

w0	At zero pressure in Wyk's model	
x, y	In-plane directions	
z	Transverse direction	
*	Normalized	

GREEK SYMBOLS

α	Dimensionless flow coordinate	-
ϕ	Porosity	-
κ	Bulk compressibility	-
μ	Viscosity	Pa . s
$\mu(X)$	Mean value of X (statistical)	-
ρ	Density	kg / m^3
σ	Standard deviation	-
ξ	Laminate thickness	m

1 INTRODUCTION

Open moulding processes potentially expose the composite manufacturing workforce to unhealthy levels of styrene emissions. Awareness of this fact is high throughout the composite manufacturing industry, styrene producers and legislators. Health and safety regulations, which would virtually eliminate all open moulding processes, are expected. A processing replacement is therefore necessary.

1.1 OPEN MOULDING PROCESSES AND THE ENVIRONMENT

In the UK alone, over 60 000 tonnes of polyester resin are processed annually in the composite manufacturing industry, 60 % of which is used in open moulds (Nixon, 2000). As a result, these industries release considerable amounts of volatile organic compounds (VOC), primarily styrene into the work environment. In fact, consuming only five percent of the overall production of styrene, composite manufacturing is, according to Nixon (2000), the only industry that exposes its work force to appreciable levels of VOC emissions: more than one hundred times the norm. Industrial awareness has led globally to self-imposed rational styrene emission limits. In the UK, this self-control was recently simplified through a self-assessment sheet prepared by the Health and Safety Executive (HSE, 2003). The current maximum exposure limit (MEL) of 100 ppm in force in the UK is already lower than the typical emissions in gel coating and hand laminating (200 ppm). It is however at least twice as lenient as other European countries or where the MEL is 50 ppm or lower.

Research results reviewed by Nixon (2000) show that below 50 ppm, there is no evidence of long-term harm and, at less than 25 ppm, no carcinogenic risk exists: seven European countries have already adopted MELs of 25 ppm or lower (Figure 1.1). Furthermore, it is foreseeable that an EU directive will unify emission limits throughout Europe at 50 ppm or below. In this framework it is clear that the composites industry in the UK should reassess its procedures.

This work focuses on one of the possible avenues which show promise of attenuating the problem: liquid composite moulding (LCM) in closed moulds. It is acknowledged that others exist, such as low styrene emission resins.

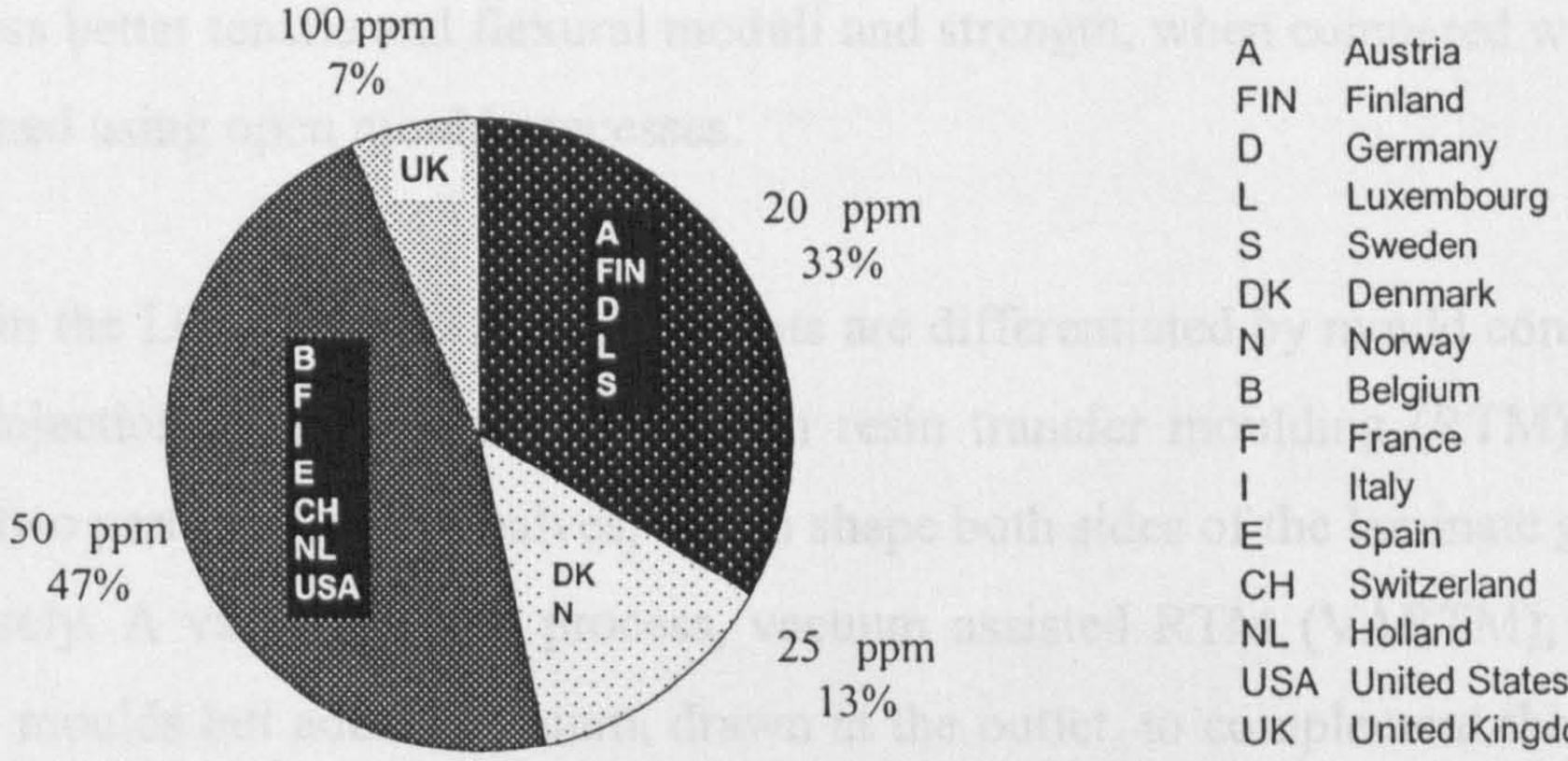

Figure 1.1 – Division of maximum exposure limits to styrene in European and North American countries (Nixon, 2000)

1.2 CLOSED MOULDING PROCESSES

Closed moulding does not suffer from the same emission problems as hand laminating, because VOCs are encapsulated in the matrix during the curing process. For this reason LCM processes are suitable replacements for open moulding in any of their variants. The diverse nature of this family of processes (LCM) is due to different requirements in terms of cost, mechanical properties and finish. In making large parts, vacuum infusion stands out as one of the most promising. Closed mould processing is not new but higher mould cost or complexity has pushed it to high performance or mass production where economies of scale or component cost can give good reason for the extra tooling investment. Because of these environmental concerns however, even some non-structural or one-off applications may soon need to carry the added costs of closed mould techniques. Due to this added cost, one must address the issue of understanding the physics of closed moulding processes better. This work addresses some of the gaps in LCM knowledge, from the physics of flow in some of these processes to reinforcement properties, flow modelling capabilities and manufacturing reliability issues. It will show that development of closed moulding alternatives, such as LCM, is vital if they are to be effective in mass production scenarios. LCM can be broadly described as a process where a liquid

thermosetting resin is injected or drawn into an enclosed fibre preform, filling the mould cavity, and curing once the flow process has completed. Due to the compaction pressures acting on the reinforcement, the resulting LCM products possess better tensile and flexural moduli and strength, when compared with those obtained using open mould processes.

Within the LCM process family, variants are differentiated by mould construction and injection concept. The well-known resin transfer moulding (RTM) process uses two part rigid mould halves, which shape both sides of the laminate geometry precisely. A variant of this process, vacuum assisted RTM (VARTM), uses the same moulds but adds a vacuum, drawn at the outlet, to complement the positive injection pressure at the inlet. This reduces fluid pressure on the mould walls and, due to an increased pressure gradient, accelerates the flow. Both processes involve the same closed mould infusion principle but RTM is shown in Figure 1.2.

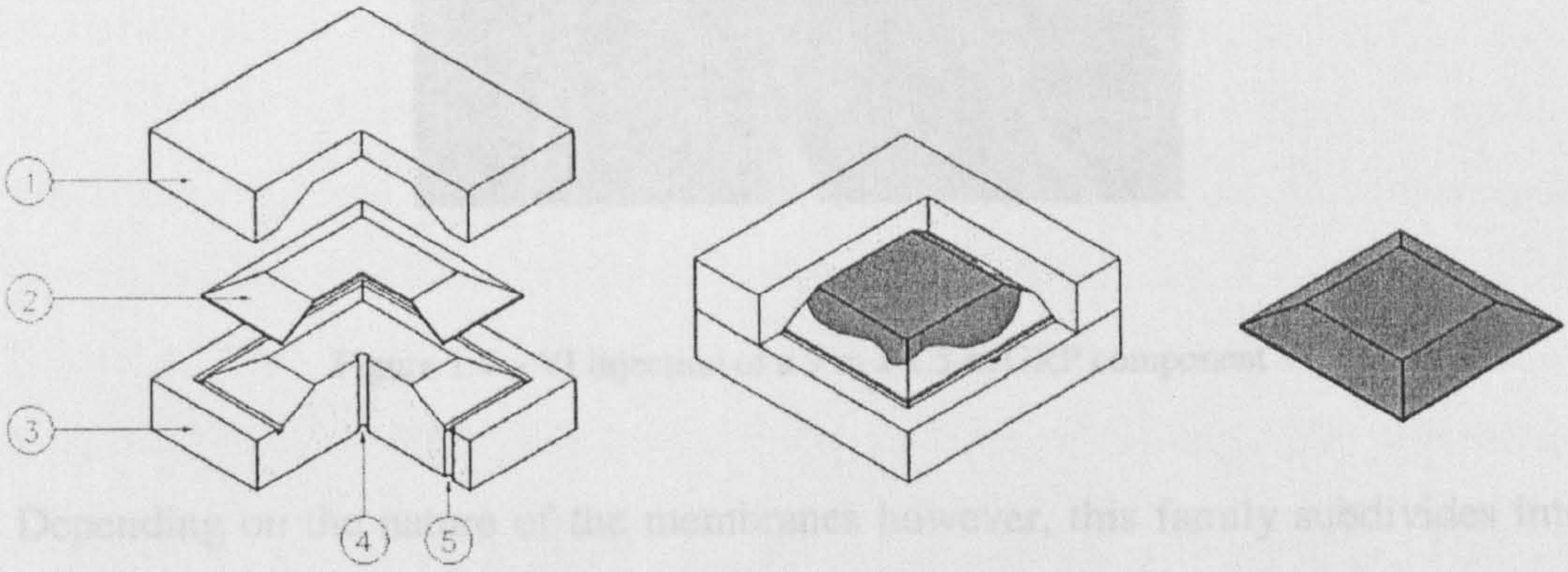

Figure 1.2 – The typical LCM process. Left: Mould components: 1 – Female matched mould, 2 – preform, 3 – male matched mould, 4 – injection gate and 5 – vent. Centre: Resin injection (transfer). Right: Moulded component is removed (after curing)

Other LCM moulding techniques use a single rigid tool surface and a flexible membrane (or shell), which is sealed onto the mould, closing the cavity. Air is extracted from the cavity and the atmospheric pressure outside the bag compresses the reinforcement onto the mould. When the inlet is opened, the differential between atmospheric pressure outside and the vacuum inside forces the thermosetting resin into the mould, filling the cavity. This process is schematically shown in Figure 1.3 and illustrated for a real injection case in Figure 1.4.

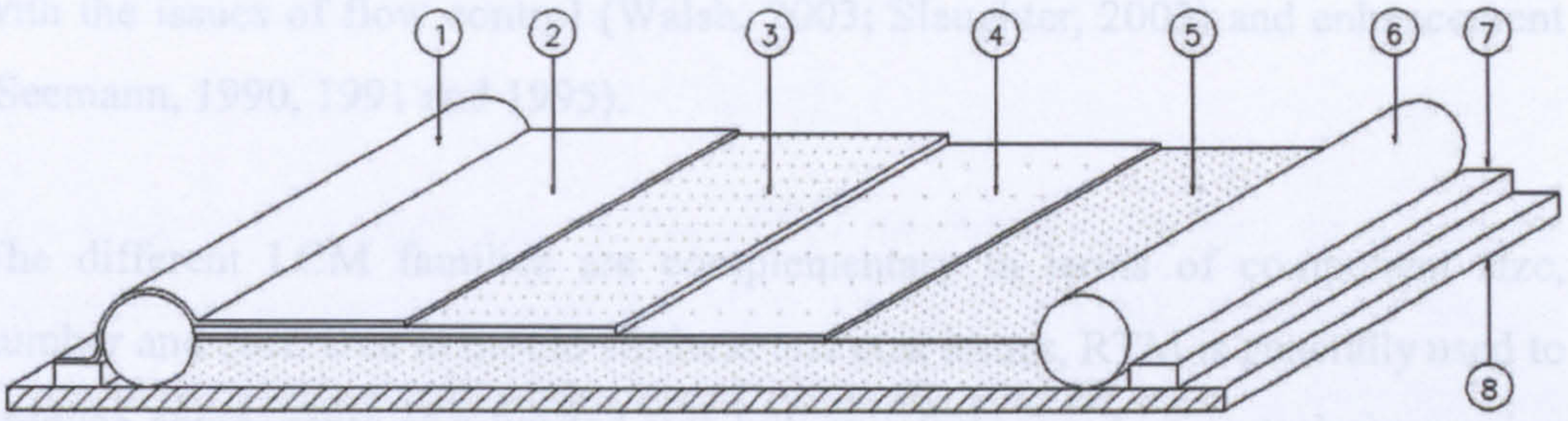

Figure 1.3 – VI mould assembly: 1 – inlet, 2 – vacuum bag, 3 – distribution medium, 4 – peel ply, 5 – reinforcement, 6 – outlet, 7 – vacuum seal, 8 – mould die

Figure 1.4 – VI injection of a 9 m x 2.5 m GRP component

Depending on the nature of the membranes however, this family subdivides into resin infusion under flexible tooling (or RIFT) when thin GRP shells are used and VI with vacuum bags (polymeric membranes). Note that vacuum infusion, is also known as SCRIMP™ (Seeman Composite Resin Infusion Manufacturing Process), RI (resin infusion) or VARTM. Note that this last acronym conflicts with the rigid mould RTM based process described above.

VI and its variants go back a little over half a century. Marco, Smith, Green, Seemann have all patented processes similar to VI from the 1950's through to the 90's (Summerscales *et al*, 1996; Seemann, 1990). In fact, this LCM family has never ceased to evolve and to generate new patents and ideas. Mathematical modelling of VI has been slow when compared to processes such as RTM (Summerscales, 1996). Recent patents in this process are principally concerned

with the issues of flow control (Walsh, 2003; Slaughter, 2003) and enhancement (Seemann, 1990, 1991 and 1995).

The different LCM families are complementary in terms of component size, number and cost. Due to mould stiffness and cost issues, RTM is generally used to produce components of a limited size but, as a faster production technique using robust moulds it is synonymous with higher production numbers. A major development in VI was the recent introduction of distribution media (DM) layers to promote faster flow. Typical DMs are disposable knitted thermoplastic textiles, embossed membranes or channels, either in the mould or, in the case of sandwich materials, the cores.

Parts obtained by RTM or VI based processes differ substantially. Due to its matched mould, RTM components often have high surface quality on all faces and small design tolerances. On the other hand it will be shown in this work that VI components present a more challenging set of characteristics such as variable thickness, fibre volume fraction (and, consequently, mechanical properties) and obviously a lower surface quality on the bag face. Furthermore, the material costs associated with large structures, which often characterize VI, involve a high financial risk and rely significantly on the expertise of the workshop personnel. This experience based approach is complemented with already established RTM flow simulations which, while valuable, do not explore the aforementioned parameters in VI and cannot predict final component weight, dimensions and mechanical properties. Not only are the output properties of these processes different, they are directly influenced by preform properties and mould and gate design. Due to its flow dependent cavity thickness, VI experiences a higher degree of variability than that observed in RTM. Nevertheless, for large components (typical of open moulds), VI is still the only realistic option and its characteristic problems must therefore be addressed.

1.3 LOW INVESTMENT MANUFACTURING OF LARGE TRANSPORTATION STRUCTURES

This work was conducted in the context of the RoadLite project, in which the University of Nottingham participated. RoadLite is a LINK Foresight Vehicle programme which aims to develop a lightweight composite semi-trailer (the non-motorized load carrying structure in a lorry) for use in the United Kingdom.

According to the 2002 Key Note report UK government policy in the 1980's and 1990's enforced road as the dominant mode of freight transportation with a present share of 61% of all goods moved (tonne km) and a 79% of goods lifted (tonnes) as shown in Table 1.1 (KeyNote, 2002). Investment in rail transportation has fallen: its outdated network does not service most industries/retail centres located at the periphery of town. It is therefore not foreseeable, to have a reversal of roles between the rail and road (KeyNote, 2002). There is therefore good cause to design lighter and more fuel efficient trailers with larger payloads since that would reduce traffic pressure and emissions of oxides of nitrogen (NOx), particulate matter, carbon monoxide, and hydrocarbons.

Table 1.1 – Road transport statistical summary (Key Note, 2002)

Goods transported by road (EU)	75 %
Goods transported by road (UK)	79 %
HGV share of road transportation	87 %
European energy consumption with transportation of goods	10 %
HGV related CO_2 emissions (of total EU transport emissions)	30 %
HGV related NO_x emissions (EU)	47 %
Projected growth in haulage (next 15 years)	25 %

Even with its predominance over other types of transportation, road haulage continues to be a fiercely competitive field that is now witnessing a "technology race" between larger players. So far, this race has been focused on organizational aspects, such as remote tracking of vehicles in transit but it has been suggested that lighter materials and structures could have a significant role to play in the near future. (KeyNote, 2002). The market is also moving away from smaller rigid

trucks in favour of large articulated trailers having gross vehicle weights (GVWs) of up to 44 tonnes. The case for lightweight composite semi-trailers is therefore strong in the UK, as is already the case worldwide. Similar attempts have been researched and developed in Belgium, Holland, and Scandinavia. There are already a number of demonstrators of the technology such as the Dutch TNO "Coldfeather". In the USA a combined effort of the US Departments of Energy, Transportation, Defence, the US Environmental Protection Agency, and 16 industrial partners which should conclude in 2010 (US DOE, 2000) is also working on this area within the 21st Century Truck Program. Current demonstrators of this concept are shown in Figure 1.5.

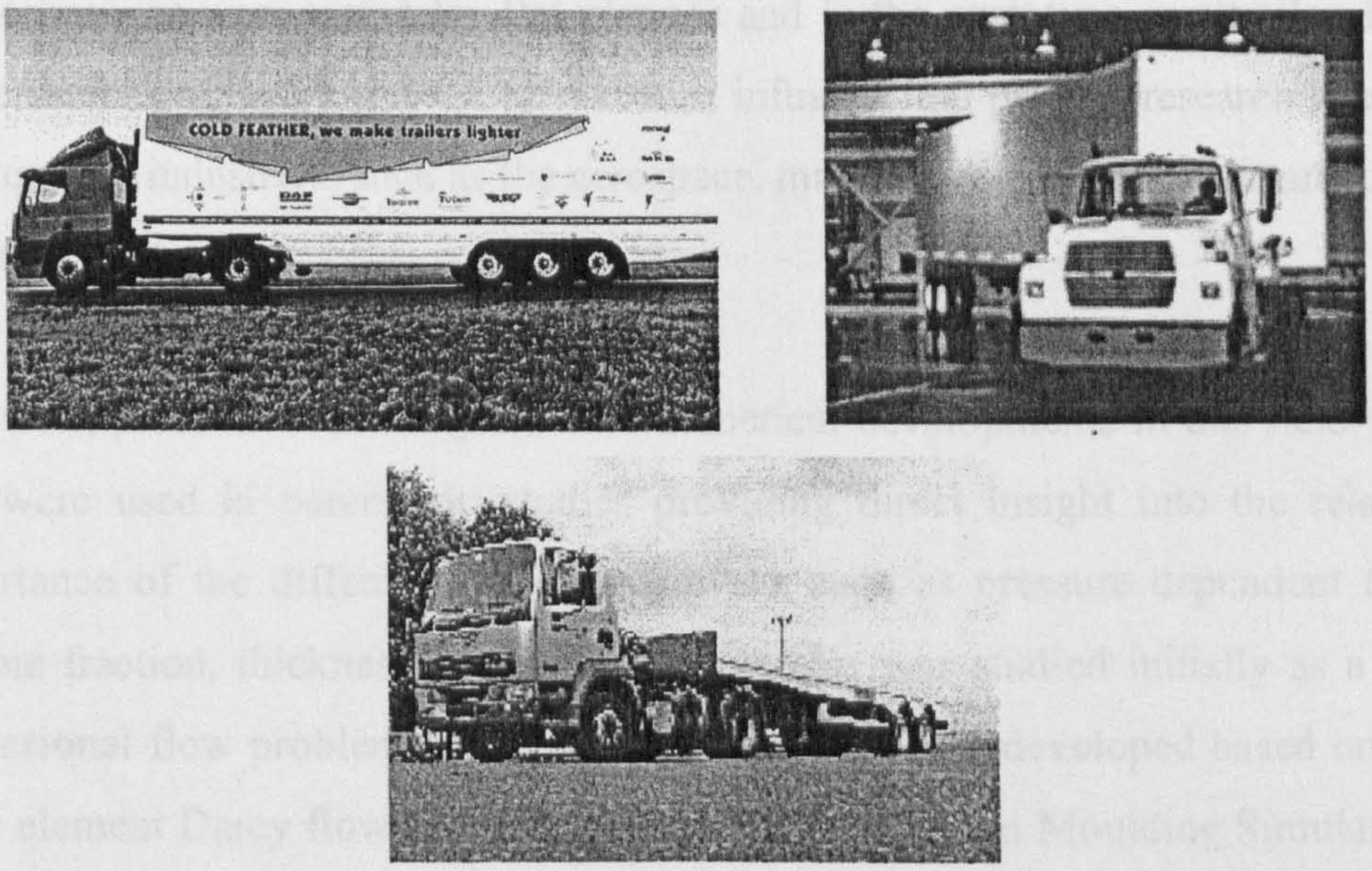

Figure 1.5 – Current demonstrators of the composite trailer concept. Top left: Cold Feather (The Netherlands); Top right: Marietta composite trailer (developed in Belgium. Manufactured in the USA); Bottom: First RoadLite flat bed trailer prototype (UK)

The RoadLite project consists of a number of UK companies specializing the composites or road transport industries. They include composite structural design (Europrojects, Ltd) and manufacturing (VT Group plc), trailer manufacturing (Southfields Coachworks) and testing (LTC, Ltd) as well as the University of Nottingham. The project was funded by the UK DfT (Department for Transport) and the Engineering and Physical Sciences Research Council (EPSRC).

1.4 AIMS AND OBJECTIVES OF THIS WORK

Within the RoadLite programme, the University of Nottingham aims to extend the understanding of vacuum infusion to improve the manufacturing of large composite components. This is achieved through experiments model development and validation. The work programme was divided between two researchers. The present work pertains to the modelling and control aspects. Co-worker A. Ragondet will present a parallel study related to the experimental work.

During the course of this work, practical guidelines and computational tools for process prediction, monitoring and control of VI were developed. These new tools and techniques were tested for flat plaques and in the prototype semitrailer. Due to the increasing industrial use of vacuum infusion, the present research applies also to other industries, such as the aerospace, marine, energy production and civil sectors.

This work presents both analytical and numerical developments in this field. The first were used in parametric studies providing direct insight into the relative importance of the different variables at work such as pressure dependent fibre volume fraction, thickness and permeability. This was studied initially as a one dimensional flow problem. A numerical model was then developed based on the finite element Darcy flow software LIMS (Liquid Injection Moulding Simulation, U. of Delaware), introducing the possibility of modelling VI in commercial software for the first time. This was done at the University of Delaware, over a period of seven months, some of which involved preliminary experimental validation work (Correia *et al, 2004*). In Nottingham, these models were used to explore the effects of variability of surface density, permeability and thickness on flow. This work, applicable to RTM and VI alike, pioneered statistical modelling in Darcy flow (Correia *et al*, 2003) and permitted simulated global strategies to be examined. This work is believed to be novel at the time of writing. The modelling strategies were supported by experimental validation and material characterization.

1.5 FUNDAMENTALS: FLOW THROUGH POROUS MEDIA

The study of flow through porous media started with Darcy (1856) and, what became known as Darcy's law has since been used to model flow through a wide variety of different media – particulate beds, porous solids, fibre beds, etc. Biot (1941) pioneered the work on flow through compressible sediments but work on flow (as in the present case) through compliant fibre beds (which are not linear elastic) is recent (e.g. Hammami *et* al, 2000 and Gutowski *et al*, 1986).

Darcy (1856) established the proportionality between flow rate Q, cross-section A and pressure gradient ΔP: the proportionality term K_h, representing the ease of flow through the medium, is known as hydraulic conductivity:

$$Q = -K_h \cdot A \cdot \frac{dP}{dx} \tag{1.1}$$

However, hydraulic conductivity is not very useful because it combines properties of the fluid with those of the porous medium. According to Scheidegger (1974) it was only after Wyckoff *et al* reported a series of successful experiments in 1933 that these factors became separated (Scheidegger, 1974). Permeability K was then defined from hydraulic conductivity K_h and fluid viscosity μ as:

$$K = K_h \cdot \mu \tag{1.2}$$

The validity and limits of Darcy's law have been tested, and theoretically confirmed (Scheiddeger, 1974). It has been shown that for liquids at very high velocities and gases at very low and very high velocities it is invalid (de Boer, 2000; Scheidegger, 1974). Hence, for liquids at a low Reynolds number it is possible to obtain the fluid velocity from the Equation (1.1). One must however recognize that, as long as the container cross-section remains constant, the velocity measured experimentally by Darcy in pipes (superficial velocity u) is smaller than the average fluid velocity in the porous medium (or filter velocity v). The ratio between them is termed porosity. This concept is illustrated in Figure 1.6.

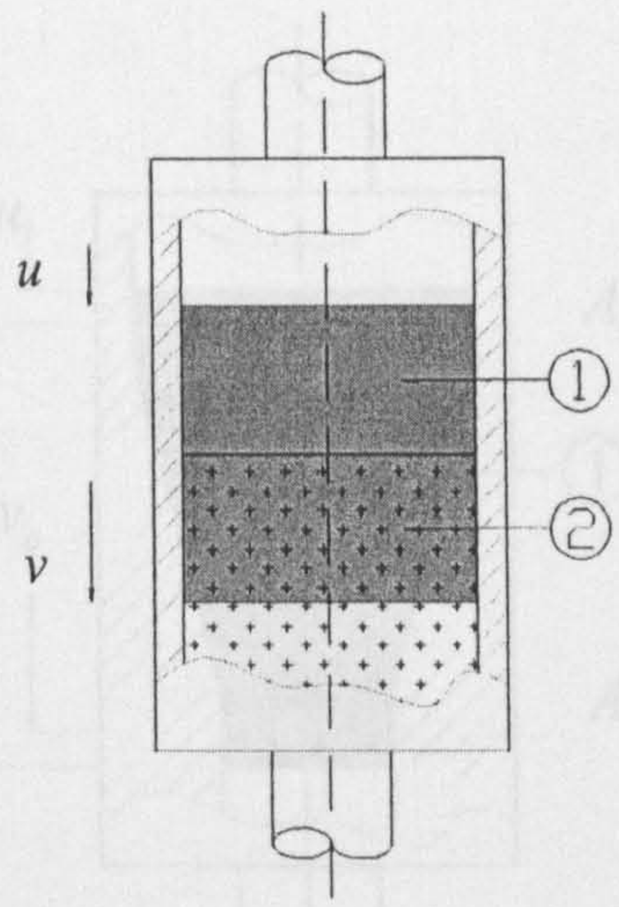

Figure 1.6 – Superficial u vs. filter v velocities. 1) Fluid, 2) porous medium

Accordingly, filter velocity v is given by:

$$v = \frac{dx}{dt} = -\frac{K}{\phi \cdot \mu} \cdot \frac{dP}{dx} \tag{1.3}$$

where ϕ represents porosity. The well-known 1D integral form of Darcy's Law then becomes:

$$x^2 = -\frac{2 \cdot K}{\phi \cdot \mu} \cdot \Delta P \cdot t \tag{1.4}$$

Another aspect of flow modelling is continuity. The continuity Equation, outlined for fluids by Euler in the early 1770's (de Boer, 2000), states the mass balance principles that govern flow. Namely that, in the simplified case shown in Figure 1.7, velocities through the porous medium are related as described in Equation (1.5).

$$u_i \cdot A_i = v_i \cdot \phi_i \cdot A_i = u_o \cdot A_o = v_o \cdot \phi_o \cdot A_o \tag{1.5}$$

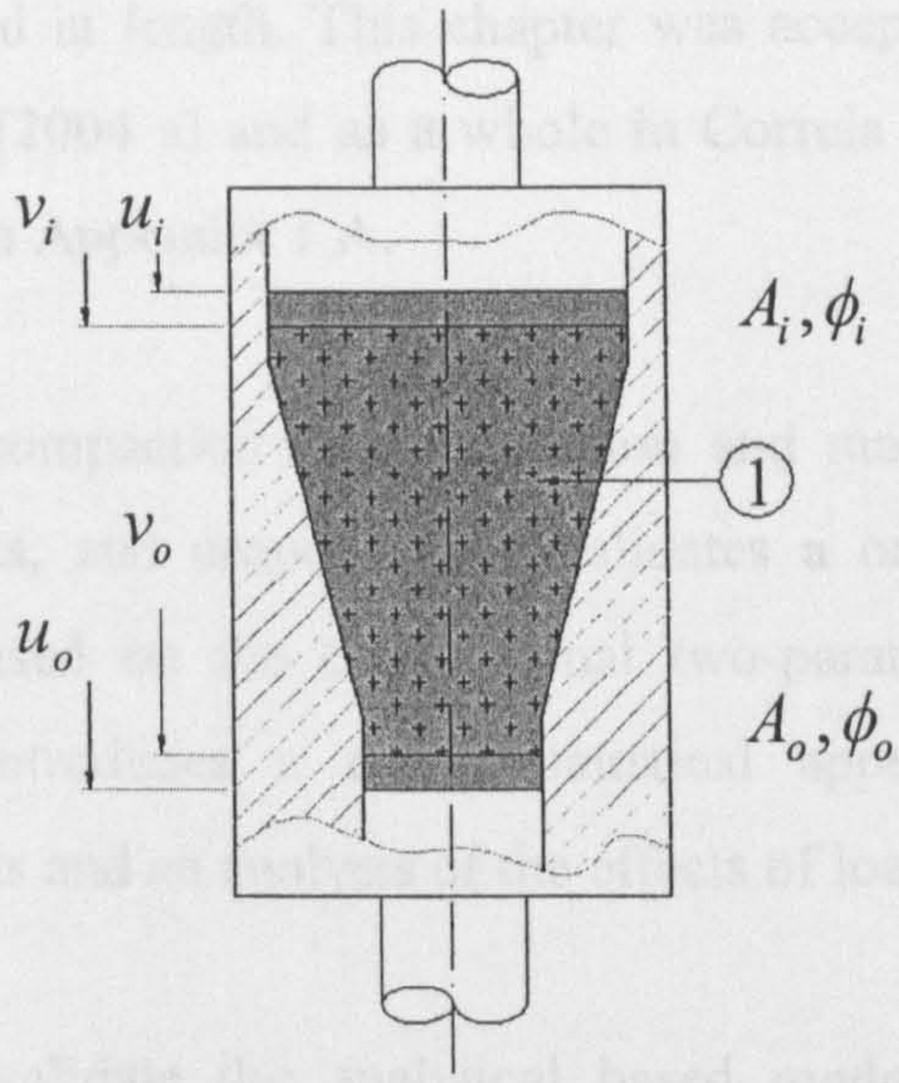

Figure 1.7 – Mass balance in flow through porous media. (1) indicates the porous medium. Ai and A_o and ϕ_i and ϕ_o represent the cross-section and porosity in the top and bottom surfaces respectively

It was not until 1948, with the works by Farrandon and, in 1950 with Litwiniszyn, that a full tensorial form of Darcy's law for anisotropic media was available. It takes the form:

$$\mathbf{u} = \frac{\mathbf{K}}{\mu} \cdot \nabla \mathbf{p} \tag{1.6}$$

Where **K** is the second order symmetric permeability tensor.

1.6 FRAMEWORK

This work is structured so that each chapter stands on its own, containing an introduction and review, the work done in that discrete section and the main conclusions. There is also an overall conclusions chapter which synthesises the information of all chapters in a broader context.

Chapter 2 discusses the mathematical development of a model of the VI process, from analysis and correlation of available models to further analytical developments and numerical solutions to the differential Equations. The implications of compressible media for flow, pressure field and component

thickness are discussed at length. This chapter was accepted for publication, in part, in Correia *et al* (2004 a) and as a whole in Correia *et al* (2004 b) both of which are referenced in Appendix 1.A.

Chapter 3 discusses compaction characterization and modelling for textile and random reinforcements, and proposes and validates a one-parameter empirical compaction model based on the conventional two-parameter power law. The experimental work introduces a novel statistical approach to quantify the variability of the results and an analysis of the effects of load cycling is proposed.

Chapter 4 seeks to validate the analytical based model for, firstly, pressure distribution, secondly, by confirming thickness distribution predictions and, thirdly, impregnation times. This last component was accepted for publication as a part of Correia *et al* (2004 a).

Chapter 5 describes the finite element control volume numerical model. It discusses development and validation with experimental and analytical based predictions. It was also submitted for publication as a part of Correia *et al* (2004 a).

Chapter 6 discusses the issues of variability and control. It explains the statistical flow modelling work and both applications and implications of this type of analysis. Typical codes are discussed and variability studies are shown for flat plates and complex geometries (such as the RoadLite project demonstrator) for both RTM and VI. The chapter also introduces the topic of virtual control for real-life materials, discussing the possibilities of real-time application to flow monitoring and control.

Chapter 7 contains the overall discussion, further work, and conclusion sections.

2 AN ANALYTICAL STUDY INTO THE VACUUM INFUSION PROCESS

This chapter is primarily concerned with the analytical formulation of governing Equations for flow of incompressible fluids through compacting porous media and their application to VI. The literature on VI modelling, incorporating the effects of compliant media on permeability and flow, is reviewed. A complete development of the proposed governing Equation is shown along with a suggested numerical solution. The proposed model is subsequently used to quantify the effect of process parameters such as inlet and outlet pressures, fibre architecture and lay-up on flow. Implications for industrial production are discussed.

2.1 OVERVIEW

As established in Chapter 1, the replacement of open mould techniques by LCM moulding is advantageous both environmentally and in terms of mechanical properties, especially for large components. Unfortunately, while there are many industrial patents for this process, a dedicated flow-modelling tool, which can account for the compliant medium, does not yet exist. The research presented here addresses the issue of the development of analytical fluid dynamics models for such cases and provides a background for future finite element models. It is hoped that such models will benefit the composites industry by helping design and producing manufacturing guidelines (such as the ones presented in chapter 3 and summarized in Appendix 3.D). This chapter also addresses the relevance of such models by discussing the relative importance of reinforcement compliance and flow parameters in pressure field and fill time solutions. Conversely, it also highlights the need for development of presently available models, for example in situations where the medium is highly compliant and merits specialised modelling capabilities.

This chapter builds on current knowledge of VI (through a comparative study of the mathematical models in the literature) and adds to it in the development of a more complete model of flow through compliant media. The developments shown

here do not however lead to a fully analytical solution for the problem. Hence Section 2.7 discusses a possible numerical solution (through a finite difference approach) of this problem. Nevertheless, while a fully analytical solution is not achieved, it is believed that this work is relevant since the issue of compliance-dependent fluid pressure field and fill time had not, at the time of writing, been clearly addressed in flow through porous media. The pressure-compliance dependence is illustrated in Figure 2.1.

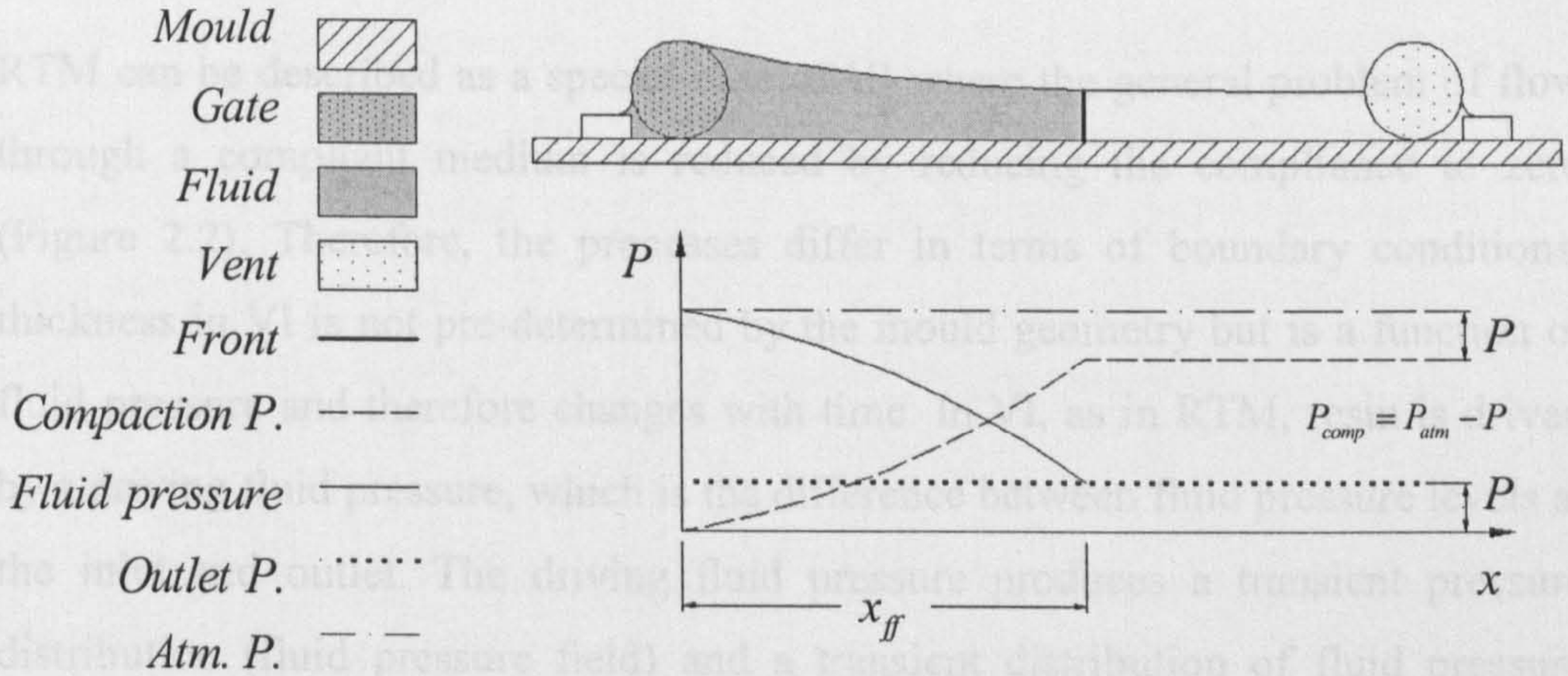

Figure 2.1 – Schematic of effect of fluid pressure on compaction in VI

The objectives of the present chapter are therefore to:

1. Develop fill time and pressure solutions to the problem of flow through compliant media.
2. Establish the relevance of this model and study the impact of different parameters on the solutions.
3. Lay the ground work for further developments in modelling VI for complex geometries.

Since the practicalities of modelling complex geometries require flexible FE models this chapter will not look into the 3D nature of the problem (which is addressed in chapters 5 and 6) but will focus on in depth developments for a 1D flow case. It is acknowledged that distribution media (Figure 1.3) are regularly used in an industrial context, inducing through-thickness flow in the

reinforcement and forming a three dimensional flow front which advances first through the distribution medium and lags in the reinforcement. This lead-lag effect is not studied here. Nevertheless, this flow enhancement medium also acts as a compacting reinforcement and, therefore, falls within the scope of this work. The association between highly dissimilar materials is part of the work by A. Ragondet (2004) and is integrated in the same project.

2.2 MODELLING TERMINOLOGY

RTM can be described as a special case of VI where the general problem of flow through a compliant medium is reduced by reducing the compliance to zero (Figure 2.2). Therefore, the processes differ in terms of boundary conditions: thickness in VI is not pre-determined by the mould geometry but is a function of fluid pressure and therefore changes with time. In VI, as in RTM, resin is driven by a driving fluid pressure, which is the difference between fluid pressure levels at the inlet and outlet. The driving fluid pressure produces a transient pressure distribution (fluid pressure field) and a transient distribution of fluid pressure gradients (fluid pressure gradient field).

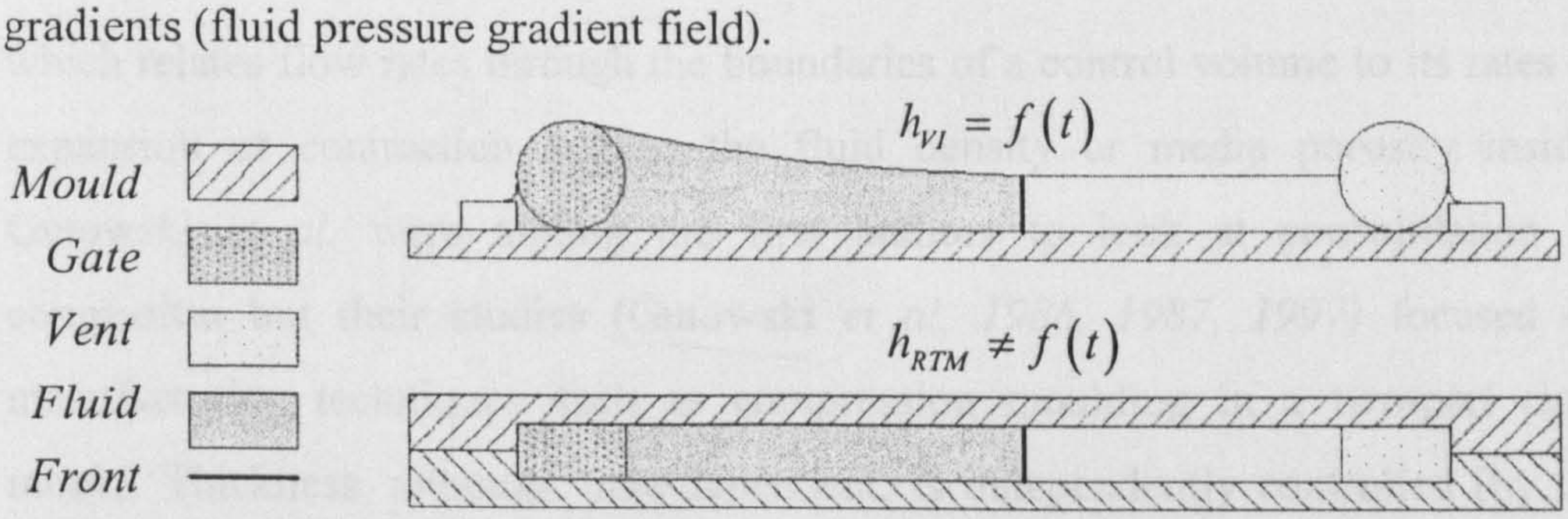

Figure 2.2 –Thickness distributions in VI (top) and RTM (bottom)

The infusion of two identical preforms by RTM and VI, using the same driving fluid pressure, typically involves different fluid pressure fields. Whereas in RTM compaction is often constant throughout the preform, in VI it varies locally. VI preforms are compacted by a compaction pressure field, which is equal to the atmospheric pressure minus the local fluid pressure field, and varies with location and time.

2.3 BACKGROUND

2.3.1 Models of the VI process

Hydrological flow in consolidating soil was initially discussed by Biot (1941). Hydrology is primarily concerned with saturated diffusivity studies, i.e. pore water movement in consolidating saturated soil and deformation of a saturated porous mass. Major hydrological theories on flow through compacting media assume non-coupled permeability and fluid pressure (Scheidegger, 1974). More recent consolidation research (de Boer, 2000) still makes assumptions such as uniform compaction pressure. Hydrological theories have been adapted to composites manufacturing by Gutowski, Cai, Kingery and Wineman (1986), Gutowski, Morigaki and Cai (1987), Gebart (1992), and Gutowski and Dillon (1997). The basis of all models is the continuity equation (Equation (2.1)).

$$\oint_S \rho \cdot \mathbf{u} \cdot \hat{\mathbf{n}} \cdot dS + \frac{\partial}{\partial t} \cdot \int_V \rho \cdot \phi \cdot dV = 0 \tag{2.1}$$

which relates flow rates through the boundaries of a control volume to its rates of expansion or contraction and to the fluid density or media porosity inside. Gutowski *et al.* were among the first authors to look at consolidation of composites but their studies (Gutowski *et al, 1986, 1987, 1997)* focused on manufacturing techniques such as compression moulding in a two-part rigid mould. Thickness, although time-dependent, is independently controlled (by the compression moulding machine parameters) and there is no fluid injection. In the one dimensional flow case they show that the pressure field can be described by:

$$P(x) = \frac{\mu}{2 \cdot K_x \cdot v_f} \cdot \frac{dv_f}{dt} \cdot \left(a^2 - x^2\right) \tag{2.2}$$

This is illustrated in Figure 2.3.

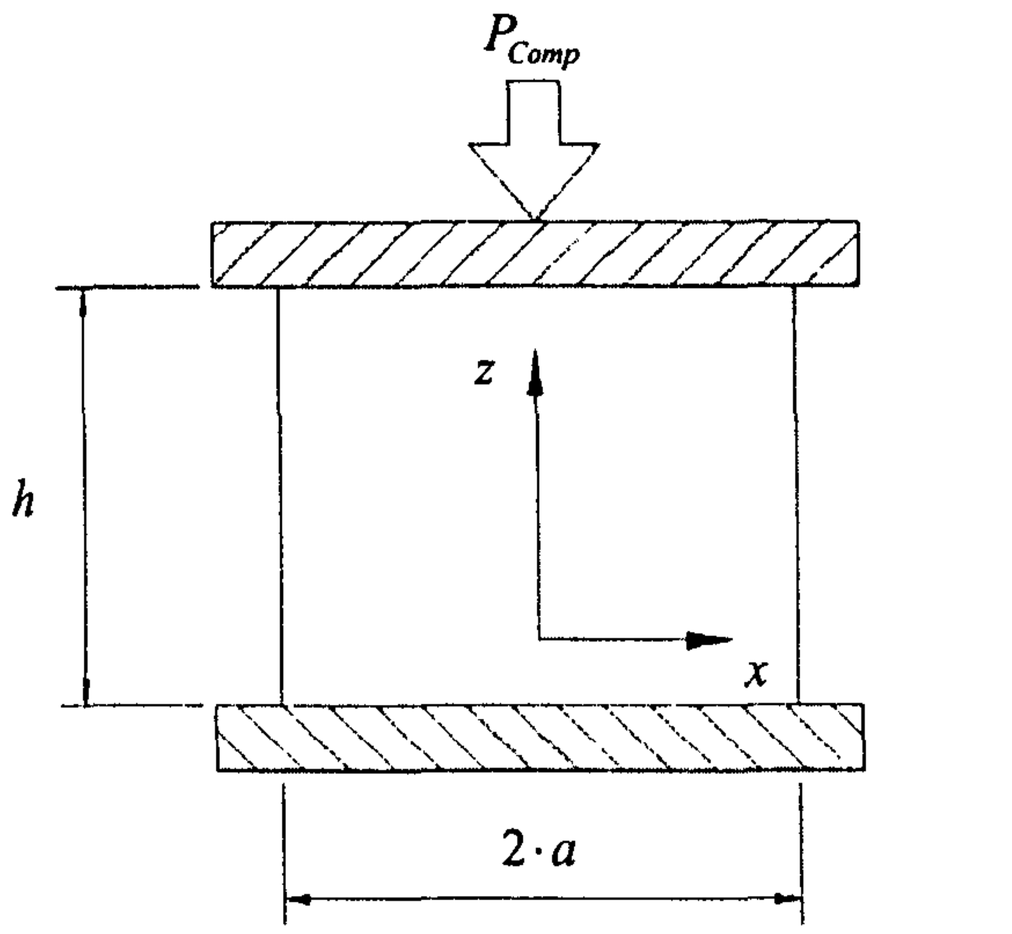

Figure 2.3 – Compression moulding of a representative volume element described by Equation (2.2) (Gutowski et al, 1997)

Note that while compression moulding is similar to VI, in that permeability changes throughout the process, compression moulding imposes a constant permeability in x at any moment. Nevertheless, it is interesting to note that a fully parabolic pressure field distribution is obtained by Gutowski *et al* (1997) for this case since, as will be shown in chapter 3, that can be a good approximation for the VI case. Figure 2.4 illustrates the variables on a VI control volume.

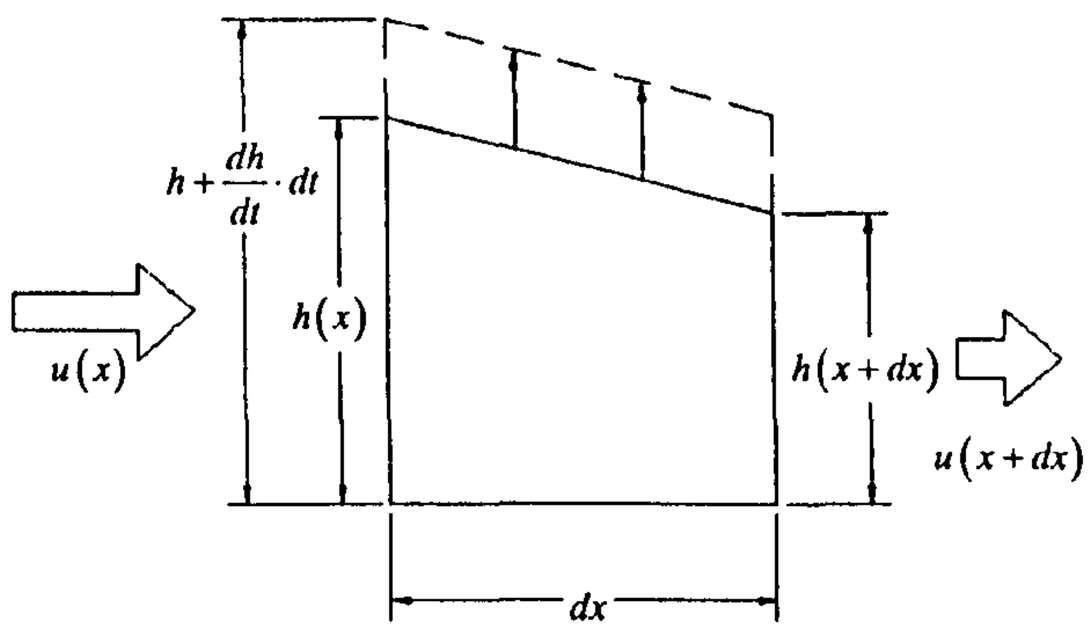

Figure 2.4 – Representative volume element for the vacuum infusion process. Expansion rate: dh/dt. Velocity of flow through the boundaries of the element: u. Thickness: h

Hammami and Gebart (1998, 2000) modelled the vacuum infusion process focussing on 1D flow. As Appendix 2.A shows, applying Equation (2.1) to a 1D flow case along x where the control volume is defined over the whole thickness h of the laminate results in:

$$\frac{\partial h}{\partial t} = -\frac{\partial (u.h)}{\partial x} \tag{2.3}$$

Despite the fact that different algebraic forms of the same governing Equation (2.3) are suggested by Gutowski *et al.* in 1987 and Hammami *et al.* in 2000, both are identical and represent the same approach. Their equivalence is presented in Appendix 2.B.1.

Han, Jiang, Zhang and Wang (2000) used a different approach based on earlier work by Scheidegger (1974) for soil compaction. This model can be re-written in a form comparable to the above Equations, as shown in Appendix 2.B.2:

$$\frac{\partial h}{\partial t} = h_0 \frac{\partial u}{\partial x} \tag{2.4}$$

Kang, Lee and Hahn (2001) offer another model of the vacuum infusion process. Based on the original work by Davé (1990) they propose:

$$-\frac{1}{v_f} \cdot \frac{\partial v_f}{\partial t} = \frac{\partial}{\partial x}\left(\frac{K}{\mu} \cdot \frac{\partial P}{\partial x}\right) \tag{2.5}$$

Appendix 2.B.3 shows that, once more, an apparently dissimilar model can be converted to a format comparable to Scheidegger-Han (2.4) and Gutowski-Hammami (2.3), specifically:

$$\frac{\partial h}{\partial t} = -h \cdot \frac{\partial u}{\partial x} \tag{2.6}$$

2.3.2 Unification of published models of vacuum infusion

As shown in Appendix 2, an exact correspondence between the models proposed by Gutowski *et al* and Hammami *et al* can be established. Nevertheless, these

models do not agree with those of Han *et al* and Kang *et al*. The dissimilarities in Equations (2.3), (2.4) and (2.6) can be grouped into two types (I and II) by algebraic form of their velocity differential terms:

$$\text{Type I: } \frac{\partial(uh)}{\partial x} \qquad \text{Type II: } h\frac{\partial u}{\partial x} \tag{2.7}$$

Clearly, Type II is a subset of Type I, if one assumes:

$$\frac{\partial h}{\partial x} \approx 0 \tag{2.8}$$

and does:

$$\frac{\partial(uh)}{\partial x} = h\frac{\partial u}{\partial x} + u\frac{\partial h}{\partial x} \tag{2.9}$$

The above establishes the similarity between the model by Kang *et al* and the one developed by Gutowski-Hammami. Scheidegger and Han *et al* assume a further simplification on type II by stating that

$$h \approx h_0 \tag{2.10}$$

where h_0 is the initial thickness of the porous medium. The authors are therefore neglecting variations in thickness in the RHS of Equation (2.6) but not in the LHS. Furthermore, this analysis highlights the difference in sign in the RHS of Scheidegger and Han, when compared with all other authors, which is not compatible with the physical mechanisms of VI, namely that, due to continuity (Equation (2.1)), the velocity gradient in VI is positive and therefore requires the minus sign in Equation (2.4).

The four apparently dissimilar models offered in the literature by six different authors can therefore be unified into a single model given in Equation (2.3) and described in detail in Appendix 2.A, with variations due to different assumptions.

In line with the above discussion, the present work implements the Gutowski-Hammami governing Equation (2.3) as the foundation for further analytical developments. Through these developments, it explores the fundamental differences and highlights the similarities between VI and RTM in terms of fluid pressure field and flow front position, and provides a background for the development of functional 2D/3D FE models of this process. In parallel with the results for this model, the Han-Scheidegger Equation is also solved for comparison, as it is the least similar to the unified model.

2.4 COMPACTION MODELLING

Variable thickness in VI has quantifiable implications for permeability, porosity and flow. For illustration purposes, a typical thickness distribution for a vacuum-infused, chopped strand mat panel is shown in Figure 2.5.

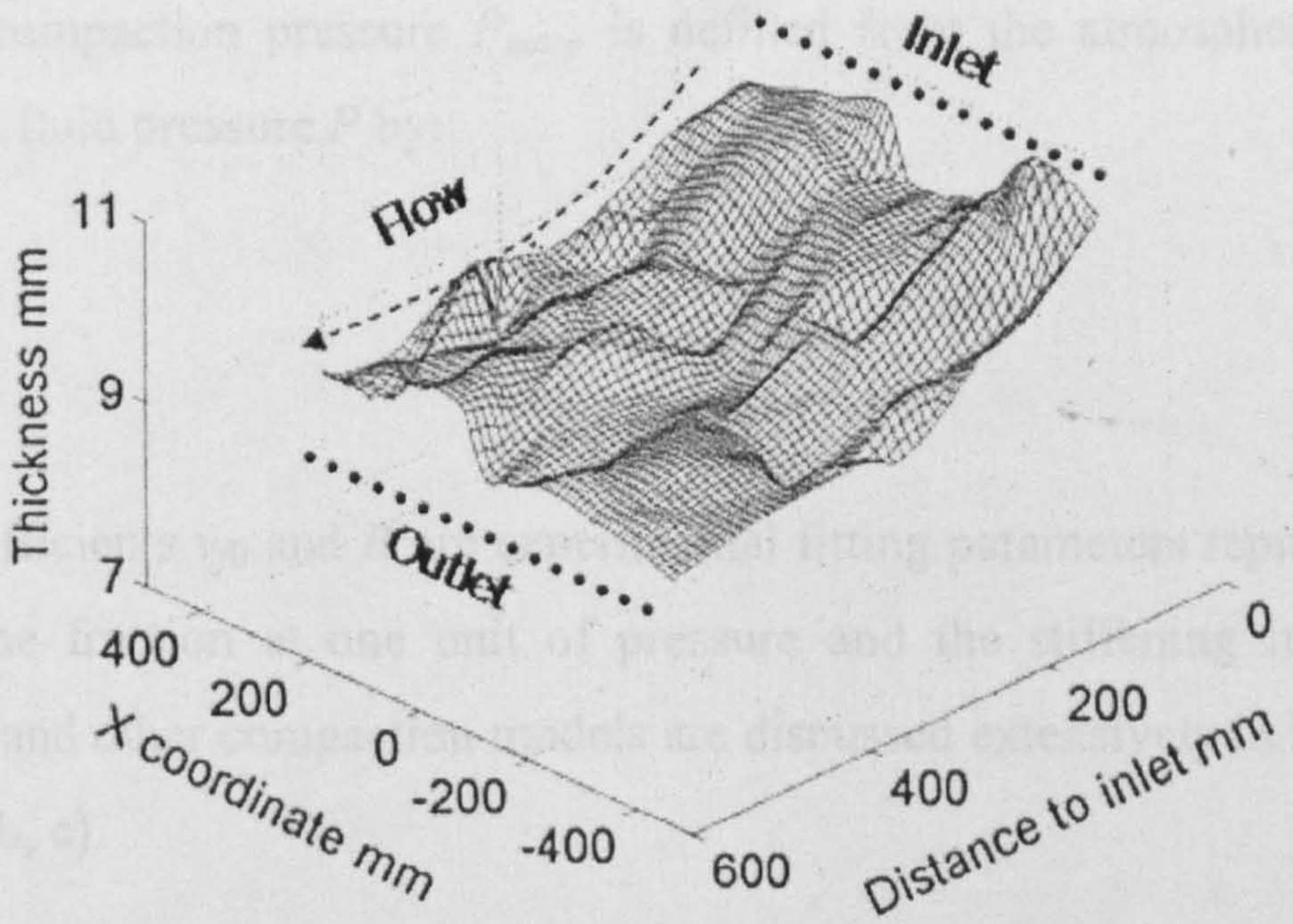

Figure 2.5 – Cured thickness of a vacuum infused CSM panel

This flat panel, consisting of 12 layers of CSM reinforcement was infused with polyester resin using a line injection scheme. Once cured, the panel was cut and

its thickness measured by dial gauge at 104 locations (details on thickness measurement can be found in Section 4.5, and shown in Figure 4.15 on page 91). The thickness is clearly dependent on position, in this case distance from inlet, showing the effect of local fluid pressure and preform compressibility: the higher local fluid pressure at the inlet reduces compaction pressure on the reinforcement and increases thickness. In this example, the total difference in thickness is 2.2 mm, which corresponds to 22% of the average thickness of the panel.

2.4.1 Compaction models

This section aims to introduce the compaction model used in the present analysis while a detailed discussion on compaction modelling is left for chapter 3. Compaction of fibre preforms was studied experimentally and analytically by several research groups resulting in more or less complex empirical or analytical based models. Nevertheless, for the purpose of this study, an empirical power law model of compaction was used:

$$v_f = v_{f0} \cdot P_{comp}{}^{B} \tag{2.11}$$

where the compaction pressure P_{comp} is defined from the atmospheric pressure P_{atm} and the fluid pressure P by:

$$P_{comp} = P_{atm} - P \tag{2.12}$$

and the coefficients v_{f0} and B are experimental fitting parameters representing the fibre volume fraction at one unit of pressure and the stiffening index. These parameters and other compaction models are discussed extensively in Robitaille *et al* (1999 a, b, c).

2.4.2 On compaction hysteresis and dry vs. saturated compaction

The compaction behaviour of fibre reinforcement is different from its expansion behaviour. Reinforcement compaction hysteresis is illustrated in Figure 2.6 where the two first compaction cycles of a saturated Formax™ FGE 117 stitched triaxial

textile are shown. Dry compaction properties differ from those found in saturated conditions (Figure 2.7). The mechanism that drives this change is a reduction in fibre friction coefficient due to lubrication. This has important implications for VI given that the reinforcement is compacted in a dry state and, as fluid pressure increases, expands in saturated conditions. Representative data should therefore be obtained in saturated compaction experiments whenever possible. This chapter will use dry compaction data for illustration purposes.

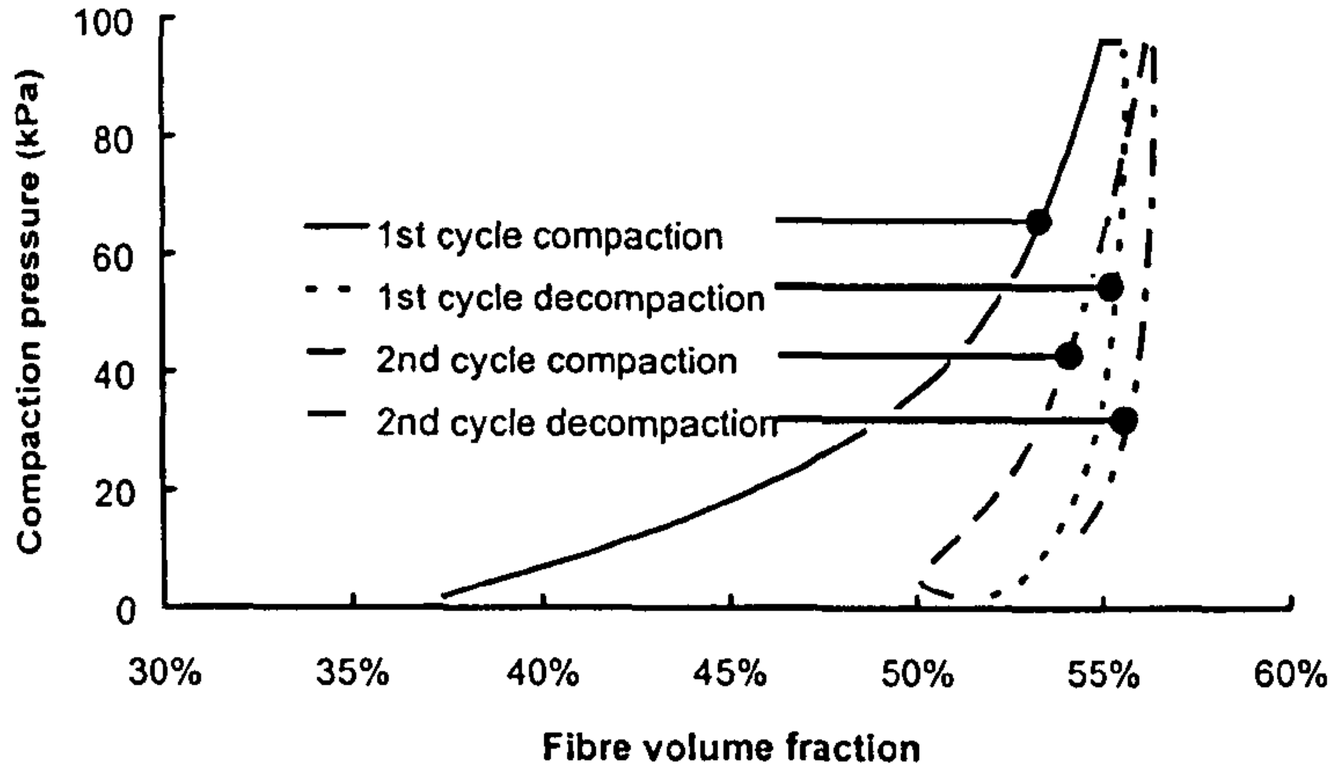

Figure 2.6 – Compaction - expansion cycle for saturated Formax™ FGE117 stitched triaxial reinforcement (3 layers)

Note that at the end of all compaction cycles there is a discontinuity in the plot. This results from a one minute pause which was allowed for fibre reorganization and measurably increases the fibre volume fraction at the end of the cycle. The value of the increase in fibre volume fraction reduces from cycle to cycle.

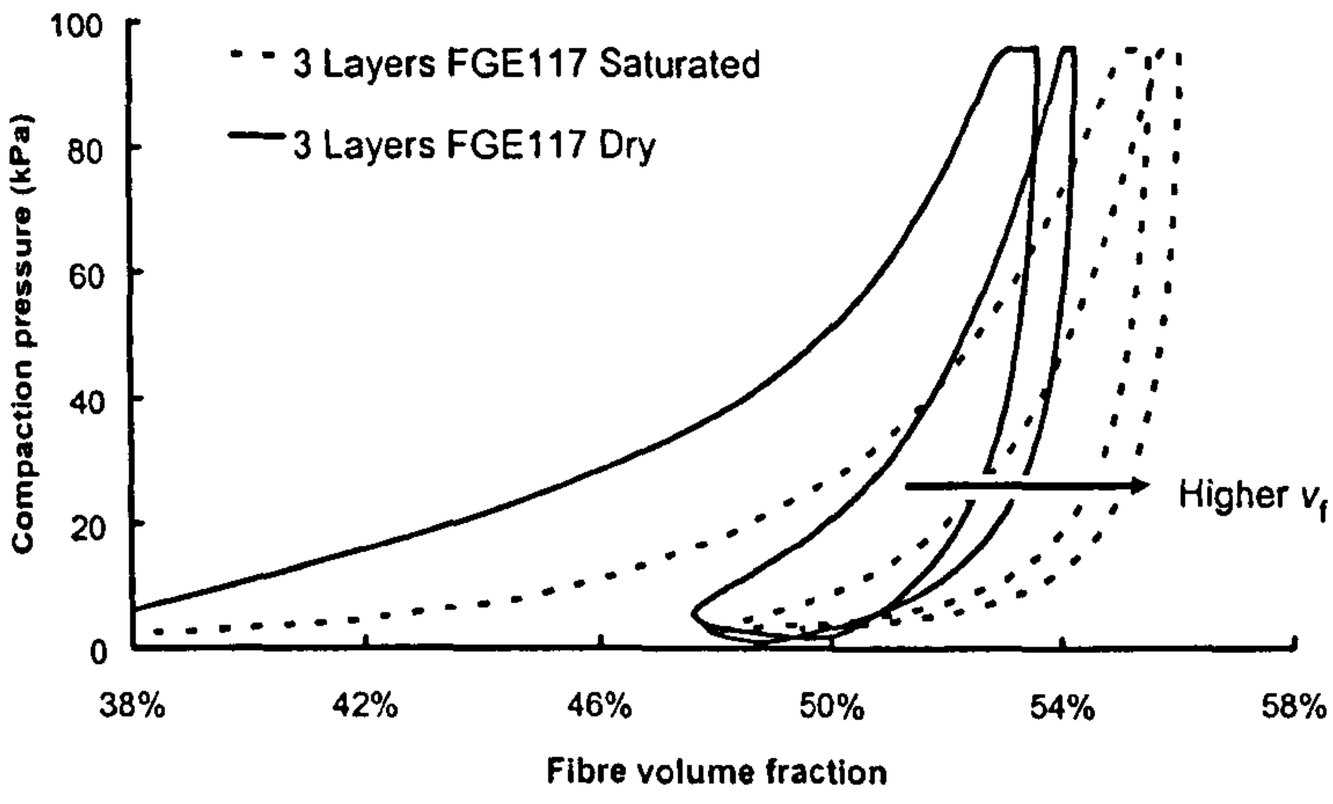

Figure 2.7 – Comparison of dry and saturated compaction for three layers of FGE117

As will be discussed in depth in chapter 3, fibre lubrication results in an easier network reorganization process leading to higher fibre volume fractions v_f in saturated reinforcements.

2.5 PERMEABILITY MODELS

Originally developed in 1927 for flow through an array of channels of varying cross-sections, the Kozeny-Carman model of permeability (2.13) has been used extensively to model different types of porous media and applied with reasonable success to woven or aligned fibres (Scheidegger, 1974; Gutowski *et al,* 1987):

$$K = k_c \cdot \frac{1}{S_0^{\,2}} \cdot \frac{\phi^3}{(1-\phi)^2} \tag{2.13}$$

where S_0 is the specific surface exposed to fluid, as proposed by Carman and k_c represents the Kozeny constant. S_0 represents the exposed surface of a single fibre per unit volume of that fibre (bulk glass). It is therefore dependent only on the radius of the fibre and, considering that it is cylindrical, is equal to $2/r$ (where r is the fibre radius). As for the value of the constant k_c, Kozeny calculated that it should be approximately ½. Carman, however, proposed a value of $1/5$ based on experimental evidence. This is one of the common apprehensions with this model (Scheidegger, 1974). For the purpose of this study the name "Kozeny constant" k will be used to signify the combination of the classical Kozeny constant (k_c) and of the exposed surface function proposed by Carman. One can justify this simplification by acknowledging that since the model is not fully predictive, k could be seen as an experimental fitting parameter. Algebraically:

$$k = \frac{k_c}{S_0^{\,2}} \tag{2.14}$$

Another problem with the Kozeny-Carman Equation is that it calculates transverse permeability values greater than zero at fibre volume fractions that would otherwise block transverse flow in unidirectional reinforcements (Gutowski *et al*, 1987). In order to resolve this problem, they propose a modified model:

$$K = k' \frac{\left(\sqrt{\frac{v_{fa}'}{v_f}} - 1\right)^3}{\left(\frac{v_{fa}}{v_f} + 1\right)} \tag{2.15}$$

This coincides with Equation (2.13) at a maximum theoretical fibre volume fraction v_{fa} of one but differs at lower values. Nevertheless, due to the dependence of permeability on orientation, different experiments have to be performed to fit the above models to an orthotropic reinforcement. Gebart *et al* 1992 offered a different approach in their study of flow through oriented fibres. They proposed models to fit the permeability values in both the fibre and the transverse directions:

$$K_1 = c_1 \cdot \frac{\left(1 - v_f\right)^3}{v_f^{\,2}} \quad and \quad K_2 = c_2 \left(\sqrt{\frac{v_{f_a}}{v_f}} - 1\right)^{\frac{5}{2}} \tag{2.16}$$

Note that the parameters c_1 and c_2 are also functions of fibre radius and packing and have been determined through an analytical development. In 1996 Rudd *et al* propose a tensorial weighted method to combine these Equations in materials composed of a number of layers with different orientations. Bruschke and Advani (1993) approach the permeability problem from a different perspective. The basic capillary model used in the formulations above is replaced with an analytic cell model at lower fibre volume fractions and a number of closed form solutions are obtained for different fibre packing arrangements. Nevertheless, due to the one-dimensional nature of this work, the Kozeny-Carman Equation (2.13) is used for its simplicity. As was mentioned Equation (2.13) does not represent the behaviour of the reinforcements with complete accuracy but permeability and compaction models can be seen as separate (or modular) fitting functions: replaceable or adapted at any stage.

2.6 ANALYTICAL DEVELOPMENT

In-plane flow through a porous medium which is compacting in the thickness direction can be expressed by Equations (2.3), (2.11), (2.12) and (2.13). Equation (2.17) represents superficial velocity, given by Darcy's law:

$$u_x = -\frac{K}{\mu}\frac{dP}{dx} \tag{2.17}$$

Focussing on 1D flow in the x direction and combining Equations (2.3) and (2.17) one obtains:

$$\frac{\partial h}{\partial t} = -\frac{\partial\left(-\frac{h \cdot K}{\mu} \cdot \frac{\partial P}{\partial x}\right)}{\partial x} \tag{2.18}$$

The partial differentials can be expanded to:

$$\frac{\partial h}{\partial t} = \frac{1}{\mu} \cdot \left[\left(K \cdot \frac{\partial h}{\partial x} + h \cdot \frac{\partial K}{\partial x}\right)\frac{\partial P}{\partial x} + h \cdot K \cdot \left(\frac{\partial^2 P}{\partial x^2}\right)\right] \tag{2.19}$$

Since both thickness and permeability are functions of pressure, which is a function of position in the mould x ($h[P(x)]$ and $K[P(x)]$) Equation (2.19) can be recast as:

$$\frac{\partial h}{\partial t} = \frac{1}{\mu} \cdot \left[\left(K \cdot \frac{dh}{dP} + h \cdot \frac{dK}{dP}\right) \cdot \left(\frac{\partial P}{\partial x}\right)^2 + h \cdot K \cdot \left(\frac{\partial^2 P}{\partial x^2}\right)\right] \tag{2.20}$$

A characteristic of the pressure field solution for VI arises from Equation (2.20), which does not feature partial derivatives of h and K with respect to x. Pressure remains constant in time if it is calculated not at the position x of a point inside the flow but at its relative location between the inlet and the flow front. For example, pressure is constant midway between the inlet and the outlet, even though the

physical location of the mid-point changes at each moment. This stems from the fact that permeability K is a function of porosity and therefore can be written as a function of stack thickness h. The in-plane fluid pressure field can therefore be solved once and scaled with flow front movement. This is achieved by performing a variable substitution

$$\alpha = \frac{x}{L} \tag{2.21}$$

where L is the instantaneous flow front position. In terms of this dimensionless parameter, the flow front is located at $\alpha = 1$ while the inlet is at $\alpha = 0$ regardless of time. This change of variable introduces a new function in the pressure term, making pressure P a composite function. In view of this, the pressure field differential becomes:

$$\frac{\partial\left(P\left(\alpha(x)\right)\right)}{\partial x} = \frac{\partial P(\alpha)}{\partial \alpha}\frac{\partial \alpha(x)}{\partial x} \tag{2.22}$$

Applying (2.22) to (2.20) one obtains:

$$\frac{\partial h}{\partial t} = \frac{1}{\mu \cdot L^2}\left[\left(K \cdot \frac{\partial h}{\partial P} + h \cdot \frac{\partial K}{\partial P}\right) \cdot \left(\frac{\partial P}{\partial \alpha}\right)^2 + h \cdot K \cdot \left(\frac{\partial^2 P}{\partial \alpha^2}\right)\right] \tag{2.23}$$

Furthermore, in this new coordinate system, $h(t)$ is also a composite function of $\alpha(t)$ and the LHS of Equation (2.23) can be written as:

$$\frac{\partial h}{\partial t} = \frac{\partial\left(h\left(\alpha\left(L(t)\right)\right)\right)}{\partial t} = \frac{\partial\left(h(\alpha)\right)}{\partial \alpha} \cdot \frac{\partial\left(\alpha(L)\right)}{\partial L} \cdot \frac{\partial\left(L(t)\right)}{\partial t} \tag{2.24}$$

The development of the LHS of (2.24) is shown in Appendix 2.C and leads to:

$$\frac{\partial h}{\partial \alpha}\frac{\partial \alpha}{\partial t} = \frac{h^* \cdot \alpha \cdot K}{\mu \cdot L^2} \cdot \frac{\partial h}{\partial P} \cdot \left(\frac{\partial P}{\partial \alpha}\right)^2 \quad \text{with} \quad h^* = \frac{h}{[h]_{\alpha=1}} \tag{2.25}$$

Where h^* is the thickness value normalised with the thickness at the flow front. Through the normalised coordinate α, which leads to the developments shown in Equations (2.24) and (2.25), one can convert the partial differential Equation (2.23) into an ordinary differential Equation (ODE). Applying the variable substitution on the RHS and rearranging Equation (2.23) results in:

$$\frac{d^2P}{d\alpha^2} = \left(\left(\frac{h^* \cdot \alpha - 1}{h}\right) \cdot \frac{\mathrm{dh}}{\mathrm{dP}} - \frac{1}{K} \cdot \frac{\mathrm{dK}}{\mathrm{dP}}\right) \cdot \left(\frac{dP}{d\alpha}\right)^2 \tag{2.26}$$

where $^{dh}/_{dP}$ and $^{dK}/_{dP}$ are functions of pressure resulting from the derivative of the compaction and permeability models. If one chooses to use the expression for compaction pressure given in Equation (2.11) these derivatives become:

$$\frac{dK}{dP} = k \cdot B \cdot \frac{\left(-3 \cdot {P_{Comp}}^{-(B+1)} \cdot {v_{f0}} + {P_{Comp}}^{B-1} \cdot {v_{f0}}^3 + 2 \cdot {P_{Comp}}^{-2 \cdot B-1}\right)}{{v_{f0}}^2} \tag{2.27}$$

And

$$\frac{dh}{dP} = \frac{\rho_{surface}}{\rho} \cdot \frac{B}{v_{f0} \cdot {P_{comp}}^{B+1}} \tag{2.28}$$

Importantly, Equation (2.26) eliminates the variable "time" t from the pressure field solution. In one dimensional flow this equates to the acknowledgement that the pressure field is of a scalable nature, being invariant in the normalised referential α. The implications for 1D flow calculation are relevant since it is no longer necessary to calculate the pressure field at every time step. Other repercussions, such as the time-independent comparison between VI and flow through non-compressing media (such as RTM), which reveals the equivalence of these processing techniques, will be discussed in later sections.

2.7 NUMERICAL SOLUTION

A finite difference implementation of Equation (2.26) was obtained from the discrete central difference form of the pressure field Equation (2.26):

$$\left(P_{n+1}-2P_n+P_{n-1}\right)\Big|_i = \left[\left(\frac{P_{n+1}-P_{n-1}}{2}\right)^2 \cdot \left(\frac{h^*_n \cdot \alpha_n - 1}{h_n} \cdot \left(\frac{dh}{dP}\right)_n - \frac{1}{K_n}\left(\frac{dK}{dP}\right)_n\right)\right]\Big|_{i-1} \tag{2.29}$$

Equation (2.29) is then expressed as:

$$\mathbf{A}\cdot\mathbf{p}_i = \mathbf{c}\left(\mathbf{p}_{i-1}\right) \tag{2.30}$$

Where **A** is the sparse symmetric matrix of coefficients and **c** is the vector of constants obtained from the solution of the RHS of Equation (2.29) with the previous iteration's fluid pressure field and the boundary conditions at the inlet ($\alpha = 0$) and the flow front ($\alpha = 1$):

$$\begin{cases} P_1 = P_{inlet} \Leftarrow \alpha = 0 \\ P_n = P_{outlet} \Leftarrow \alpha = 1 \end{cases} \tag{2.31}$$

The pressure field solution is then obtained by the inversion of the sparse-square coefficient matrix **A**, achieved through Gaussian elimination (Matlab™ function reference, 2002 and Anderson *et al*, 1999), and subsequent multiplication:

$$\mathbf{p}_i = \mathbf{A}^{-1}\cdot\mathbf{c}\left(\mathbf{p}_{i-1}\right) \tag{2.32}$$

In light of the non-linearity of Equation (2.26), the finite difference solution of the pressure field can only be achieved through an iterative approach. The required initial estimate of the pressure values was obtained by imposing **c**={0}, leading to the typical pressure field solution of RTM. Convergence of consecutive iterations is calculated through the norm of the vector formed by the pressure differences in

each node and is limited by the user (a value of 1 x 10^{-6} Pa was used). Note that norm is the Euclidean length of a vector. The error r between iterations k and k-1 is therefore:

$$r = \sqrt{\sum \left(P_i^k - P_i^{k-1} \right)^2} \tag{2.33}$$

The numerical algorithm presented in Figure 2.8 was implemented in Matlab™.

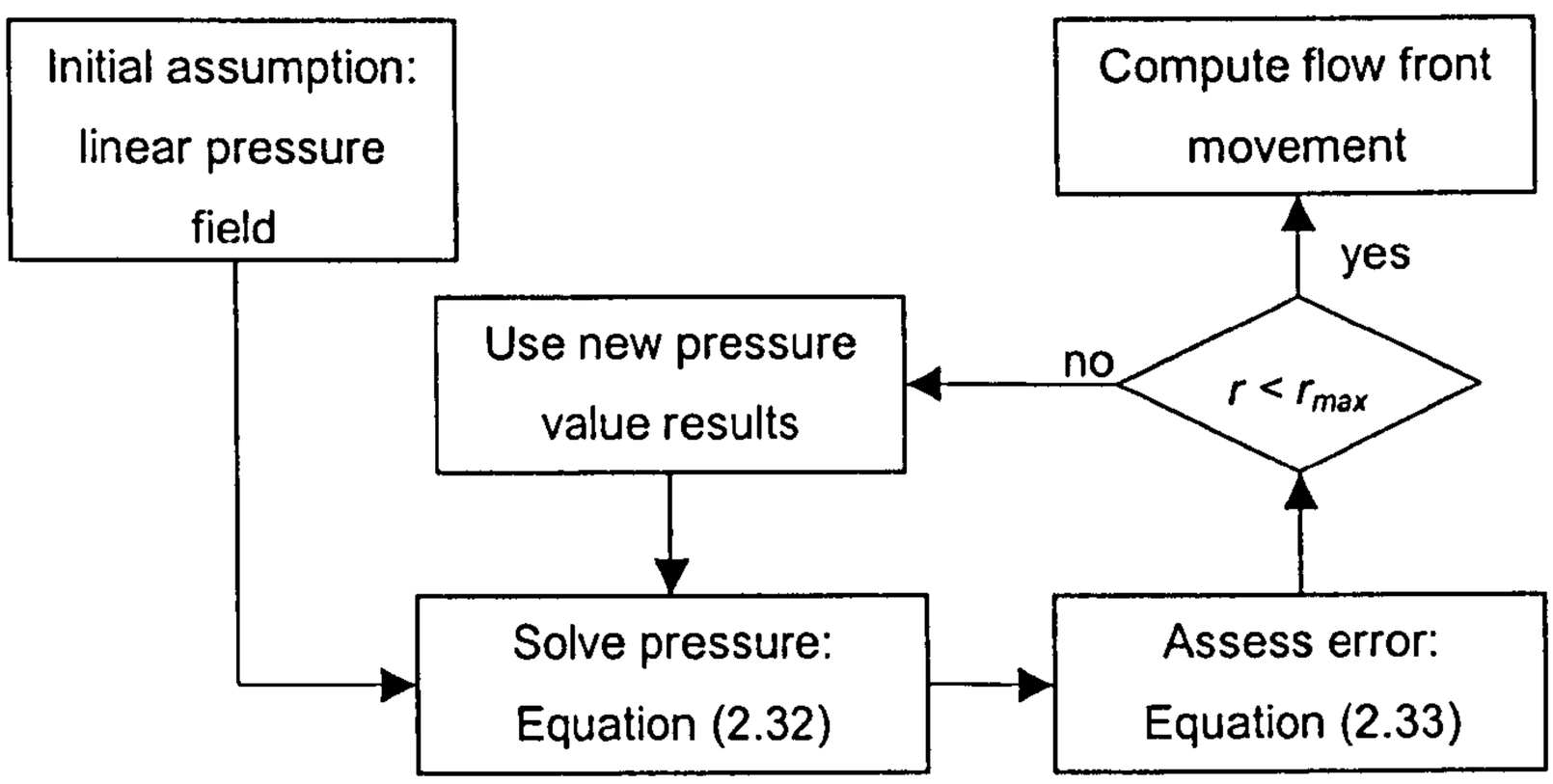

Figure 2.8 – Coupled fluid pressure calculation

As Equation (2.26) shows, fluid pressure is a function of α (relative position of a point between inlet and flow front, not x. Hence, one needs to calculate the VI fluid pressure field in 1D only once and subsequently use the flow front position to determine local fluid pressure fields. This requires a change of coordinate system:

$$\frac{\partial P(x(\alpha))}{\partial \alpha} = \frac{\partial P(x)}{\partial x}\frac{\partial x(\alpha)}{\partial \alpha} = \frac{\partial P(\alpha)}{\partial \alpha}\cdot\frac{1}{L} \tag{2.34}$$

Flow front movement is subsequently obtained from a backward difference version of Darcy's law (Equation(2.17)) at the flow front.

2.8 FLUID PRESSURE FIELDS

Solutions of the fluid pressure field described in the above section were obtained for a representative combination of materials which are characterised in Table 2.1 and Table 2.2. Table 2.1 presents the input data that was used in all simulations. Compaction properties of individual materials are presented in Table 2.2. Note that the Kozeny constant k, glass density ρ and surface density $\rho_{surface}$ do not feature in Equation (2.26). Nevertheless, these values are still necessary in the calculation of flow front progression.

Table 2.1 – Input data for fluid pressure field solution

No. of nodes			100 -
Pressure convergence criterion			1.00×10^{-6} Pa
Outlet pressure (absolute)			0 kPa
Inlet pressure (absolute)			90 kPa
Assumed surface density		$\rho_{Surface}$	1 Kg/m^2
Bulk density of glass		ρ	2540 Kg/m^3
Kozeny constant CFMs	(Han *et al*, 2000)	k	2.5×10^{-10} m^2
Kozeny constant NCFs		k	71.8×10^{-12} m^2
Resin viscosity		μ	0.2 Pa.s

Table 2.2 – Compaction model data. From Robitaille *et al* (1998 a,b,c)

Material	Type and no. layers		Vf_0 (%)	B
Vetrotex U812	Random mat.	3	0.50	0.316
		6	0.54	0.301
Vetrotex U101	Random mat	3	2.09	0.216
		6	1.85	0.231
NCS 81053	Stich. Bidirect	3	6.78	0.170
		6	11.0	0.126
EBX 936	Stich. bidirect.	3	13.3	0.125
		6	16.8	0.104
		12	18.5	0.097

Note that this first study will look at a limited number of numerical parameters. The topic of convergence will be addressed in chapters 3 and 5. The curved profiles of the fluid pressure fields in Figure 2.9 are due to an increase in compaction from inlet to outlet. Conversely, permeability decreases in the same direction. The local fluid pressure gradient increases from the inlet to the outlet. In the incompressible media case, resistance is constant and so is the instantaneous pressure gradient. Increased compliance results in a larger departure from the linear case. Since compliance decreases with increasing initial fibre volume

fraction v_{f0} and density of fibre packing, higher v_{f0} materials such as NCS 81053 show a more linear fluid pressure field. This can also be observed in Figure 2.10. While it can be said that nesting is uncommon in NCFs one can observe from Table 2.2 that, as the number of layers increases, the material becomes less compliant (lower stiffening index B) and more densely packed (higher initial fibre volume fraction v_{f0}), resulting in an increasingly linear fluid pressure field.

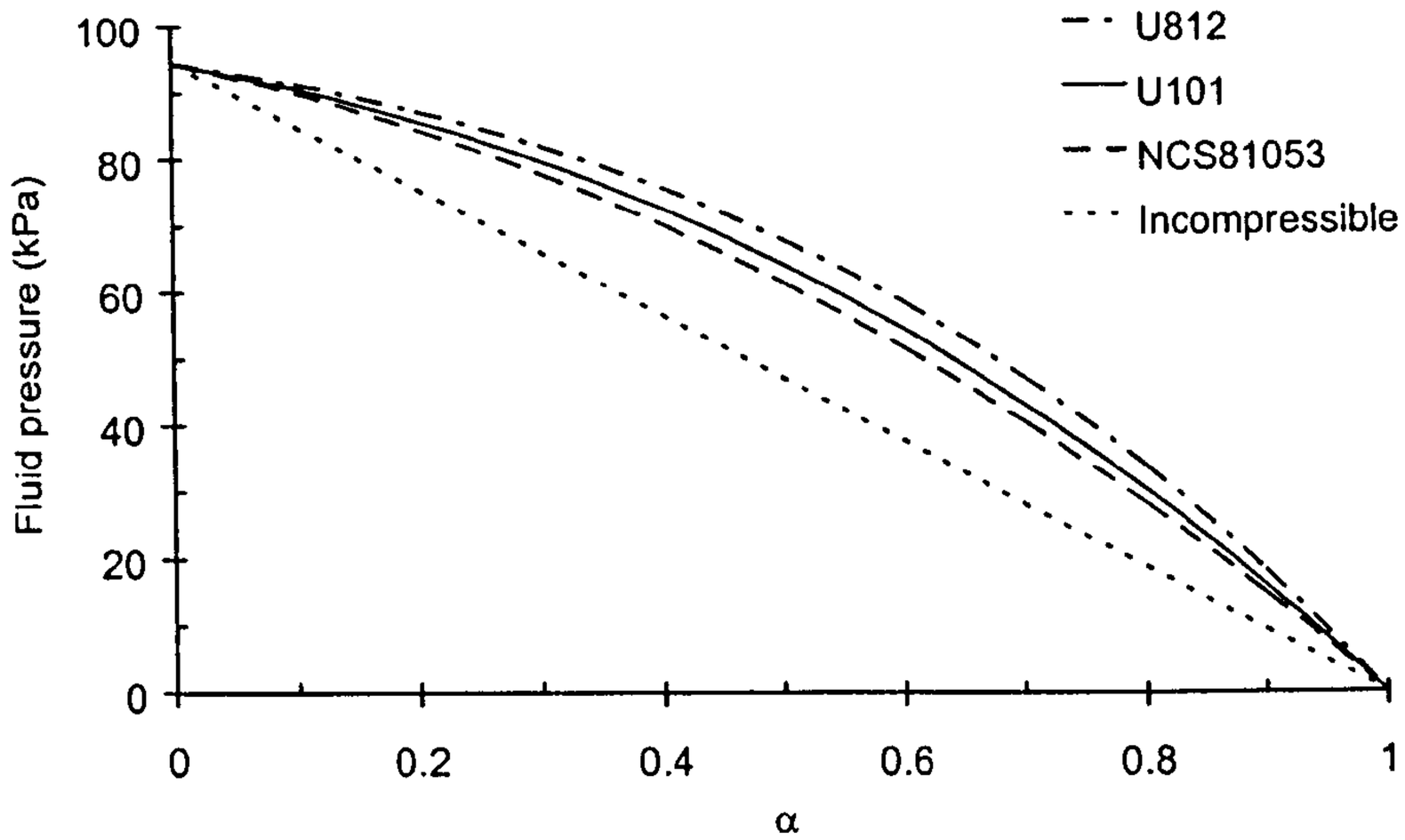

Figure 2.9 – Fluid pressure field comparison for six layers of NCS81053, U101 and U812

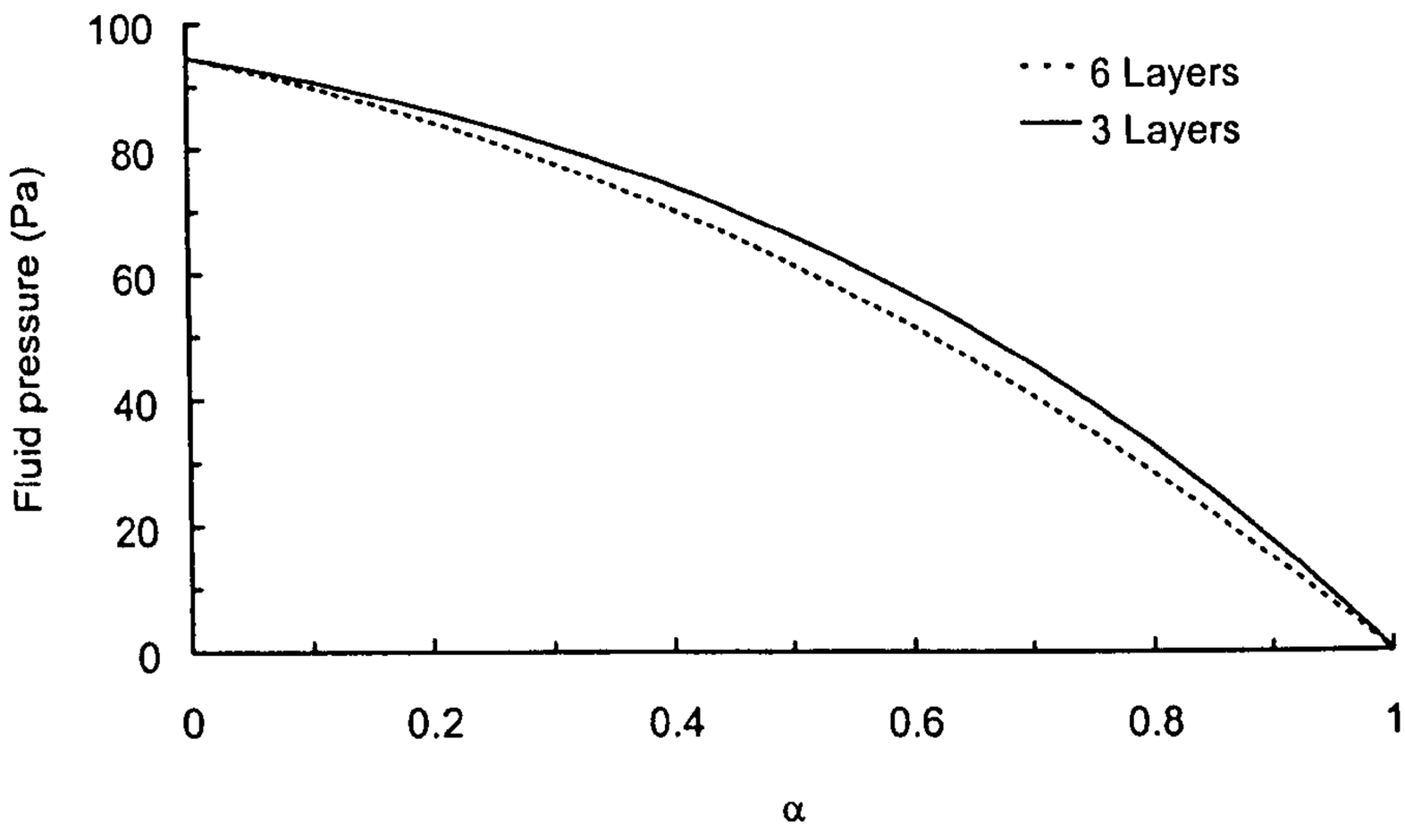

Figure 2.10 – Influence of nesting in the fluid pressure field of three and six layers of NCS 81053

Inlet and outlet pressure levels are also determinant factors in the curvature of the fluid pressure field. Figure 2.11 shows the change in fluid pressure field curvature for three cases. The choice of pressure levels is intended to reveal the different

pressure fields that can arise from equal pressure differences (curves A and B) at different pressure levels and their relation to the maximum VI pressure case (curve C). In the latter case, compaction varies substantially from inlet to outlet and the fluid pressure field is non-linear. The material in curve B is subjected to low compaction pressures, resulting in a moderate variation in fluid pressure field. Accordingly, the fluid pressure field shows an almost linear behaviour. Curve A shows the effect of higher compaction pressures from those found in B resulting in a nearly homogeneous compaction of the preform: whilst the pressure difference is identical in cases A and B the fluid pressure field is now nearly linear. This combination of fluid pressure field results and compaction modelling can be used to determine the distributions of fibre volume fraction and thickness at any point in time and importantly, in the final component. The relevant equation (Equation (3.5)) will be discussed in detail in the following section but, in this case, it is used to relate material compliance, density data and fluid pressure in order to obtain fibre volume fraction and thickness. Furthermore, thickness data, such as shown in Figure 2.12, can be used to predict resin consumption and to predict local mechanical properties. Conversely, thickness or weight can be part of the specifications of a VI component and modelling could lead to optimal inlet gate strategy design.

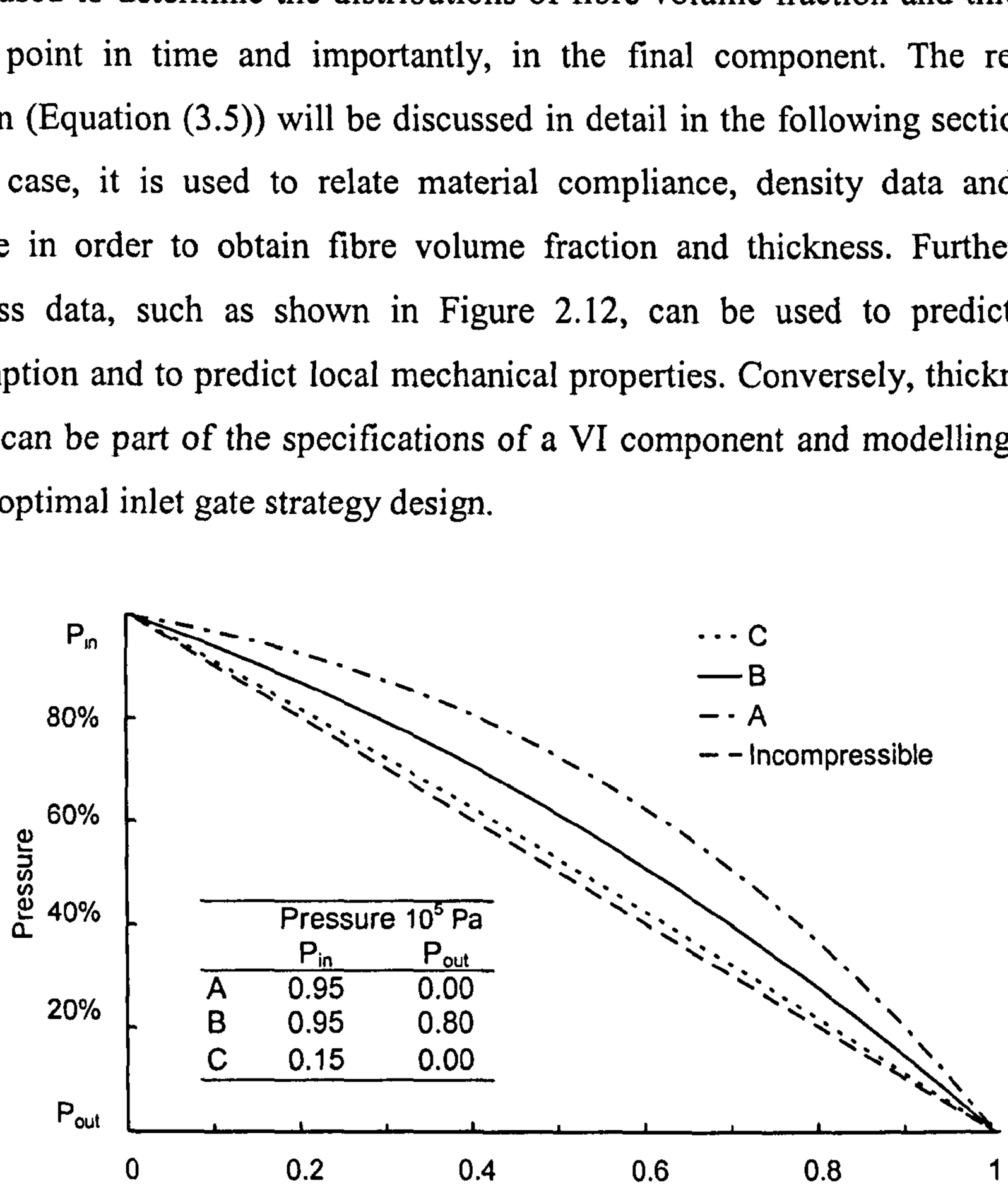

Figure 2.11 – Effect of inlet and outlet pressure settings on the fluid pressure field of U812

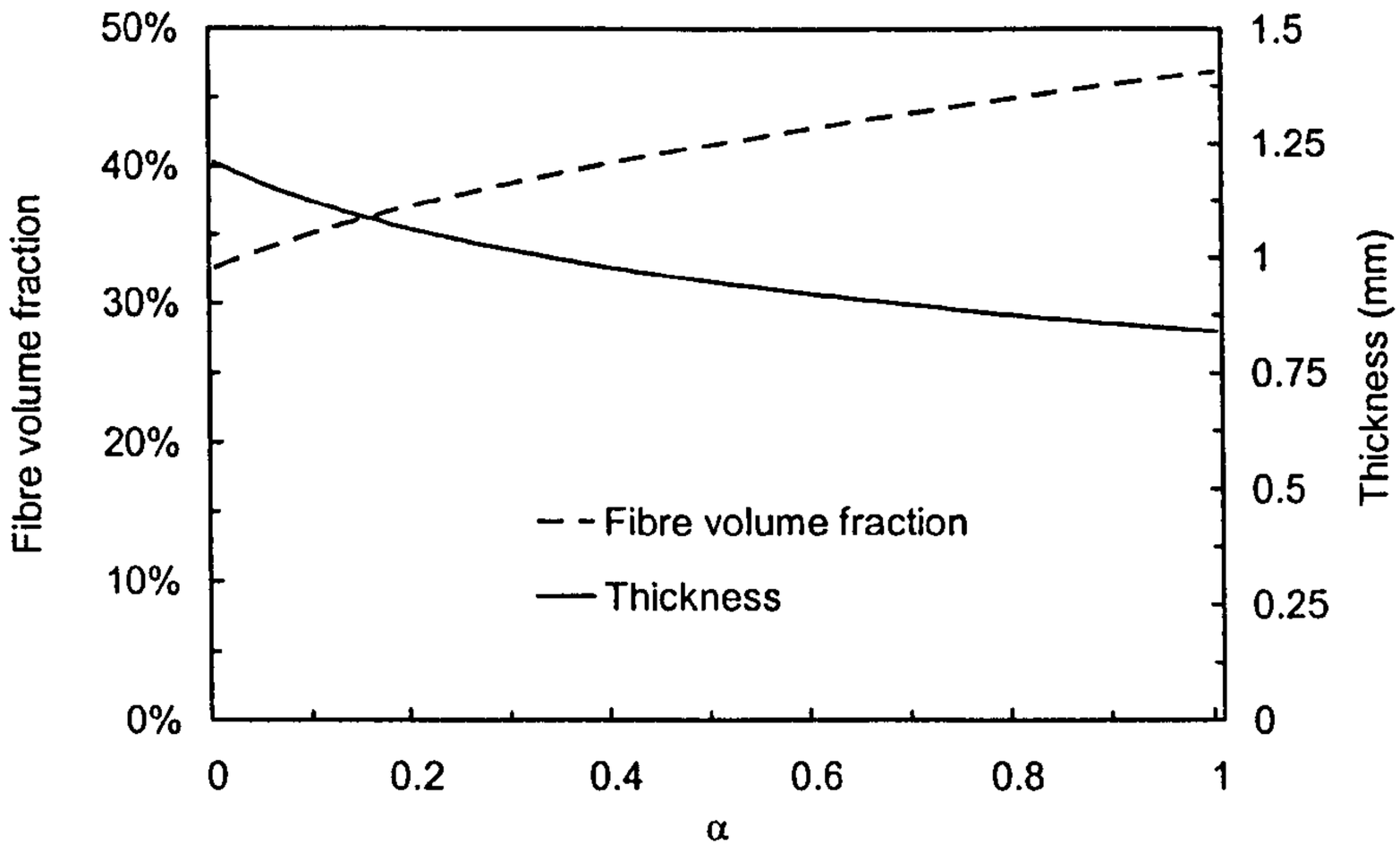

Figure 2.12 – Thickness and fibre volume fraction as a function of location for a NCS 81053 with a surface density of 1 kg / m^2

The alternative continuity Equation (2.4) proposed by Scheidegger was also implemented so that the effect of assumptions (2.8) and (2.10) could be investigated. Figure 2.13 shows resulting fluid pressure fields for both models. Material data for the Vetrotex U 812 glass random mat represented appears in Table 2.2. Both models predict the same trends in terms of pressure field curvature, with differences in pressure values.

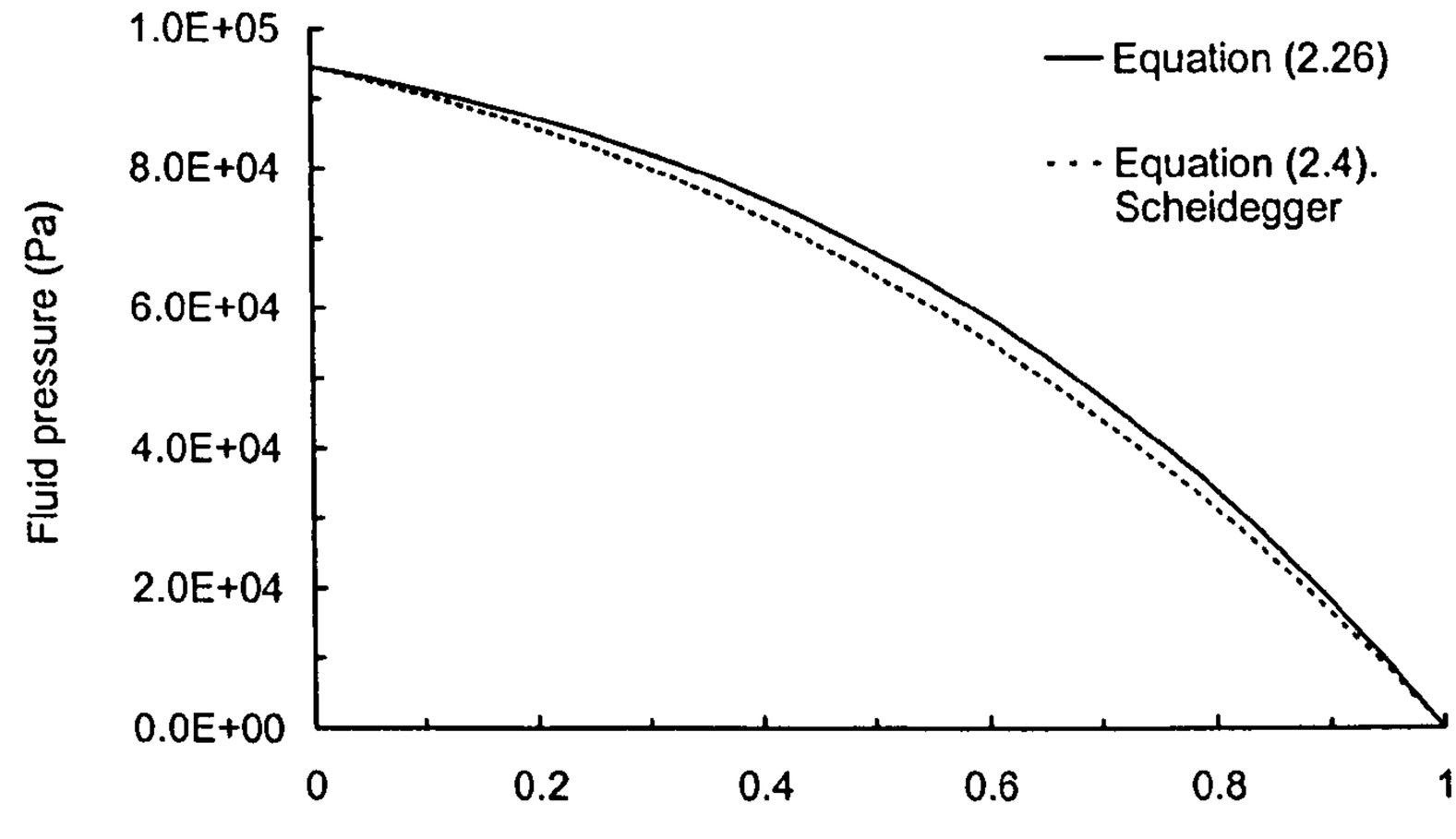

Figure 2.13 – Comparison between predicted fluid pressure fields for the proposed model and an adapted version of Sheidegger's governing Equation

The above mentioned assumptions lead to an underestimate of the fluid pressure gradient at the flow front and consequently of the flow front velocity. This effect increases with material compliance.

2.9 FLOW FRONT PROGRESSION

For incompressible media, the continuity Equation in one dimension imposes that:

$$\frac{d^2P}{dx^2} = 0 \tag{2.35}$$

Consequently fill time can be obtained by integrating Darcy's law (2.17), resulting in:

$$t_{RTM} = -\frac{\phi \cdot \mu}{2 \cdot K} \cdot \frac{L^2}{\Delta P} \tag{2.36}$$

where ϕ, μ, K and ΔP represent the porosity, viscosity, permeability and driving pressure. Equation (2.36) shows that fill time is inversely proportional driving pressure. For constant porosity, viscosity and permeability:

$$t_{RTM} = \frac{t^*}{\Delta P} \tag{2.37}$$

where $t^* = \phi \cdot \mu \cdot L^2/(2 \cdot K)$.

As was established, the pressure field in VI is no longer linear for one-dimensional flow because Equation (2.35) becomes invalid and must be replaced with Equation (2.26). Consequently, the fill time solution in Equation (2.36) is also invalid. Expressing fluid pressure P as a function of the non-dimensional $\alpha = x / L$ and noting that the pressure gradient at the flow front governs flow front progression, it is possible to express Darcy's law for VI as:

$$\frac{dL(t)}{dt} = \frac{1}{\mu} \cdot \left(\frac{K}{\phi} \right)_{\alpha=1} \cdot \left[\left(\frac{dP}{d\alpha} \right)_{\alpha=1} \cdot \frac{1}{L(t)} \right] \tag{2.38}$$

where $(\phi)_{\alpha=1}$, $(K)_{\alpha=1}$ and $(dP/d\alpha)_{\alpha=1}$ represent porosity, permeability and pressure gradient at the flow front ($\alpha = 1$). Integrating yields the VI fill time:

$$t_{VI} = -\frac{\mu}{2} \cdot \frac{L^2}{\left(\frac{K}{\phi} \frac{dP}{d\alpha} \right)_{\alpha=1}} \tag{2.39}$$

Comparing Equation (2.39) with Equation (2.36) one observes that whether thickness is or is not pressure dependent, fill time remains a function of the square of the flow front position. Note that, in the non-compliant case, $dP / d\alpha = \Delta P$ reducing Equation (2.39) to (2.36). Equation (2.39) also implies that VI fill times are directly proportional to the cases where thickness is not pressure dependent. Assuming, for comparison purposes, that permeability is equal in an idealised incompressible media mould and at the flow front of a VI mould ($K_{RTM} = (K_{VI})_{\alpha=1}$) a constant proportionality between these two fill times fill times can be identified:

$$C_\alpha = \frac{t_{RTM}}{t_{VI}} = \frac{\left(\frac{dP}{d\alpha} \right)_{\alpha=1}}{\Delta P} \tag{2.40}$$

The term C_α equates to the effect of compaction and permeability properties on flow and therefore characterizes a material's behaviour in VI when compared to an idealized incompressible reinforcement case. Under similar compaction conditions at both RTM and VI flow fronts, fill times are only equal if higher driving pressures are used in RTM

2.9.1 Equivalent VI permeability

One can however combine Equations (2.39) and (2.40) to calculate VI fill time as function of driving pressure in much the same way as RTM:

$$t_{VI} = -\frac{\mu \cdot L^2}{2\left[\frac{K}{\phi}\right]_{\alpha=1}} \cdot \frac{1}{C_\alpha \cdot \Delta P} \tag{2.41}$$

where the proportionality constant defined in Equation (2.40) is a function of the VI fluid pressure field solution. Furthermore, using the same material and thickness at the flow front in both the non-pressure dependent thickness and the VI cases, the overall permeability in the first case is equal to the permeability at the flow front in VI:

$$if \left[\left(P_{Comp}\right)_{\alpha=1}\right]_{VI} = \left[P_{Comp}\right]_{RTM} \therefore \left(K\right)_{\alpha=1} = K_{RTM} \tag{2.42}$$

The apparent VI permeability K_{VI}, can therefore be determined by combining Equation (2.41) with its RTM analogue (2.36):

$$K_{VI} = C_\alpha \cdot K_{RTM} \tag{2.43}$$

Unlike permeability in RTM, the apparent overall permeability K_{VI} is a function of the compaction pressure field and material compaction properties. Nevertheless, Equation (2.43) can be used to relate K_{RTM} and K_{VI} and determine the permeability of a certain material in VI through RTM experimental results or vice versa. To do this one must know the compaction properties of the material and solve the fluid pressure field equation. In fact, the non-dimensional number C_α, defined in Equation (2.40), can be seen as a measure of the effect of compliance on flow in VI.

2.9.2 VI fill time

Unlike the pressure field, fill time values depend on the relation between permeability and fibre volume fraction and, specifically in the case of the Kozeny-Carman model, on the experimentally determined Kozeny coefficient *k*. Values of $k = 2.5 \times 10^{-10}$ m^2 for random fibres and $k = 71.8 \times 10^{-12}$ m^2 for non-crimp bidirectional reinforcement were used (based on Han *et al,* 2000). Fill times represented in Figure 2.14 are obtained with material data which appear in Table 2.2. Note that due to the formulation of Equation (2.41), the time vs. position plots follow second order polynomials, which is the case in experimental observations of flow in VI (see Chapter 3). Furthermore, it highlights the evident similarity between RTM and VI.

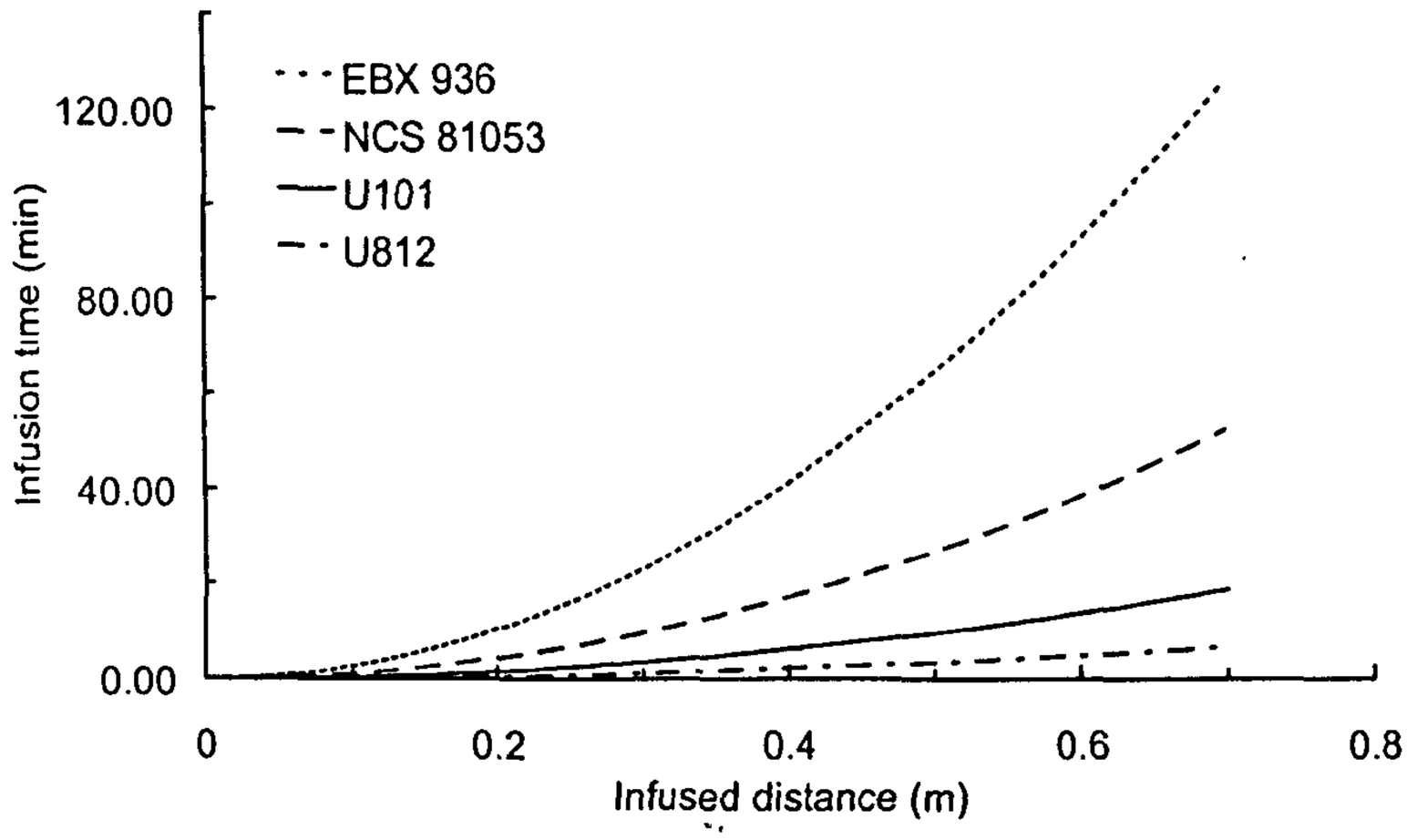

Figure 2.14 – VI fill time as function of infused distance for EBX936, NCS81053, U101 and U812

Figure 2.15 represents the difference in fill times observed in VI and flow through incompliant media, under the compaction conditions described in Equation (2.42). As expected, the ratio between fill times is constant, as prescribed by Equation (2.43) and vacuum infusion fill time is lower than in incompressible media. Physically, this equates to an advantage in VI when compared to RTM. However, this higher apparent permeability does not lead necessarily to lower fill times because of the larger driving pressures available in RTM.

Figure 2.16 shows the effect of variation in outlet pressure on the ratio between non-pressure dependent thickness and VI fill times (C_{α}). Figure 2.16 was obtained by keeping the inlet pressure constant and imposing different outlet pressures, in the conditions of Equation (2.43). This figure illustrates the expected reduction in the effect of material compaction as driving pressures are reduced.

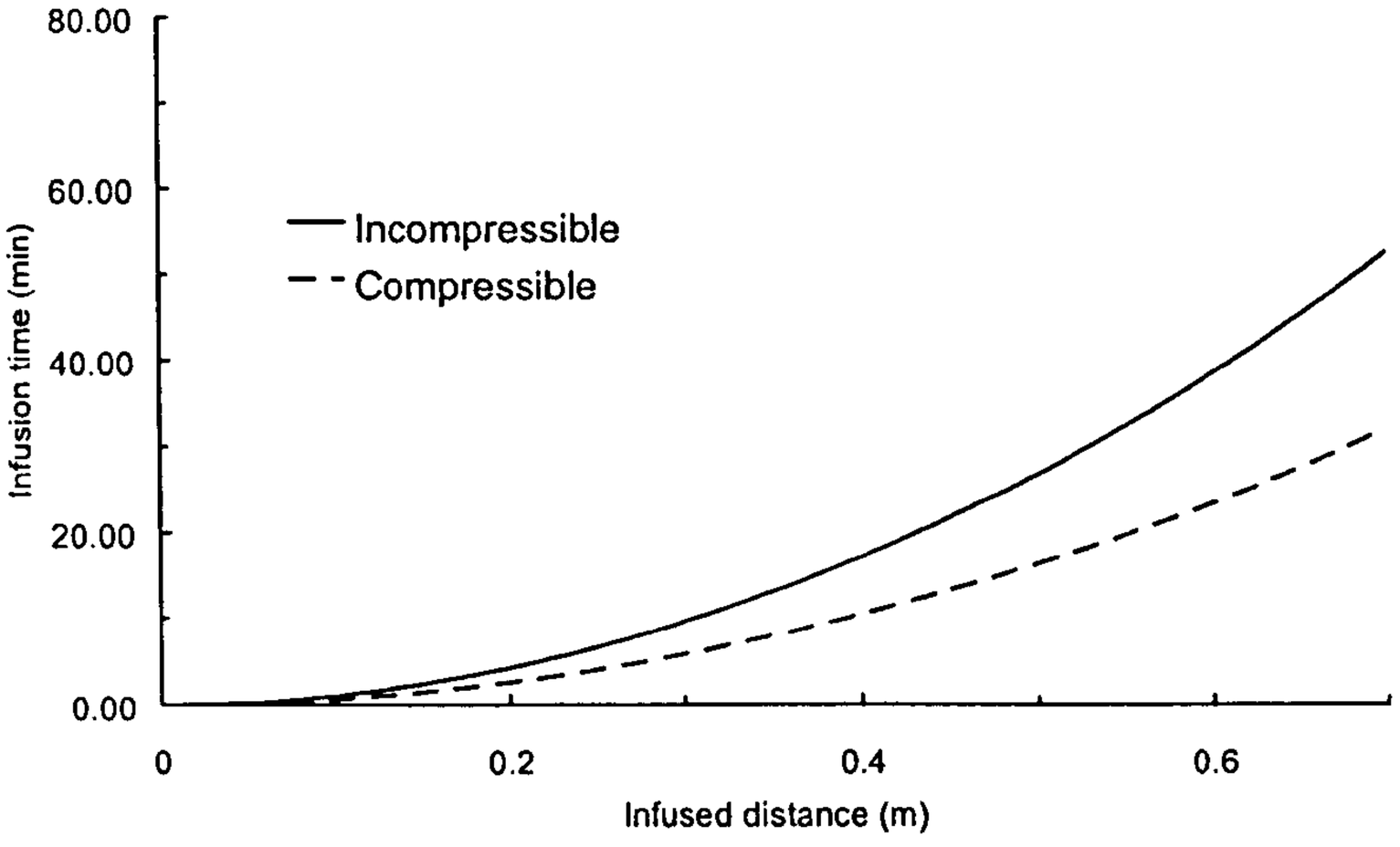

Figure 2.15 – VI and incompressible media infusion times for NCS 81053

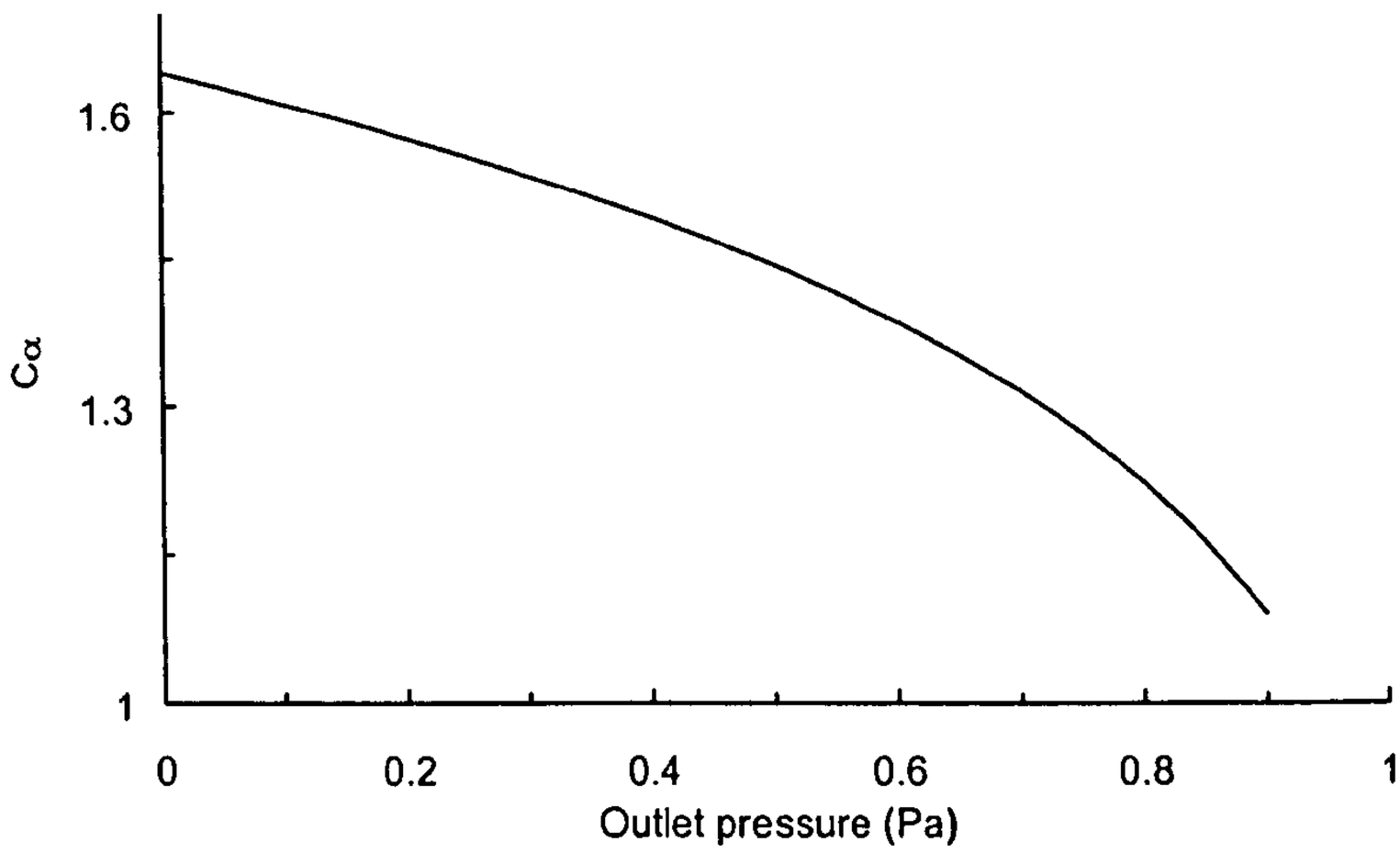

Figure 2.16 – Ratio between VI and incompressible media infusion times at different outlet pressures. Obtained for NCS 81053

2.10 CONCLUSIONS

This chapter details the algebraic development of a flow model for VI. It is shown how this model can be independent of rate effects in a non-dimensional coordinate system and that, as is the case with RTM, the fluid pressure field in VI is of a scalable nature. Typical quantitative solutions of the fluid pressure field are analysed for several materials noting that even within the same material one might find different fluid pressure profiles depending on inlet and outlet pressures or number of layers.

The similarities between flow in RTM and VI are explored in detail and it is shown that there is a characteristic constant, C_α, which fully characterises the flow behaviour of a material in VI, accounting for its compressibility. Furthermore, it is noted that this similarity can be explored in conjunction with the unified model, to obtain the apparent permeability in VI from the compaction properties of a material and its permeability in RTM or, in fact, any one from the other two. The relation between flow front position and time is explored further and the modelling results are used to show that the scalable nature of the fluid pressure field explains the similarity between RTM and VI since both follow a second degree polynomial.

As was shown, VI specific models are required when one intends to study the full impact of preform compaction properties on flow and gating optimisation. In order to do that however one must first quantify the compliance of typical fibre beds – which is the aim of chapter 3. One must also validate the model (chapter 4) and expand its applicability to complex geometries (chapter 5).

3 PARAMETRIC STUDIES ON FLOW THROUGH COMPLIANT POROUS MEDIA

The objective of this chapter is to perform a parametric study on the pressure field model for flow through compliant media derived in chapter 2. To that end, it describes the experimental and data reduction compaction studies done during this project. Its foremost outcomes are the parametric study on the flow model and a rationalised model for compaction which is both mathematically simpler than existing models and experimentally straightforward. Another novel outcome is the characterization of variability in compaction properties which helps predicting resin flow and final mechanical properties of composite components.

3.1 INTRODUCTION

It follows from chapter 2 that the physical behaviour of fibre beds under varying compaction loads influences flow through media which are not constrained in the thickness direction. The difficulty in obtaining compaction data can therefore hinder the modelling exercise since all materials used must be characterized. While compaction databases or analytical models are possible solutions to this problem, this chapter proposes novel alternative: starting from the assumption that compaction is dominated by fibre volume fraction alone it will be shown that it is possible to determine compaction properties for all textile architectures so long as the initial unloaded density of each is known. This not only simplifies the experimental procedures but also opens new modelling avenues for both compaction and flow.

This study extends the compaction work of Robitaille *et al* (1999 a, b, c), Gutowski *et al* (1986, 1987 a, b) and others. The chapter is divided into four main sections. The first starts with a background on compaction where the existing models are discussed, and continues with an analysis of the issues that affect compaction results before discussing the experimental methodology and the data

fitting techniques. The next section discusses the results and statistical studies of the experiments. This is followed by the synthesis of the compaction results into a master compaction model and its applicability to modelling flow through compliant porous media. Finally, the master curve model is used to perform parametric studies with the flow model. It shows possible analytical approximations for the fluid pressure field and provides guidelines for the determination of this from simple tests of compaction properties.

3.2 BACKGROUND ON COMPACTION OF POROUS MEDIA

3.2.1 Compaction models

Analytical models of compaction cover most possible fibre architectures, from the compaction of random fibres (van Wyk, 1946) to aligned unidirectional fibres (Gutowski, 1986, 1987 a, b) and multi-layer woven textiles (Chen 1999 a, b, c and d). Nevertheless while analytically derived, these models still require empirically determined constants. Wyk's model, for example, requires a constant C and the knowledge of the volume occupied by the sample at zero pressure (h_{w0}):

$$P_{comp} = \frac{C \cdot E \cdot m^3}{A^3} \cdot \left(\frac{1}{h^3} - \frac{1}{h_{w_0}{}^3} \right) \tag{3.1}$$

where the parameters E, m, A and h represent the Young's bulk modulus of the reinforcement and the mass, area and thickness of the sample respectively. Three other parameters are required in the recent work by Chen *et al* (1999 a,b) on woven textiles which is again cast in a form which relates compaction pressure to thickness:

$$P_{comp} = \frac{1}{C_b(h)} \cdot \left(1 - \frac{h_0}{h} \right) \tag{3.2}$$

were the initial thickness h_0 and the function C_b are fitted. C_b is a complex function of thickness and the mechanical properties of the fibres and of the

architecture. Assuming that compaction is not time dependent, Gutowski's model is expressed as:

$$P_{comp} = A_s \cdot \frac{\sqrt{\frac{v_f}{v_{f_0}}} - 1}{\left(\sqrt{\frac{v_{f_a}}{v_f}} - 1\right)^4} \tag{3.3}$$

The parameters A_s, v_{f0} and v_{fa} represent the reinforcement spring constant, the fibre volume fraction at zero compaction pressure and the theoretical maximum fibre volume fraction, which all depend on reinforcement architecture. In reality all parameters must either be estimated or determined experimentally. Therefore, globally, these analytically derived expressions do not simplify the compaction problem and invariably require experimentation.

Possibly, the simplest compaction modelling approach uses an empirical power law fit to relate compaction pressure to fibre volume fraction (Robitaille and Gauvin, 1998 a,b,c). Again, assuming that compaction is not rate dependent, this model takes the form:

$$v_f = v_{f0} \cdot {P_{comp}}^B \tag{3.4}$$

where the fitting parameter v_{f0} can be thought of as the fibre volume fraction at 1 Pa and B represents the stiffening (non-linear) behaviour, which again depends on the material. A least squares fit algorithm is used on the experimental data to obtain both coefficients. In practice, Equation (3.4) can reproduce compaction data accurately and coefficients of correlation of 0.98 or higher are common. Note that, unlike the previous models, Equation (3.4) has been demonstrated for all fibre architectures and might therefore be preferred. Laminate thickness is obtained from the compaction model predictions through Equation (3.5):

$$h\left(P_{comp}\right) = \frac{\rho_{sup}}{\rho \cdot v_f\left(P_{comp}\right)} \tag{3.5}$$

However, unlike the analytical alternatives it is possible to argue that a power law model has little to do with the physics of the compaction process. Bak (1997) suggests that in the critical points which mark the separation between two different states: i.e. liquid / solid or in this case contacting/free fibres; the transition can often be described by power laws. Furthermore, it cannot be said that the coefficients of this model (Equation 3.4) have no real physical meaning: they represent the fibre volume fraction at 1 Pa (related to the uncompacted density of the reinforcement) and stiffening index (a measure of the non-linearity of the material).

3.2.2 The physics of compaction of fibre beds

This section explores two types of compaction: *i* the compaction of dry porous media and *ii* the compaction of saturated porous media. Squeeze flow is addressed in Appendix 3.A. Overall, it is assumed that any intermediate state is a combination of the two principal states:

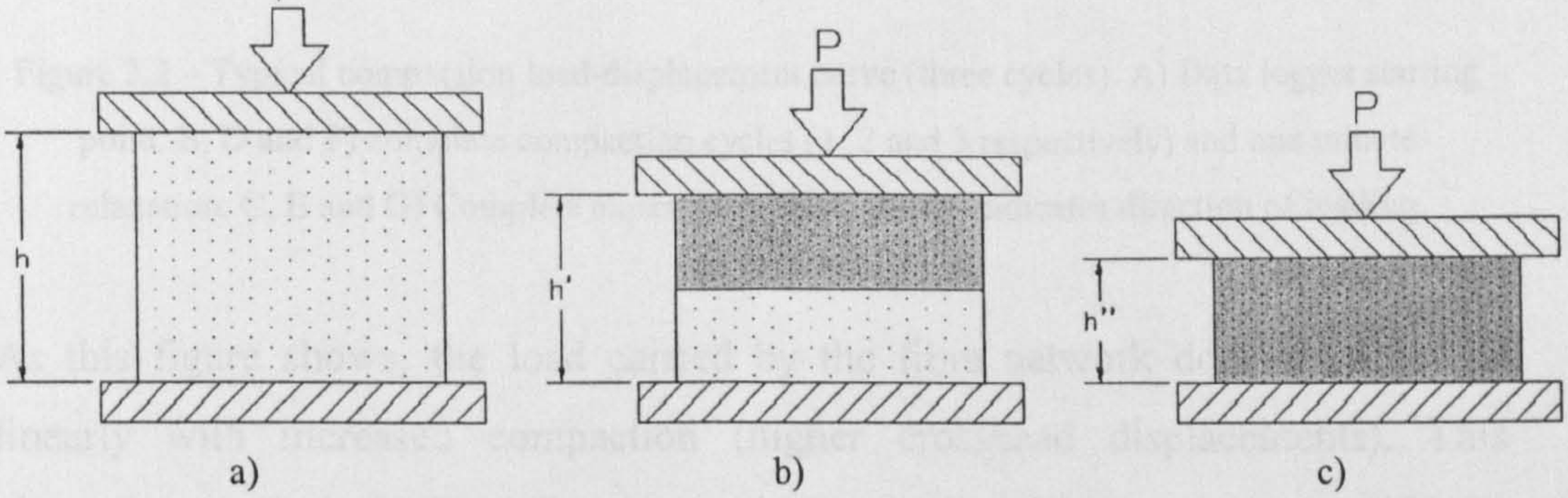

Figure 3.1 –Compaction for the same load as a function of saturation. a) dry, b) intermediate and c) saturated compaction

Figure 3.1 represents the observed effect of saturation in compaction: as fibre lubrication increases (from a) to c)), fibre beds deform more under the same loads (assuming negligible hydraulic resistance). Kim *et al* (1991) show that initial thickness is reduced due to the increased ease of fibre rearrangement. This progression is entirely characteristic of liquid composites moulding. Furthermore, unlike autoclave processing, LCM processes such as VI require information on both positive and negative compaction strains, i.e. compaction and expansion,

requiring tests which cycle the load in the material. All experimental results discussed in this chapter where obtained by applying the increasingly larger compaction load (at a constant loading rate) until the maximum pressure is reached, allowing a period of one minute for further relaxation of the material (Figure 3.2) and removing the load at the same absolute rate as it was initially applied. This is a different approach from the constant crosshead speed used in past research by for example Robitaille *et al* (1999), Saunders (1997), Kim *et al* (1991) and others. A typical test result is presented in Figure 3.2.

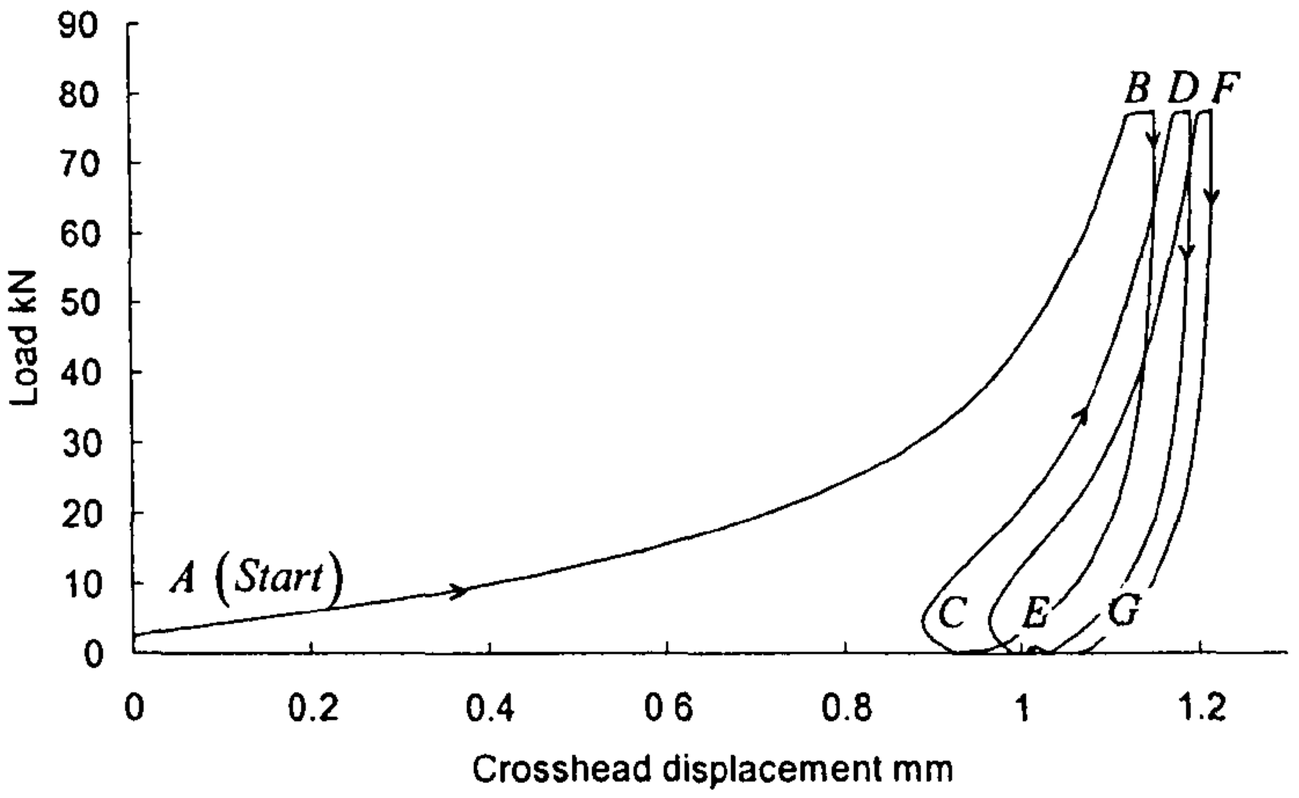

Figure 3.2 – Typical compaction load-displacement curve (three cycles). A) Data logger starting point. B, D and F) complete compaction cycles (1, 2 and 3 respectively) and one minute relaxation. C, E and G) Complete expansion cycles. Arrow indicates direction of loading.

As this figure shows, the load carried by the fibre network does not increase linearly with increased compaction (higher crosshead displacements). This phenomenon, typical of textile compaction, was described as early as 1925 by Eggert (Wyk, 1948) and is attributed to the increasing number of contacts between fibres forming a network which increases in density with increasing fibre volume fraction (Wyk, 1948; Gutowski et al, 1986; Kim *et al*, 1991; Robitaille, 1999 a). It is this nonlinear behaviour which is described by Equation (3.4).

The one minute relaxation period is also linked to the choice of test fluid and adds another dimension to the analysis. As was shown by Robitaille *et al* (1999, c) while the test fluid does not seem to affect the energy loss in the first cycle it does play an important role in the second. The reasons for this are not clear but it was

suggested that it is linked with superior lubrication of oil relative to that of distilled water. Hence, in the absence of a model which can anticipate the effect of viscosity on fibre-fibre friction, an effective test fluid should posses lubricating properties close to the resin systems used.

Typical energy loss in a cycle is shown in Figure 3.3. The observed dissipation of energy (proportional to the hatched area) during the cycle highlights the hysteresis due to a combination of fibre network reorganization or breakage. Note that the compaction line is broken at maximum load (dashed circle in a)). When moulding, textile reinforcements are not cycled instantaneously and therefore there is a time window for further fibre network reorganization once the maximum compaction pressure is achieved. To simulate the manufacturing conditions, the load control on the testing machine adjusts the crosshead position to compensate for any pressure drop.

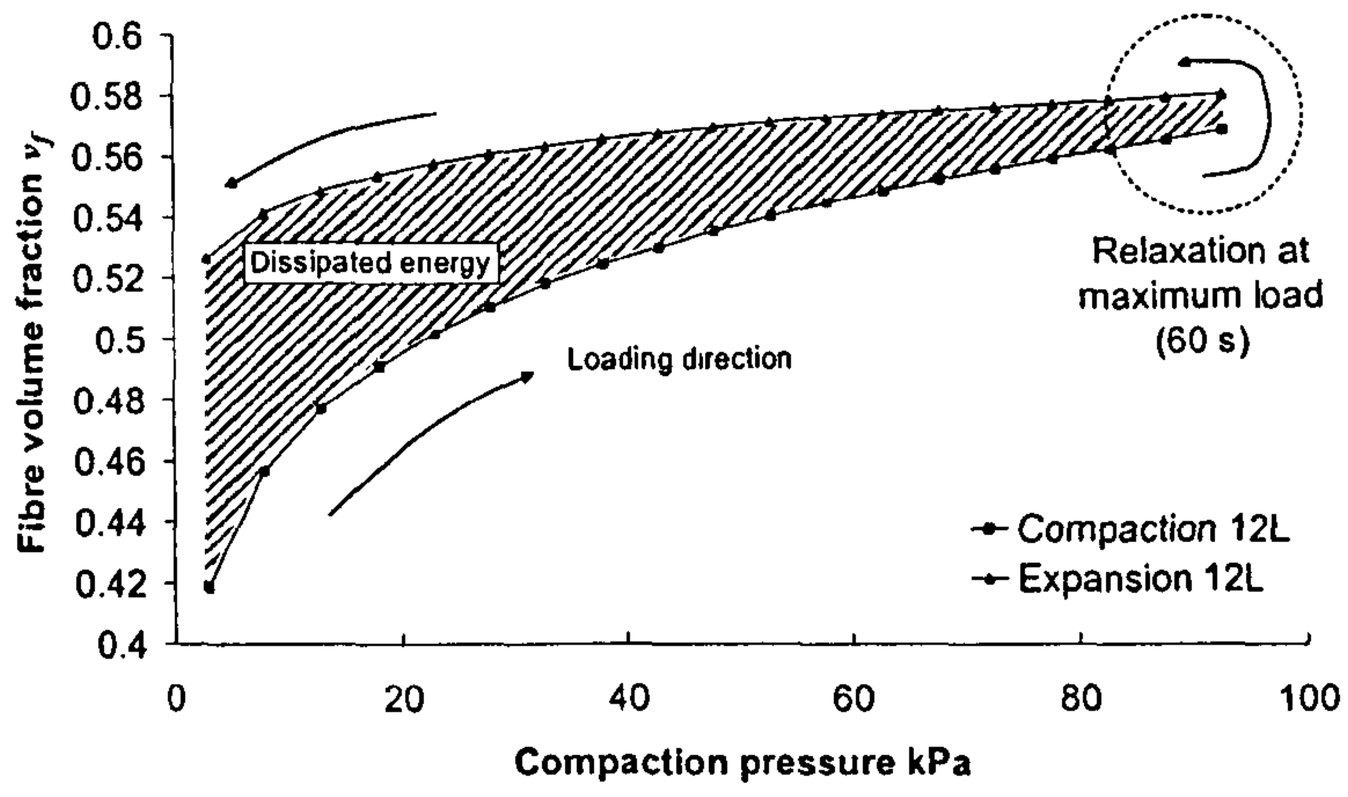

Figure 3.3 – Typical compaction-expansion plot (first cycle): compaction cycle showing a change in maximum v_f due to dwell time at maximum load

This relative rate of fibre volume fraction variation (left hand side of Equation (3.6)) can be approximated by the logarithmic expression:

$$\frac{\Delta v_f(t)}{v_f(t)} \cdot \frac{1}{\Delta t} = \xi \cdot \log(t) + \zeta \tag{3.6}$$

where ξ and ζ are experimental parameters. While it is not the purpose of this study to define these parameters it is possible to say that, as Figure 3.4 shows, the relative rate at which fibre volume fraction evolves with time during this period tends to nought in less than 1 minute. This is valid for all studied architectures and therefore a 1 minute stop was included in all tests.

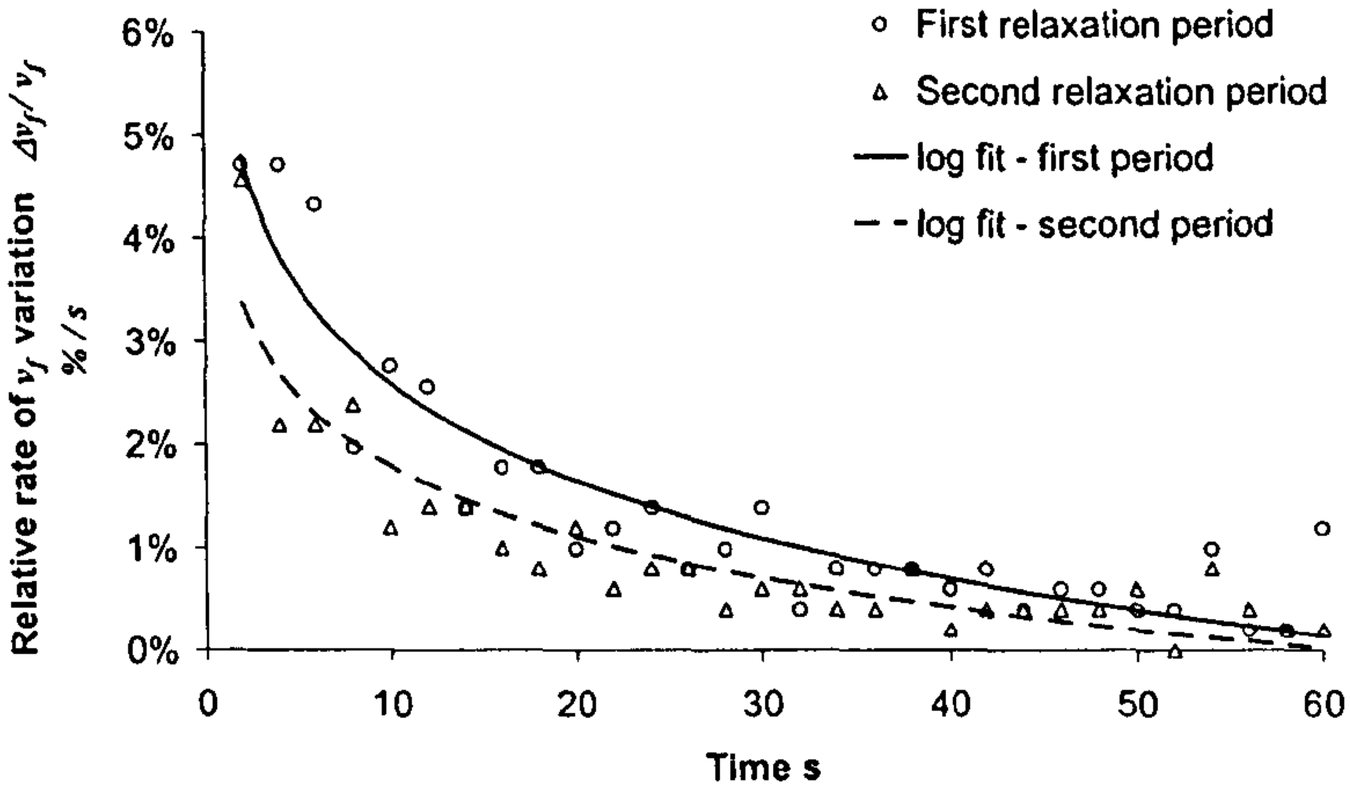

Figure 3.4 – Typical compaction-expansion plot (first cycle): fibre volume fraction rate of change during the dwell time showing that the rate reduces and tends to zero as time approaches 60s.

The choice of compaction rate is also relevant because, in conjunction with the test fluid viscosities, it changes the saturated compaction/expansion viscoelastic response. Appendix 3.A discusses how the contribution of the viscoelastic squeeze-flow term was determined and shows that, at the compaction rates which are used in this study it is negligible. This work is based on a model of radial flow through isotropic porous media described by Saunders (1997) and was used to determine the contribution of squeeze-flow of Newtonian fluids to the total compaction force:

$$P_{\text{Squeeze flow}} = \frac{\mu \cdot R^2}{8 \cdot K \cdot h} \cdot \frac{dh}{dt} \tag{3.7}$$

In summary, accurate modelling of compaction for flow through unconstrained media requires knowledge of the influence of the compaction rates, of dry compaction and expansion and of saturated compaction and expansion. Therefore, before beginning the tests a study was conducted on the effect of rate (and

squeeze flow) on compaction results. This study is summarized in Appendix 3.A. It is shown that, at the rate of 10 N / s which was used throughout these experiments, there is no significant influence of squeeze flow on reinforcement compaction properties.

Figure 3.5 shows a flow chart containing the most important parameters that were analysed in this study.

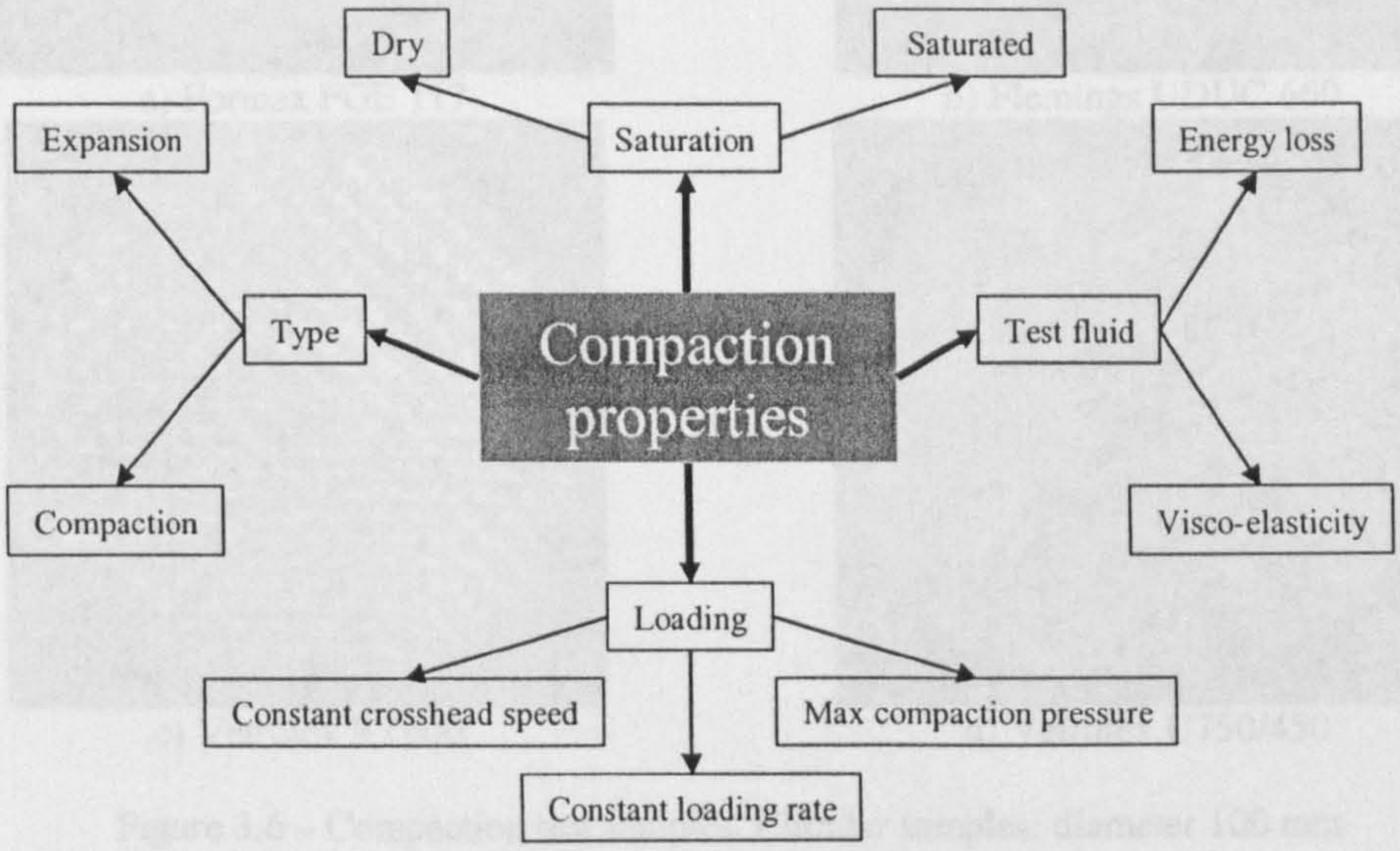

Figure 3.5 - Compaction testing parameters

3.2.3 Experimental methodology and materials

Reinforcement textiles and test procedures: These experiments were done by compressing a multi-layered reinforcement sample of diameter 100 mm, either dry or in an oil bath, to 90 kPa, removing the load and repeating the cycle two or more times. The four tested reinforcements, are specified in Table 3.1.

Table 3.1 – Specification of sample materials

	Designation	Manufacturer	Structure	Layer orientation	Surface density g / m^2
1	FGE 117	Formax™	Stitched triaxial	[0/±45]	567/300/300
2	UDUC	Flemings™	Unbalanced bidirectional	[0/90]	660/55
3	RT 600	Vetrotex™	Plain weave	[0/90]	300/300
4	U750	Vetrotex™	Continuous filament random mat	-	450

These represent a broad range of available architectures, as Figure 3.6 shows.

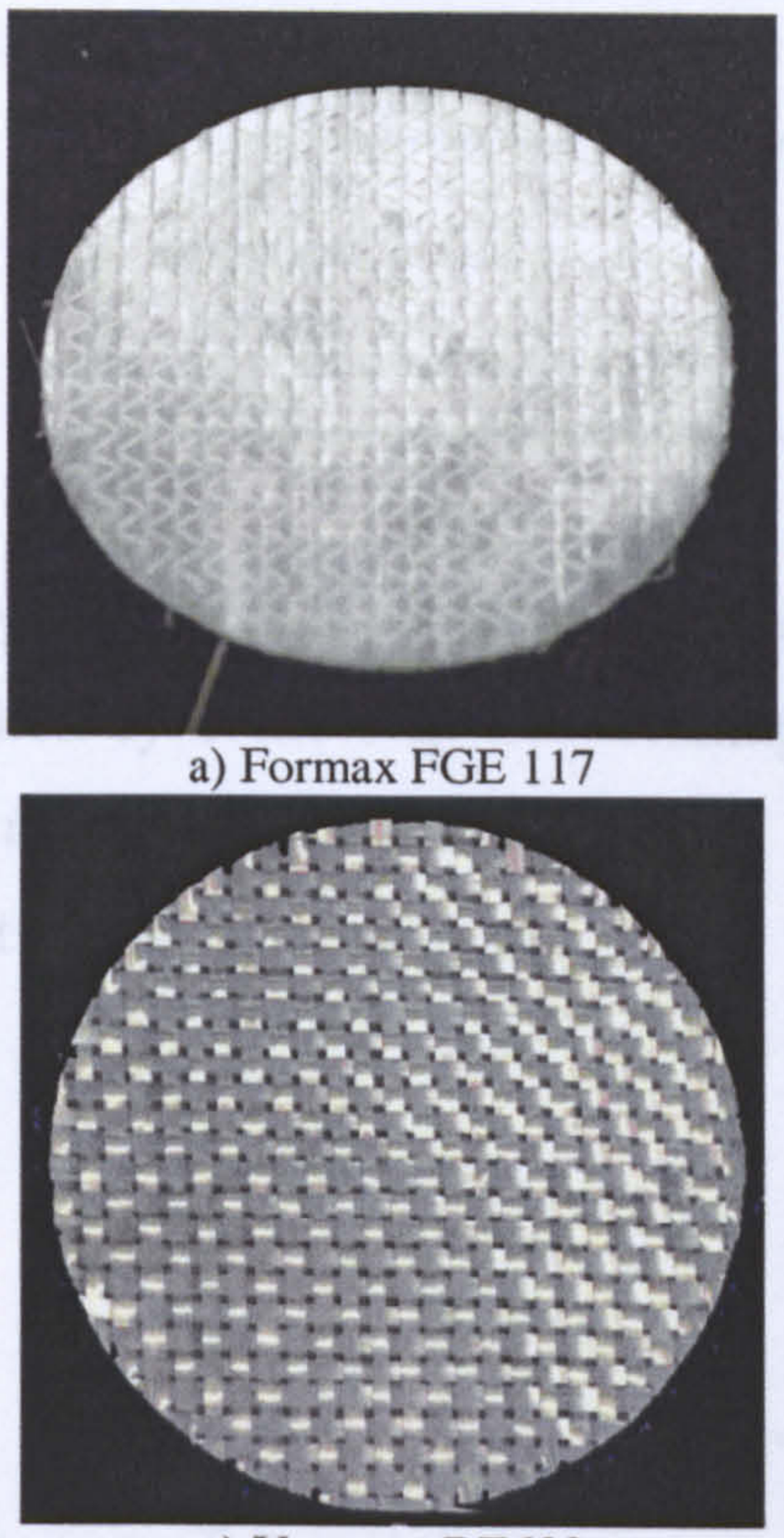

a) Formax FGE 117

b) Flemings UDUC 660

c) Vetrotex RT600

d) Vetrotex U750/450

Figure 3.6 – Compaction test samples. Circular samples: diameter 100 mm

The experimental plan consisted of tests on three different layer numbers per material: three, six and twelve. Both compression force and sample thickness were logged. These data were then converted to compression stress and fibre volume fraction from the known applied force, sample area, thickness and weight, and the bulk density of E-glass (2540 kg/m^3), using Equations (3.8) *a* and *b*.

$$(a)\ \ P_{comp} = \frac{F_{comp}}{A_{sample}} \quad (b)\ \ v_f = \frac{\rho_{\sup}}{\rho} \cdot \frac{1}{h} \tag{3.8}$$

The test matrix is shown in Table 3.2.

Table 3.2 – Experimental compaction plan.

Number of test repeats vs. material, lay-up and saturation

Designation	3 Layers		6 Layers		12 Layers		
	Dry	Sat.	Dry	Sat.	Dry	Sat.	Total
FGE 117	1	12	1	12	1	12	39
UDUC	1	4	1	4	1	4	15
RT 600	1	4	1	4	1	4	15
U750	1	4	1	4	1	4	15

2) Test fluid. All saturated experiments were done using HDX 30 silica oil supplied by Trent Oil, Ltd - Nottingham. The viscosity of this Newtonian fluid was measured using a Brookfield rheometer model DV-II. The oil viscosity results are shown in Figure 3.7.

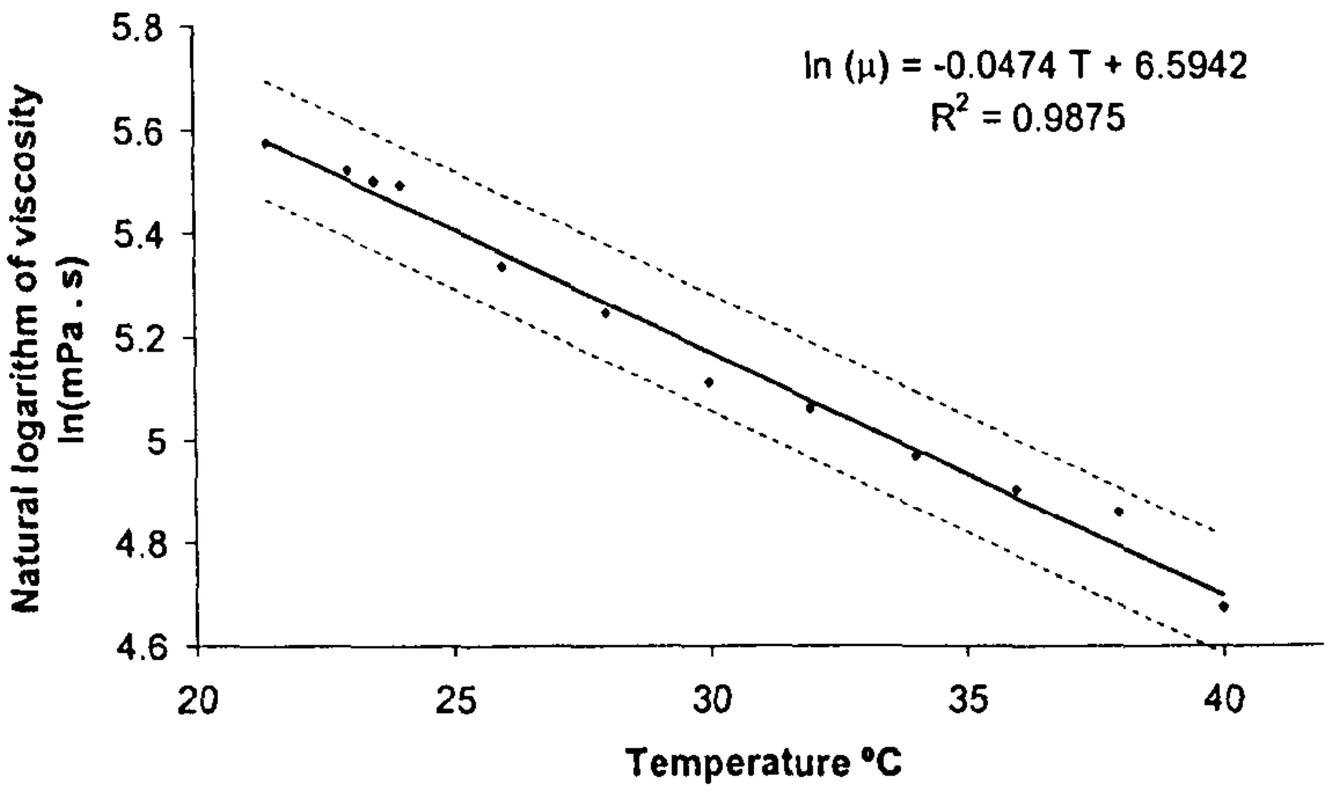

Figure 3.7 - Temperature vs. viscosity for HDX 30 Oil.
Shown with 95% experimental confidence interval.

In saturated tests, the samples were prepared by submersion in oil for 5 minutes, resulting in complete saturation. The excess oil was allowed to flow through a 5 mm gap between the upper and lower tools of the compaction rig and, when overflowing, was recovered in a separate container.

3) Compaction rig setup: The experimental work was done on a Mayes™ ESM100 servo-mechanical universal testing machine. Force-displacement data was acquired from a load cell and LVDT by a Solartron Instruments™ *si*3535D logging system. The overall assembly is shown in Figure 3.8 and the individual components are shown in Figure 3.9.

The compaction experiments were preceded by rig parallelism and compliance tests. Results indicated that the faces were parallel to within ± 0.05 mm and that the deflection of the rig due to compaction loads was negligible. These tests are discussed in detail in Appendix 3.B. A datum was established before each series of experiments by dial gauge measurement of the empty rig.

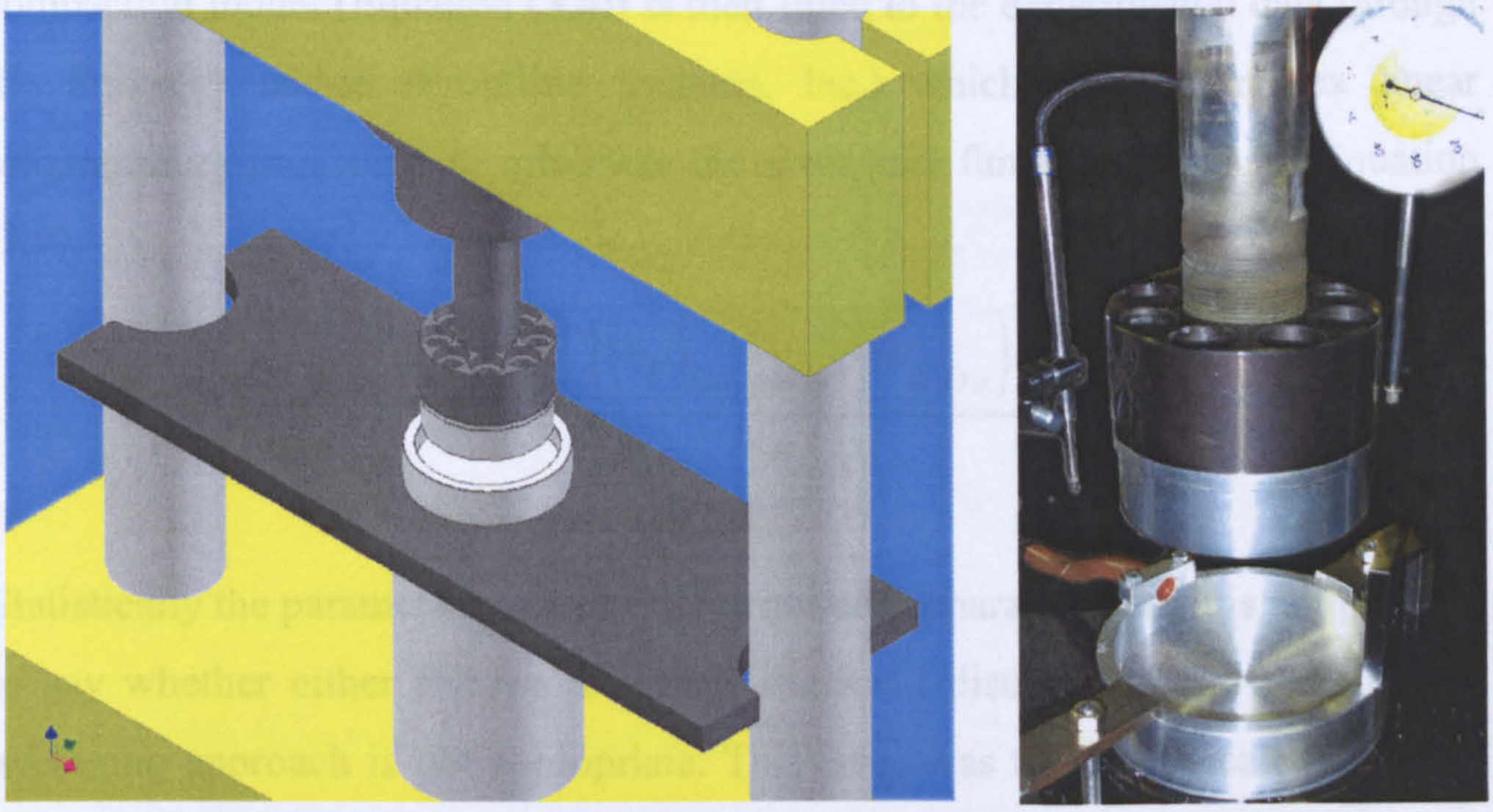

Figure 3.8 - Compaction rig assembly.

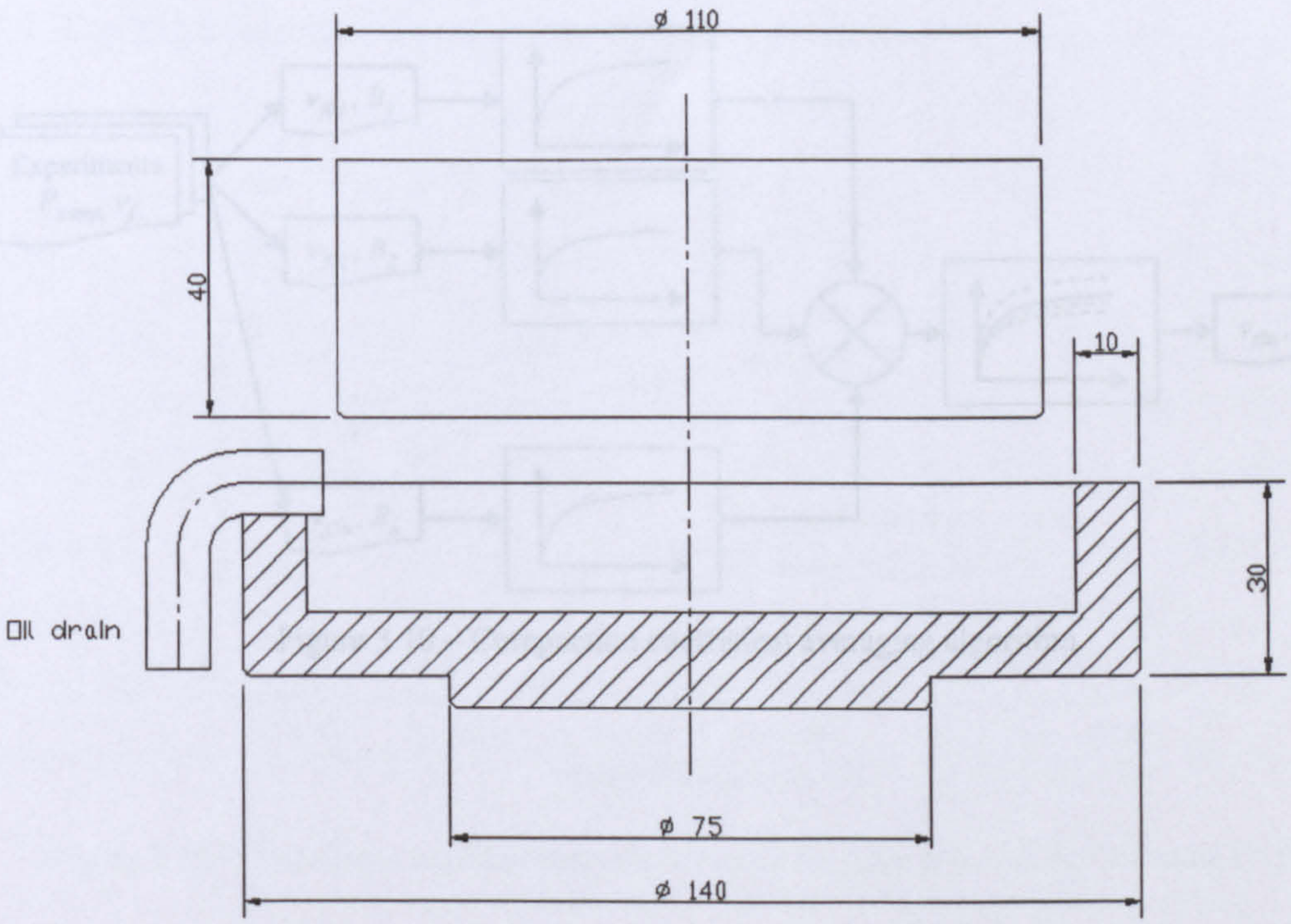

Figure 3.9 – Compaction rig dimensions.

3.2.4 Data fitting techniques

The data analysis was performed in Microsoft™ Excel™ where a Visual Basic™ algorithm for automated raw data sorting and cycle selection was implemented. This is followed by conversion of the force and displacement data into compaction pressure and fibre volume fraction as described above. The compaction model (Equation (3.4)) is then fitted to the experimental data through the Solver™ add-in (Frontline Systems, Inc.) which uses a simplex linear programming procedure to minimize the error cost function shown in Equation (3.9):

$$R^2 = \frac{\sum_{i=1}^{n}\left(\left(v_{f_i}\right)_{Experimental} - \left(v_{f_i}\right)_{Fit}\right)^2}{n} \tag{3.9}$$

Statistically the parameters v_{f0} and B have not been characterized: it is not possible to say whether either follows a normal statistical distribution and therefore an averaging approach is not appropriate. This issue was tackled by calculating the average compaction curve and then obtaining the representative parameters. The procedure is shown in Figure 3.10.

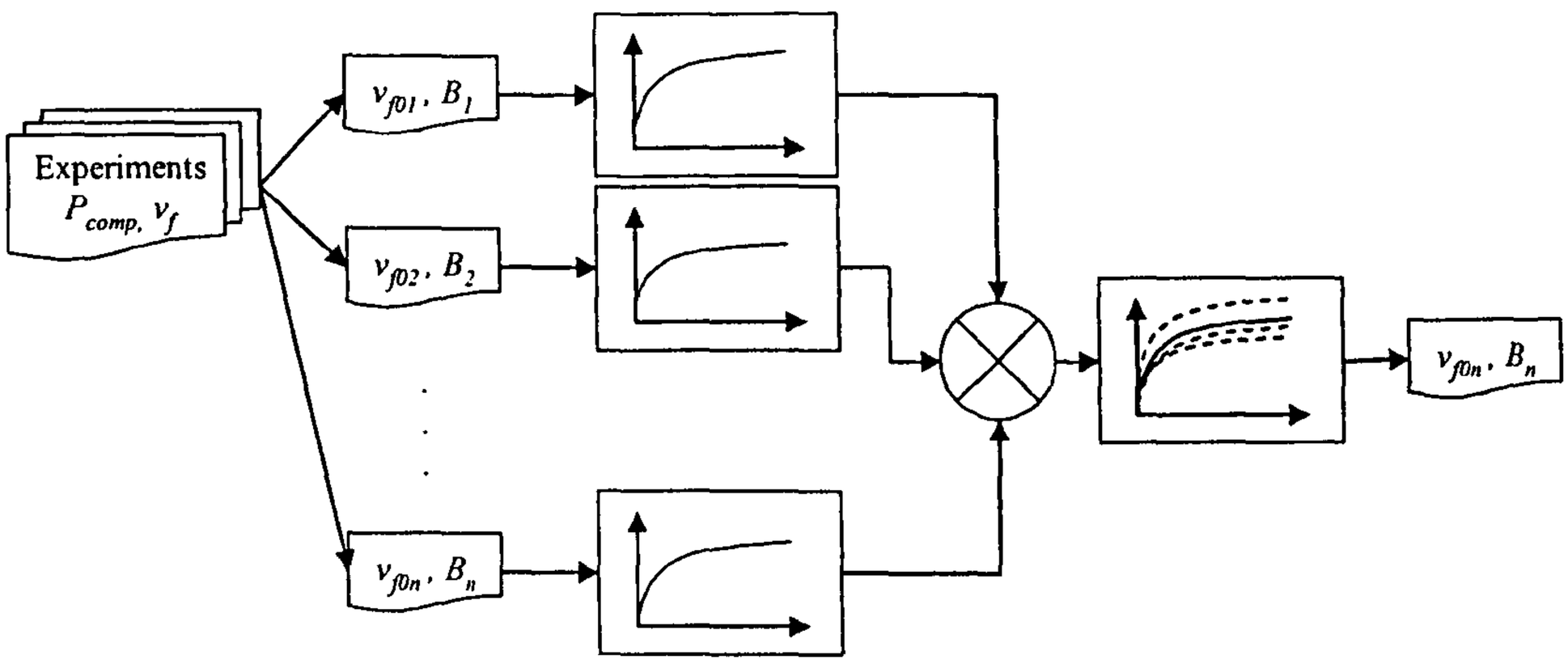

Figure 3.10 – Compaction coefficient averaging algorithm

3.2.5 Adequacy of the empirical compaction power law

The adequacy of the power law model of fibre bed compliance is illustrated in Figure 3.11 for the material with higher fibre content (FGE 117) and in Figure 3.12 for the one with the least fibre content (Vetrotex U750).

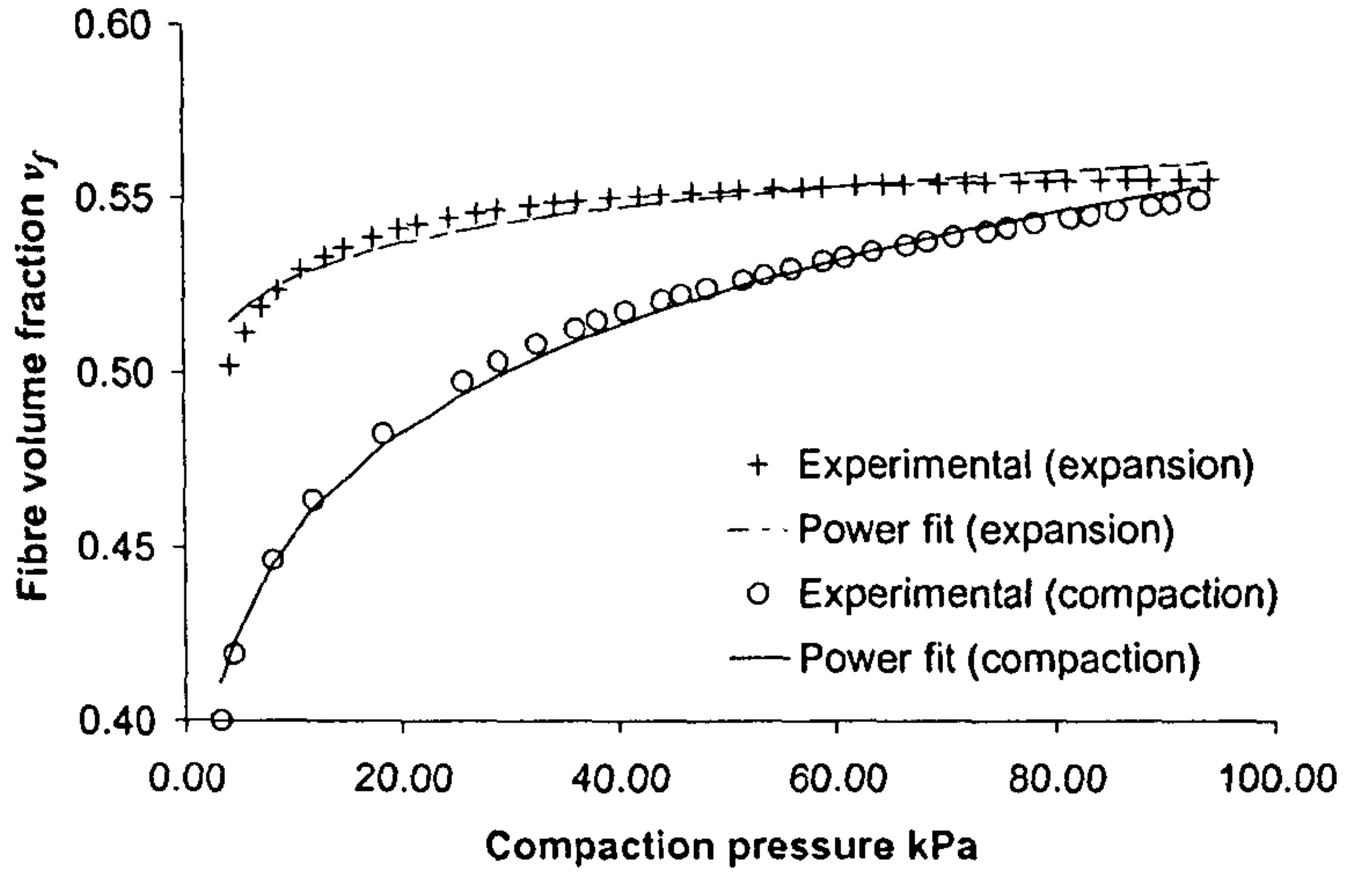

Figure 3.11 – Compliance experimental and fit results for three layers of dry FGE 117

These figures give a qualitative impression not only of the goodness of the fit but also how its quality is affected by different materials and compaction vs. expansion. They highlight that at low stiffening indices (small changes in fibre volume fraction) the model is not very precise. This effect is quantified in Table 3.3 where the correlation coefficients of these fits are shown.

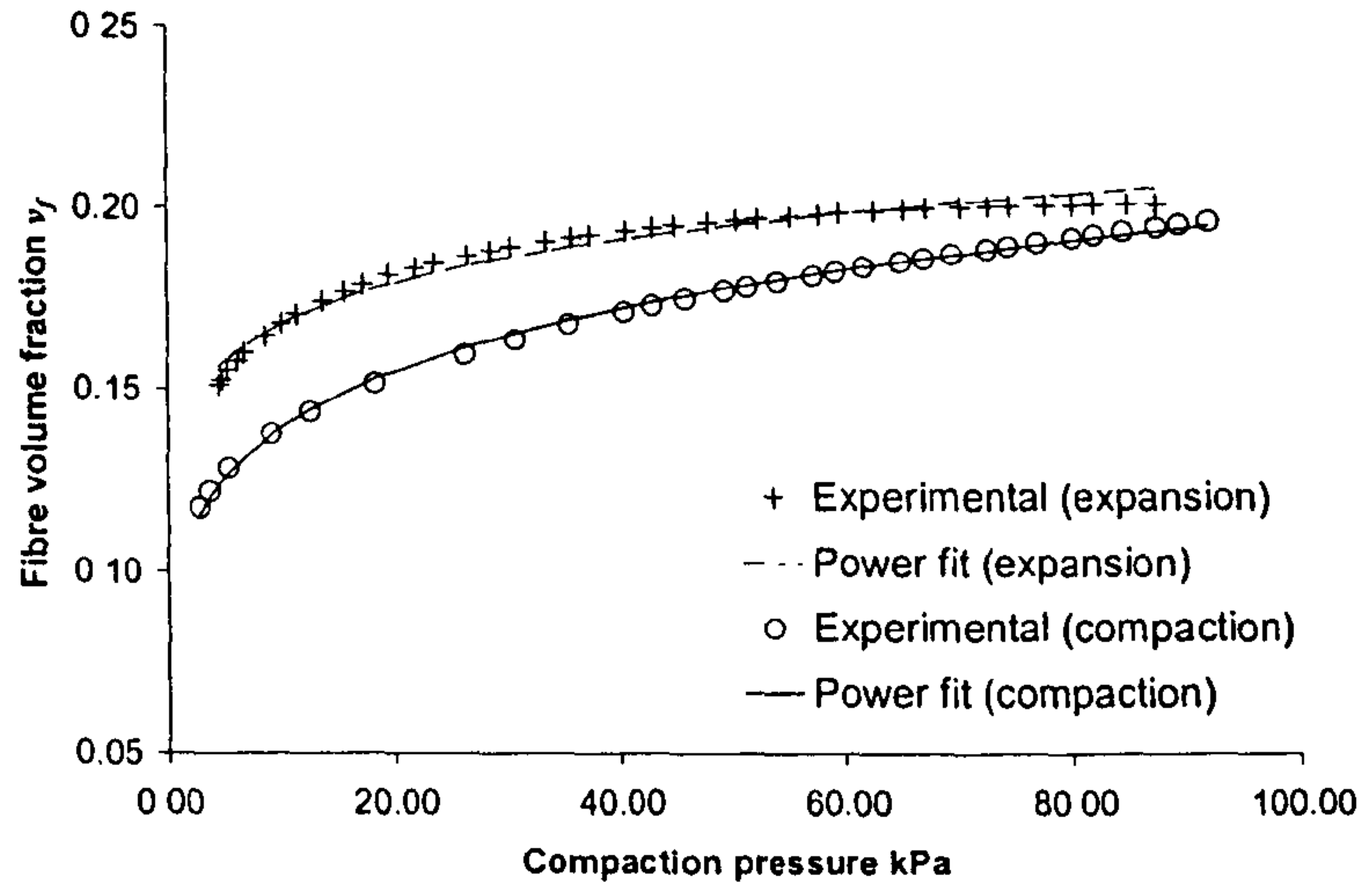

Figure 3.12 - Compliance experimental and fit results for three layers of dry Vetrotex U750

Table 3.3 – Correlation coefficients (R^2) of the power law fit to the experimental results for the four tested materials (dry).

			Compaction	Expansion				Compaction	Expansion
Vetrotex U750	3L	1	99.89%	98.76%	Vetrotex RT600	3L	1	99.99%	95.85%
		2	99.89%	98.74%			2	99.95%	95.34%
		3	99.88%	98.75%			3	99.75%	95.79%
	6L	1	99.94%	99.04%		6L	1	99.44%	96.68%
		2	99.88%	98.90%			2	99.56%	96.57%
		3	99.77%	98.90%			3	-	-
	12L	1	99.88%	98.95%		12L	1	99.05%	97.49%
		2	99.74%	99.71%			2	99.32%	97.74%
		3	-	-			3	99.49%	-
UDUC 660	3L	1	99.69%	97.93%	FGE 117	3L	1	99.62%	96.03%
		2	99.67%	97.91%			2	99.98%	95.60%
		3	99.81%	97.95%			3	99.94%	96.05%
	6L	1	99.76%	97.80%		6L	1	99.76%	96.89%
		2	99.40%	97.86%			2	99.83%	97.05%
		3	99.52%	97.74%			3	99.92%	97.40%
	12L	1	99.58%	98.37%		12L	1	99.89%	97.19%
		2	99.34%	98.14%			2	99.59%	97.21%
		3	99.52%	97.88%			3	99.74%	97.01%

Note that correlation is high (R^2 > 99%) in all compaction cycles of these experiments. Conversely, expansion is not as accurately modelled.

3.3 COMPACTION RESULTS

Having established the theoretical and methodological basis of this study, the following sections will explore the results obtained in the experimental plan. As shown this consists of two main groups: compaction and expansion properties of fibre beds. Dry compaction of textile reinforcements is a fundamental part of the flow mechanisms in LCM processes: in VI, dry compaction during mould evacuation influences permeability and flow front advancement. The other important property is saturated expansion behaviour, which controls the compliant behaviour of the fibre bed in VI described extensively in chapter 2. Of less importance are dry expansion, which happens when the materials are subjected to a number of dry cycles, and saturated compaction, which occurs in mould bleeding: a technique used to reduce component mass and thickness variation by reducing inlet pressure (lower fluid pressures hence higher compaction pressures).

Section 3.3.1 discusses dry compaction and 3.3.2 saturated compaction. The subsequent sub-sections deal with statistical analysis of the results. Expansion is

not discussed at length but is included in the summary of the average compaction and expansion properties shown in Appendix 3.C

3.3.1 Dry compaction

The dry compaction experimental results highlight three features of compaction: the effect of tow nesting on compaction, the effect of repeated compaction cycles on the mechanics of the textile and the relaxation at constant load.

Figure 3.13 shows the dry compliance behaviour of FGE117 in compaction. Firstly, from a) the first cycle compaction behaviour of the six and twelve layer samples was virtually identical. This suggests that tow nesting differences become negligible at higher layer numbers in FGE 117 [0/±45] non-crimp textile.

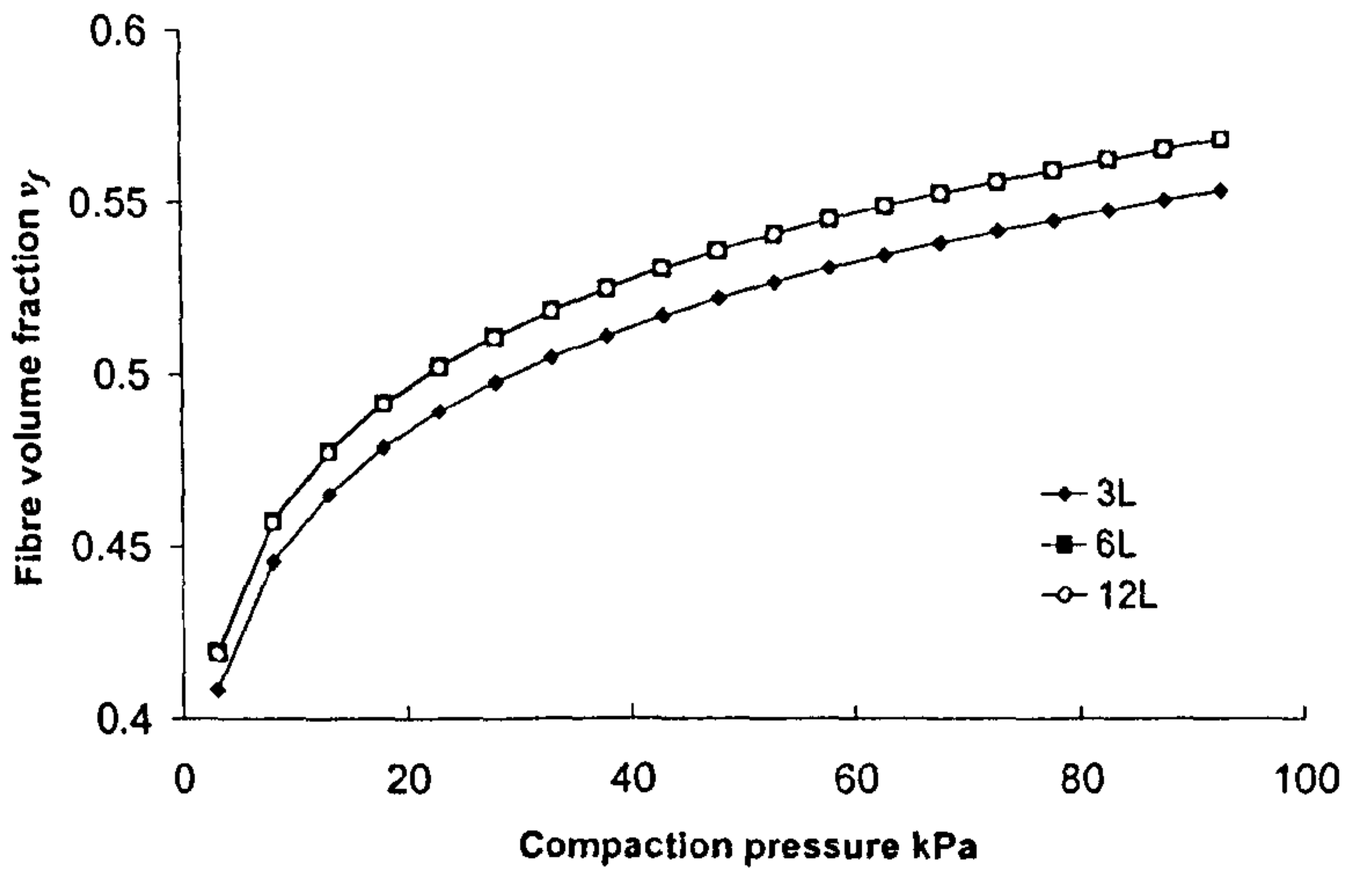

Figure 3.13 – Formax FGE 117 compaction results: compaction versus number of layers.

In Figure 3.14 one can see the effect of load cycling on compaction properties. As fibres become more optimally arranged the stiffness increases along with the initial fibre volume fraction v_{f0}. Note also that apart from a vertical shift, the response of fibre volume to the increasing compaction pressure is almost identical in the second and third cycles.

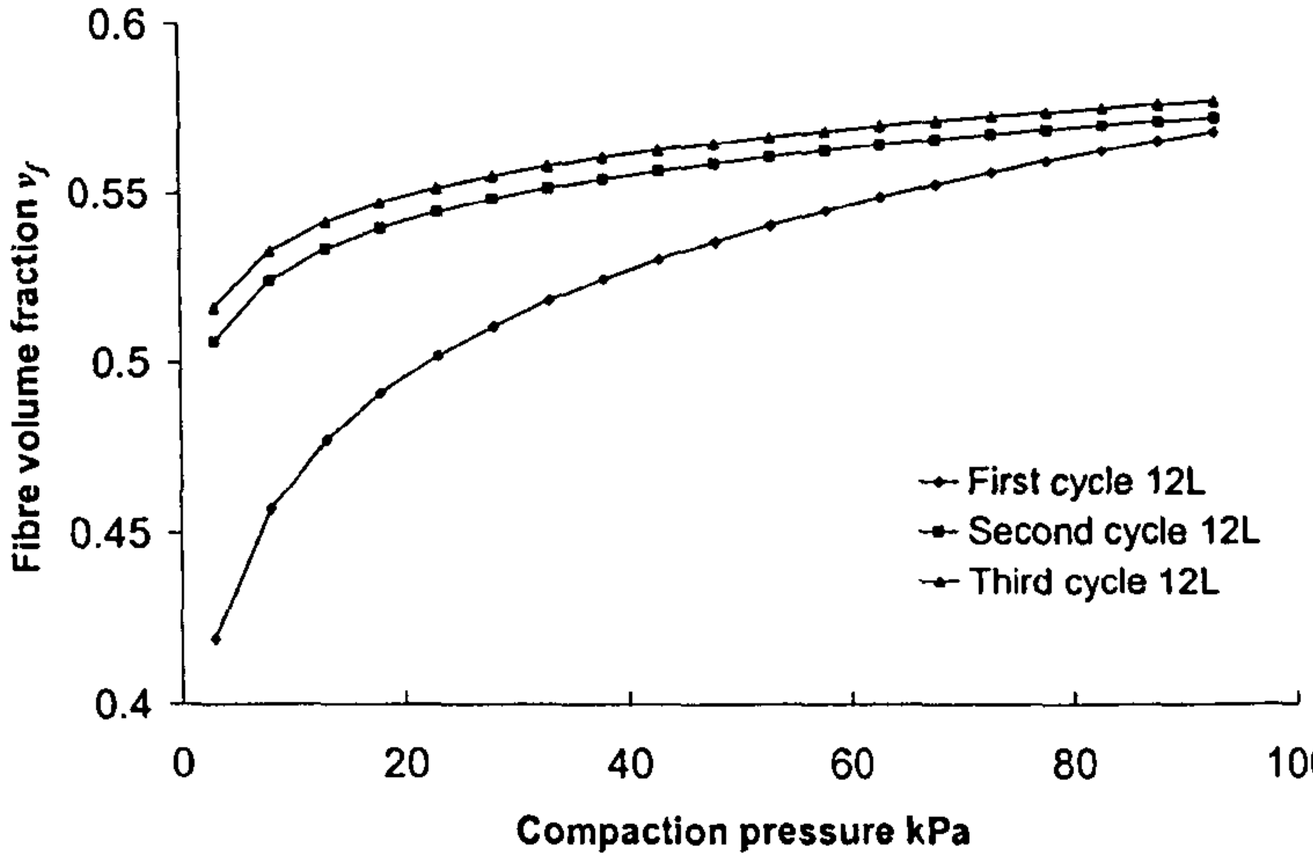

Figure 3.14 – Formax FGE 117 compaction results: compaction versus cycle number for 12 layers

Unlike the previous case, the Flemings UDUC textile shows a measurable difference in compaction (Figure 3.15) between the three, six and twelve layer cases: this was attributed to the tow spacing in the uni-directional textile which allows significantly different nesting. Nevertheless the difference between results obtained in three vs. six layer experiments is larger than that found in the six vs. twelve layers.

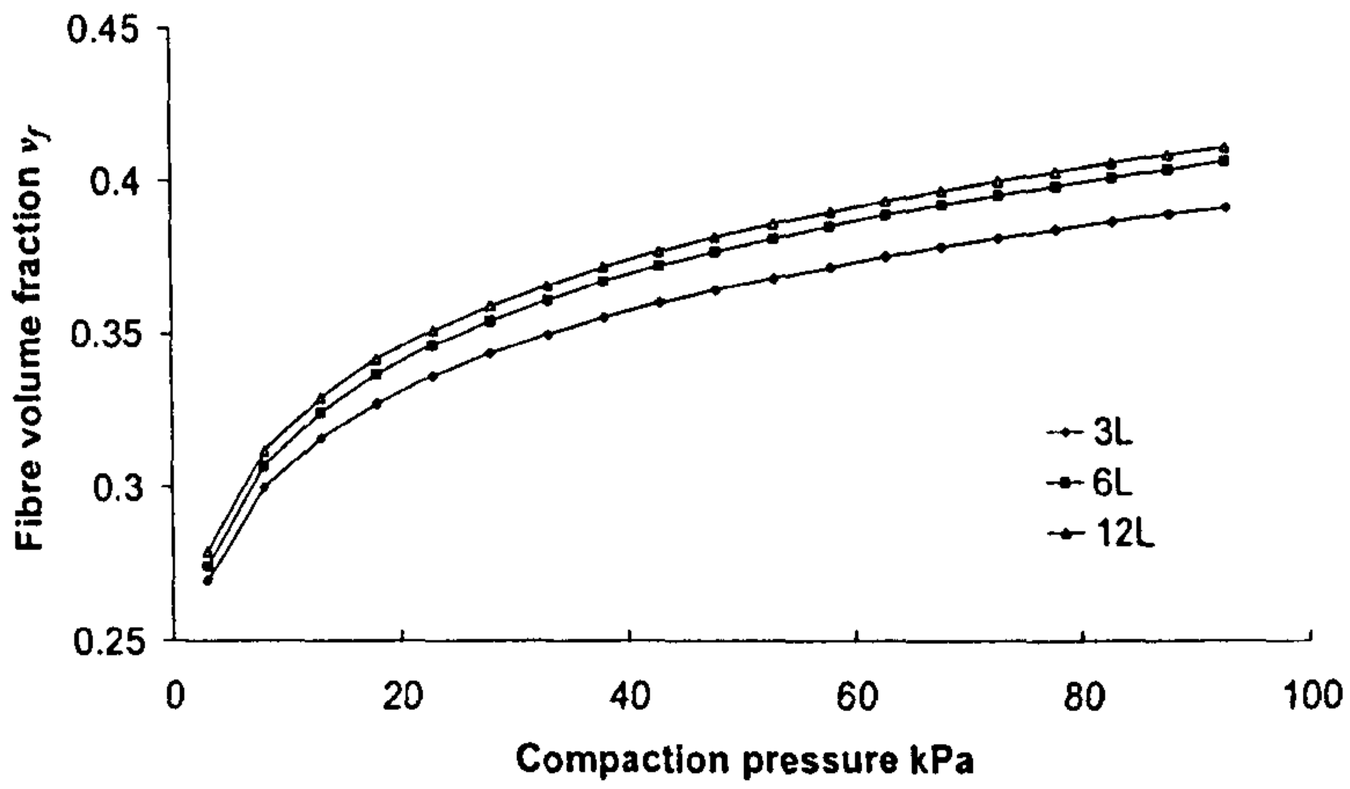

Figure 3.15 - Flemings UDUC compaction results: compaction versus number of layers.

Figure 3.16 indicates that, as expected, the considerable difference between first and second cycle behaviours is not observed between the second and third.

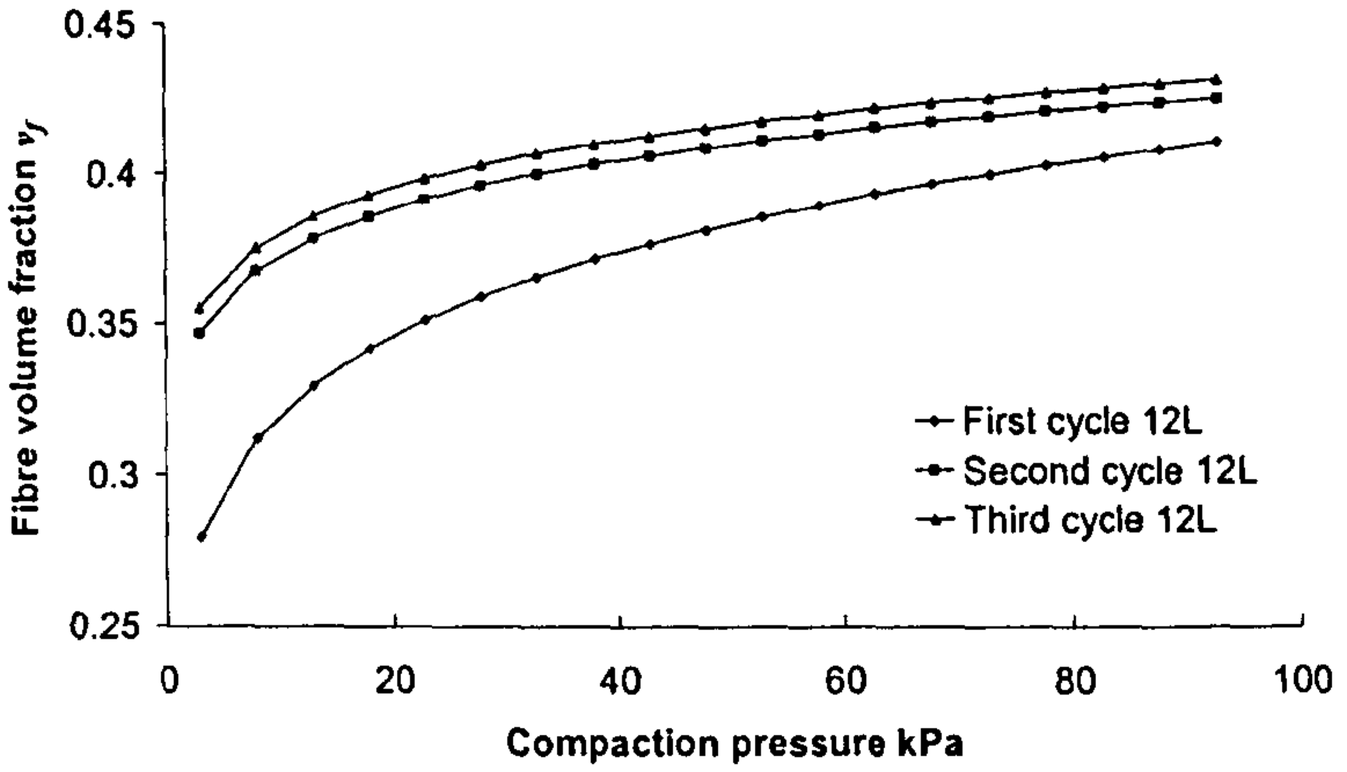

Figure 3.16 - Flemings UDUC compaction results: compaction versus cycle number for 12 layers

The woven textile (Vetrotex RT600) was expected to show evidence of nesting and that is clearly the case. This material presents the larger difference between compaction curves versus number of layers indicating a substantial effect of fibre nesting (Figure 3.17).

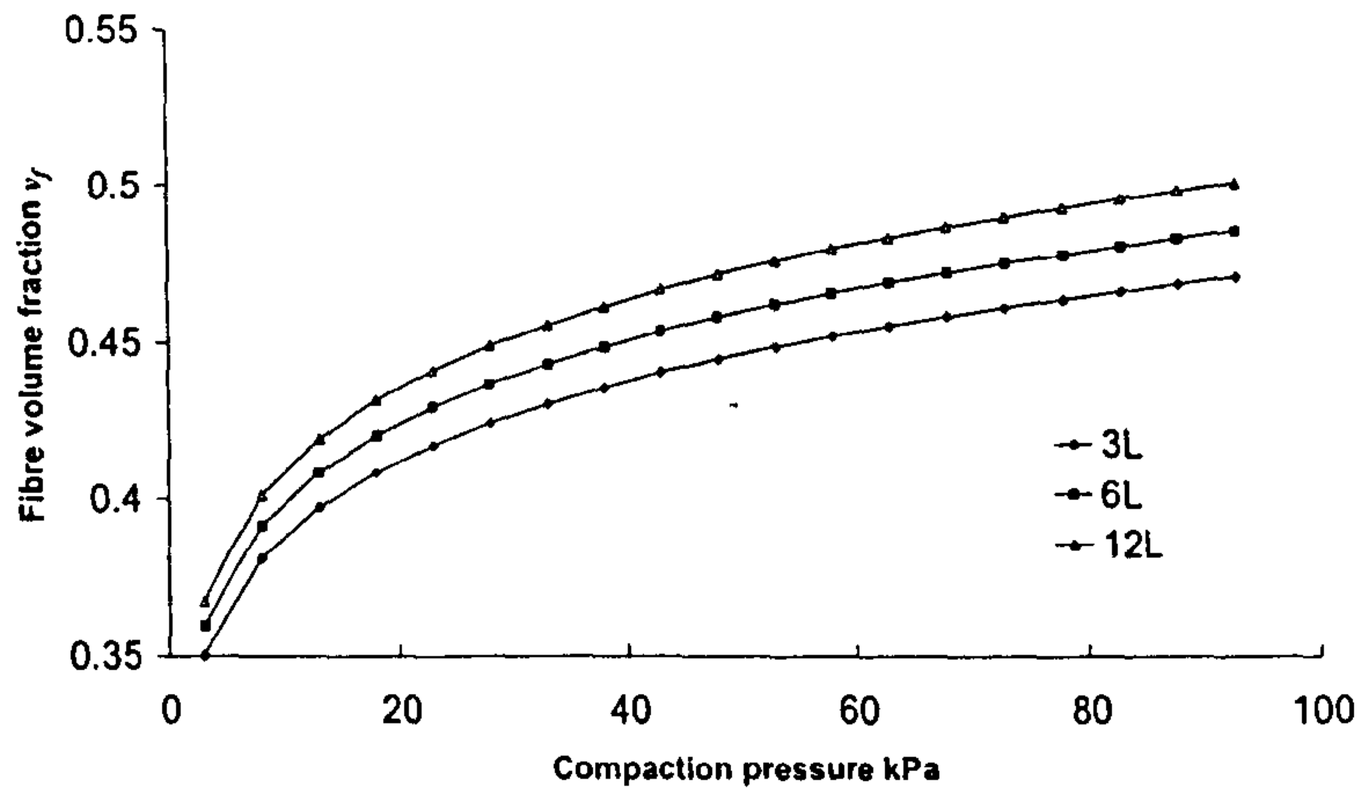

Figure 3.17 – Vetrotex RT600 compaction results: compaction versus number of layers.

Figure 3.18 indicates that, unlike non-crimp textiles, there is a larger difference between second and third cycle behaviours.

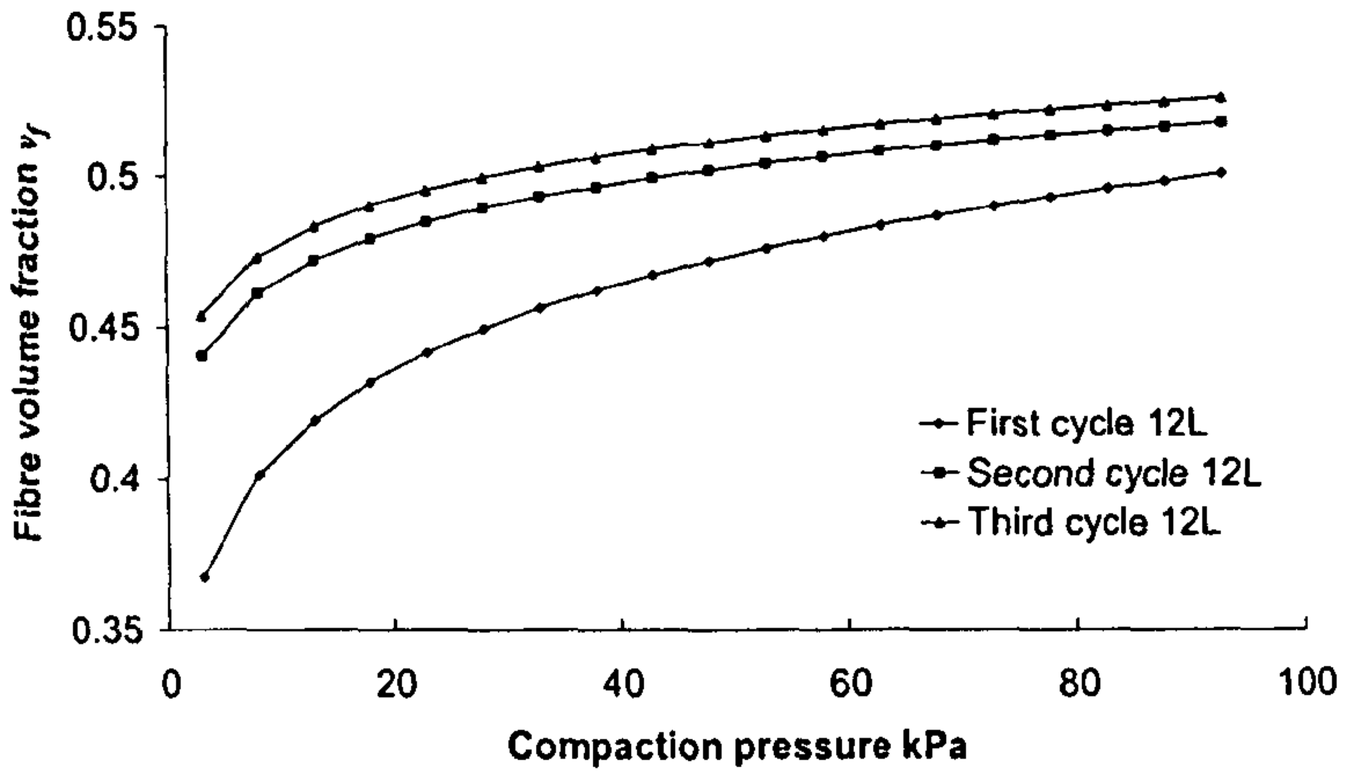

Figure 3.18 – Vetrotex RT600 compaction results: compaction versus cycle number for 12 layers

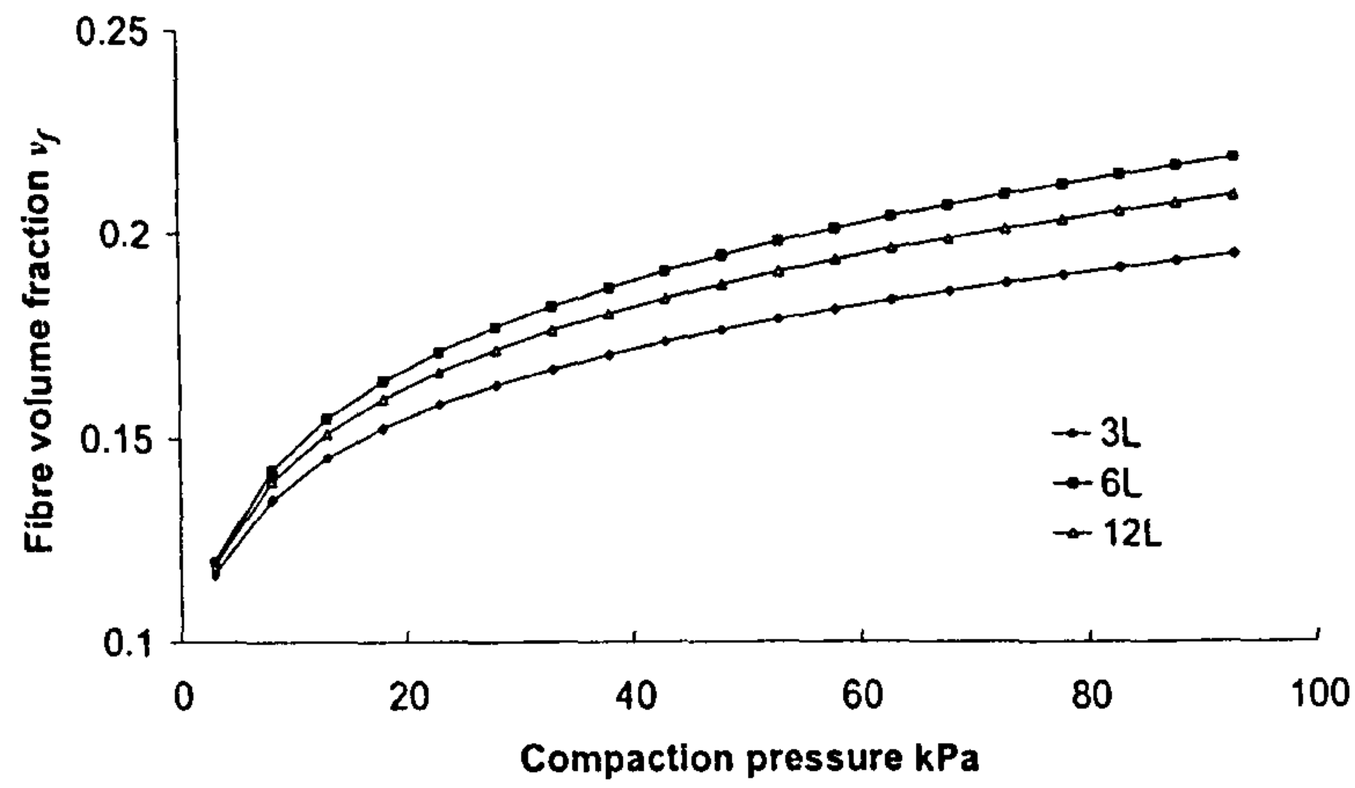

Figure 3.19 – Vetrotex U750 compaction results: compaction versus number of layers.

The continuous strand mat CSM reinforcement (Vetrotex U750) presents a different behaviour (Figure 3.19): for all layer numbers, the initial fibre volume fraction is very similar. This is not found in the other materials and is typical of a material which does not naturally nest at low pressures. Nevertheless, while compaction properties diverge, that divergence is apparently not linked to the number of layers - it may be due to a natural variability. Only two cycles were recorded in this experiment, limiting the analysis of pressure cycling on compaction properties (Figure 3.20). Nevertheless, one can observe that, as before, there is an increase in initial fibre volume fraction v_{f0} accompanied by a decrease in stiffening index B from the first cycle to the second. This is observed by noting that fibre volume fractions at lower pressures are higher in later cycles but are normally associated with a smaller change in fibre volume fraction with compaction pressure.

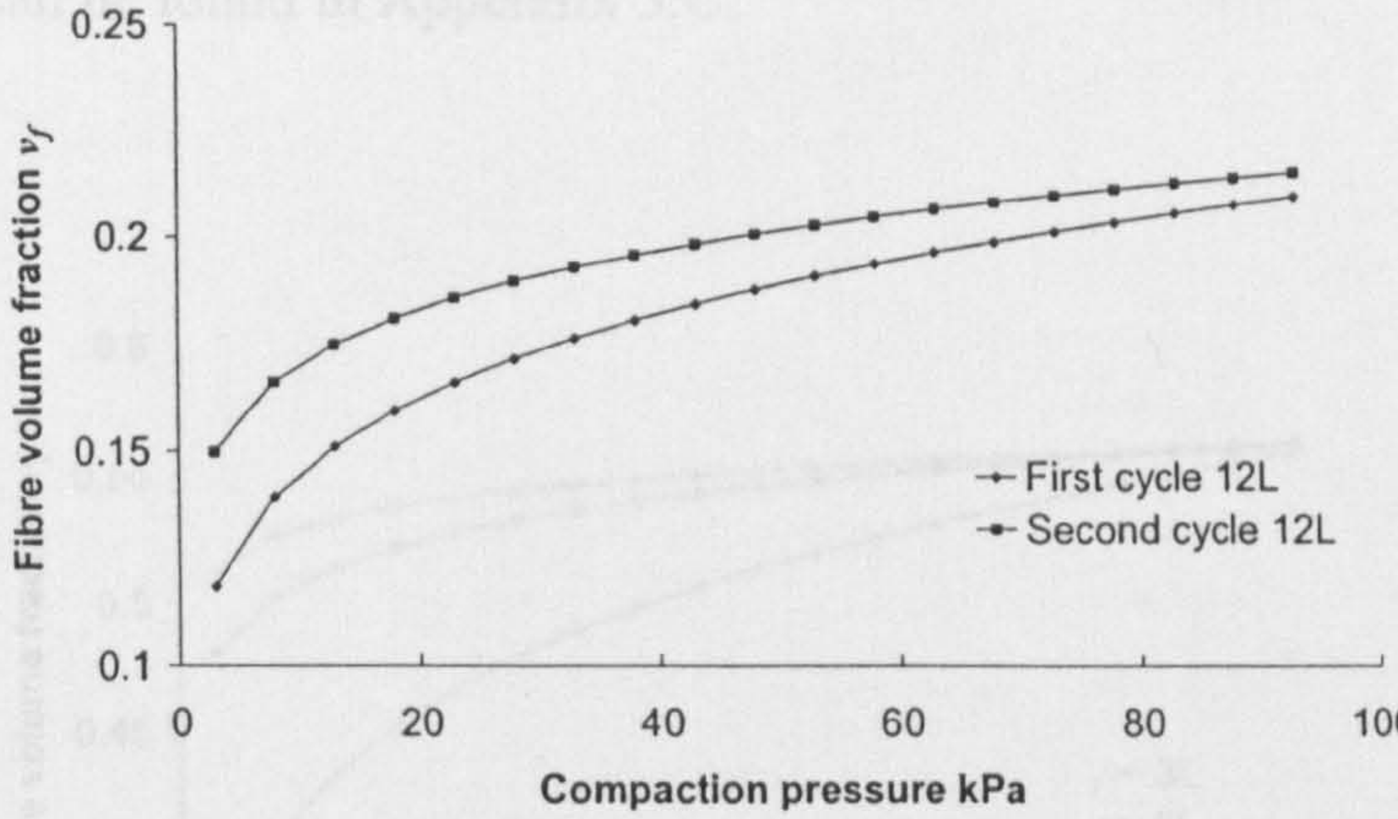

Figure 3.20 – Vetrotex U750 compaction results: compaction versus cycle number for 12 layers.

Note that, as Figure 3.21 shows, the unidirectional Flemings UDUC does not present the highest attainable fibre volume fraction in this group, being situated in the range of 27% - 41%. Moreover, it is positioned below the plain woven Vetrotex RT600 (35% - 49%) and does not even intersect the fibre volume fraction range found in the triaxial Formax FGE 117 (41% - 56%). Nevertheless, this behaviour is expected from a highly constrained warp stitched textile were the tows cannot expand sufficiently (the stacking sequence was constant: $[0/90]_n$).

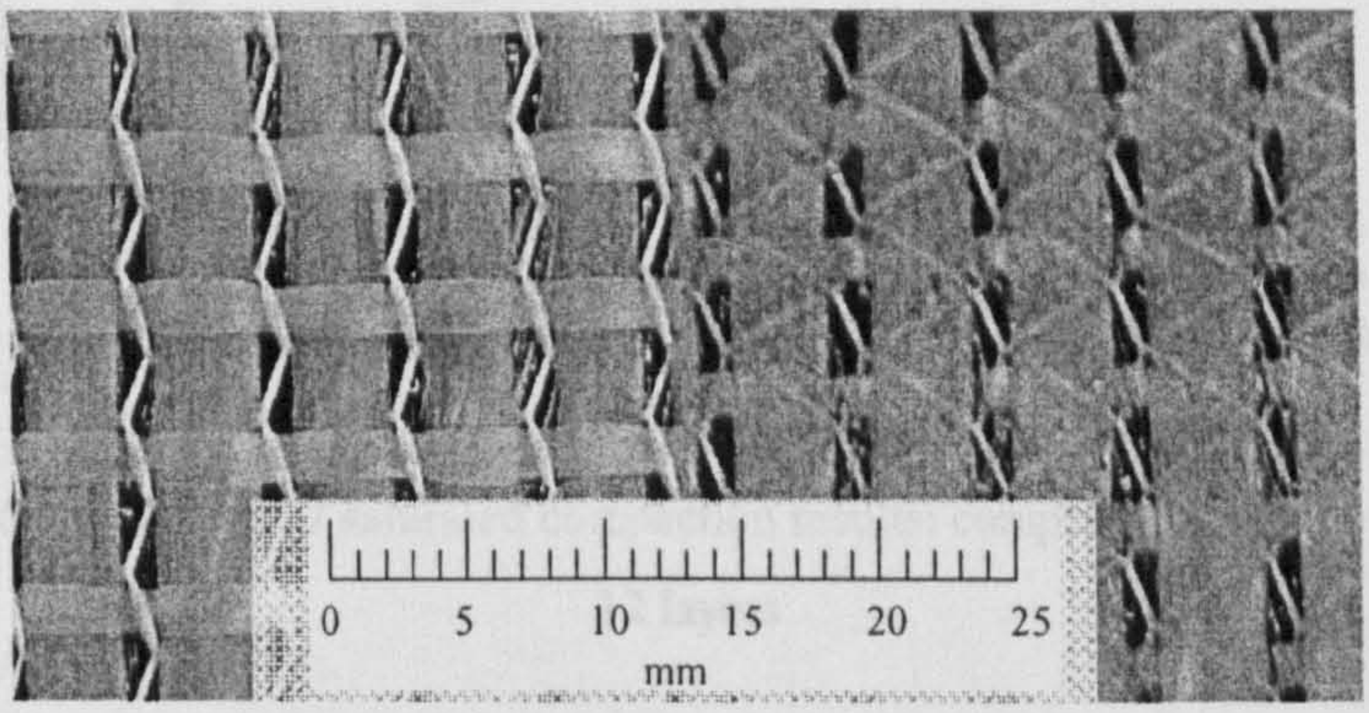

Figure 3.21 – Details of top and bottom surfaces of the Vetrotex RT600 textile showing a dense knit

3.3.2 Saturated compaction

The same analysis was performed for all saturated compaction results on the four materials. The differences in behaviour (as can be seen by comparing the dry FGE

117 results in Figure 3.13 with the saturated results in Figure 3.22). All relevant coefficients can be found in Appendix 3.C.

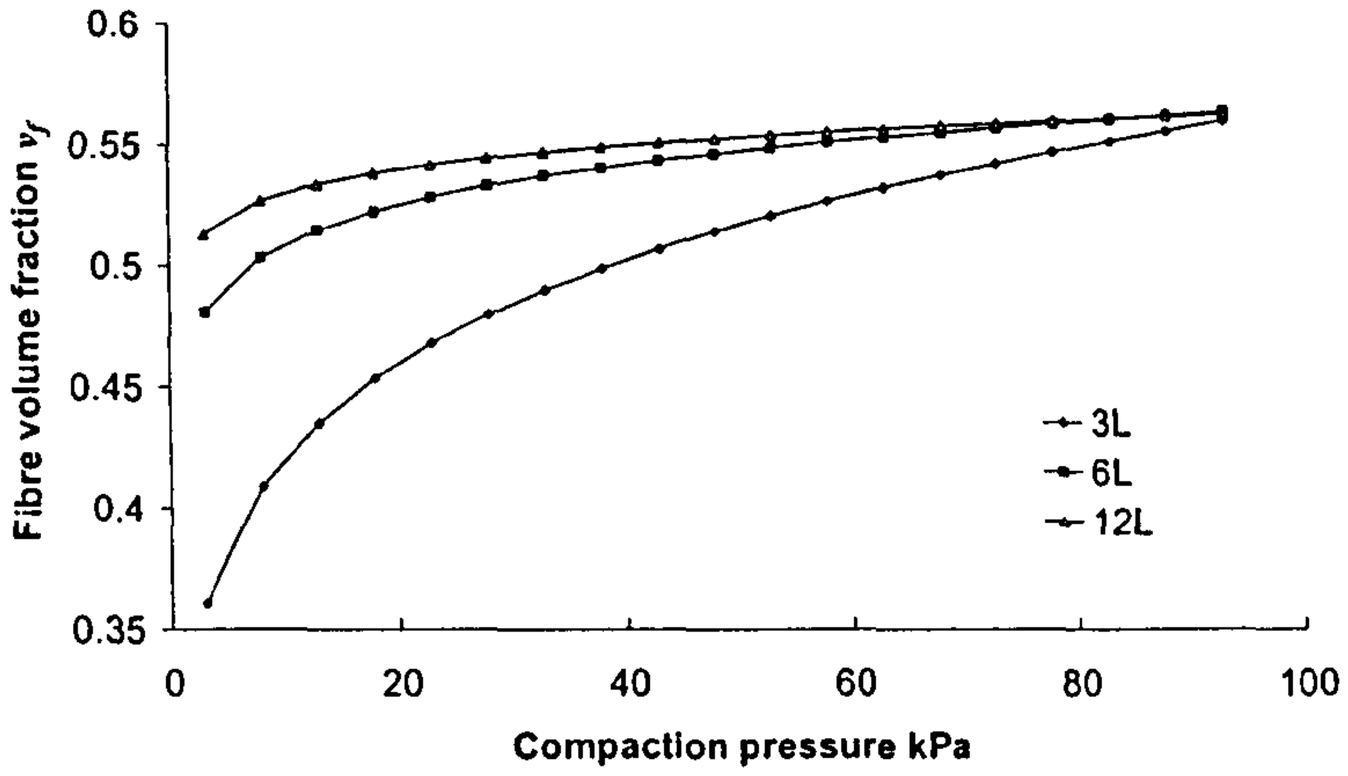

Figure 3.22 – Formax FGE 117 saturated compaction results: compaction versus number of layers

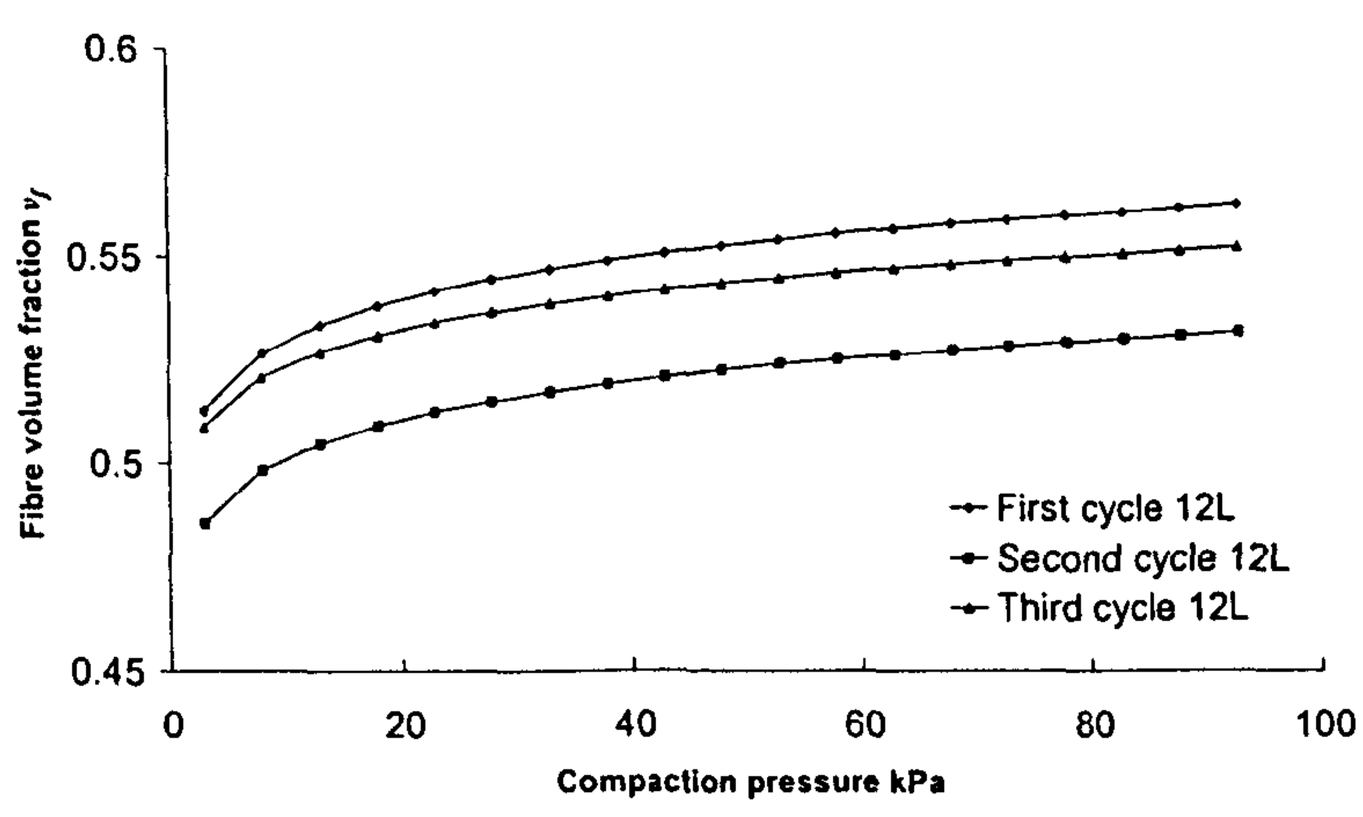

Figure 3.23 – Formax FGE 117 saturated compaction results: compaction versus cycle number for 12 layers

3.3.3 Statistical studies on the compaction properties

Another problem that exists in compaction of composites is repeatability between nominally identical samples. A graphic example of experimental scatter from 12 compaction experiments is shown in Figure 3.24 (3 layers of FGE 117).

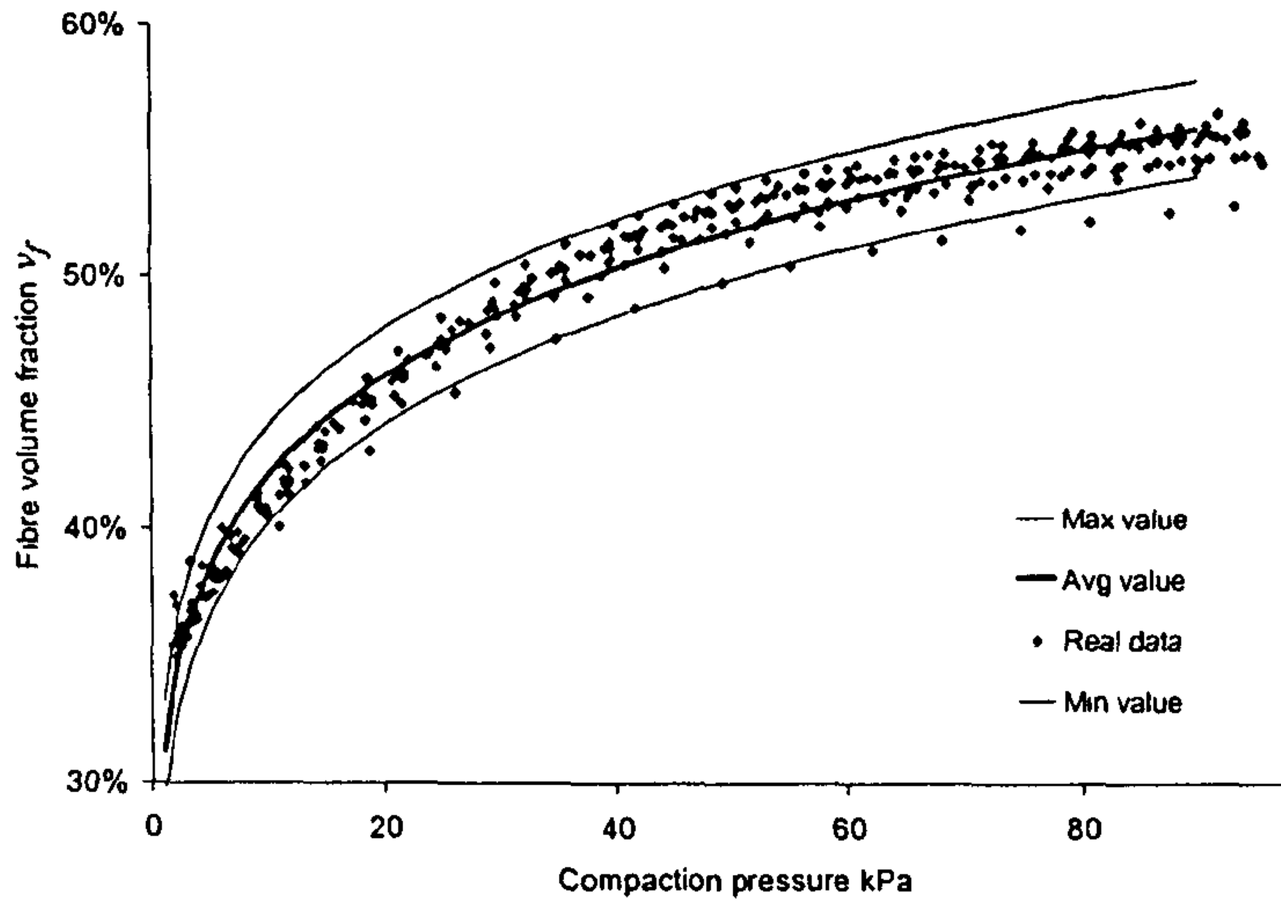

Figure 3.24 – Distribution of experimental observations of fibre volume fractions for three layers of FORMAX FGE 117. Saturated observations (Trent oil ™ HDX30). Results show a high level of fibre volume fraction variation at any given pressure

The hypothesis that both v_{f0} and B fit coefficients follow normal distributions was tested with a Lilliefors statistical test (Conover, 1980; Mathworks, 2002). It is not possible to reject that hypothesis; nevertheless, this can be due to insufficient data. This work was done for the triaxial fabric only because of the number of samples (12 as opposed to 4 in the other materials).

3.4 COMPACTION MASTER CURVES

3.4.1 The compaction master curve

The four studied architectures represent a cross-section of available reinforcements; nevertheless, to achieve a broader view of compaction of textiles these results (Appendix 3.B) are complemented with previously published empirical data (Robitaille *et al 1999 a, b, c)*. When all data are compiled it is possible to infer that v_{f0} and B are linked (Figure 3.25).

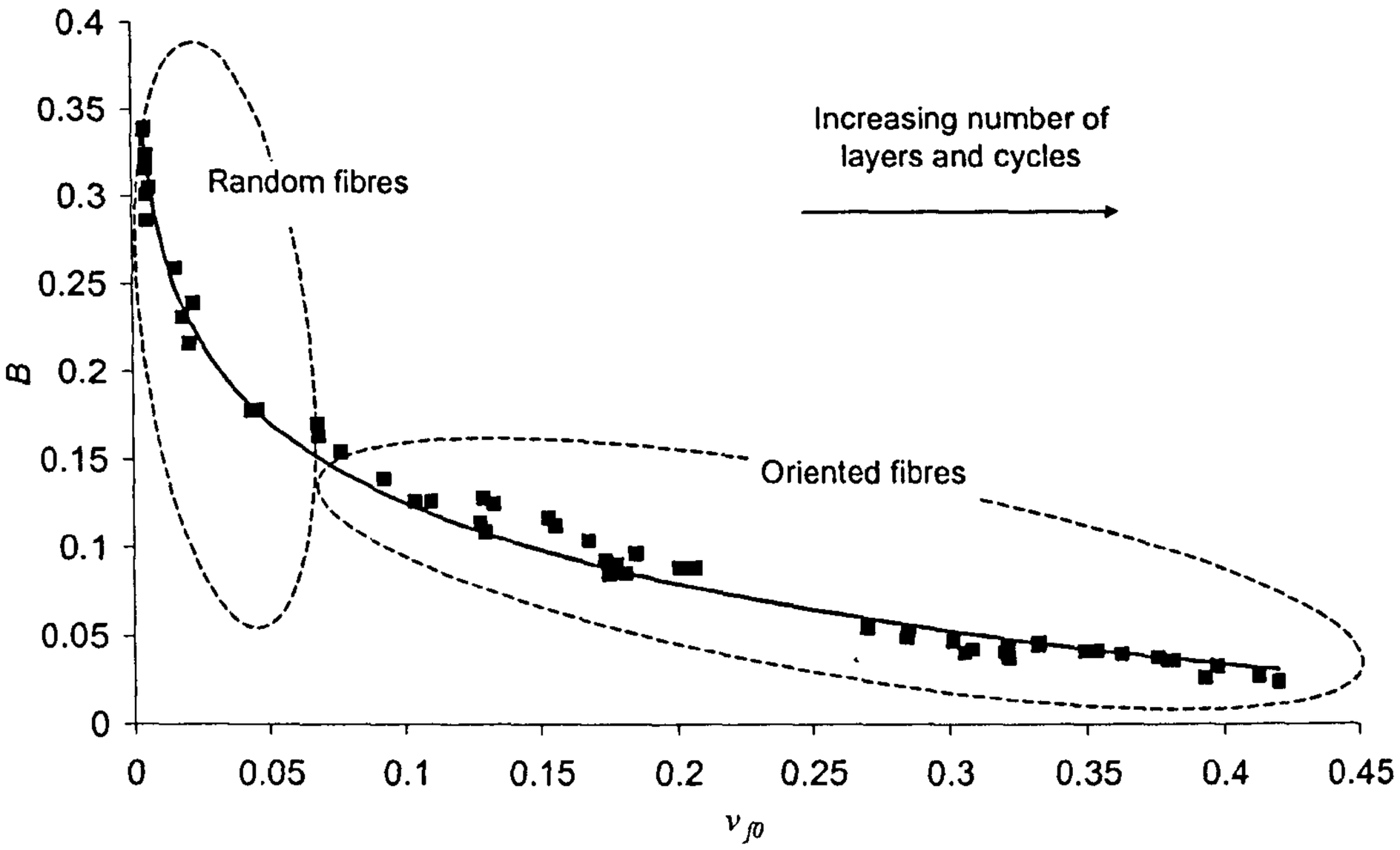

Figure 3.25 - Compaction master curve for both dry and saturated materials

The relation between parameters v_{f0} and B can be described by the expression:

$$B = C_1 \cdot \ln\left(v_{f_0}\right) + C_2 \tag{3.10}$$

where the coefficients C_1 and C_2 and relevant fit data are presented in Table 3.4.

Table 3.4 – Compaction master curve fit data. Statistical report of fit to experimental data.

Coefficients (with 95% confidence bounds):		
C_1	=	-0.06567 (-0.06789, -0.06344)
C_2	=	-0.02745 (-0.03356, -0.02135)
Goodness of fit		
Sum of square errors:		0.005559
Coefficient of correlation		0.9868
Root mean square error		0.01088

Figure 3.26 shows the 95% probability bounds for the region where new experimental values should be located assuming that the master curve fit is correct (Table 3.4).

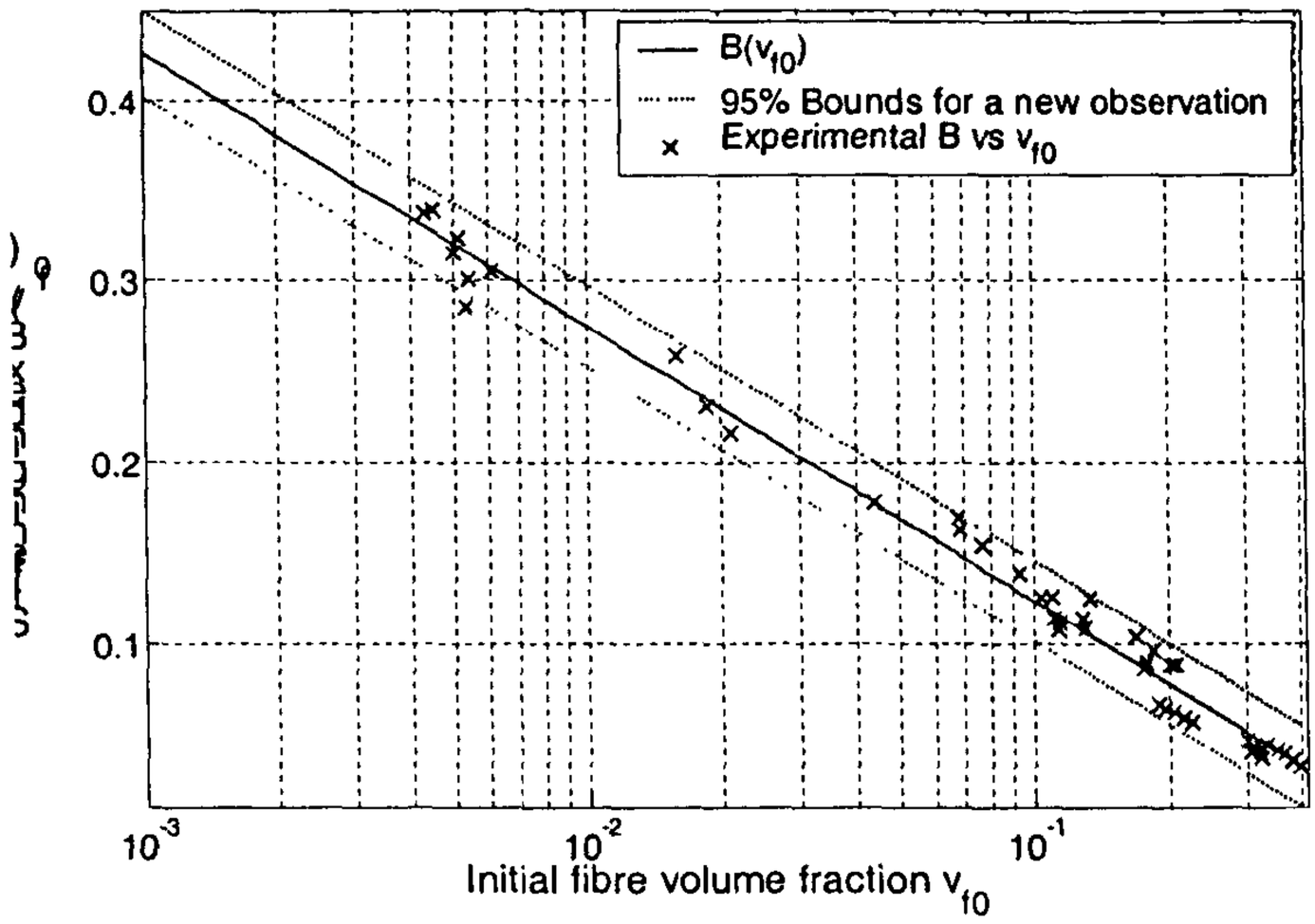

Figure 3.26 - Log plot of the master curve showing the 95% bounds for a new observation. The prediction bounds are equally separated from the fitting function. These are obtained by direct evaluation of standard deviation of observations vs. fitting function. $B(v_{f0})$ is given in Equation (3.10)

3.4.2 Experimental validation of the compaction master curve

One can argue that the above predicted variability of new observations is too high. Nevertheless, experiments show that it is acceptable considering the nature of these materials. As Figure 3.24 shows, the scatter of compaction data for 12 experiments on the triaxial stitched FGE material is significant. This figure clearly illustrates that for a single material and lay-up the fibre volume fraction is predicted to vary up to 9% at maximum pressure.

As was shown, there is statistical evidence to substantiate the master curve model (Equation (3.10)) where C1 and C2 are constants (Table 3.3) determined by fitting the existing experimental data with a logarithmic curve. The power law can then be written as:

$$v_f = v_{f_0} \cdot P^B = v_{f_0} \cdot P^{C_1 \cdot \ln\left(v_{f_0}\right) + C_2} \tag{3.11}$$

$$v_{f_0} = e^{\frac{\ln\left(v_f\right) - \ln(P)\, C_2}{1 - \ln(P) \cdot C_1}}$$

So that any fibre bed compaction mechanism (e.g. a mass with known area) can measure fibre volume fraction v_f to obtain v_{f0}.

Experiments were performed with a static pressure of 36.5 kPa, representing roughly a third of the maximum pressure used in dynamic tests. The results in Table 3.5 show good agreement for the first cycles but diverge for higher cycles and lower density materials. This is due to the lower compaction pressure used, which leads to a lower degree of reorganization of the fibre network.

Table 3.5 – Static (S) vs. dynamic (D) compaction coefficients.
Static results were obtained at a pressure of 36.5 kPa

FGE 117	Cycle		2		3	
	Type		v_{f0}	B	v_{f0}	B
		D	0.332	0.045	0.350	0.041
		S	0.364	0.039	0.383	0.036
UDUC	Cycle		1		2	
	Type		v_{f0}	B	v_{f0}	B
		D	0.113	0.108	0.190	0.066
		S	0.104	0.121	0.113	0.116
RT600	Cycle		1		2	
	Type		v_{f0}	B	v_{f0}	B
		D	0.175	0.086	0.306	0.041
		S	0.202	0.078	0.236	0.067
U750	Cycle		1		2	
	Type		v_{f0}	B	v_{f0}	B
		D	0.035	0.150	0.059	0.107
		S	0.011	0.270	0.013	0.259

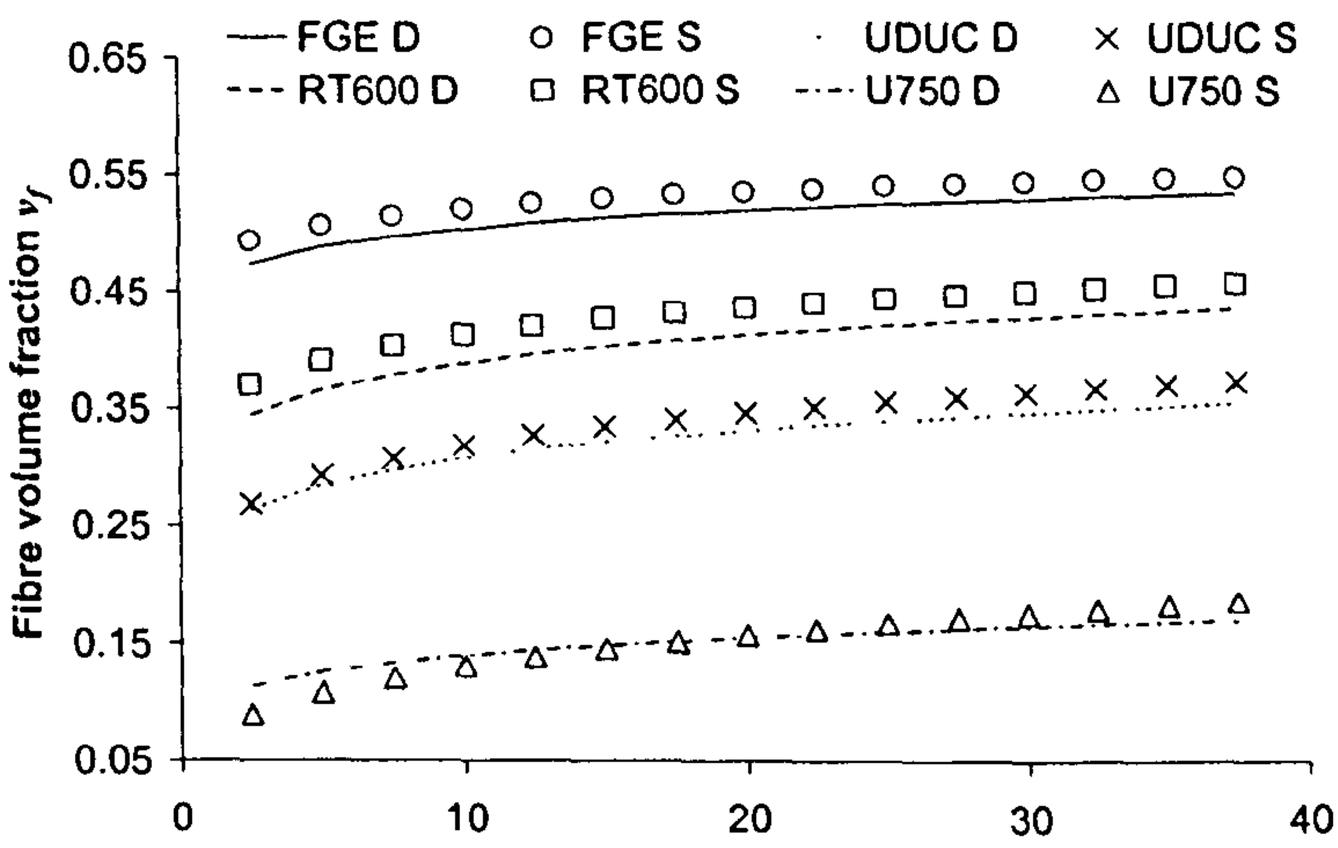

Figure 3.27 – Static (S) vs. dynamic (D) compaction curves. Lines represent full load-displacement experimental results

The results in the first column are shown in Figure 3.27 where it can be observed that the compaction master curve based static tests show good agreement with the dynamical tests. However, it is also clear that the static tests on textile reinforcements resulted invariably in an overestimation of fibre volume fractions. As Figure 3.28 illustrates, this overestimation has a clear trend – implying that the method does not replicate the material's behaviour completely. Nevertheless, in light of the small value of the residuals, one can conclude that the proposed static test method is able to obtain an adequate initial estimate of a textile's compliance.

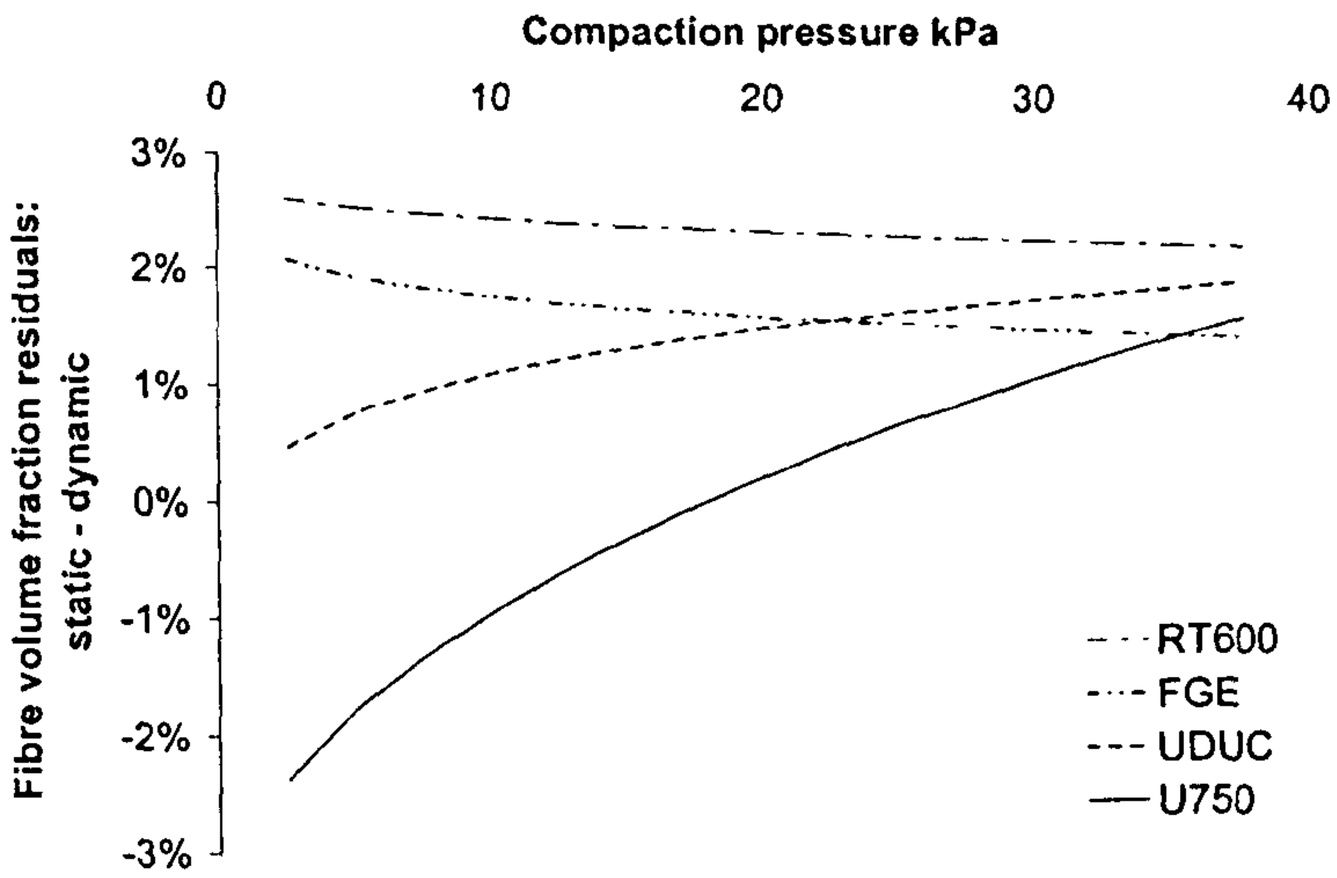

Figure 3.28 – Static-dynamic test residuals

3.4.3 The expansion master curve

Table 3.6 contains the expansion master curve coefficients. These are obtained following the procedure in section 3.4.1 but contain only the results from the experiments done during this work and are not complemented with published data. Nevertheless, the coefficient of correlation between model and data remains significant.

Table 3.6 – Expansion master curve fit data.

Statistical report on the log fit to experimental data

Coefficients (with 95% confidence bounds):		
C_1	=	-0.04538 (-0.04746, -0.04331)
C_2	=	-0.01597 (-0.01907, -0.01288)
Goodness of fit		
Sum of square errors:		0.001944
Coefficient of correlation:		0.9711
Root mean square error:		0.005839

Figure 3.29 shows the expansion master curve obtained with both saturated and dry experimental results for the four materials tested:

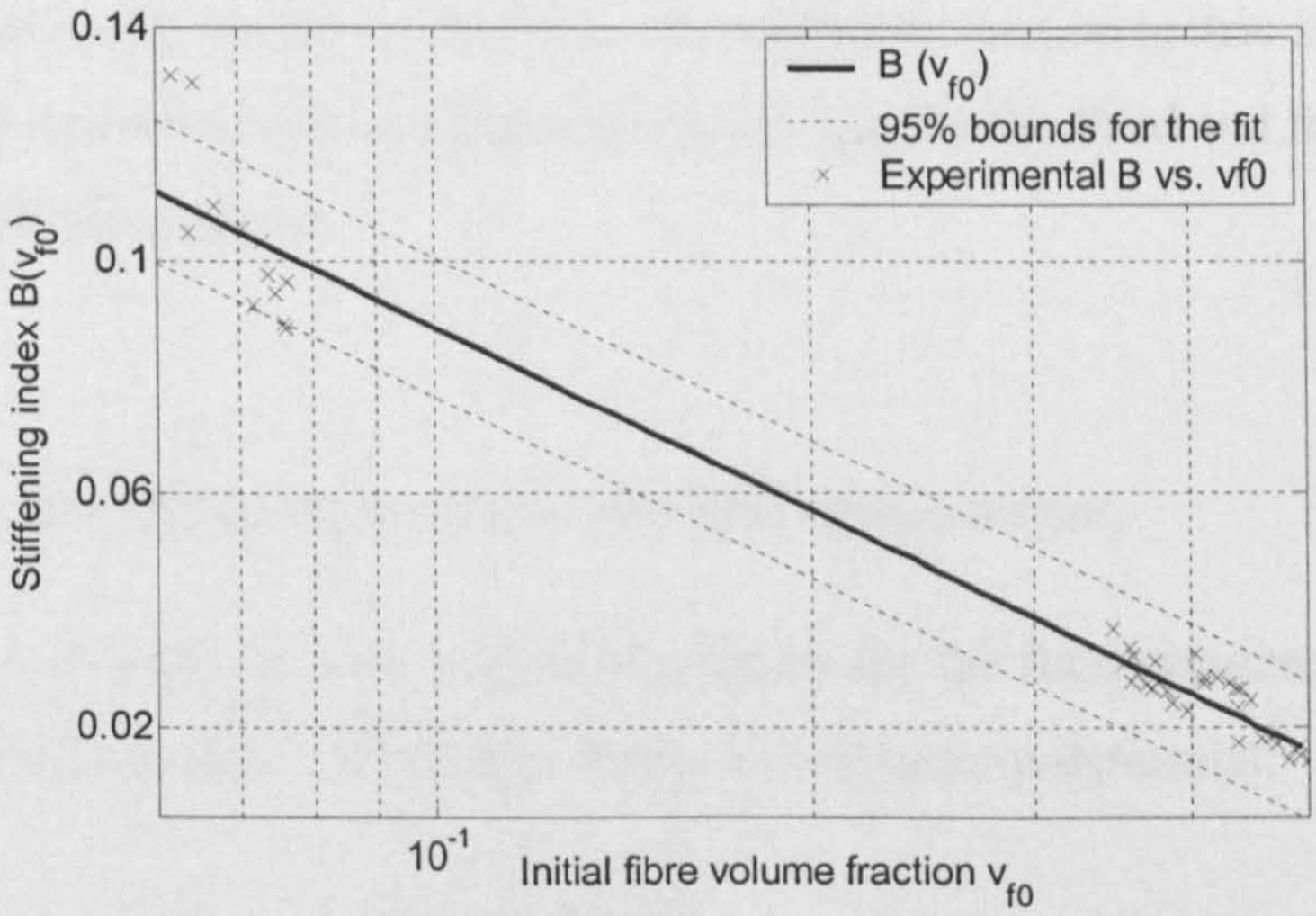

Figure 3.29 - Log plot of the expansion master curve showing the 95% bounds for a new observation. The prediction bounds are equally separated from the fitting function. These are obtained by direct evaluation of standard deviation of observations vs. fitting function

3.5 PARAMETRIC STUDY OF THE FLUID PRESSURE SOLUTION

Having shown (Figure 3.25) that the compaction of textile reinforcements can be described by a single parameter model it follows that the parametric study of the pressure field solution for flow through compliant media (Equation (2.26)) is reduced to material/process parameters: inlet pressure, outlet pressure and initial fibre volume fraction and one numerical parameter: the number of nodes (P_i, P_o, v_{f0} and n). Furthermore, while chapter 2 demonstrates the difficulty of obtaining a

closed form solution for the fluid pressure field it will also be shown that it follows a second order polynomial with small error.

$$\begin{aligned} P_i &= \{50, 60, 70, 80, 90\}\, kPa \\ P_o &= \{0, 10, 20, 30, 40\}\, kPa \\ v_{f_0} &= \{0.10, 0.15, 0.20, 0.25\} \\ n &= \{10, 50, 100, 500\} \end{aligned} \tag{3.12}$$

These values were chosen because of their applicability to real scenarios: inlet and outlet pressures are within what were perceived as the most relevant ranges, initial fibre volume fractions reflect the most common dry compaction cases while focussing on highly compliant materials. In summary, the parametric study looked into five levels for the first two parameters and four for the third and fourth giving 5x5x4x4=400 simulations:

3.5.1 Second order polynomial pressure field approximation

The absence of a closed form analytical solution for the fluid pressure field led to polynomial fitting trials. These show that a second order polynomial:

$$P(\alpha) = a \cdot \alpha^2 + b \cdot \alpha + c \tag{3.13}$$

can describe the pressure field with a coefficient of correlation which is, in the worst case scenario (least number of nodes, highest pressure difference and smallest compaction coefficient), higher than 0.99. This is illustrated in Figure 3.30

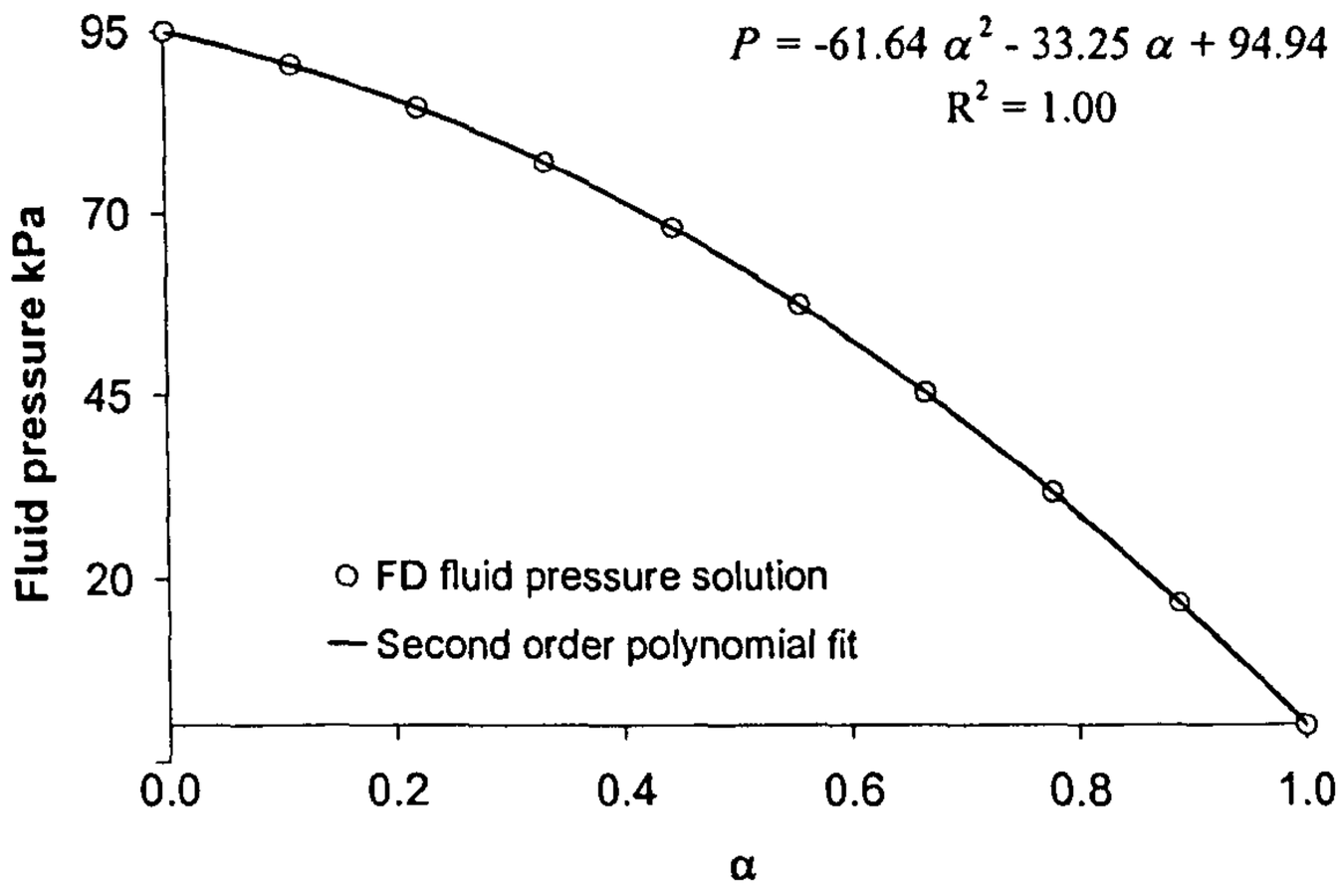

Figure 3.30 – Second order polynomial fit to a 10 node finite difference solution of a fluid pressure field (according to Equation (2.29))

Furthermore, because of the boundary conditions at $\alpha=0$ and $\alpha=1$ one can say:

$$c = P_i$$
$$and \tag{3.14}$$
$$b = P_o - P_i - a$$

Simplifying Equation (3.13) to:

$$P(\alpha) = a \cdot \alpha^2 + (P_o - P_i - a) \cdot \alpha + P_i \tag{3.15}$$

and allowing the parameter C_α to be written as:

$$C_\alpha = \frac{a + P_o}{P_o - P_i} \tag{3.16}$$

3.5.2 Convergence studies

When measuring the errors found in the numerical solutions of Equation (2.26) obtained with different numbers of nodes a good quantitative parameter is the area

between two curves in question. This is represented by the difference between the integrals of the respective polynomial forms:

$$\int_0^1 \left(\left(a_2 - a_1\right) \cdot \alpha^2 + \left(b_2 - b_1\right) \cdot \alpha + \left(c_2 - c_1\right) \right) d\alpha = \frac{a_2 - a_1}{3} + \frac{b_2 - b_1}{2} + c_2 - c_1 \tag{3.17}$$

All errors were determined in relation to the best solution, namely the pressure fields obtained in the 500 node simulations.

The highest error (Equation (3.17)) was observed between the 10 and 500 node simulations at the highest inlet pressure and lowest outlet pressure for all compaction parameters. It is shown in Figure 3.31 relative to 500 node simulation.

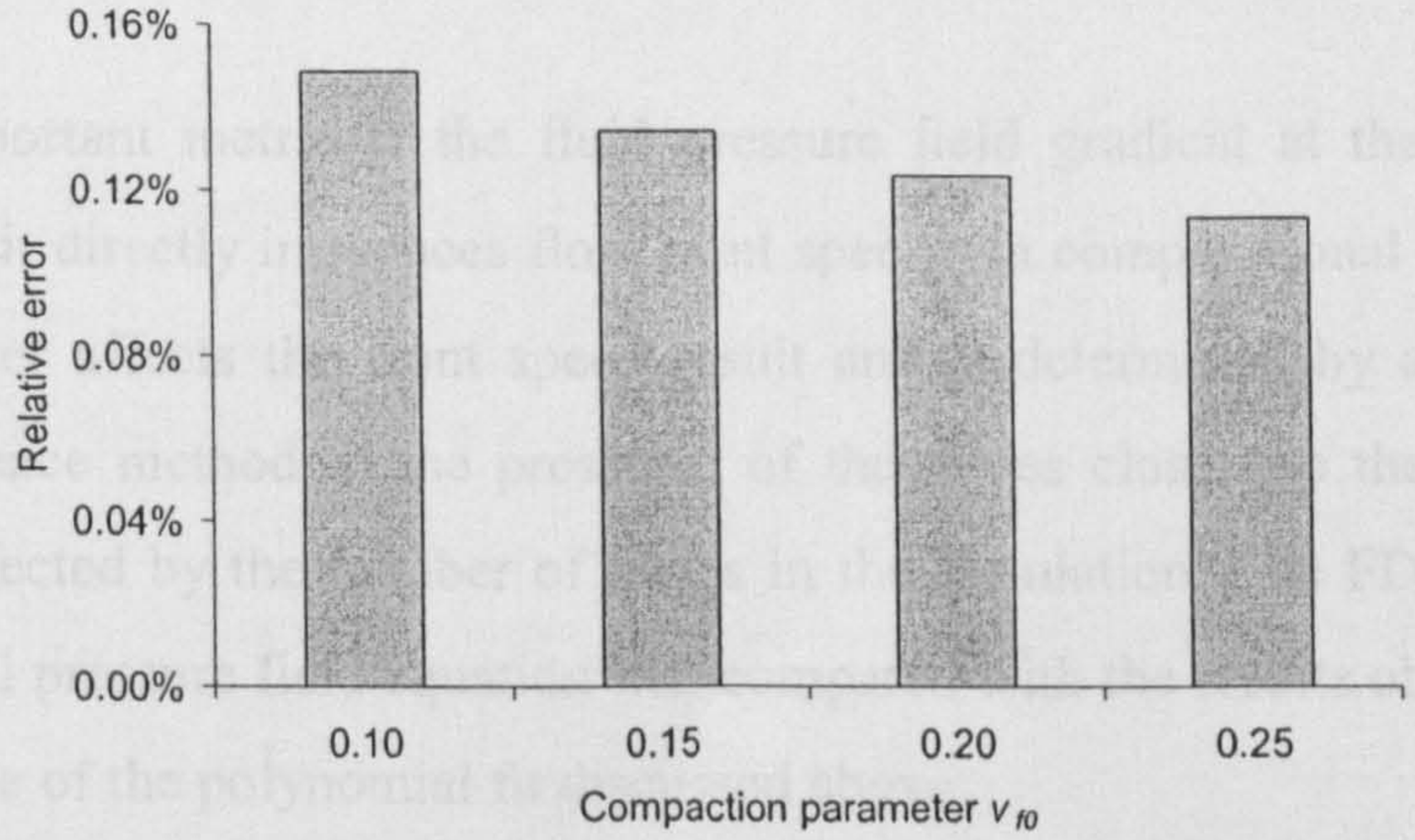

Figure 3.31 – Maximum observed relative error between the 10 and 500 node simulations for different compaction parameters at P_i= 90 kPa and P_o = 0 kPa

It is worth mentioning that in this study, the average relative error between the 100 500-node solutions and the 100 10-node solutions was 0.038% and its standard deviation was 0.035%. Furthermore, the observation of the evolution of the maximum observed error between simulations with increasing number of nodes shows that the error tends to zero. Figure 3.32 shows the evolution of the worst case scenario.

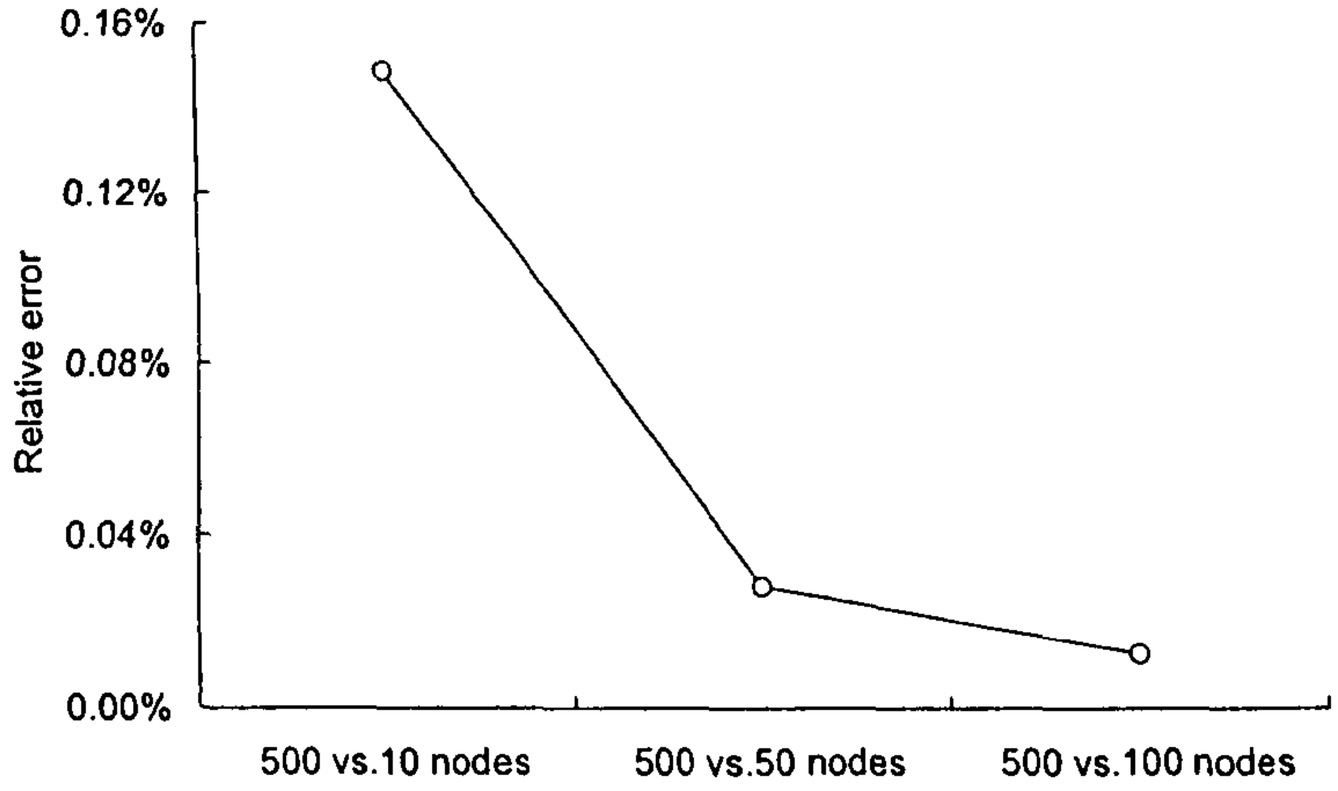

Figure 3.32 – Evolution of the relative error between simulations with different numbers of nodes for vf0 = 0.1, P_i= 90 kPa and P_o = 0 kPa

It is important to note that, even at low node counts, the observed error is not significant in practical applications of this model and that the error is always positive, signifying that models with fewer nodes always underestimate *a*.

Another important metric is the fluid pressure field gradient at the flow front (α=1) since it directly influences flow front speed. In computational approaches, this parameter affects the front speed result and is determined by applying the finite difference method to the pressures of the nodes closest to the front. It is therefore affected by the number of nodes in the simulation. The FD solution of the analytical pressure field equation was compared with the results obtained from the derivative of the polynomial fit discussed above:

$$\left(\frac{dP}{d\alpha}\right)_{\alpha=1} = a + P_o - P_i \tag{3.18}$$

This analysis focuses on the derivative of the fluid pressure field. Since the derivative methods are different for an FD solution and a polynomial fit (PF). The FD based derivative is a result of a quotient of differences, which assumes linear pressure progression between the last two nodes of the discrete domain. This is not the case in the PF derivative (Equation (3.18)).

For that reason one can observe that the 10 node FD solution underestimates the fluid pressure field gradient at the front. As the number of nodes increases this linear approximation becomes less relevant. On the other hand, since this does not affect the fluid pressure gradient derived from the PF: as Table 3.7. shows, a 10 node PF solution can model the process as accurately as the 500 node FD.

Table 3.7 – Convergence of polynomial and FD solutions at 10 and 500 nodes

Parameters			dP / dα | (α)=1						
			Fluid pressure field gradient *Pa*				Relative error		
P_{out}	P_{in}	v_{f0}	Finite diference		Polynomial		FD vs. Polyn.		FD	Polyn.
			10	500	10	500	10	500	500 vs 10	500 vs 10
0	90000	0.10	-133532	-139598	-138603	-139304	3.66%	-0.21%	4.35%	0.50%
		0.15	-126027	-130693	-131928	-132635	4.47%	1.46%	3.57%	0.53%
		0.20	-120344	-124052	-126476	-127146	4.85%	2.43%	2.99%	0.53%
		0.25	-115649	-118632	-121691	-122302	4.97%	3.00%	2.52%	0.50%

Another effect that can be observed is that while the error between FD and polynomial solutions increases with increasing textile stiffness, it tends to decrease or remain constant if each method is evaluated independently for the sensitivity to the number of nodes. Finally, as the last column shows, if one approximates the pressure field solution through a polynomial fit the result is almost insensitive to the number of nodes. The results for the overall parametric studies are summarized in Table 3.8.

Table 3.8 – Summary of the parametric study on fluid pressure field gradient

	Relative error			
	FD vs. Polyn.		FD	Polyn.
Average	2.55%	0.91%	1.92%	0.27%
Standard deviation	1.14%	0.71%	0.90%	0.14%
Maximum	4.97%	3.00%	4.35%	0.53%

It is therefore possible to conclude that an efficient flow solution method would use a small number of nodes, perform a polynomial fit and use the derivative of that fit as an approximation to the fluid pressure field gradient at the flow front.

3.5.3 Sensitivity studies on the coefficient *a* (P_i, P_o, v_{f0})

As was described in section 3.5.4, while the solution of the fluid pressure field Equation is not attainable directly, it is possible to propose a polynomial

approximation. Furthermore, as Equation (3.14) shows, the boundary conditions for this problem make the polynomial solution a function of a single coefficient *a*, which, for reasons pointed out in the previous sections and also in section 2.6 is a function of three parameters: P_{in}, P_{out}, v_{f0}. Note that *a* is also a measure of the non-linearity of the solution: *a* is zero in flow through a non-compliant porous medium. Figure 3.33 shows the value of *a* as a function of two parameters (inlet and outlet pressure) in two surfaces for the extreme compaction coefficients in this study: v_{f0}=0.10 and v_{f0}=0.25.

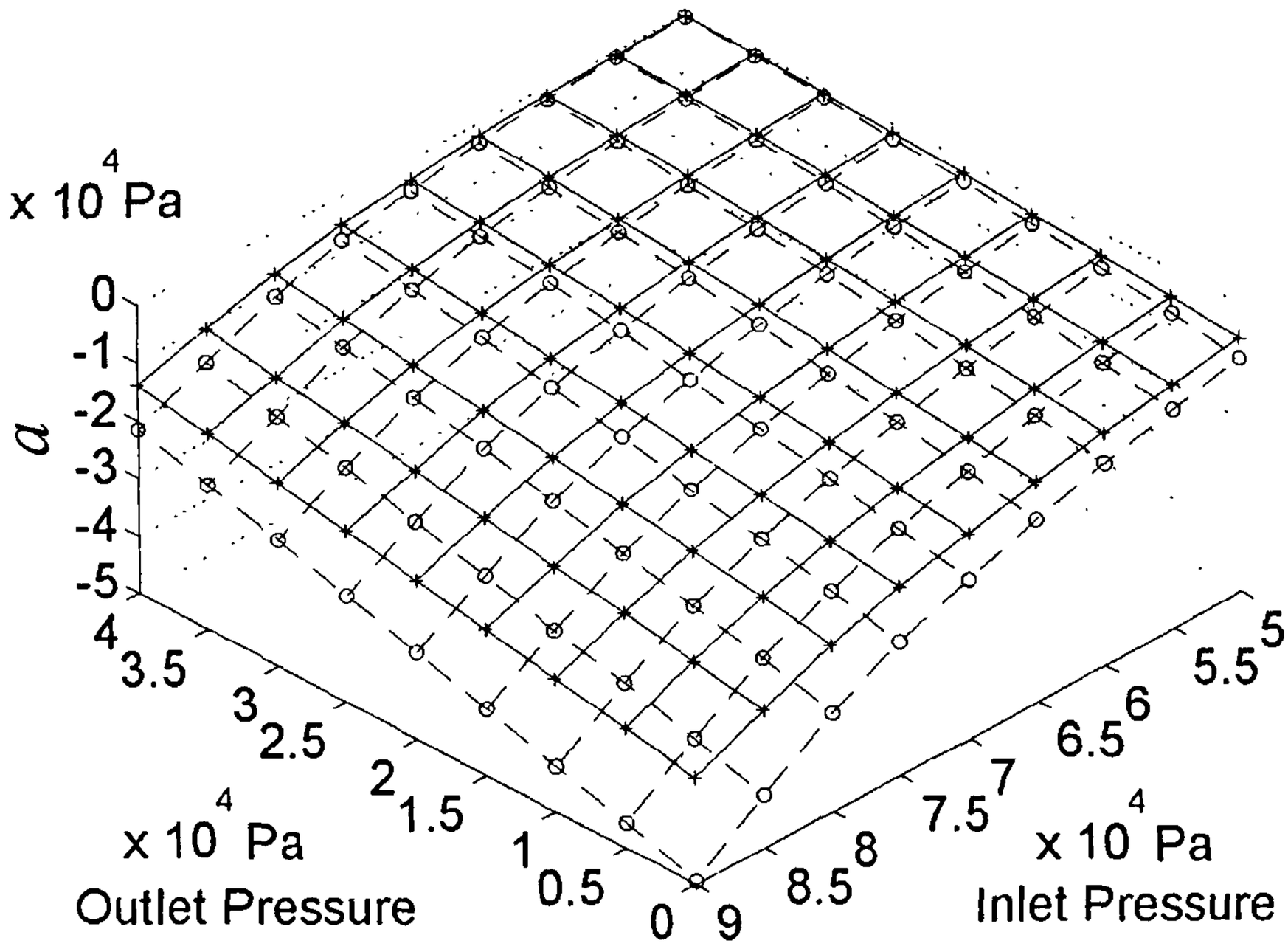

Figure 3.33 – Coefficient a as a function of inlet and outlet pressure for vf0 = 0.10 for the bottom surface and vf0 = 0.25 in the top surface

One can observe that the sensitivity to outlet pressure is less pronounced that to inlet pressure. This is expected, since the same is found in the relation between fibre volume fraction vs. compaction pressure, i.e. fibre volume fraction is most sensitive to compaction pressure at near zero values. In fact, the compaction power law implies that:

$$\lim_{P_{comp}\to 0} \frac{dv_f}{dP_{comp}} \to \infty \tag{3.19}$$

It follows that at near atmospheric inlet pressures, compaction varies greatly throughout the reinforcement adding to the non-linearity of the fluid pressure field. Also, as expected, increasing material compliance magnifies a.

Note that Equation (3.19) also implies that the compaction power law is not applicable at near zero compaction pressures.

3.6 CONCLUSIONS

As was shown, the pressure field solution obtained in chapter 2 can be studied parametrically with a reduced number of terms. This presents several implications for the applicability of the model since it is possible to propose simple guidelines to account for media compliance in flow modelling. The parametric study results show that, as outlined in the previous chapter, non-linear pressure solutions are produced by the most compliant materials and the highest driving pressures. This is relevant for VI model development, as it provides a knowledge on the worst case scenarios for model testing and convergence studies.

This chapter also proposed an analytical solution (second order polynomial fit) for the coupled model of flow through compliant media. This work stemmed from a proposed extension of published compaction work in the form of a single parameter compaction model.

The subsequent parametric study explores the impact of several factors on these properties: i.e. saturation state of fibres, hysteresis, number of layers and cycles and fibre network relaxation at constant load. It is shown that the number of layers and cycles does not affect the master curve: cycled samples just act as different materials. Nevertheless, hysteresis means that separate master curves must be defined for the compaction and expansion cycles with the expansion master curve placed at lower stiffening indices and higher initial fibre volume fractions than the compaction master curve. The study of 36 compaction and expansion cases of a triaxial textile shows that it is not yet possible to discard the hypothesis of normal distribution of coefficients but that it has not been proven either. This problem is

not concluded and requires additional work if the statistical distribution of coefficients is to be used in Monte-Carlo simulation studies (as used in chapter 6).

Having developed a model of flow through compliant media and obtained the relevant experimental characterization data for a number of materials, validation becomes possible. This is addressed in chapter 4. Nevertheless, as mentioned above, the need for a model of flow through compliant media with complex geometries requires the flexibility of finite element packages. These will will be introduced in chapter 5 – using data and concepts discussed in this chapter.

The relevance of the statistical characterization of compaction data will become clearer in chapter 6, where statistical flow modelling will be discussed.

4 EXPERIMENTAL VALIDATION OF THE VI MODEL

This chapter focuses on the experimental validation of the Darcy flow model proposed in chapter 2. The experiments explore fill time and fluid pressure as a function of permeability and compaction in instrumented moulds. The results show that the model produces accurate predictions of the evolution of fill time with pressure as well as of the fluid pressure field itself for simple test panels.

4.1 INTRODUCTION

The present chapter follows the previous work by measuring how a fluid pressure field, driving flow through compliant media, modifies the local compaction state of the reinforcement and thereby alters local permeability. It is possible to observe these thickness variations both in the mould filling phase and as overall trends in cured components. Measurement of laminate thickness during filling has been done by Williams *et al* (1997), Hammami *et al* (1998, 2000), Grimsley *et al* (2001) and Anderson *et al* (2003). All published results show that thickness varies by location in the mould and that it changes with time. This work will be extended here with measurements of cured components, and will show that the fluid pressure dependent thickness variations are still present in finished components.

Experimental flow studies of VI tend to fall into two separate categories: the study of lead lag caused by faster flow in the distribution medium, and the study of flow through compliant porous media. Examples of the first are the analytical and experimental works by Hsiao *et al* (2000) where a 1D closed form solution for lead lag in VI is discussed and validated by Mathur *et al* (2001) and the work by Loos (2001) where a numerical approach is taken (which is an expansion on earlier work on resin film infusion in Loos *at al*, 1996). However, Loos did not discuss the impact of the number and shape of their 8-node 3D elements on solution convergence. This is discussed in detail in section 5.2.3 but one should highlight that the shape factor of FE elements in Darcy flow (and therefore the method's accuracy) are not only a function of geometry but also of the

permeability anisotropy of the reinforcement. In fact, since through thickness permeability is typically an order of magnitude lower than in-plane values (Mathur, 2001) one should expect errors due to element shape factors in modelling through thickness flow. These problems with numerical accuracy of 3D FE modelling of through thickness flow are further amplified by conservation of mass issues at the nodes which lie at the interface between the two dissimilar materials (Modi *et al*, 2002).

The development of a fully applicable model of through thickness flow must however acknowledge that, as Andersson *et al* (2002) and Ragondet *et al* (2002) have shown, the lead lag distance quickly tends to a value which does not then change with flow front advancement. It is suggested by Hsiao *et al* (2000) that this value is a function of the ratio of thicknesses and porosities of the two materials and of the square root of the ratio between the in-plane permeability of the distribution medium and the through thickness permeability of the reinforcement. Observing that these values are constant one can explain the constant lead-lag which was experimentally observed. This constant lead-lag justifies the convenient-to-use plug-flow model where permeabilities are calculated using weighted average algorithms. Among available plug-flow averaging schemes, one can point out the study of the effective average permeability of multi-layer preforms by Calado *et al* (1996) for an unlimited number of layers or, when the different materials are anisotropic in plane, the approach suggested by Rudd *et al* (1996). A more complete description of these techniques is given in section 5.2.3.

The second category of study is related to the analysis of flow through compliant porous media, sometimes neglecting the distribution medium layer or using an effective average permeability. The studies discuss the effects of reinforcement compaction on permeability and flow and observe the relation between properties such as the thickness vs. time and on the evolution of the fluid pressure field. Both Hammami et al (1998, 2000) and Andersson et al (2003) present simulations based on this premise. None of these groups have however reported measurements of the transient fluid pressure field or of the interaction between compaction pressures and fill time. Notably, measurements of the fluid pressure field are one

direct measurement of the accuracy of the models since they correlate directly with the predictions of any governing Equation for VI. In terms of the fill time dependence on pressure (and therefore compaction) published work is also not common. One such reference is Corden *et al* (1997) who report the measurement of "effective" permeability as a function of outlet pressure but are unable to show a clear trend due to the high variability observed.

This chapter will discuss the experimental validation of the flow model proposed in chapter 2. It does not therefore look into validating models of flow through combinations of dissimilar materials. It will start with an analysis of the problem of thickness change at the flow front and how that can affect flow. That is followed by the experimental validation sections. First, the effect of driving pressure on fill time is linked to the predictions of the Darcy flow model in terms of impact on fluid pressure field and fill time. The following section then looks into the validation of the fluid pressure field solutions. The chapter concludes with the work on experimental observation and validation of laminate thickness.

4.2 THICKNESS VARIATION AT THE FLOW FRONT

In theories which describe saturation and void formation (Amico *et al*, 2000; Kang *et al*, 2000; Parnas *et al*, 1991, 1994) flow advances primarily through high permeability areas, which can be intra-tow, in the case of high capillary pressure or more commonly inter-tow, due to the lower permeability in the interstitial spaces between fibres in a bundle. These models have been developed to predict void formation but all describe the same principle. The general saturation fingering process is illustrated in Figure 4.1. The dry areas can represent either fibre tows or inter-tow areas depending on flow speed, contact angles and reinforcement architecture.

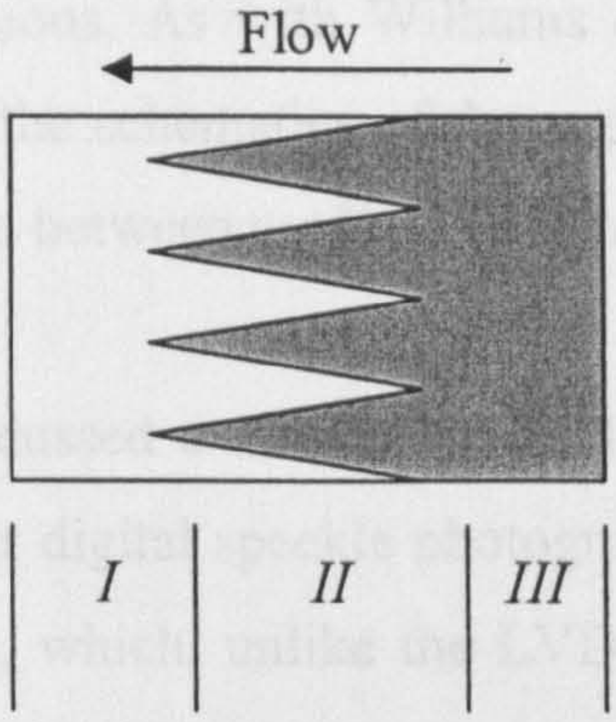

Figure 4.1 - Flow fingering and the three stages of saturation: I is the dry region, II is the partly saturated region and III is the fully saturated region

Using linear variable differential transformer (LVDT) transducers to monitor the displacement of the vacuum bag, Williams et al (1997) identified the three related phases of compaction that can be observed in VI (Figure 4.2). The first (denoted by I) is a phase of dry compaction which leads to a constant thickness throughout the dry laminate. As the flow front passes a second phase (*II*) of initial lubrication of the fibres leads to a considerable reduction in thickness. The third and final phase (*III*) consists of an increasing thickness in the saturated reinforcement as the compaction pressure reduces due to the rising fluid pressure. They also showed pressure transducers in the schematics of the experimental set-up but do not discuss the results from these experiments. Furthermore, their work does not discuss possible modelling approaches for the different phases or how they could influence flow.

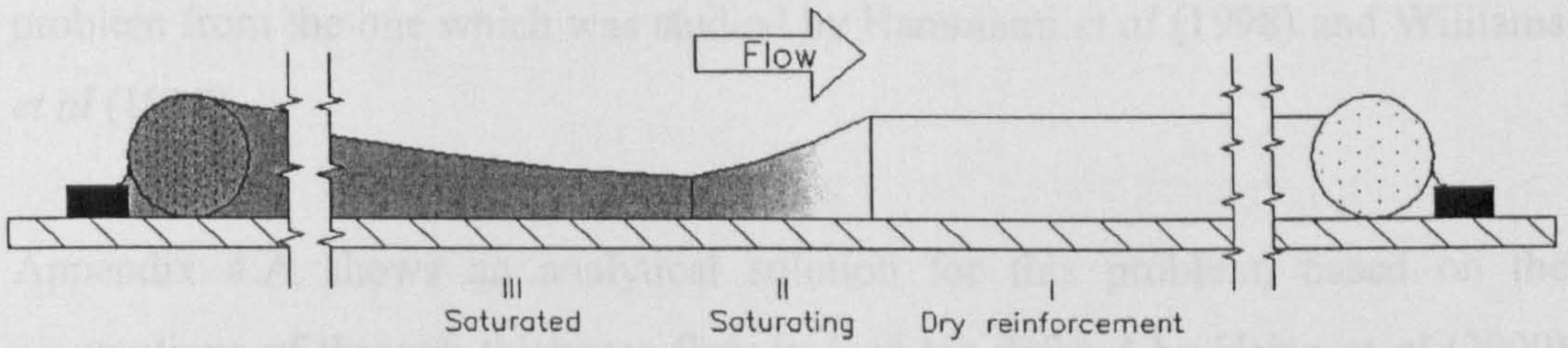

Figure 4.2 - Thickness phases during VI. (Adapted from Williams et al, 1997)

Hammami *et al* (1998, 2000) used a motorized laser system to monitor the variations of thickness, identifying the same phases as Williams *et al* (1997). They went on to introduce VI flow modelling (as discussed in the previous chapter) but, in their modelling approach, they ignored these thickness observations without

substantiating their assumptions. As with Williams *et al* (1997), while pressure transducers were present in the schematics of the experimental set-up, their work did not provide a comparison between predicted and measured pressure fields.

Andersson *et al* (2003) discussed a novel process for monitoring the thickness changes in large areas. Their digital speckle photography monitoring system uses stereoscopic image analysis, which, unlike the LVDT point measurements done by Williams *et al* (1997) or the laser line measurements by Hammami *et al*, is capable of monitoring areas. This system is also used to show the thickness change effect in radial flow. In modelling the process, they develop a fully numerical approach to study the thickness variations at the flow front without distribution media. They do not however provide a validation of pressure field results, which in parallel with front velocity constitute the main quantifiable outcome of any VI model.

In their experimental study of thickness and pressure in VI Grimsley *et al* (2001) explored the local pressure data. Unlike the previous authors however, the experiments used flow enhancement media which leads to a different saturation problem. In fact their work showed a measurable increase in fluid pressure as the saturated flow front reaches the pressure transducer, which implies that there is a significant pressure change in the lead-lag region. As will be shown, this is caused by the distribution medium and is not due to the typical fingering observed in single materials. This dependence on through thickness flow poses a different problem from the one which was studied by Hammami *et al* (1998) and Williams *et al* (1997).

Appendix 4.A shows an analytical solution for this problem, based on the assumptions of through thickness flow in lead-lag defined by Hsiao *et al* (2000) and validated in Mathur *et al* (2001) but, unlike their work, explores the case of thickness variation which occurs in flow through compliant media and is therefore specifically applicable to VI, in the derivation of flow front permeability.

In the present work it is observed that the partly saturated regions rarely exceed a few tow widths (Figure 4.3). In the typically large VI components, they are

therefore relatively small which leads to the assumption that they can be neglected. While undoubtedly this eliminates one possible void formation mechanism from the analysis, it makes the problem of modelling flow and fluid pressure in VI more practical.

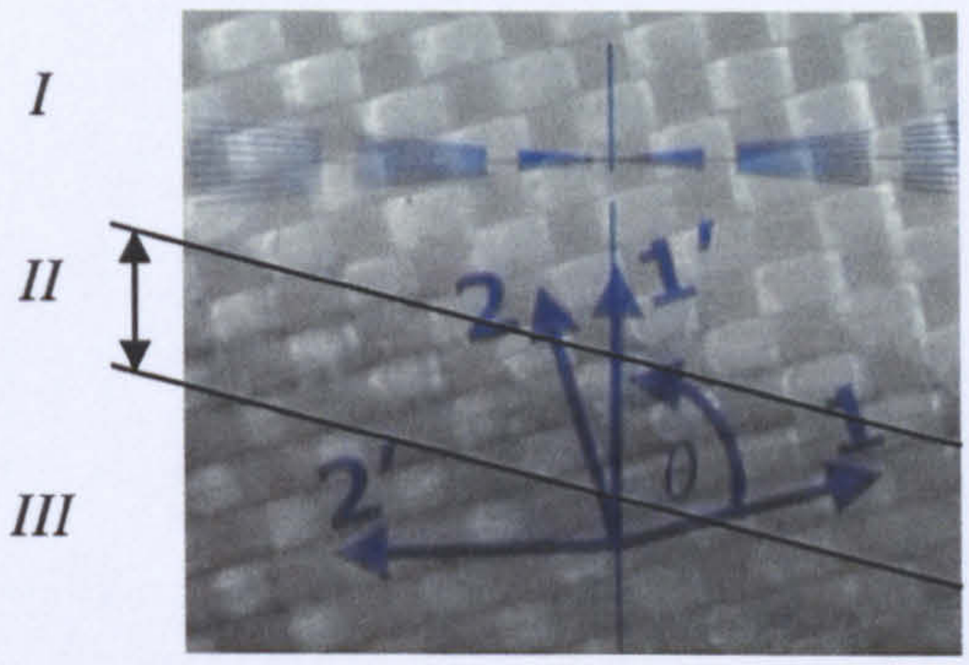

Figure 4.3 - Magnified view of the flow front region of a Vetrotex WR324 plain weave used in the first set of flow experiments. It is possible to see partly saturated tows in region II. 1 and 2 are the principal permeability directions. 1' is the flow direction. 2' is parallel to the inlet (line injection)

4.3 THE INFLUENCE OF OUTLET PRESSURE SETTINGS ON FILL TIME

As was shown in the previous chapter, driving pressure is one of the parameters that affects flow through compliant media. This first validation section discusses the experimental observation of this dependence (driving pressure vs. time) and validation of the model predictions. The algebraic form of this dependence will be discussed in detail in this section, followed by the discussion of the related experimental work.

4.3.1 Analytic background

Fill time in one dimensional flow parallel to the x axis through non-compliant porous media is described by the well known integral form of Darcy's law:

$$t_{RTM} = -\frac{\phi \cdot \mu}{2 \cdot K} \cdot \frac{L^2}{\Delta P} \tag{4.1}$$

and therefore, for constant porosity, viscosity and permeability, fill time is inversely proportional to driving pressure:

$$t_{RTM} = \frac{t^*_{RTM}}{\Delta P} \tag{4.2}$$

where $t^*_{RTM} = \phi \cdot \mu \cdot L^2/(2 \cdot K)$. As was established in chapter 2, compaction changes this time-pressure relation in VI. It was also proposed that fill time in VI follows Equation (4.3):

$$t_{VI} = -\frac{\mu \cdot L^2}{2\left[\frac{K}{\phi}\right]_{\alpha=1}} \cdot \frac{1}{C_\alpha \cdot \Delta P} \tag{4.3}$$

where fill time remains a function of the square of the flow front position and, when thickness is not pressure dependent ($dP / d\alpha = \Delta P$), Equation (4.3) reduces to Equation (4.1). In the normalization procedure that follows, the constants in Equation (4.3) are eliminated in order to obtain the physical relation that controls fill time in flow through compliant media. One can then use the model to characterize the effect of compaction properties on the general form of the driving pressure-time relation:

$$t^* = t_{VI} \cdot \left(\frac{2 \cdot k}{L^2 \cdot \mu}\right) = -\frac{k}{\left[\frac{K}{\phi}\right]_{\alpha=1}} \cdot \frac{1}{C_\alpha \cdot \Delta P} \tag{4.4}$$

In running the model, the expansion master curve (Table 3.6) was used to eliminate one variable by making the stiffening index B a function of v_{f0}. The inlet pressure was also assumed to be constant and equal to 100 kPa. With these assumptions, the normalized fill time t^* becomes a function of two variables: the initial fibre volume fraction v_{f0} and the outlet pressure P_{out}.

$$\begin{cases} P_{in} = 100\ kPa \\ B = -0.0454 \cdot \ln\left(v_{f_0}\right) - 0.0156 \end{cases} \Leftarrow \quad t^* = t^*\left(v_{f_0}, P_{Out}\right) \tag{4.5}$$

Note that the Kozeny constant k in the numerator of Equation (4.4) cancels with the same in the Kozeny-Carman permeability in the denominator. Equation (2.26)

was solved for 21 outlet pressure values in the interval of [0, 95] kPa and 10 initial fibre volume fractions in the range [0.01, 0.46]. Figure 4.4 shows the evolution of fill time versus driving pressure for the range of initial fibre volume fractions.

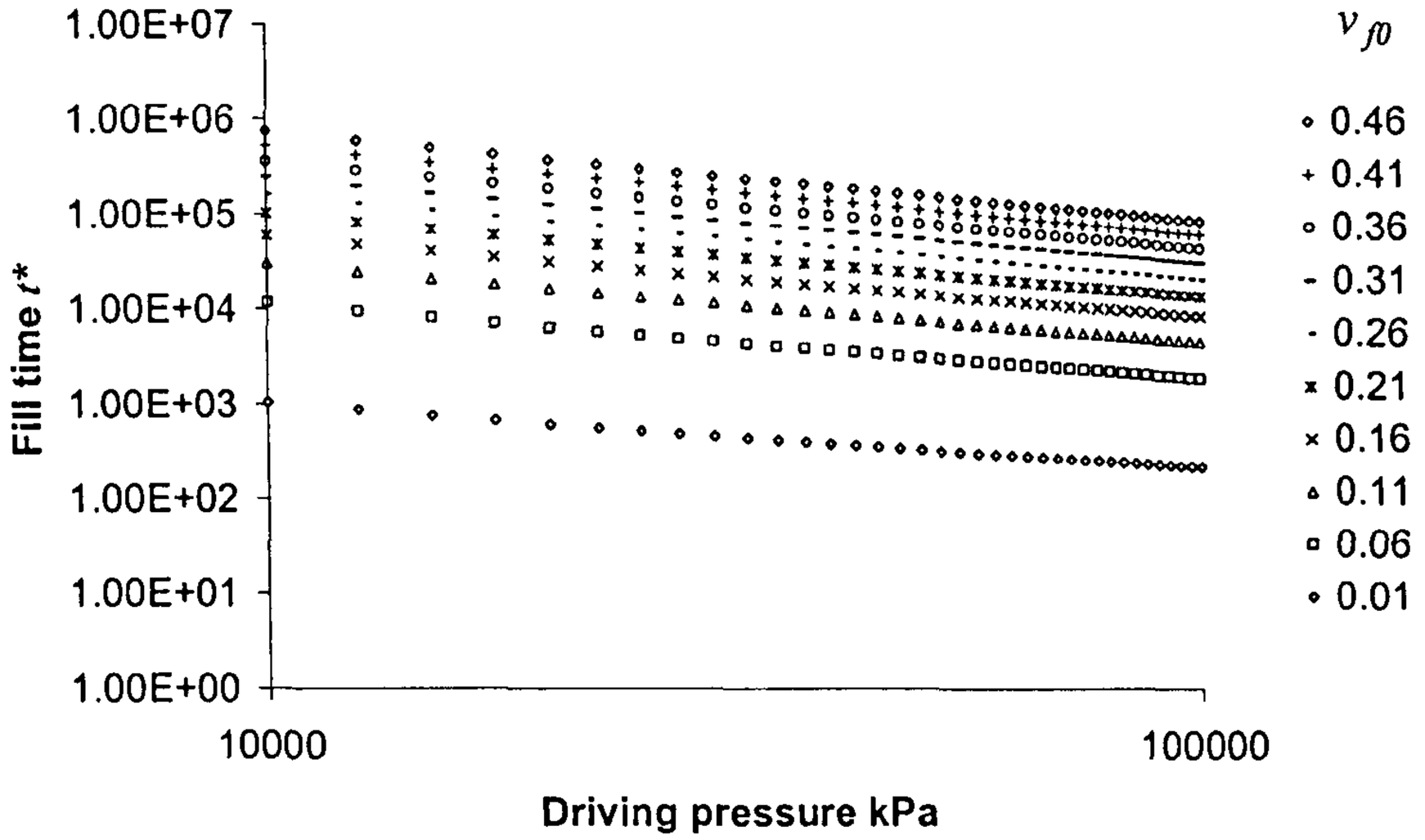

Figure 4.4 – Normalized fill time t* vs. driving pressure for a range of compaction properties.
Driving pressure equals the difference between the constant inlet pressure value (100 kPa) and the outlet value [0,95] kPa

Each of these curves follows a power law, with an average correlation coefficient of 0.998 and a minimum of 0.994. It is therefore justified to describe normalized fill time with the Equation:

$$t^* = \alpha \cdot \Delta P^{\beta} \tag{4.6}$$

The relevant coefficients α and β are given in the Table 4.1. This table also shows the relative position of different materials in relation to these coefficients. As expected, with β tending to one with reduced material compliance the fill time approaches the result for a flow through a fixed cavity height (e.g. RTM).

Table 4.1 – Normalized fill time coefficients as a function of expansion properties for different materials

Materials	v_{f0}	α	β
FGE117	0.46	$5\,10^{9}$	-0.9568
	0.41	$3\,10^{9}$	-0.9416
	0.36	$2\,10^{9}$	-0.9267
	0.31	$1\,10^{9}$	-0.9118
UDUC	0.26	$6\,10^{8}$	-0.8965
	0.21	$3\,10^{8}$	-0.8801
	0.16	$2\,10^{8}$	-0.8613
RT600	0.11	$7\,10^{7}$	-0.8376
	0.06	$2\,10^{7}$	-0.8018
U750	0.01	$6\,10^{5}$	-0.6958

4.3.2 Experimental fill time observations in VI

In order to populate the t-ΔP diagrams, an experimental plan was formulated in which three sets of experiments where carried out at 4 different driving pressures: 90kPa, 60 kPa, 30 kPa and 5kPa. These experiments predated the compaction characterization work and focussed on a plain woven E-glass textile (WR324), weighing 820 g/m^2 manufactured by Saint Gobain Vetrotex. It was not possible to perform subsequent compaction tests on this material and its properties are therefore assumed to be similar to those found in the RT600 textile. In each experiment, four layers of reinforcement measuring 0.5 m x 0.2 m were used. These were placed on a acrylic plate and vacuum bagged. Due to inlet system pressure drop issues which will be addressed in section 4.4.2, the same inlet pipes and geometry were used throughout the experimental plan. The injection strategy consisted in a line gate, created with an open pipe (Omega-Tube) placed on top of the reinforcement. The infusing fluid was dyed diluted corn syrup. Viscosity was controlled by dilution. Prior to each experiment, viscosity was measured with a Brookfield viscometer model DV-I and the results then used to normalize fill times (t / μ). The experimental set-up is shown, in Figure 4.5.

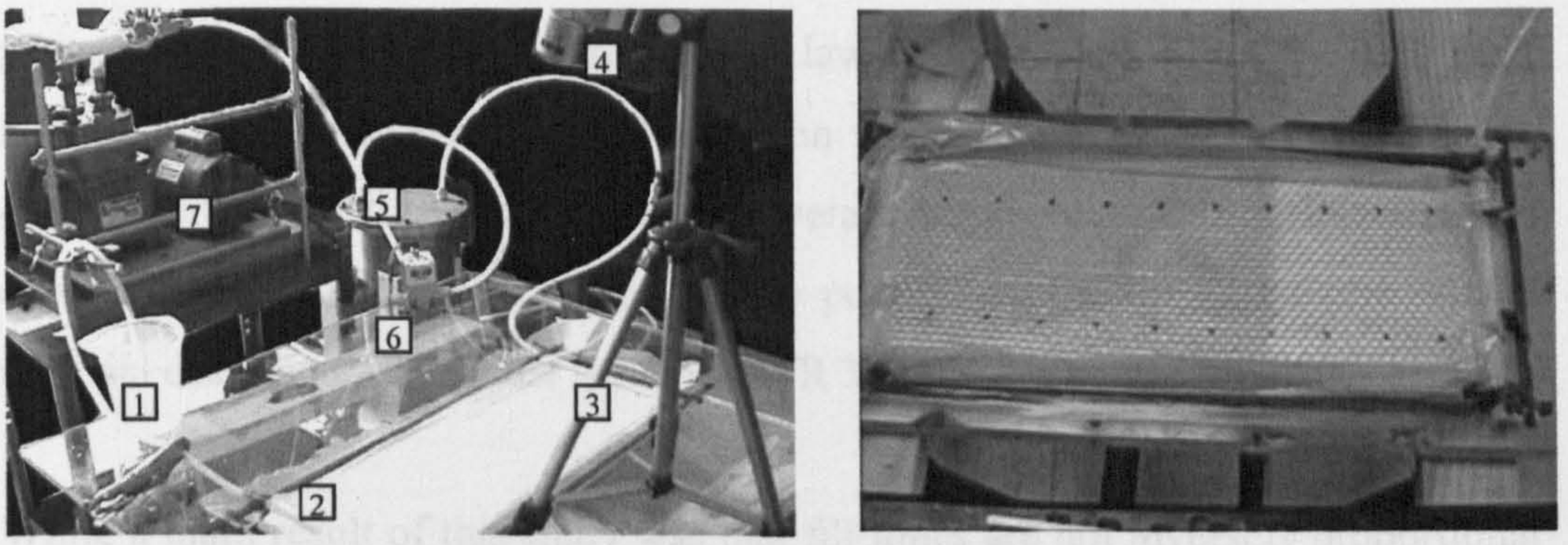

a) b)

Figure 4.5 a) Experimental set-up. 1 resin container, 2 inlet, 3 outlet, 4 video camera, 5 resin trap, 6 pressure controller and 7 vacuum pump. b) Example of image captured during an experimental injection

The inlet pressure was kept at one atmosphere by positioning the fluid container at the same height as the reinforcement, as can be seen in Figure 4.5 a).

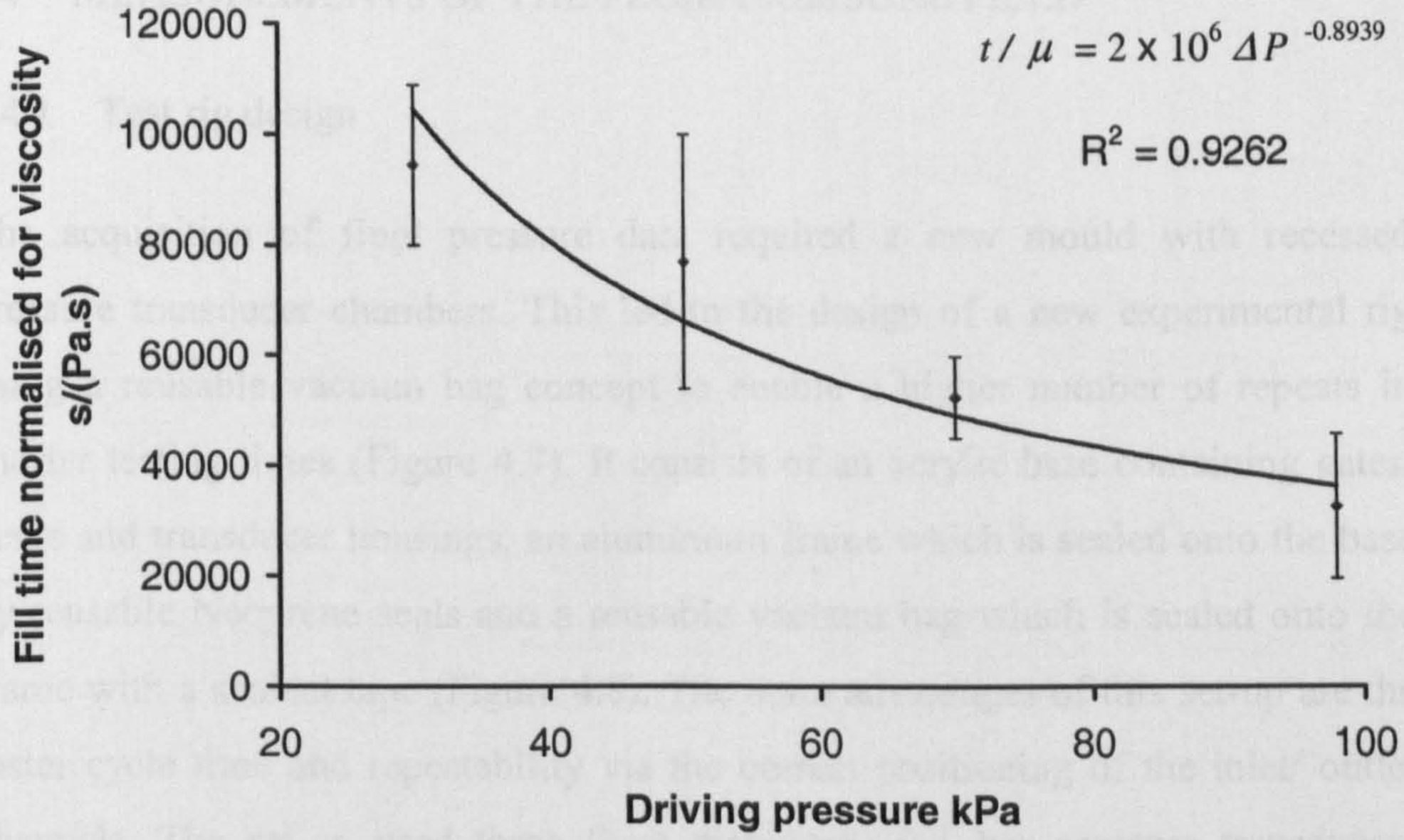

Figure 4.6 – Driving pressure vs. normalised fill time for the WR324 woven material. Driving pressure is Patm-Pvent The full lines correspond to the power law fit to the results and the symbols to the average value of experiments at specific driving pressures. Error bars represent 95% experimental confidence interval

Figure 4.6 shows the resulting plot of times vs. driving pressures, for L=1m of reinforcement. The value of β obtained in this experimental study was β =-*0.8939*. Primarily, this result confirms the dependence of fill time on driving

pressure as well as the suggested power law relation. Quantitatively this result falls within the expected range of the plain woven materials described in Table 4.1. Nevertheless it is lower than the average value of *0.92* for flow through expanding woven materials. It should be pointed out however that the woven material described in the table is not the WR 324 but the lighter RT 600.

While a main result of this study was that fill times are not inversely proportional to driving pressure and follow a predicted trend it was also noted that, due to the variability observed experimentally, this model validation approach is not reliable, especially for less compliant materials. As a first outcome, this directed the validation exercise to other flow dependent measurable quantities such as fluid pressure. Secondly, this justified the exploration of statistical flow modelling which is the topic of chapter 6.

4.4 MEASUREMENTS OF THE FLUID PRESSURE FIELD

4.4.1 Test rig design

The acquisition of fluid pressure data required a new mould with recessed pressure transducer chambers. This led to the design of a new experimental rig using a reusable vacuum bag concept to enable a higher number of repeats in shorter testing times (Figure 4.7). It consists of an acrylic base containing gates, vents and transducer housings, an aluminium frame which is sealed onto the base by reusable Neoprene seals and a reusable vacuum bag which is sealed onto the frame with a sealant tape (Figure 4.8). The main advantages of this set-up are the faster cycle time and repeatability via the correct positioning of the inlet/ outlet channels. The set-up used three flush diaphragm 0-1 bar pressure transducers (Farnell, Ltd – UK) which were logged by a LabView computer logging system. All transducers where calibrated by correlation with a calibrated transducer. A typical calibration curve is shown in Figure 4.9.

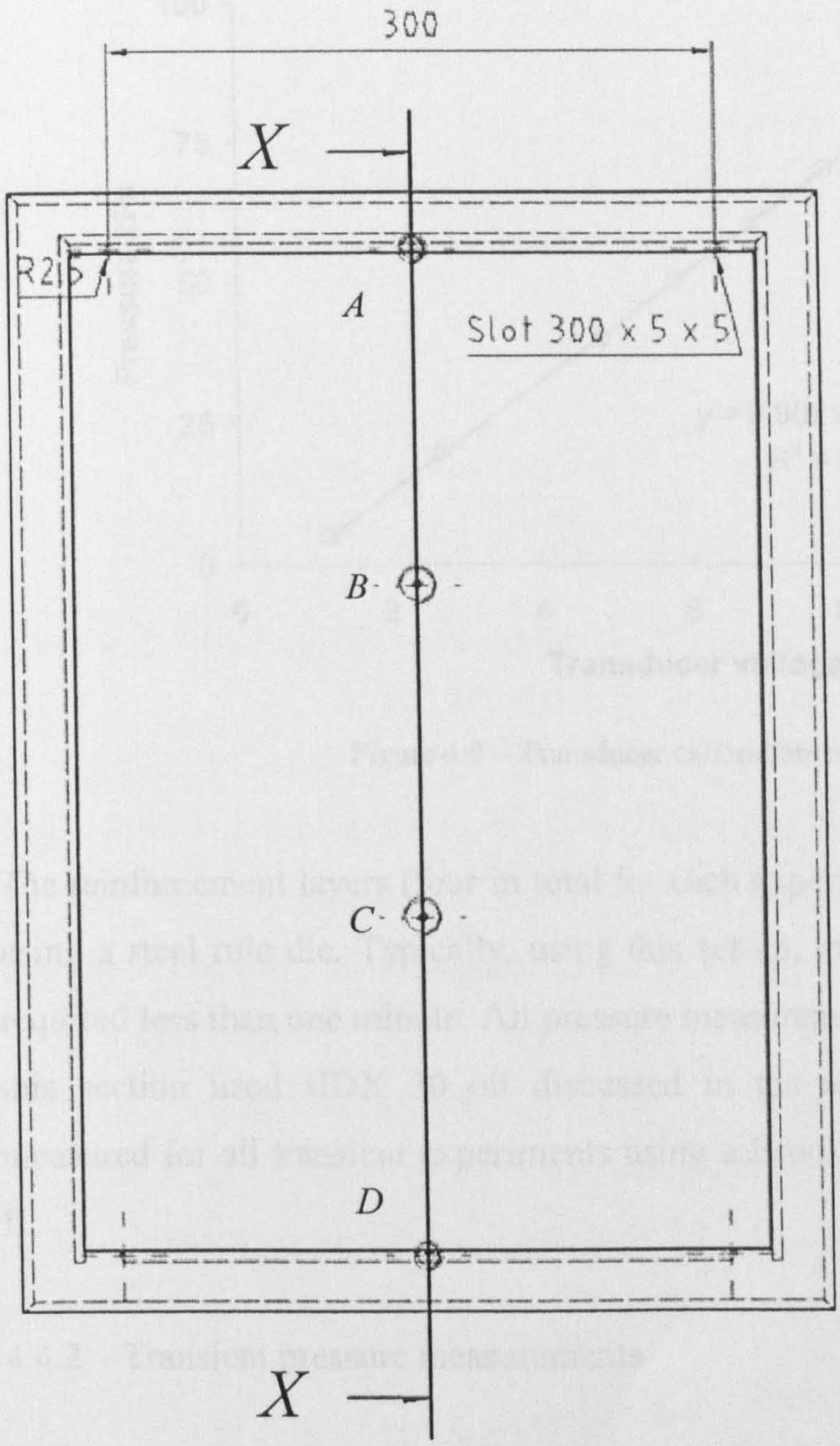

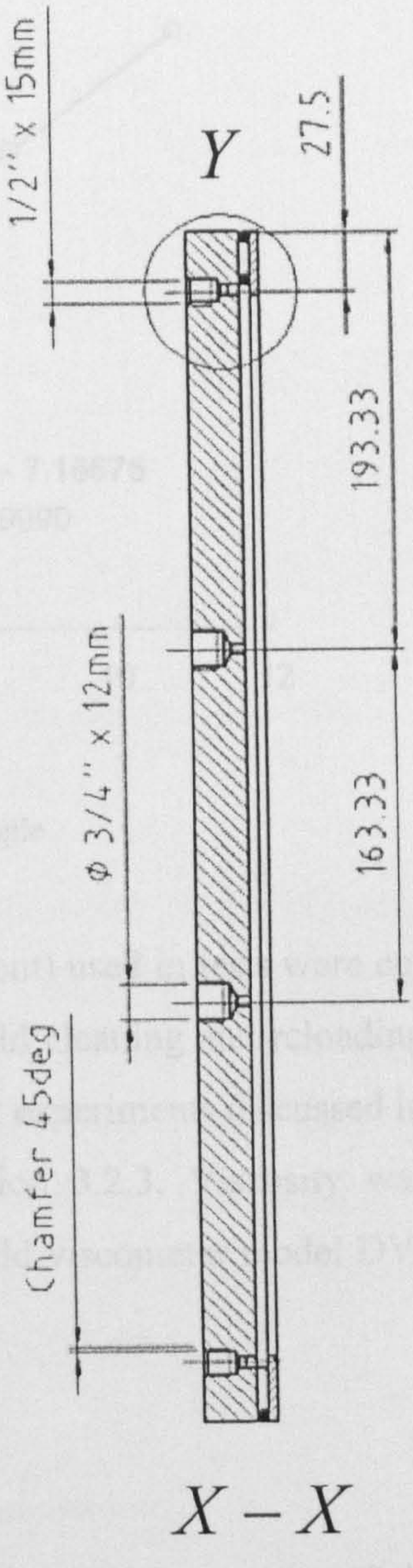

Figure 4.7 - Reusable VI experimental mould: top view and section. A, B, C, D correspond to the location of pressure transducers. A is the inlet and D the outlet

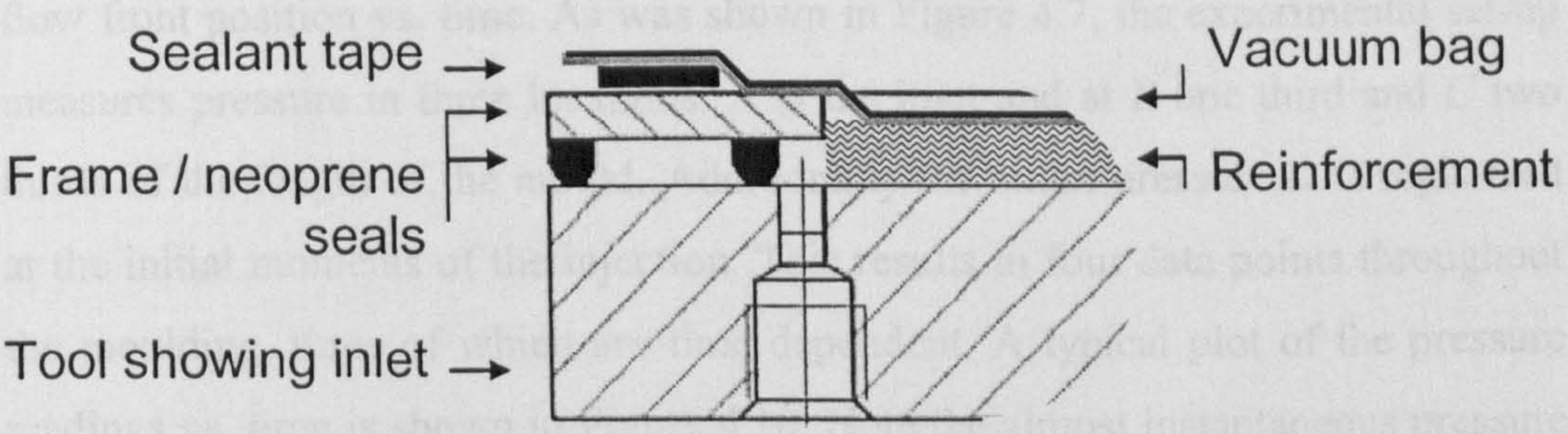

Figure 4.8 - Detail Y: showing the set-up of the frame, inlet and seals

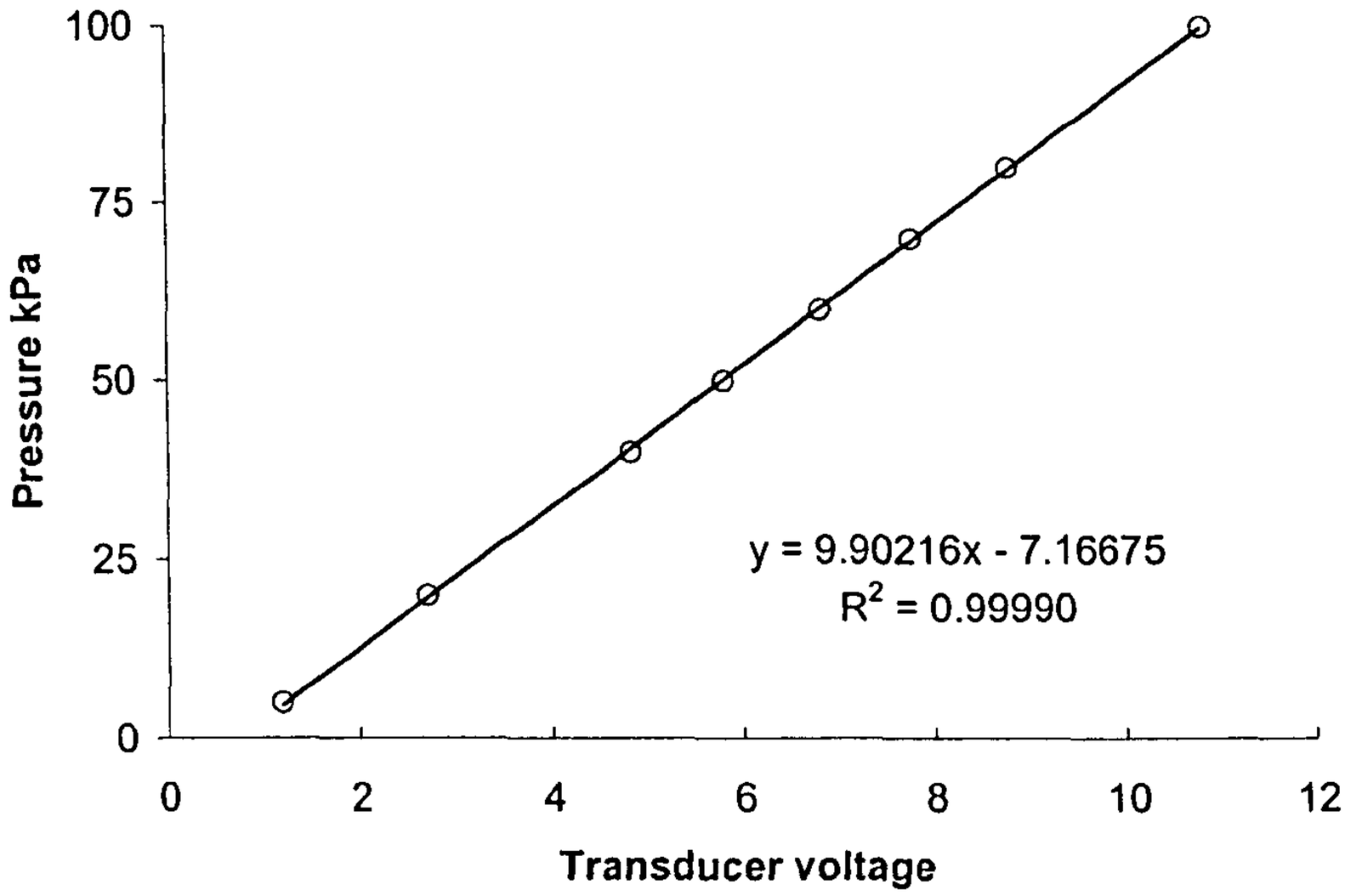

Figure 4.9 – Transducer calibration example

The reinforcement layers (four in total for each experiment) used in tests were cut using a steel rule die. Typically, using this set-up, mould cleaning and reloading required less than one minute. All pressure measurement experiments discussed in this section used HDX 30 oil discussed in the section 3.2.3. Viscosity was measured for all transient experiments using a Brookfield viscometer model DV-II.

4.4.2 Transient pressure measurements

As mentioned before, this section aims to show the validity of the pressure field solution shown in previous chapters. In the constant inlet pressure arrangement which is used in VI, typical experimental results consist of pressure vs. time and flow front position vs. time. As was shown in Figure 4.7, the experimental set-up measures pressure in three locations: *A* at the inlet and at *B* one third and *C* two thirds of the length of the mould. Additionally the outlet pressure *D* is registered at the initial moments of the injection. This results in four data points throughout the moulding, three of which are time dependent. A typical plot of the pressure readings vs. time is shown in Figure 4.10. Note the almost instantaneous pressure increase at the inlet (transducer A) and the gradual increase at one third and two thirds of the mould length (transducers B and C):

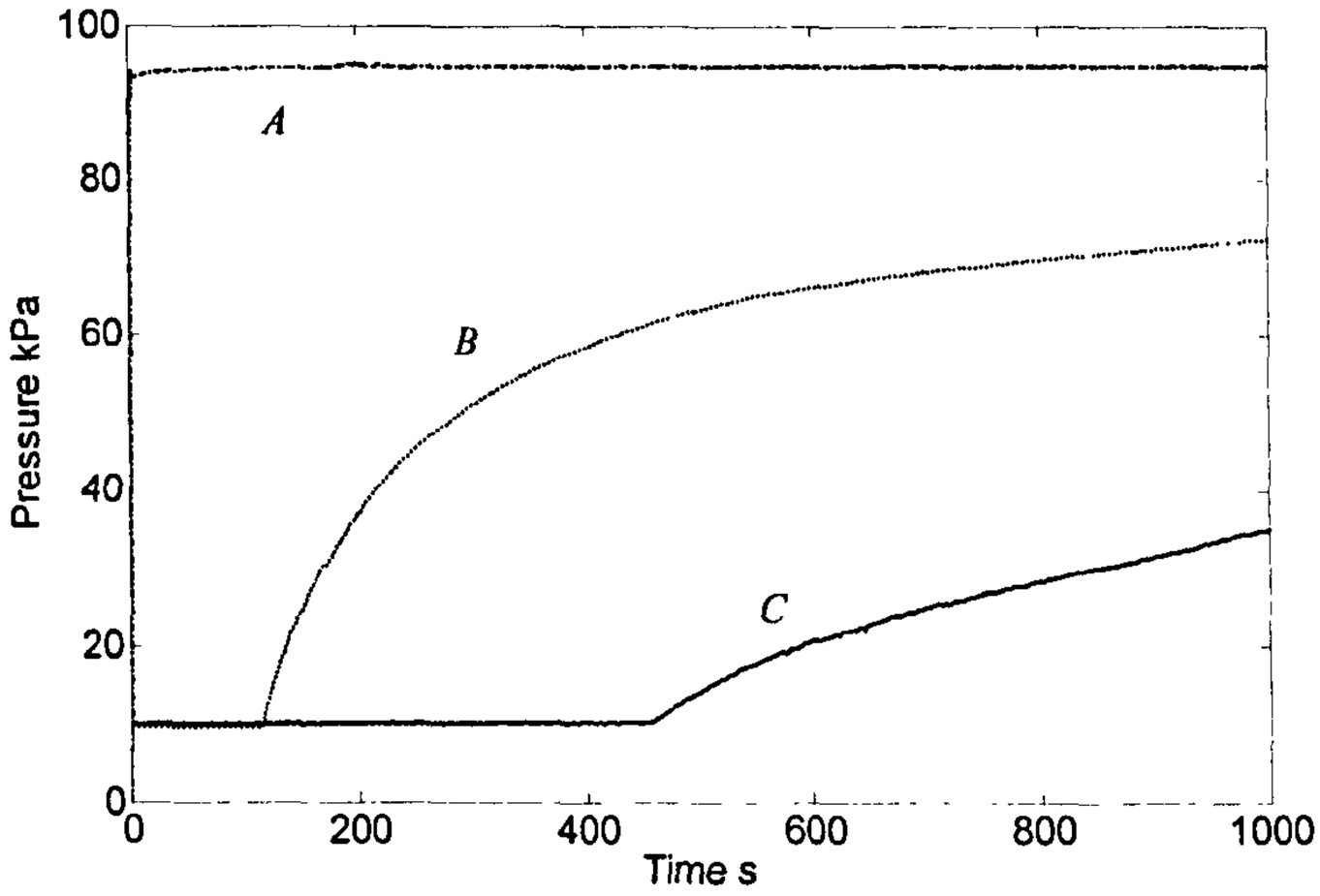

Figure 4.10 - Evolution of pressure with time for four layers of UDUC (Table 3.1) with HDX30 oil. Flow in the 0° direction

While these measurements form the basis of the fluid pressure field validation they must account for the evolution of pressure at the inlet. Therefore, prior to that discussion this must be addressed. It can however be shown that the evolution of the inlet pressure is a function of the relation between the resistance in the piping and reinforcement permeability. As Figure 4.11 shows, this has a significant effect on pressure distribution in the early stages of injection, principally in highly permeable materials and therefore one can infer that it affects time.

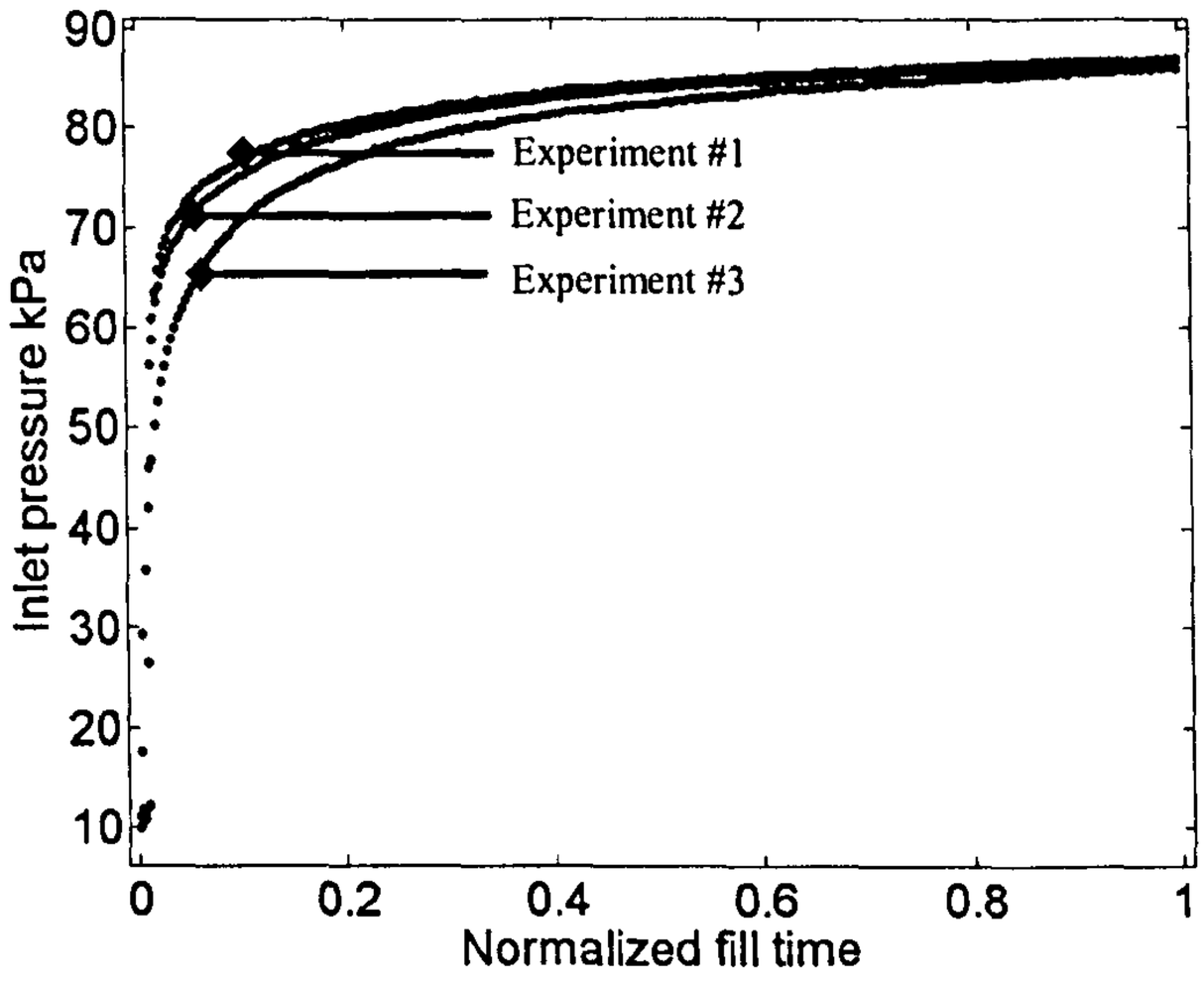

Figure 4.11 - Evolution of inlet pressure with time for three identical experimental measurements with U450 (Table 3.1) and HDX 30 oil. Time is normalized with total fill time

Due to the higher compressibility of the CSRM U750 when compared with the Flemings UDUC (Figure 4.10), the evolution of inlet pressure in Figure 4.11 presents a clear time dependence. Furthermore, these experiments show a degree of variability (note experiment #3). This behaviour is explained and analytically developed in Appendix 4.B. Using this analytical work the experimental observations in Figure 4.11 can be replicated as can be seen from Table 4.2 and Figure 4.12.

Table 4.2 – Parameters used to model the moulding arrangement in Figure 4.11. Oil data was acquired in viscosity experiments and HDX 30 data sheet

Reinforcement				Hose			
Porosity	ϕ	0.7		Diameter	D	0.008	m
Thickness	h	0.005	m	Length	L_{hose}	0.7	m
Width of mould	L_{inlet}	0.3	m	Height	$h\rho$	0.7	m
Fibre permeability	K_{VI}	1E-09	m^2				
Mould length	L	0.5	m				
Oil				**Pressures**			
Density	ρ	900	kg/m^3	Inlet pressure	P_{in}	100	kPa
Viscosity	μ	0.27	Pa.s	Outlet pressure	P_{out}	10	kPa

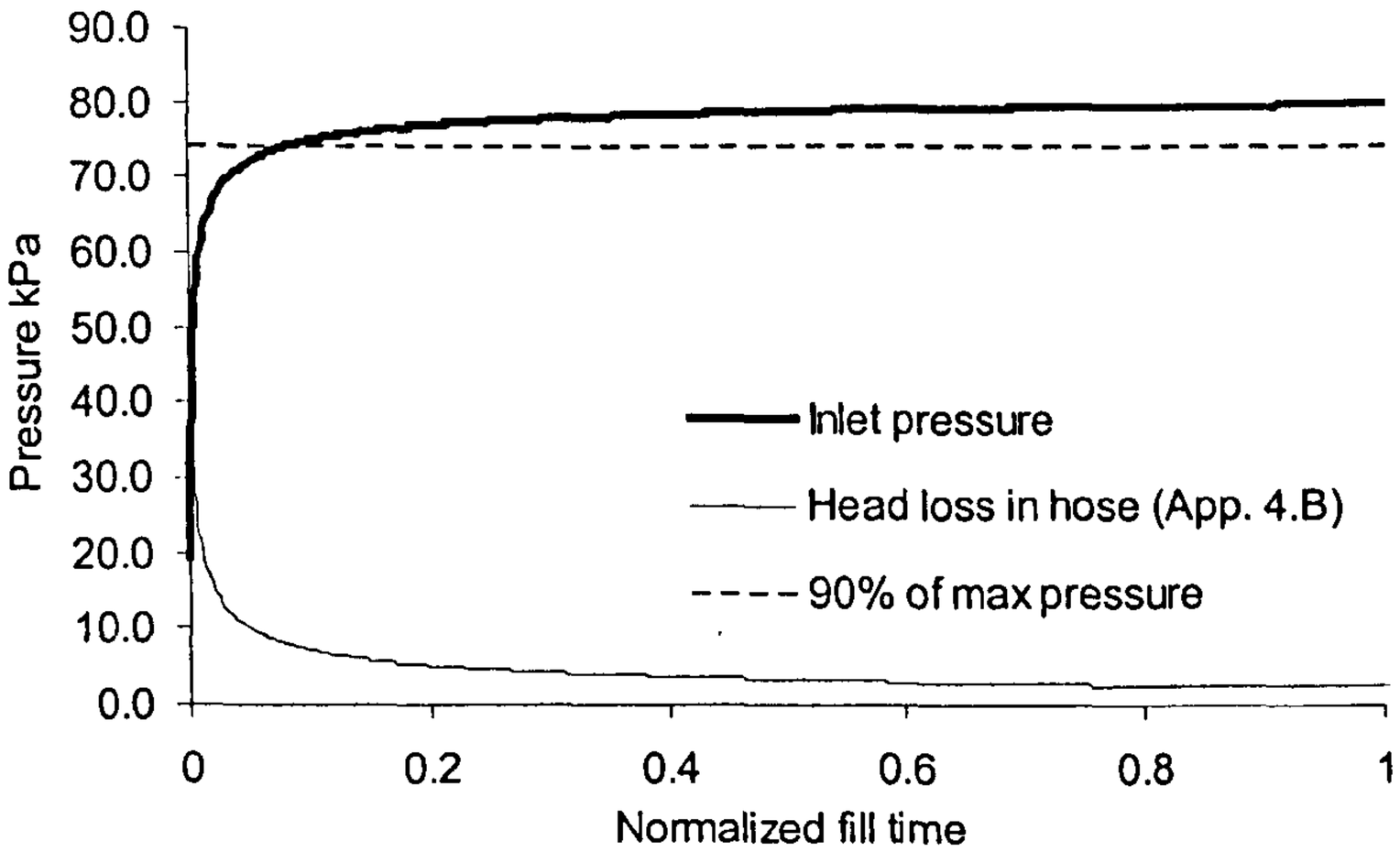

Figure 4.12 – Evolution of pressure with time for the data in Table 4.2. Fill time normalized with the maximum fill time for the mould (268 s)

It should be noted that the experimental work must account for experimental fill time not always being directly proportional to the square of the flow front position. As can be seen in Figure 4.13, while the assumption of constant inlet

pressure (topmost line) leads to a direct relation between the variables the inclusion of a variation in inlet pressure changes this relation and reduces the goodness of the fit. Clearly, the change in inlet pressure in Figure 4.11 affects the ability to model flow. For example, if this pressure dependence on time is accounted for, the flow velocities change from those expected in the constant inlet pressure assumption as shown in Figure 4.13.

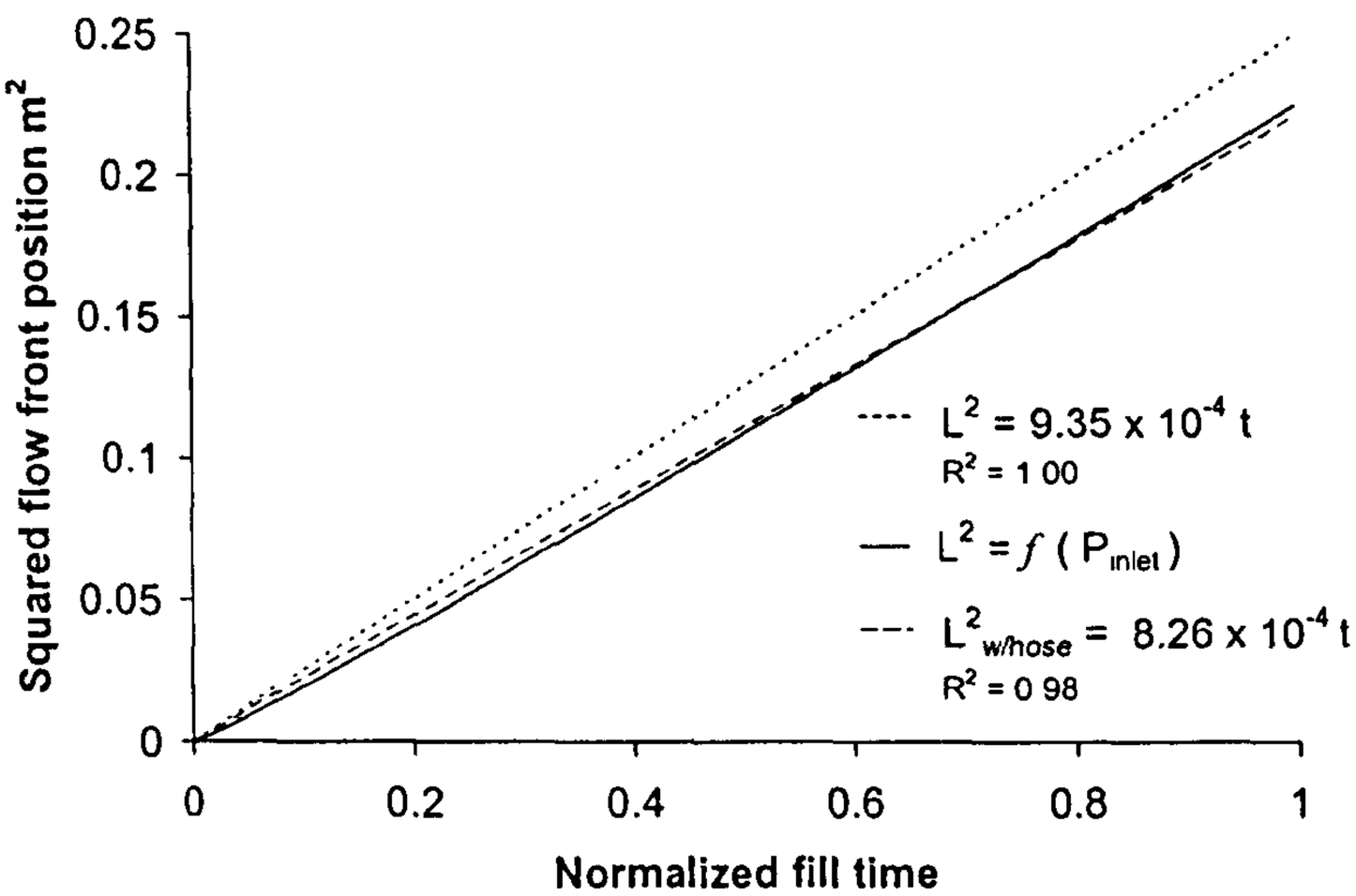

Figure 4.13 - Effect of pipe head loss on flow velocity (Table 4.2). Squared flow front position (L2) vs. normalised fill time. Top line is the flow velocity without accounting for inlet pressure changes. L2w/hose is the result from the model which includes the hose resistance in the velocity term. The continuous line (f(Pinlet)) is a linear fit to show that hose resistance changes the progression of velocity with the squared flow front position: it is no longer directly proportional to time

4.4.3 Fluid pressure field validation

One way to eliminate the influence of inlet pressure in pressure field measurements is to allow a complete saturation of the material before acquiring the pressure data. The results for four experiments on U750 are shown in Figure 4.14, for full moulds.

As shown, the model predicts pressure in transducer B with good precision. The error between the average experimental pressure and the model was 1.26% relative to the driving pressure. The predicted pressure at transducer C was not as accurate, showing a relative error of 4.9%. Nevertheless, while the variability at

transducer B is very low, there is considerable noise in transducer C. However the modelling solution is very close to the experimental results, with a maximum error of 4.9%.

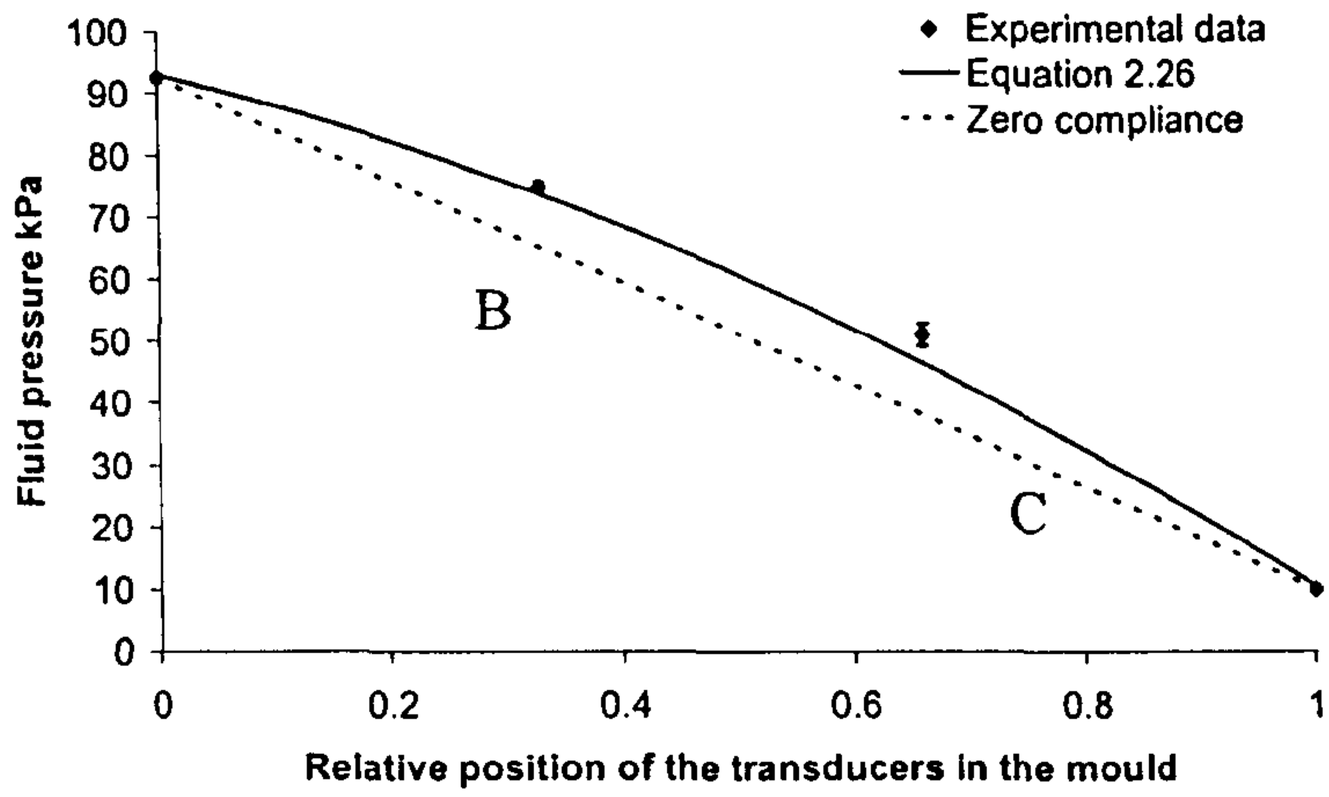

Figure 4.14 – Measured fluid pressure field for Vetrotex U750 CSRM. Results from four experiments showing the 95% confidence interval

4.5 EXPERIMENTAL OBSERVATION OF LAMINATE THICKNESS

The measurements discussed in this section relate to four experiments which were carried out on 14 layers of random mat (U750/450) from Saint Gobain Vetrotex. The laminate was vacuum infused with a Norpol 420/100 polyester resin containing 1% of accelerator (NL 49P) and between 1% and 2% of catalyst (Butanox M50) at an outlet pressure of 10 kPa and an inlet pressure of 90 kPa. Once cured, the four plates of 700 mm by 700 mm were cut and their thickness was measured at 120 points (marked with a cross) in four identical plates which were cut to allow testing (Figure 4.15).

While individually the measured data presented some variability this was reduced through averaging thickness at the same locations on all laminates and subsequently at sections of equal distance to the inlet. Figure 4.16 shows the 95% confidence interval for the measured thickness. The measurements show that there is a clear trend of thickness reduction from inlet to outlet supporting the initial hypothesis that the compliance of the porous media affects the output of the process. This hypothesis can then be tested by prediction of a thickness field which is then compared with the experimental results. In compaction experiments,

this material displayed an average saturated expansion behaviour which can be characterized by the compaction power law with an initial fibre volume fraction $v_{f0} = 0.078$ and a stiffening index $B = 0.099$. At 14 layers, the measured surface density for this reinforcement was 6.16 kg / m^2 (440 g / layer). Figure 4.17 shows the predicted thickness (continuous line) against the average cross-section thickness in the four laminates.

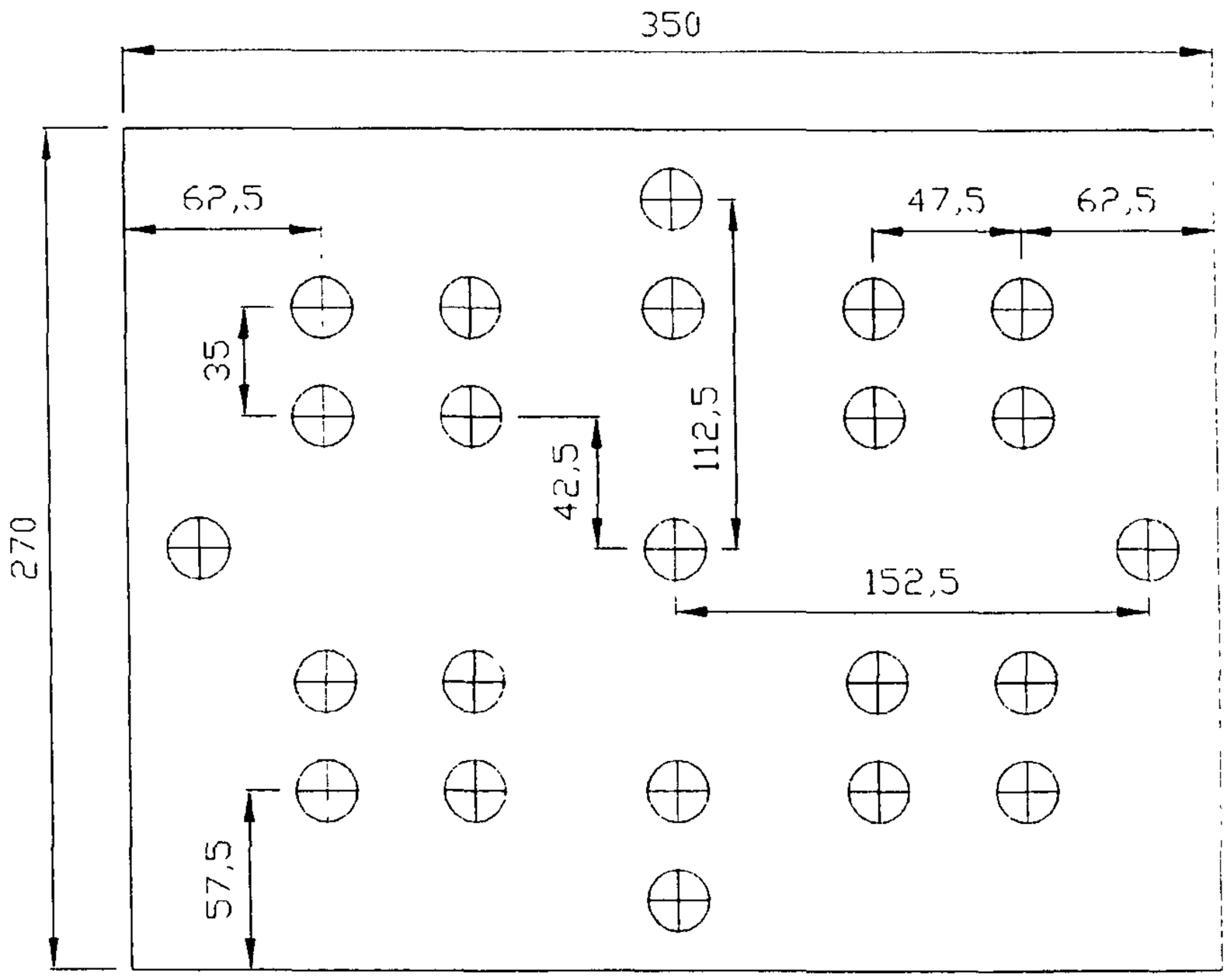

Figure 4.15 – Thickness measurement locations for a quarter test sample pattern for cutting. The thickness measurements were taken on each of the four plates which were cut from the original 700 mm x 700 mm laminates

As Figure 4.17 shows, the model provides a similar trend to the measurements but it overestimates thickness by roughly 0.5 mm. The most likely explanation for this is resin shrinkage which, being dominated by the through thickness stiffness of the laminate, would happen differently from inlet to outlet (more compaction near the inlet). A second explanation for this is the fact that a layer of peel-ply was used in the experiment. The error could then be due to the removal of resin from the surface with the peel-ply and to the increased surface roughness which limits the accuracy of the thickness measurement system.

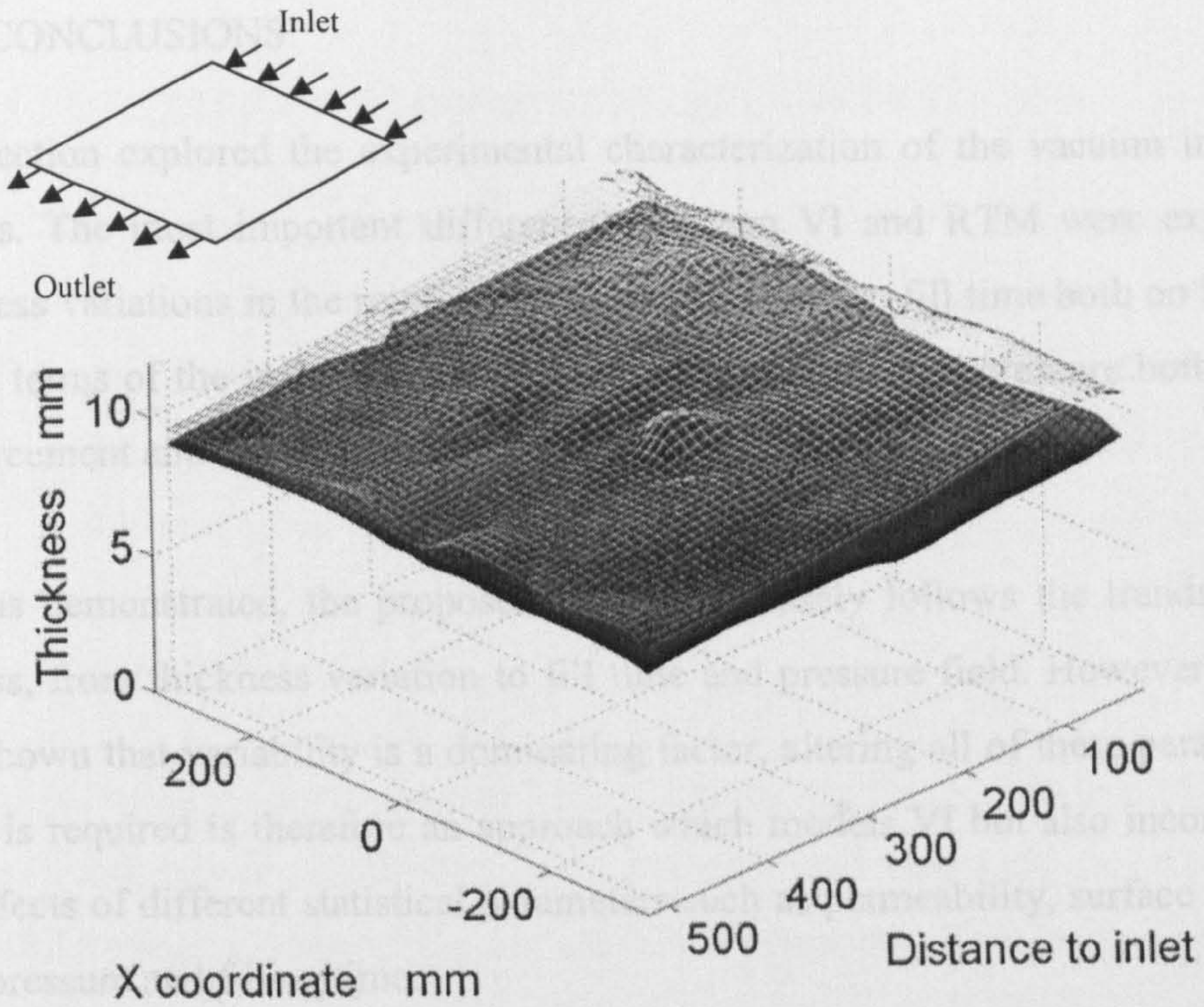

Figure 4.16 - Thickness measurements of U450. Surfaces delimit 95% confidence interval for thickness

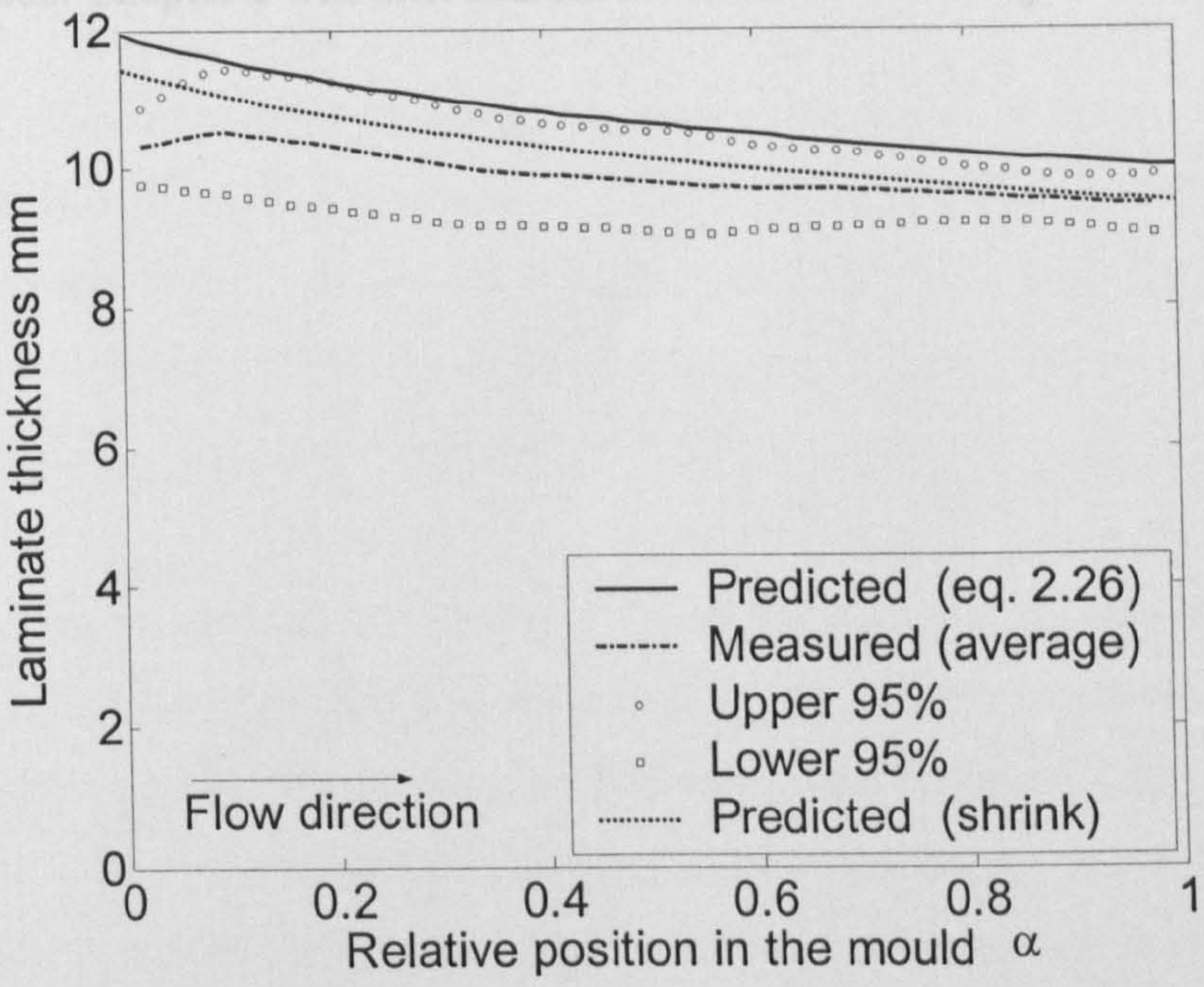

Figure 4.17 – Measured and predicted thickness for 14 layer Vetrotex U750. The dotted line in the graph shows the predicted thickness assuming a 0.5 mm thickness reduction due to these effects

4.6 CONCLUSIONS

This section explored the experimental characterization of the vacuum infusion process. The most important differences between VI and RTM were explored: thickness variations in the reinforcement and at the front, fill time both on its own and in terms of the influence of outlet pressure on flow and pressure both in the reinforcement and at the inlet.

As was demonstrated, the proposed VI model closely follows the trends in the process, from thickness variation to fill time and pressure field. However, it was also shown that variability is a dominating factor, altering all of these parameters. What is required is therefore an approach which models VI but also incorporates the effects of different statistical parameters such as permeability, surface density, inlet pressure and filling time.

The following chapters will focus on these topics. The first (chapter 5) will extend these modelling capabilities to complex geometries so that complex moulds can be analysed. Chapter 6 will then address the issue of variability in VI.

5 AN FE MODEL OF THE VACUUM INFUSION PROCESS

This chapter looks into the new problem of extending the models of flow through compacting media to two or three dimensions and complex geometries and discusses the numerical solutions for this problem. Its main objectives are therefore to develop and validate viable modelling tools for flow through compacting porous media.

5.1 INTRODUCTION

As was previously shown, flow in VI is a function of the compaction mechanics of the reinforcement, both dry and saturated, and can only be completely described through models which include the deformations of the porous materials. In fact VI is akin to the hydrological problems of flow through compacting soils and RTM represents a special case of this problem insofar as, due to mould construction, the porous medium does not deform. The rationale behind this chapter is that while the specifics of flow through compacting porous media can be investigated, in 1D, through analytical studies, this approach is not suitable for complex geometries. This was understood from the outset of the project: the aim of the analytical studies is to clarify the fundamental physics of flow through compliant media and provide a validation and benchmark base for future flow model developments. This step was to be followed by the finite element / control volume (FE/CV) approach which is explored in this chapter.

For practical reasons one must recognize that the maturity of commercial FE/CV modelling packages for RTM implies that any developments should be done by adapting these codes. Furthermore, as discussed with Equation (2.39), RTM is but a special case of flow through compliant porous media. However, this requires access to, or control over, the simulation software. The present work involved a collaboration with the University of Delaware (USA) who provided access to their RTM code "liquid injection moulding simulation" (LIMS), produced a modelling tool capable of analysing flow through compliant media. As will be shown, the adapted software was validated by comparison with the analytically based

simulations and experiments. It was also able to model complex 3D flow through compliant porous media shells.

As before, this chapter contains a specific literature review section. In the present case it discusses different flow modelling methodologies, focussing particularly on literature related to LIMS, and the problem of through thickness flow. Having established the state of the art the following sections discuss the modelling work with LIMS and the validation work by comparing LIMS results with analytical based analysis highlighting the differences and similarities in the approaches. The validated model is then used in parametric studies of the VI case of flow through compliant media and two and three dimensional flow results. It should also be mentioned that a relevant section of future work on the topic of FE/CV modelling of flow through porous media can be found in chapter 7.

5.2 LITERATURE REVIEW

5.2.1 Numerical flow modelling methods

Models of flow through porous media must consist of two components: one providing the pressure solution and another which balances flow (mass) and defines the flow front. Different numerical methods have been applied to model the pressure of the fluids in moulds containing porous media, i.e. the finite difference, finite element or boundary element methods, FE being the most common (Pillai *et al*, 1998 a, b and Rudd *et al*, 1997). Nevertheless, the moving flow front poses a problem which cannot be solved by FE alone: the domain changes in time. Solutions can either be re-meshing at each time step or to employ a method which is capable of re-defining the boundary without re-meshing. In the most common mould flow simulation technique, the flow front is defined at each time step at the nodes which are closest to the front. This is done by calculating which nodes are filled by balancing the mass of resin in the mould. The control volume method (CV) is the numerical technique which models flow between elements (cell-centred control volumes) or nodes (node-centred control volumes) as is show in Figure 5.1 (Chung, 2002).

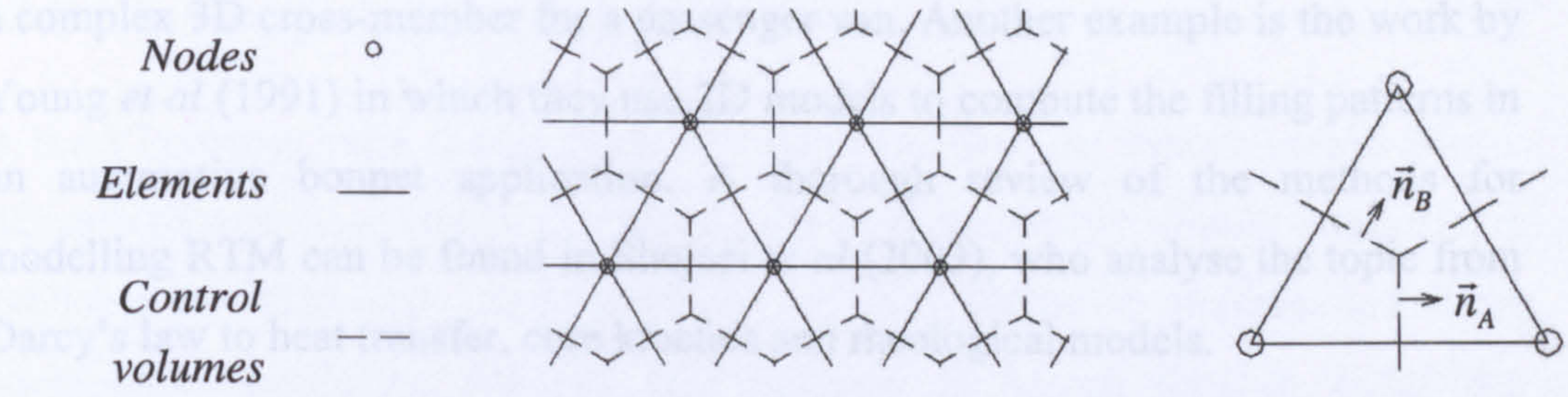

Figure 5.1 – Control volumes on an equilateral triangular mesh and a representation of the control surfaces and respective normal vectors on the control volumes

In an advancing flow, no-flow boundary conditions are applied normal to the mould walls (which are represented by the edges of the mesh). At the flow front, nodal pressure is set to the outlet pressure. In order to represent the layup accurately each of the elements is also assigned permeability, cross-section (1D) or thickness (2D shells) and porosity (or fibre volume fraction), as prescribed by Darcy's law. The finite element method can then be used to solve the fluid pressure field within a time step. (Advani *et al*, 1994, 1999). Once the pressure field is known, Darcy's law is applied to the flow front either for a specified amount of time or for the time required to fill an additional control volume. Figure 5.2 shows that nodes in partly filled control volumes define the flow front, resulting in a discrepancy between the real flow front and the one which is used in the FE pressure solution. This can only be improved on by denser meshing.

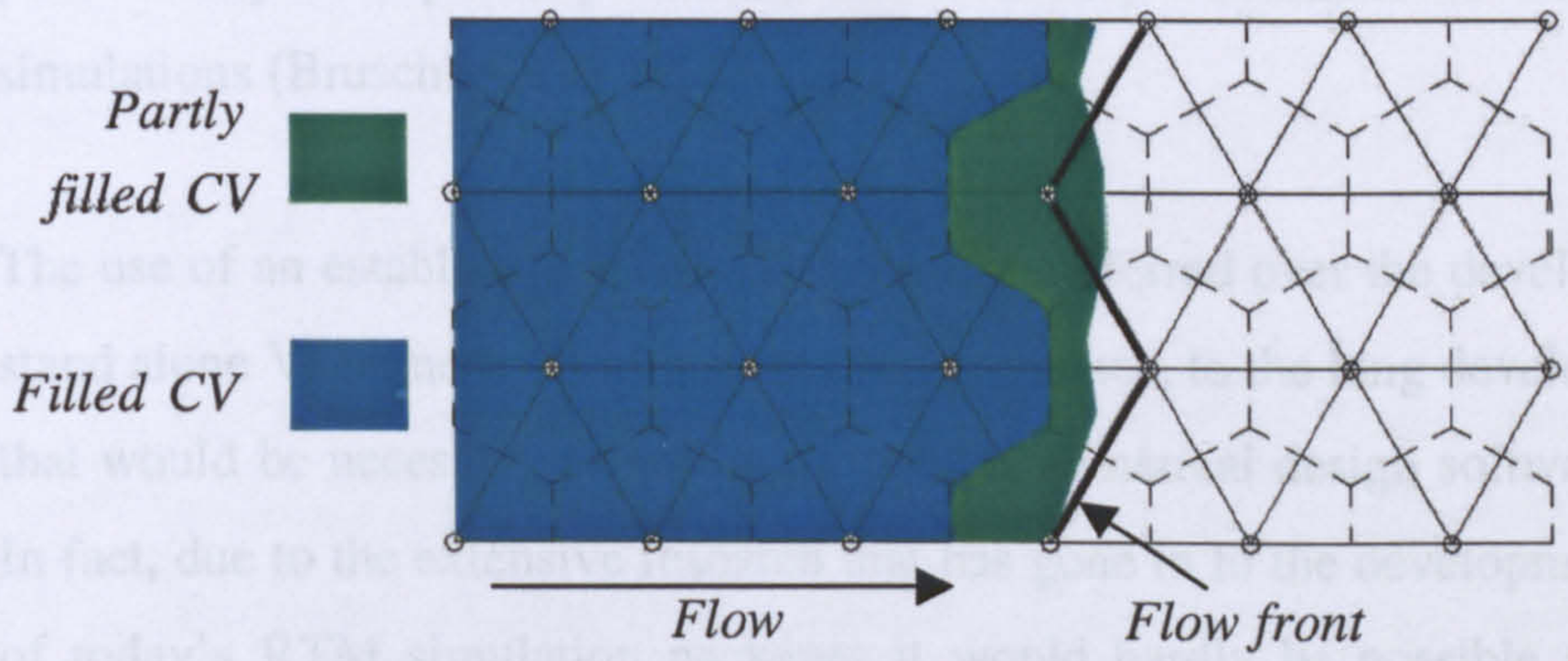

Figure 5.2 – FE/CV definition of the flow front

Early applications of the finite element control volume method (FE/CV) to flow in closed moulds are for example the work by Bruschke *et al* (1990) which is the precursor of the LIMS software from the University of Delaware and could model

a complex 3D cross-member for a passenger van. Another example is the work by Young *et al* (1991) in which they use 2D models to compute the filling patterns in an automotive bonnet application. A thorough review of the methods for modelling RTM can be found in Shojaei *et al* (2003), who analyse the topic from Darcy's law to heat transfer, cure kinetics and rheological models.

As described earlier, the aim of this chapter is not to recreate FE/CV flow modelling but to adapt existing software. Consequently, the following section describes the literature pertaining to the modelling software LIMS which was used in this work.

5.2.2 Liquid injection moulding simulation (LIMS)

All FE/CV numerical research presented here was conducted using LIMS: liquid injection moulding simulation, developed at the University of Delaware. LIMS can be described as a dedicated FE/CV based simulation of flow through porous media, capable of analysing both 2D and 3D flows (Simacek *et al*, 2001; Advani *et al*, 1999). LIMS 5.0 has a built in scripting language, LBASIC, which was added so that boundary conditions could be modified during the simulation (Mathur *et al* 2000; Kueh *et al* 2002). As is the case with other FE based simulation packages, it is necessary to supply a meshed geometry, preform permeability and porosity values, and boundary conditions to carry out the simulations (Bruschke *et al* 1990).

The use of an established RTM software was preferred over the development of a stand alone VI numerical simulation due, in essence, to the long development time that would be necessary to produce a proven numerical design software package. In fact, due to the extensive research that has gone in to the development of many of today's RTM simulation packages it would hardly be possible to reach the same level of sophistication in a short time.

5.2.3 On through thickness flow

In the VI process, resin cannot be driven with more than the atmospheric pressure. Because of this, flow speeds would typically be considerably smaller than what is available in RTM and the applicability of the process to manufacture large components would be limited. This problem is solved through either the introduction of high permeability materials in the mould or the addition of channels, or grooves, to the mould. Both approaches work by enhancing permeability and are commonly used in industrial applications (e.g. Seemann, 1990, 1991, 1995; Walsh 2003; Slaughter 2003). Figure 5.3 shows the effect of using a high permeability medium. The higher permeability at the top of the laminate (where the DM is placed) leads to through thickness permeation which adds to the dimension of the problem. In parallel, thickness is also changing as the fluid pressure field evolves. The studies of VI should therefore include multiple media in permeability and flow analysis.

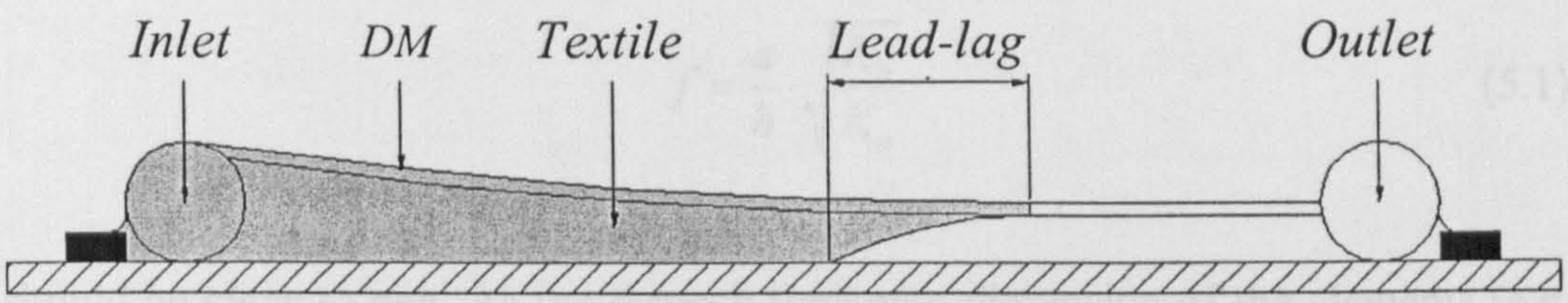

Figure 5.3 – Flow in VI with distribution medium, showing the creation of lead-lag due to permeability dissimilarities

Published studies on this topic have only addressed the problem of through thickness flow through non-compliant media (RTM):

1. FE/CV simulation of the complete geometry of the stack in either 2D, for a cross-section, or 3D for complete (non-compliant) components.
2. Advanced FE/CV (non-compliant) simulation, using scalar through-thickness saturation terms.
3. Analytical approaches, which combine the permeability of all different regions into an effective permeability value for the stack reducing the problem dimension (non-compliant).

The first approach (Sayre *et al* 2003) has the advantage of a precise calculation and possible simplicity of geometric modelling. Nevertheless it is highly computationally intensive due to the 3D nature of the problem, especially in thin complex components. The problem resides in the shape factor of an anisotropic element (Figure 5.4).

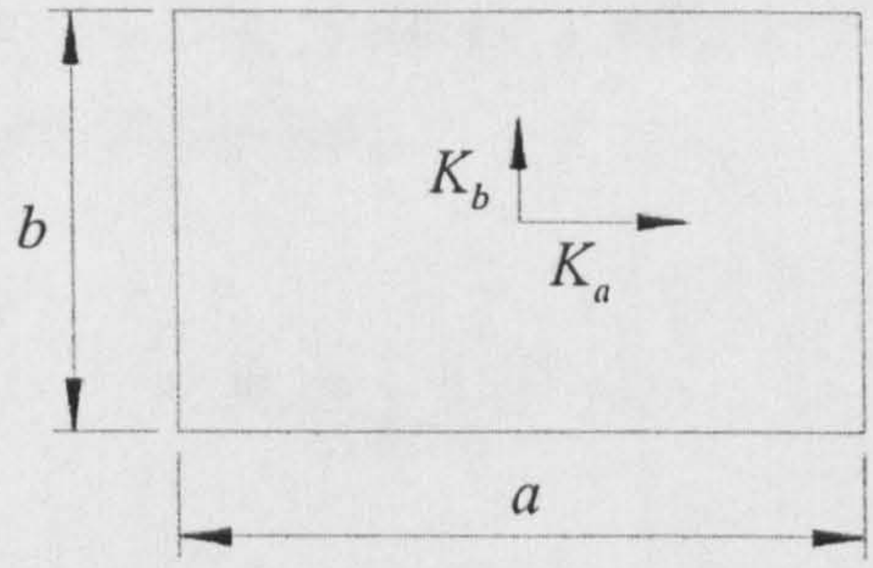

Figure 5.4 – 2D anisotropic element

Where the shape factors given by:

$$f = \frac{a}{b} \cdot \sqrt{\frac{K_b}{K_a}} \tag{5.1}$$

should be close to one. As the through thickness dimension of the elements (e.g. *b*) is the simple ratio of laminate thickness to number of through thickness elements (*n*), their in-plane dimension (*a*) is approximately fixed:

$$b = \frac{h}{n} \quad \Rightarrow \quad a \approx \frac{h}{n} \cdot \sqrt{\frac{K_a}{K_b}} \tag{5.2}$$

Consequently, in thin components with large in-plane dimensions, a 3D approach necessarily implies a large number of elements. Earlier work by Gebart *et al* (1991) had however proposed a reduction of the 3D problem to a 2.5D one by adding a saturation scalar term to the flow calculation. In their case the layers had however to be of equal thickness and porosity. Tari *et al* (1998) expanded on this work, removing these restrictions. They were then able to determine a lead-lag value from 2D FE/CV models for complex 3D shell geometries. This is a

promising technique but has not yet been introduced in common flow software packages.

The final type of techniques is analytical and can therefore be easily introduced in standard packages such as LIMS. The simplest of this family, sometimes referred to as the averaging scheme, assumes a weighted average permeability, eliminating through thickness flow from the analysis. Equation (5.3) shows the effective permeability according to this approach.

$$\bar{K}_{ij} = \frac{1}{H}\sum_{l=1}^{n} h^l \cdot K_{ij}^{\ l} \tag{5.3}$$

It should be noted that the averaging scheme should be limited in application to cases where permeabilities do not differ highly from layer to layer or, in other words, when through thickness flow is negligible (Adams *et al*, 1991). It is however a simple first approximation providing a rough estimate of the effective permeability of the preform. Advani *et al* (1994) suggested a different approach for a medium with two layers of equal thickness but significantly different permeabilities. In their work they divide the flow domain into two regions: the fully developed flow region, where there is no through thickness flow, and the lead-lag region at the front ($l_1 > x > l_2$) where there is cross flow (Figure 5.5).

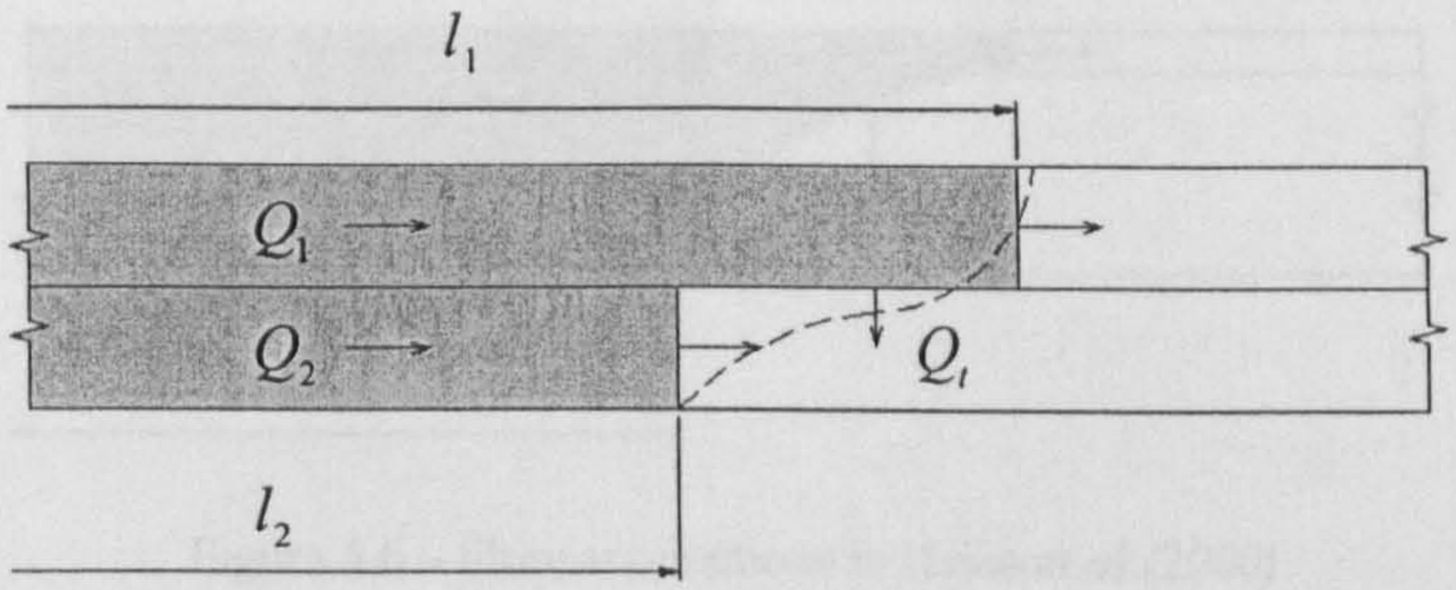

Figure 5.5 – Cross-section of a dual media flow showing the region where through thickness flow (Qt) is considered

They use the averaging scheme at $l < l_1$ and propose an expression for the lead-lag region. They also show that this expression tends to Equation (5.4) when the flow is fully developed ($l_1 >> (l_1 - l_2)$):

$$K_f = \frac{1}{2} \cdot \left(\frac{K_2}{K_1} + 1 \right) \cdot \bar{K} \tag{5.4}$$

and that the length of the lead-lag region tends to stabilize to the value:

$$\Delta l = h \cdot \sqrt{\frac{1}{4} \left(\frac{K_1 - K_2}{K_t} \right)} \tag{5.5}$$

where h is the total thickness of the laminate. Note that since K_2 is smaller than K_1 the permeability at the flow front is overestimated by the averaging scheme. This work was expanded in 1996 by Calado *et al* to accommodate a higher number of layers still of different thicknesses (but still for the non-compliant media case).

The work by Hsiao *et al* (2000) advanced this approach and produced a closed form analytical solution for the problem of lead-lag calculation with the assumption that flow at the front occurs only through the thickness (Figure 5.6). It was followed by a validation study by Mathur *et* al (2001).

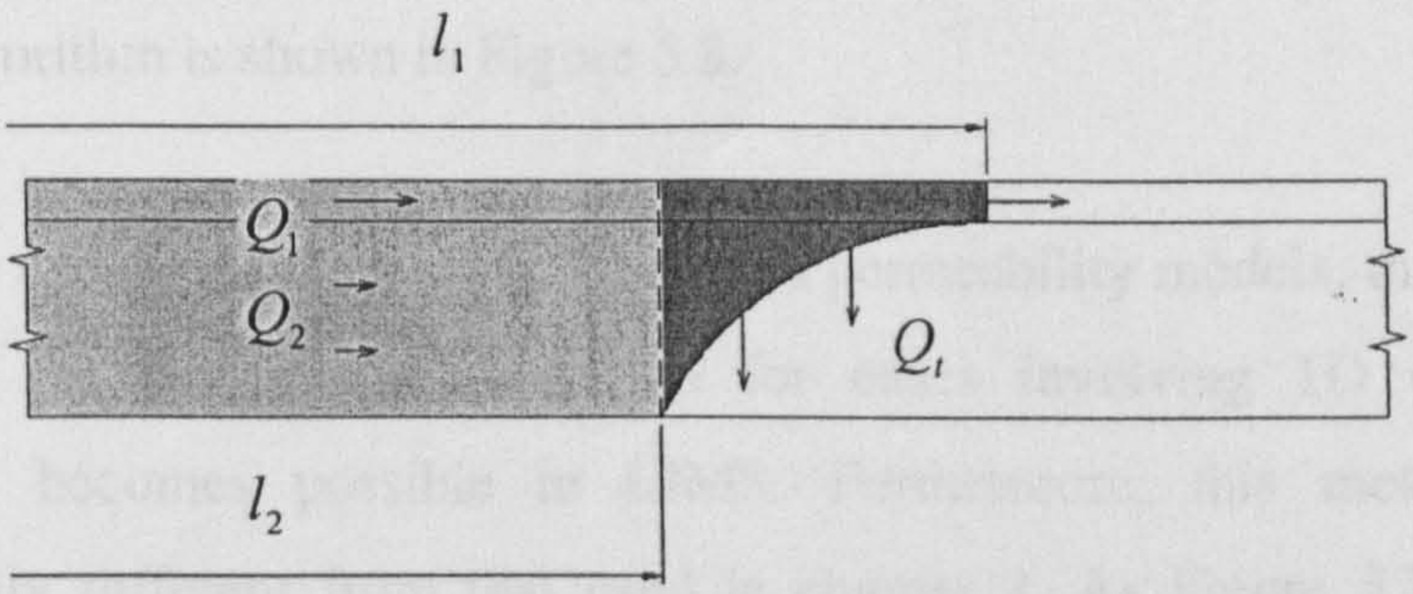

Figure 5.6 – Flow assumptions in Hsiao *et al (2000)*

This work does not explore this topic. There is no reason however why there could not be an simple implementation of any of the models by Advani or Hsiao. Figure 5.7 illustrates the plug-flow assumption.

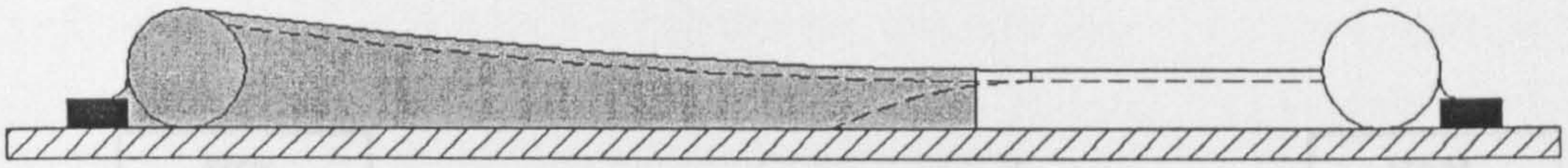

Figure 5.7 – Plug-flow simplification on a 2D cross-section of VI

5.3 MODELLING FOR VI WITH LIMS

Having established the relevant state of the art, this and the following sections will discuss the areas where this work has contributed to the field.

5.3.1 Overview

As stated above, the main advantage LIMS presents over other packages is its extensive scripting capability, allowing the incorporation of reinforcement compliance without altering the basic modelling approach. In order to simulate VI's flow through a compliant porous medium, the software needs to be capable of updating thickness, porosity and permeability locally as a function of compaction pressure. This is accomplished through an *LBASIC* code, which is able to apply the required changes and check iteratively for convergence by re-solving the pressure field under the new conditions. The flow front is then advanced and the procedure is repeated. A schematic representation of LIMS' LBASIC algorithm is shown in Figure 5.8.

Through the use of auxiliary compaction and permeability models, the calculation of flow in the compressible medium for cases involving 1D or 2D shell components becomes possible in LIMS. Furthermore, this methodology is fundamentally different from that used in chapter 2. As Figure 5.8 shows, the coupled pressure/compaction problem is solved by iteration in each time step but, unlike the analytical studies, each individual discrete element in the pressure field solution is non-compliant. The pressure solution obtained by LIMS in one iteration is therefore analogous to that obtained in a non-compliant medium having local thicknesses, porosities and permeabilities. As will be shown in the following sections, this fundamental difference makes the validation of the numerical solution with analytical results possible and therefore also with the experiments shown in chapter 4.

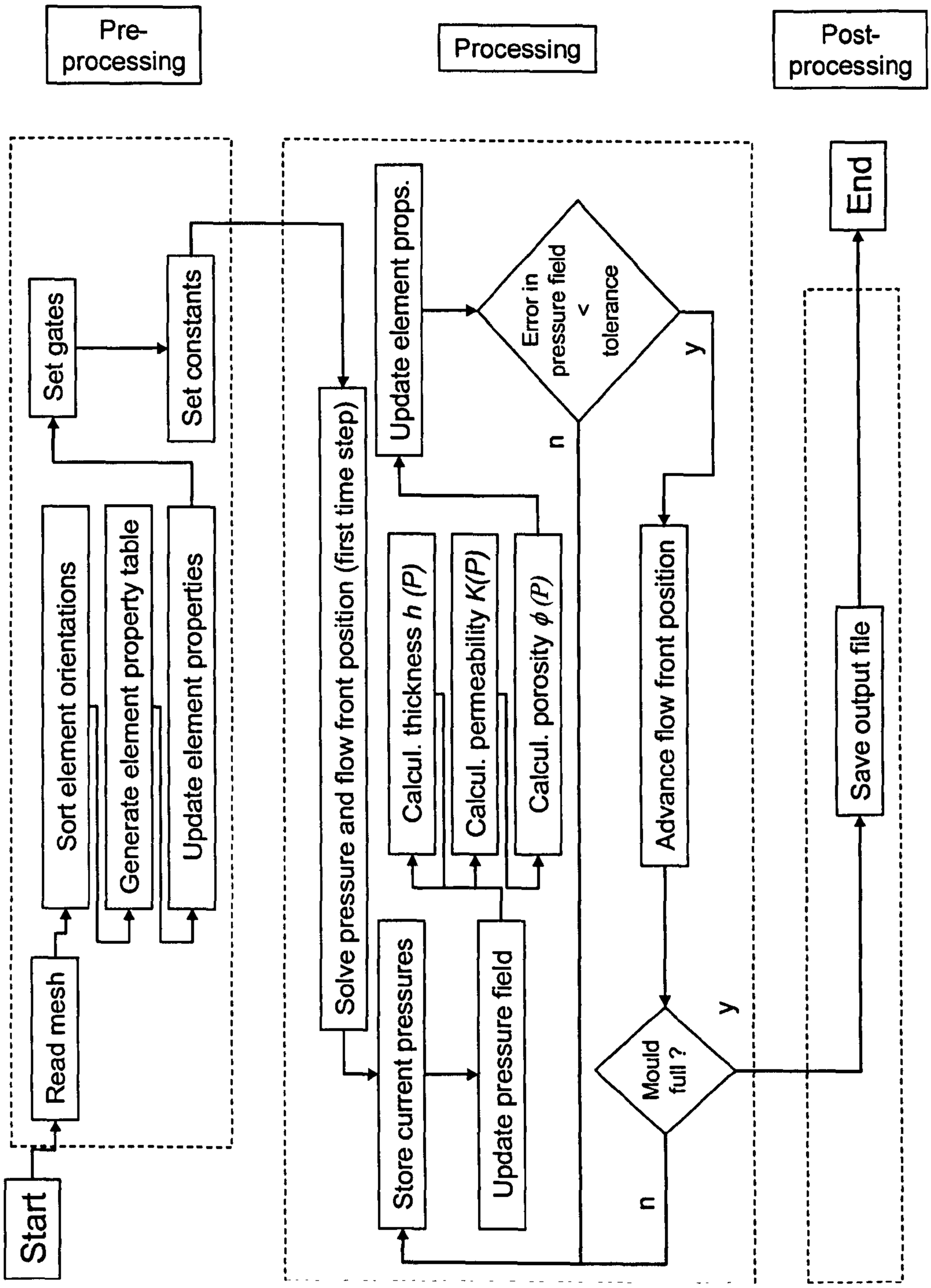

Figure 5.8 - VI algorithm used in LIMS LBASIC script

As with the analytical studies discussed in chapter 2, the LIMS based VI model requires the input of viscosity, permeability and compaction data, forming the material property basis which is required for flow simulation. Pressure dependent

material property basis which is required for flow simulation. Pressure dependent compliance and flow properties (*h(P)* and *K(P)* – Equations (2.11) and (2.13)) have been discussed extensively in sections 2.4, 2.5 and chapter 3. In parallel, the program requires a FE mesh, representing the 3D shell geometry of the component. Atmospheric pressure is assumed to act perpendicularly to the shell elements.

The LBASIC code which was developed in the collaboration period at the University of Delaware is presented in Appendix 5.1. Table 5.1 shows the list of sub-procedures used in the code and the task that each one performs. The results are synthesised in the main procedure and output to a file.

Table 5.1 – Sub-procedures invoked in the VI code

Sub procedures	
SetConstants	Setting the relevant flow properties as global variables
Propertydata	Create a property data table
TableCompletion	Feed back to the user
Flow	Computes VI flow
SortVerticalElements	Preliminary element orientation check
UpdateProperties	Updates flow properties according to the pressure field
Setting	Gate scheme settings

5.4 NUMERICAL VS. ANALYTICAL STUDIES

5.4.1 Negligible parameters

In chapter 2, it was shown analytically that the pressure field solution is not sensitive to the values of surface density, Kozeny constant or viscosity. It is therefore fundamental that the pressure field solution obtained through LIMS-VI can replicate this behaviour. A parametric study, focussing on the sensitivity of the LIMS-VI solution to these parameters, confirmed this. Each was varied at three levels differing in one order of magnitude. Table 5.2 summarizes the results, compared as to their influence on C_α . Bear in mind that C_α represents the ratio between RTM and VI fluid pressure gradient at the flow front and is therefore both a function of the fluid pressure field and a good representation of its non-linearity. The choice of material properties and driving pressure reflects the combination with the highest sensitivity in the parametric studies presented in

chapter 3: most compliant material and highest driving pressure. The study, consisting of seven numerical experiments shows that, as expected, the LIMS VI pressure field results are not sensitive to variations of density, Kozeny constant and viscosity (Table 5.2).

Table 5.2 – The influence of surface density, Kozeny constant and viscosity on the non-linearity of the fluid pressure field in the LIMS-VI solution

P_{in}	P_{out}	v_{f0}	B	ρ_{sup}	k	μ	C_a
kPa	kPa	-	-	kg/m^2	x10^{-5} m^2	Pa.s	-
90	0	0.1	0.124	0.1	1	1	1.68
				1	0.1	1	
				10	1	1	
				1	1	0.1	
				1	1	1	
				1	1	10	
				1	10	1	
				10	1	1	

These simulations were done in a one dimensional mesh, containing 100 elements.

5.4.2 Numerical vs. Analytical approaches:

In order to further establish the equivalence of the two modelling approaches it is important to compare the fluid pressure field results of the analytical studies with those from LIMS. This is illustrated in Figure 5.9 for $v_{f0} = 0.1$ which represents a highly compliant random mat material (the relative error between the two solutions – numerical and analytical – is shown in Figure 5.10)

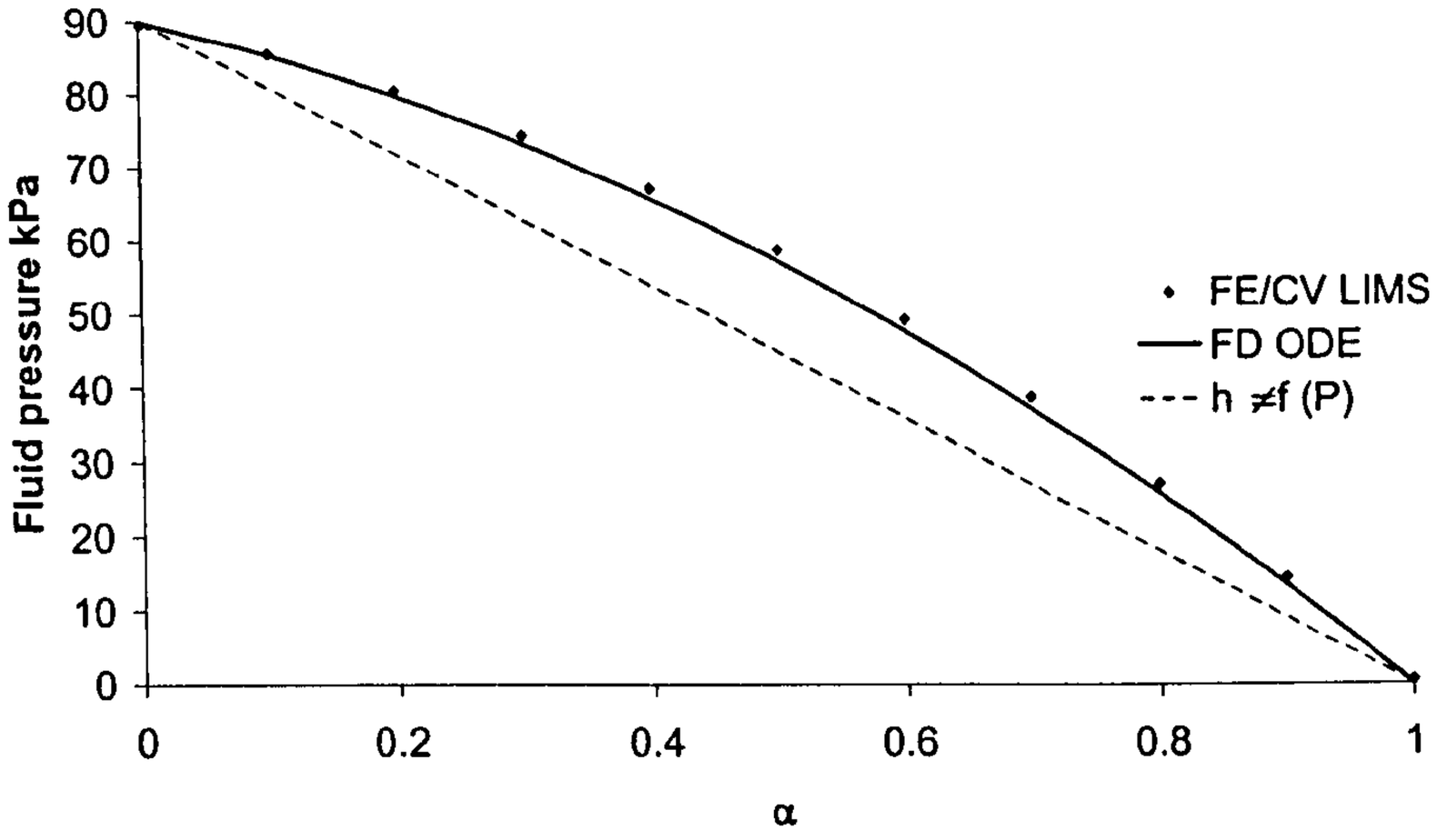

Figure 5.9 – Worst case scenario driving pressure: $P_{in} = 90\ kPa$ $P_{out} = 0\ kPa$, compaction properties of $v_{f0} = 0.1$. Results from LIMS VI and Equation (2.29).

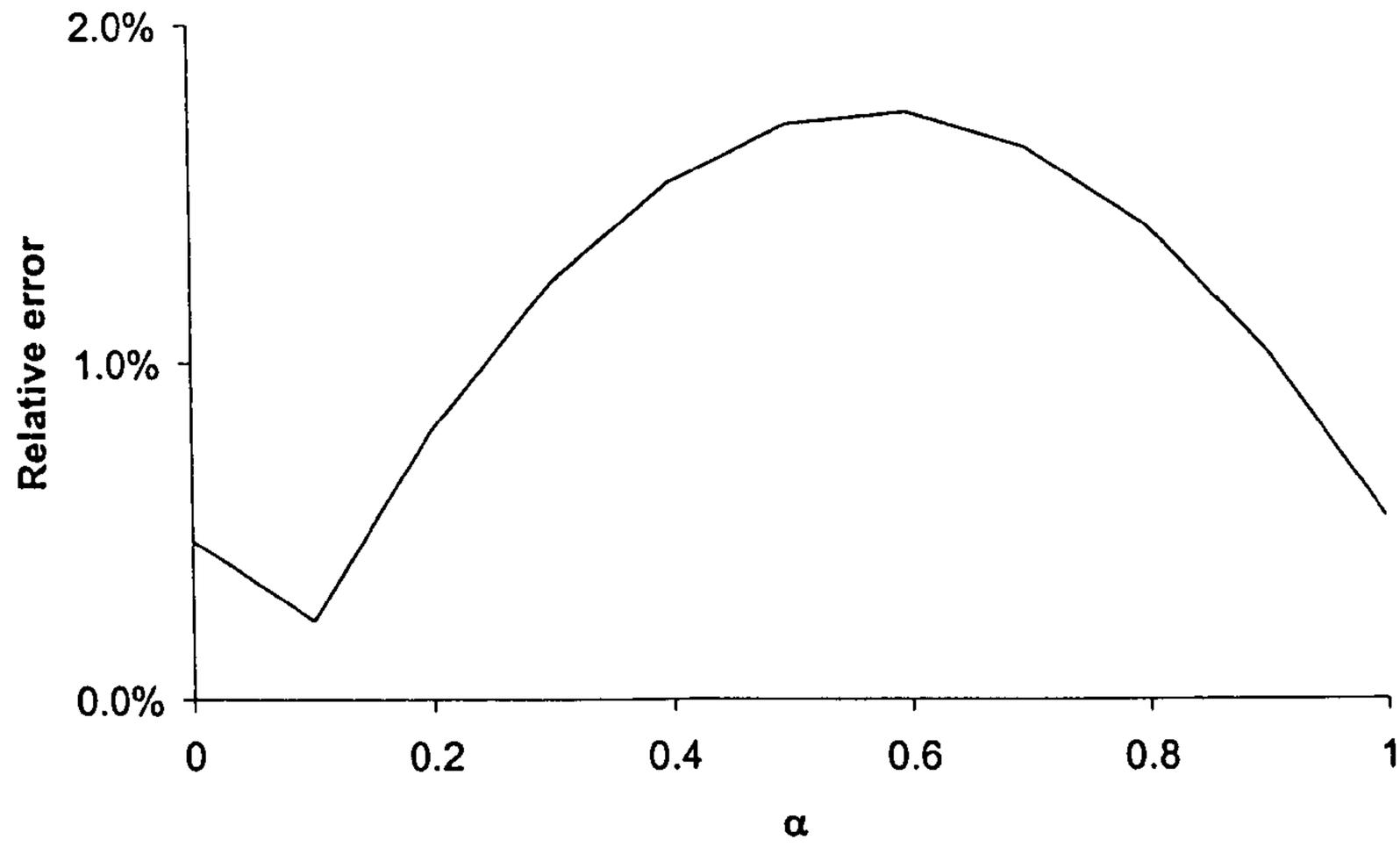

Figure 5.10 – Relative error between the two solutions relative to driving pressure $\Delta P = 90\ kPa$ for $v_{f0} = 0.1$

A stiffer material ($v_{f0} = 0.25$) is illustrated in Figure 5.11.

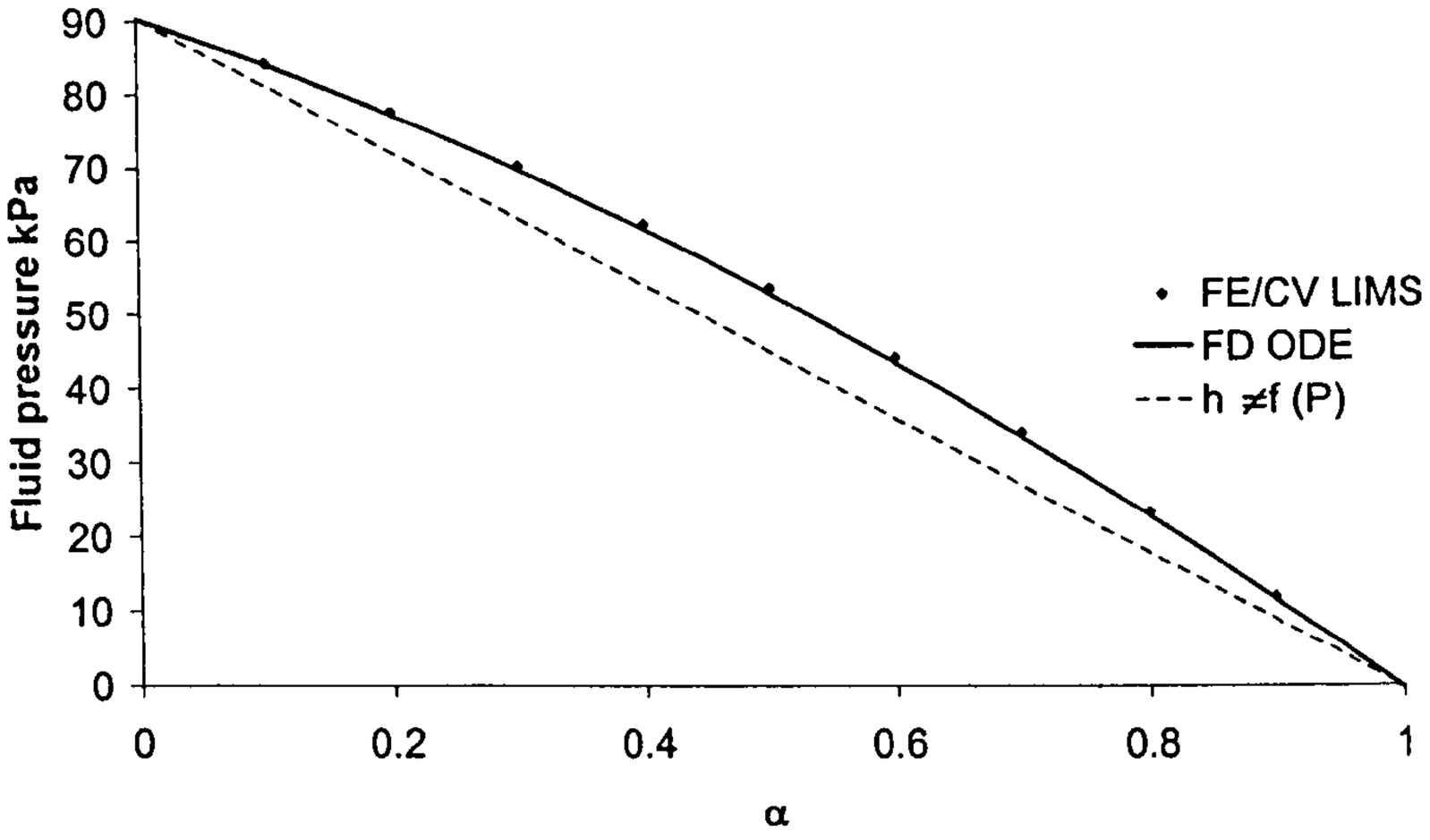

Figure 5.11 – Worst case scenario driving pressure: *Pin = 90 kPa Pout = 0 kPa,* compaction properties of $v_{f0} = 0.25$

Figure 5.12 shows the relative error between the two solutions.

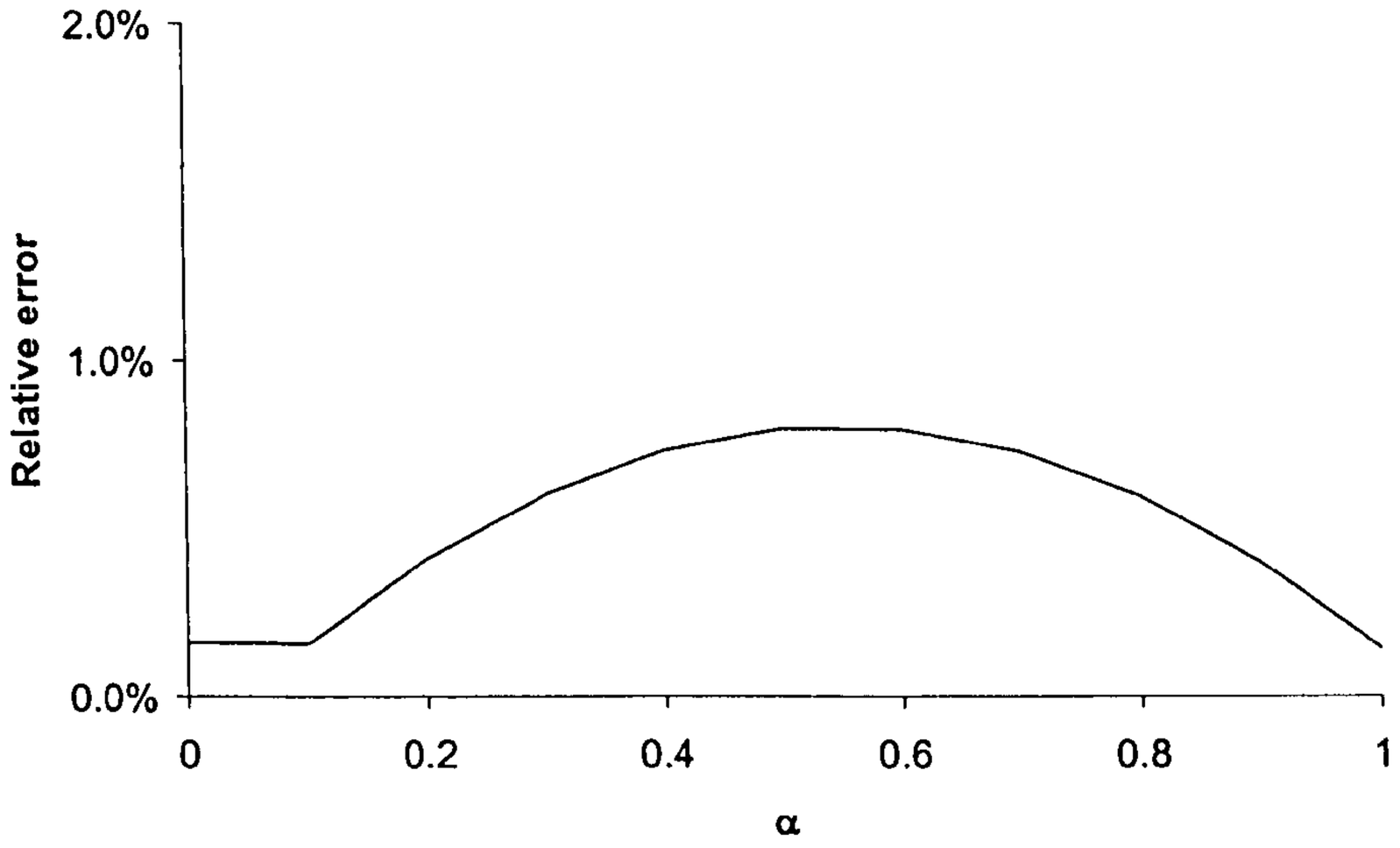

Figure 5.12 – Residuals between the two solutions relative to driving pressure $\Delta P = 90\ kPa$ for $v_{f0} = 0.25$

As shown, the error between the two solutions is negligible but decreases with increased stiffness of the reinforcement. This is expected since the reduced compliance leads to an increasingly linear pressure field, reducing the complexity of the solution of governing Equation (2.25).

Another form of comparison between the analytical based and the FE/CV solutions is the prediction of fluid pressure gradients at the flow front for different compaction properties, inlet and outlet pressures. As described in chapter 2, the fluid pressure gradient at the flow front is a function of the driving pressure ΔP (a process parameter) and of the fluid pressure field (dependent on the compliance of the medium). The compliance dependent component C_α is therefore a good measure of the ability of a method to model VI or similar techniques. Note that since ΔP is constant for the two approaches, the error in C_α equates to the error in flow speed.

As Figure 5.13 shows, the error between the two C_α solutions is negligible, i.e.: the maximum error value corresponds to a fill time error of 3.5%. One might also point out that it is expected to have such error values due to the dissimilar nature of the approaches and of their numerical implementations.

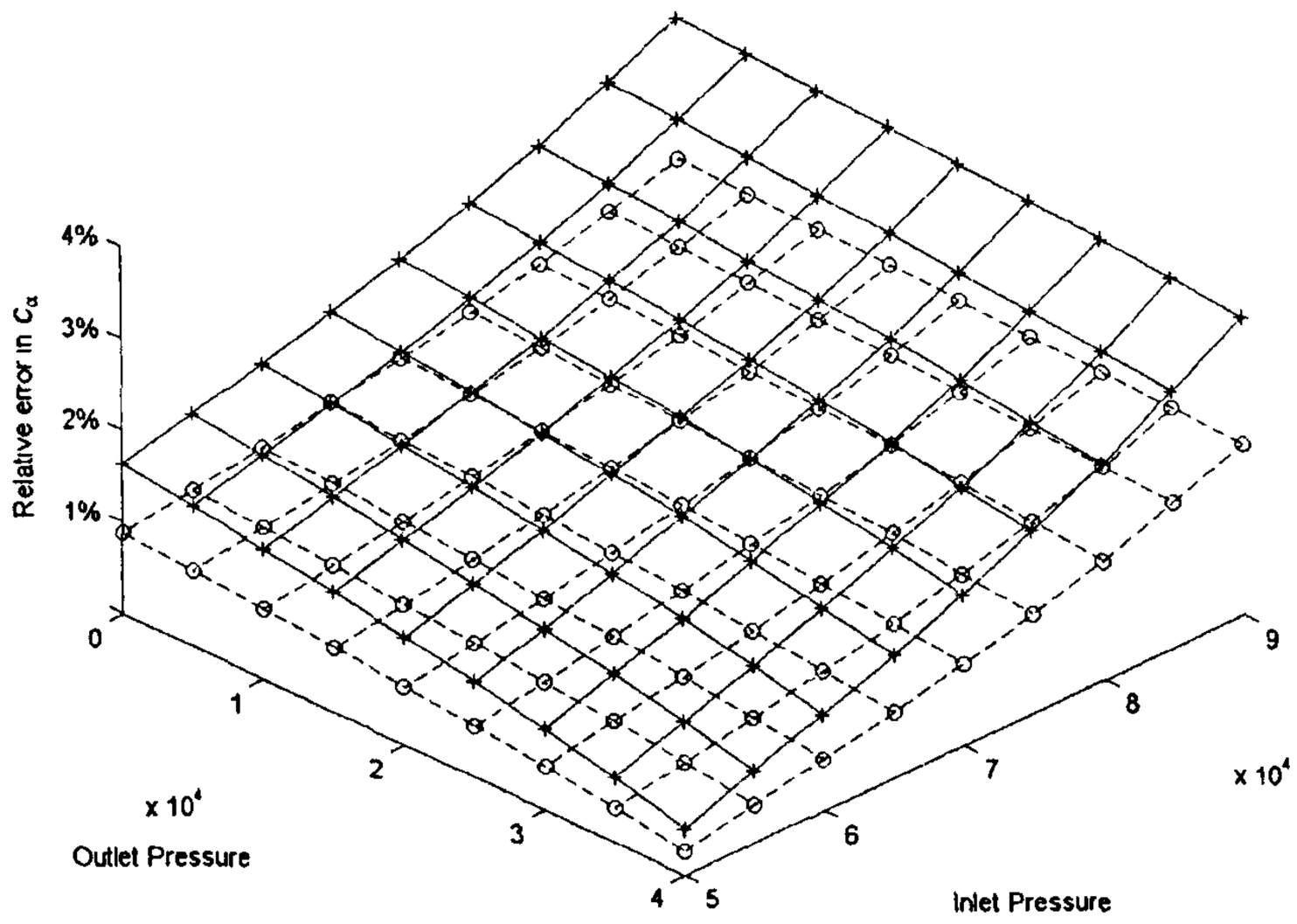

Figure 5.13 – Relative error between the analytical based and the LIMS solutions of the pressure gradient at the flow front. The top surface represents $v_{f0} = .25$ and the bottom surface $v_{f0} = .1$.

For example, as shown in Figure 5.14, while thickness is a nodal property in the analytical based approach it is an element property in the numerical approach because of code constraints.

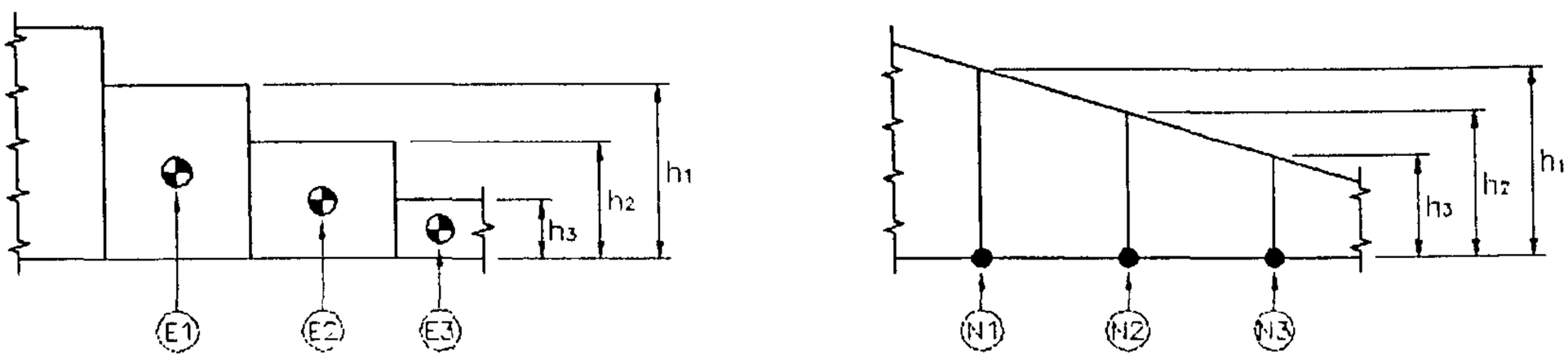

Figure 5.14 – Numerical solution with element thickness – LIMS (left) – or nodal thickness – analytical based (right). *E* stands for element and *N* for node.

Note that the implication of this result extends to the calculation of laminate thickness: both methods produce identical thickness profiles.

5.4.3 Number of nodes

Again, while the number of nodes affects the simulation results, its effect on the pressure field gradient at the flow front (and therefore fill-time) is negligible. Figure 5.15 shows the error between the 10 node and the 1000 node simulations, relative to the latter. As was discussed in Section 3.5.2 this error equals the relative difference between the integrals of polynomial forms. The maximum value observed occurred on the $P_{out} = 0$ $P_{in} = 90$ kPa $v_{f0} = 0.25$ and its magnitude is -2.052 % (top surface).

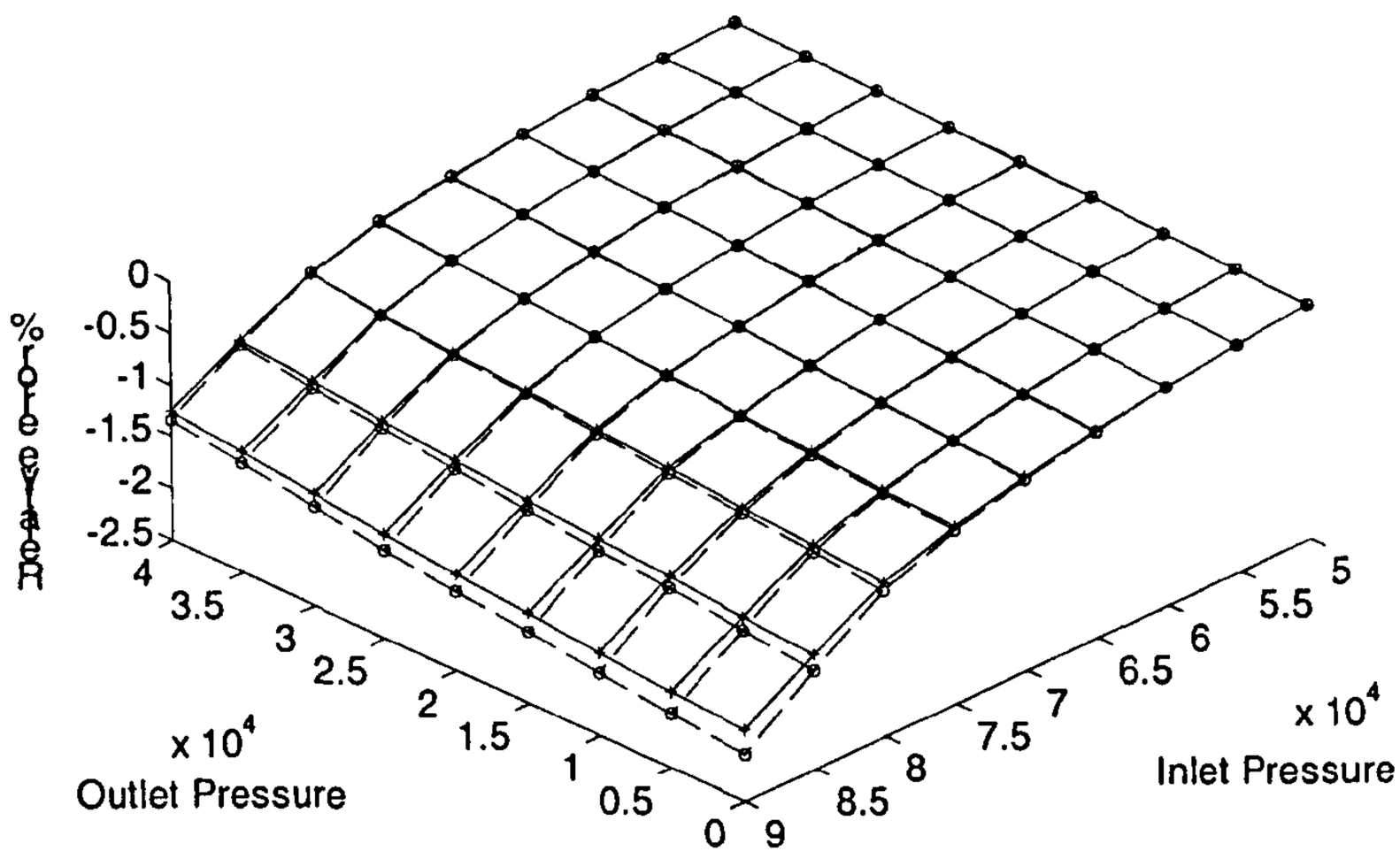

Figure 5.15 – Relative error between pressure gradients at the flow front from the 10 node simulation and the 1000 node simulation.

As with the analytical based solution, the fluid pressure field is well approximated by the 10 node simulations. This good agreement between the 10 node and the 1000 node simulations is important for FE/CV simulations as the method requires a new fluid pressure field at each time step which is obtained with a changing number of nodes (only those in the filled portion of the mould).

5.5 TWO AND THREE DIMENSIONAL MODELLING

5.5.1 Flat plaques

Having established the 1D VI modelling capabilities of LIMS, and recognizing that the same principles apply in 2D flow, it now becomes possible to model complex geometries. A pressure field in a nearly complete flat plaque is shown in Figure 5.16. The VI injection, on a square mesh with 525 nodes and 480 compliant 2D shell elements, was modelled with two gates (nodes with coordinates (0,0) and (0.8,0)), which can be identified as the points of highest pressure. The material compaction properties reflect those of six layers of NCS stitched bi-directional (Robitaille *et al*, 1999. Table 2.2) for a viscosity value of $\mu = 0.2\ Pa.s$ and an assumed Kozeny constant of $k = 5\text{x}10^{-11}\ m^2$. The results shown are illustrative of the properties of flow in VI.

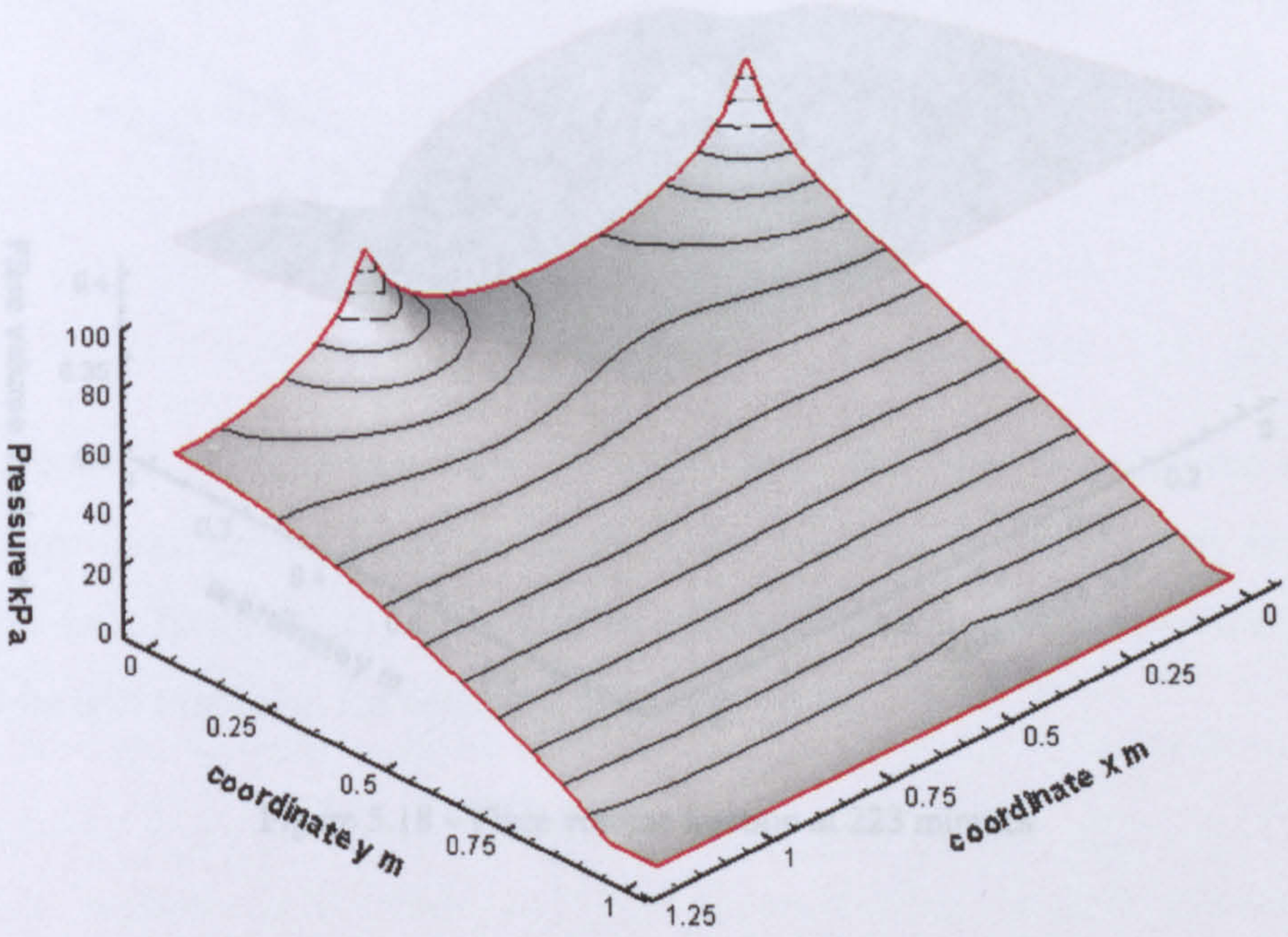

Figure 5.16 – VI pressure field at 223 minutes (50 nodes empty)

A better understanding of the relevance of the above pressure field is shown, by comparison with RTM. Figure 5.17 represents the difference between the local pressure results of RTM and VI models.

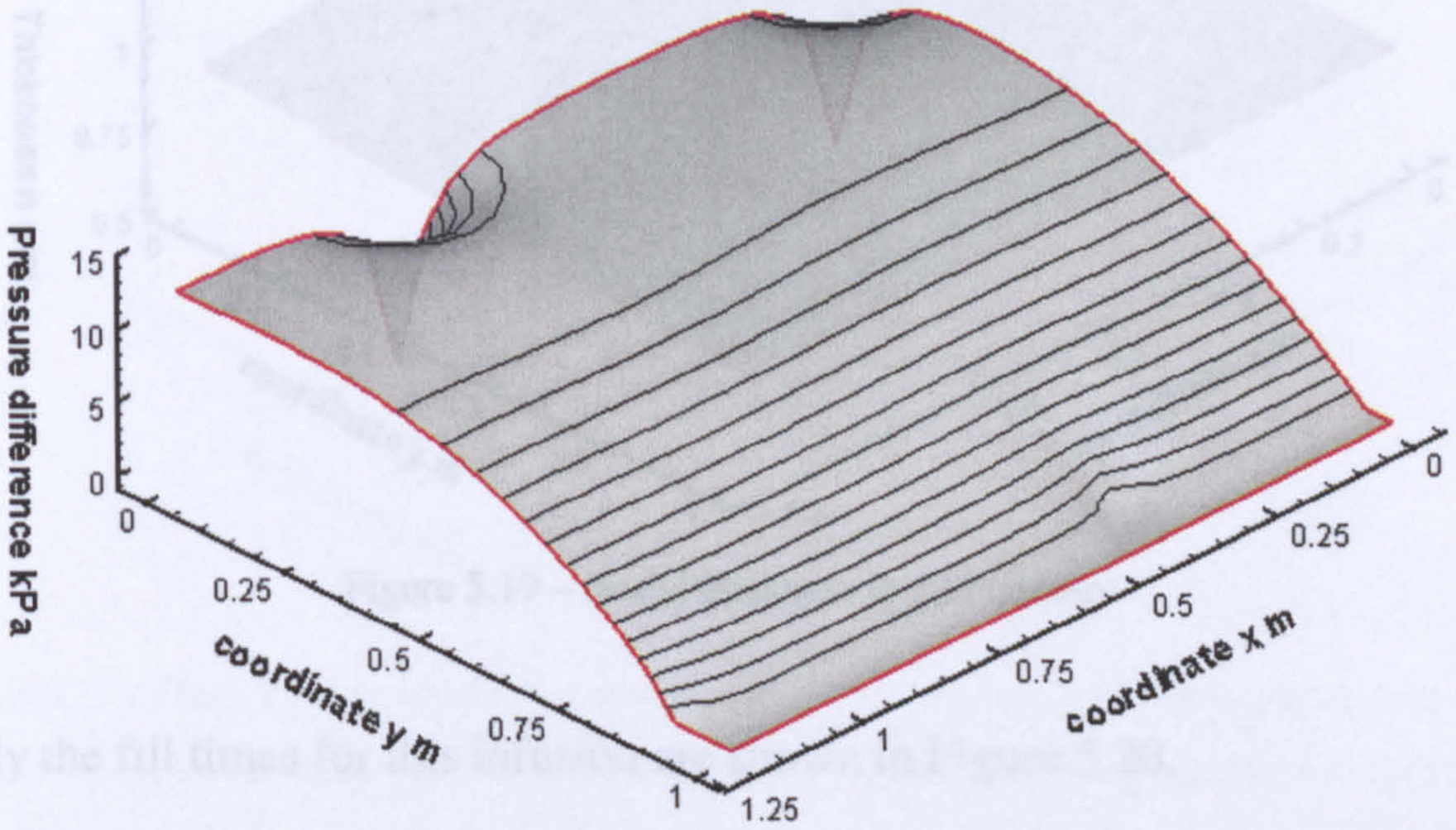

Figure 5.17 – Nodal pressure difference between VI and RTM at 223 minutes

Not that, as discussed, these pressure differences are due to the compliance of the porous medium. Figure 5.18 and Figure 5.19 show the resulting fibre volume fraction and thickness in the square plate.

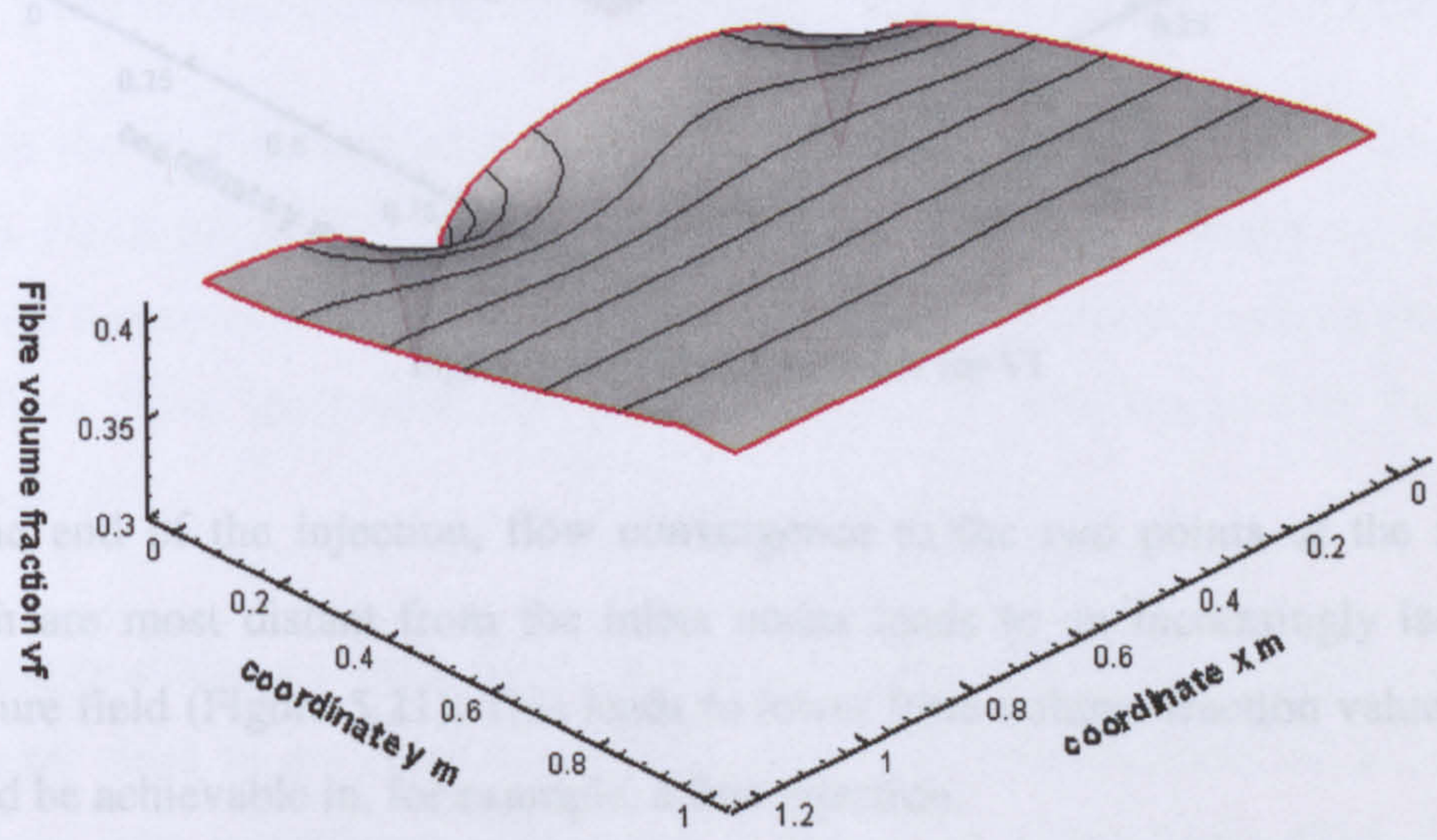

Figure 5.18 – Fibre volume fraction at 223 minutes

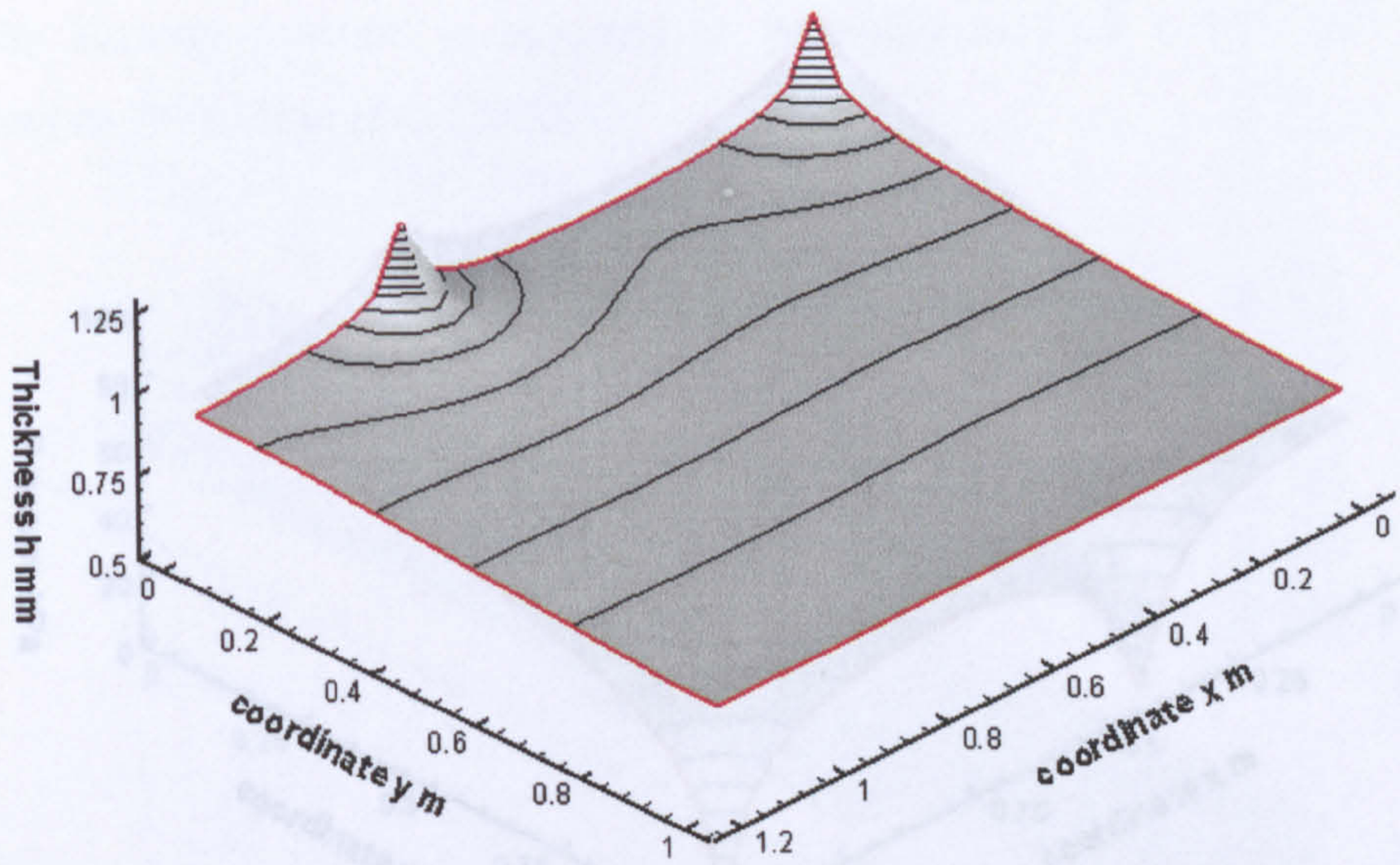

Figure 5.19 – Nodal thickness at 223 minutes

Finally the fill times for this infusion are shown in Figure 5.20.

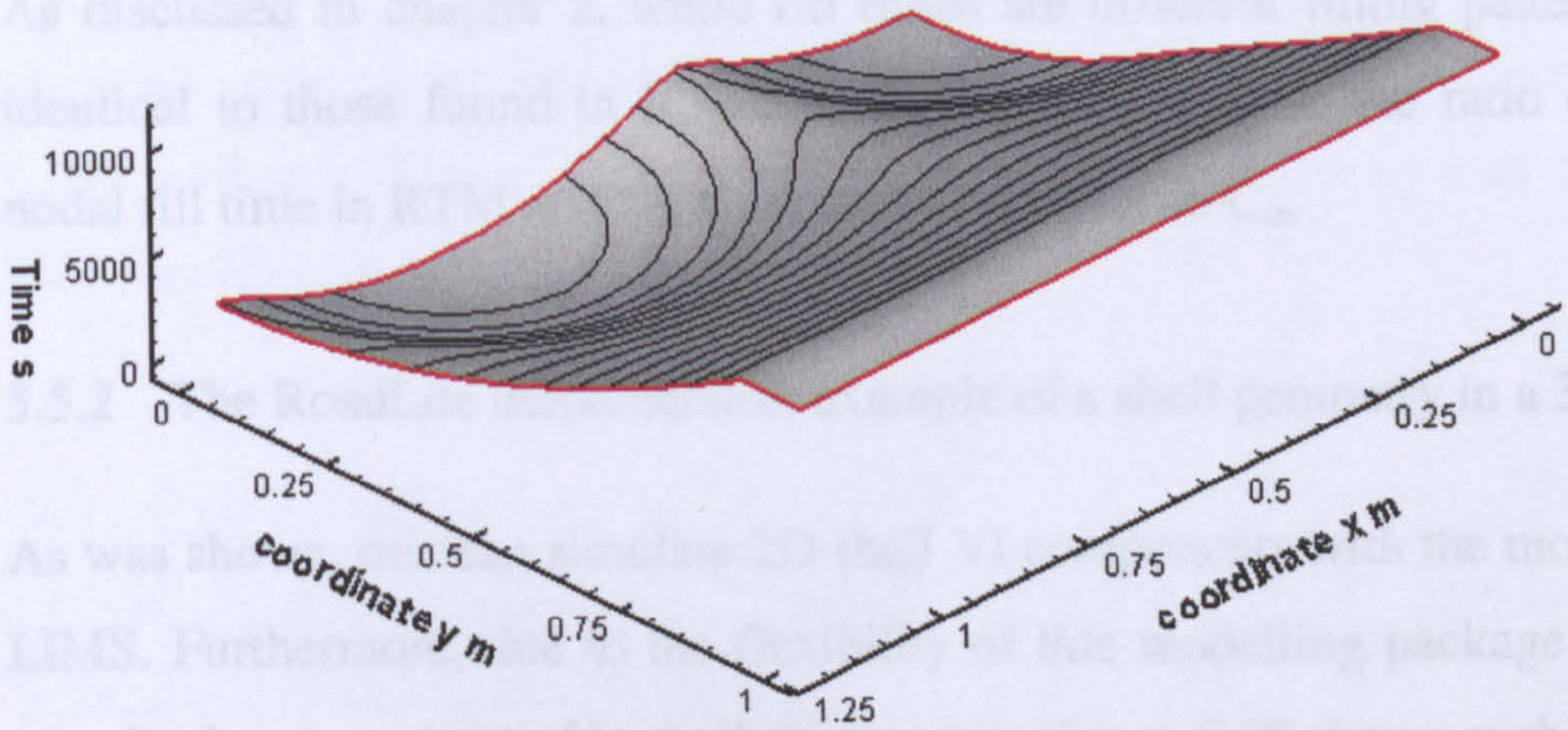

Figure 5.20 –Fill time at nodes for VI

At the end of the injection, flow convergence to the two points of the mould which are most distant from the inlets nodes leads to an increasingly isostatic pressure field (Figure 5.21). This leads to lower fibre volume fraction values than would be achievable in, for example, a line injection.

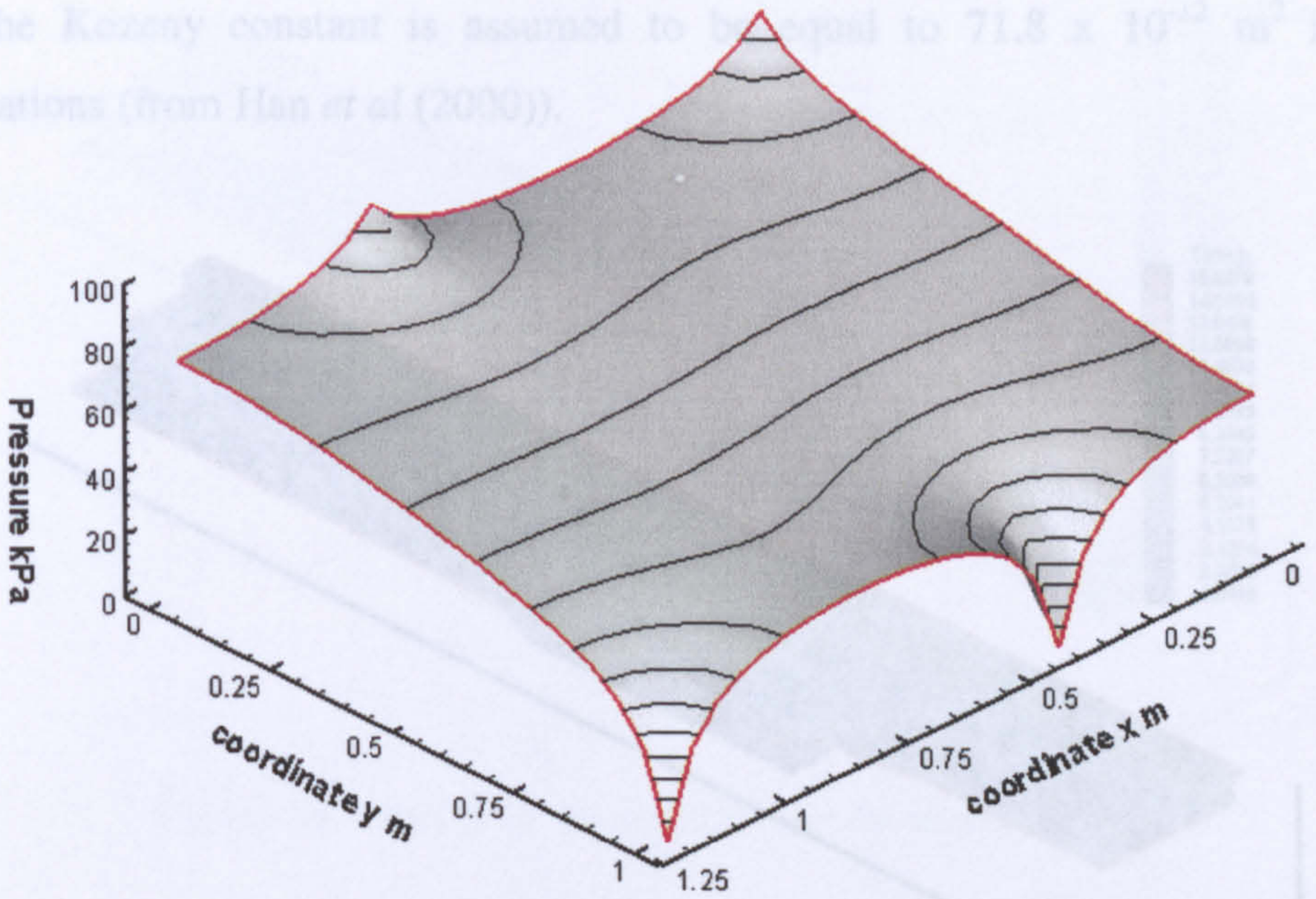

Figure 5.21 – Final VI pressure field showing a rapid convergence towards the two points of the mould which are most distant from the inlets (due to no-flow boundary condition at the mould edge)

As discussed in chapter 2, while fill times are different filling patterns must be identical to those found in RTM. This happens because the ratio of predicted nodal fill time in RTM and VI is constant and equal to C_α.

5.5.2 The RoadLite demonstrator: example of a shell geometry in a 3D space

As was shown, one can simulate 2D shell VI components with the modelling code LIMS. Furthermore, due to the flexibility of this modelling package the analysis can also be expanded to 3D shell geometries. Figure 5.22 shows such an example: the flow front isochrones for a 9 x 2.6 m VI simulation: the RoadLite demonstrator.

The figure shows a symmetric section of the trailer being injected from a central line (left side) to the outer edge (right side). The mesh consists of 1124 shell elements with compliance given equal to that of 12 layers of the FGE material discussed in chapter 3. Boundary conditions at the vent (upper right side of Figure 5.22) are constant outlet pressure of 0 kPa imposed on all nodes on that edge and at the gates 1 bar inlet pressure (all nodes on the left side). Viscosity is 120 mPa.s

and the Kozeny constant is assumed to be equal to 71.8 x 10^{-12} m^2 in all orientations (from Han *et al* (2000)).

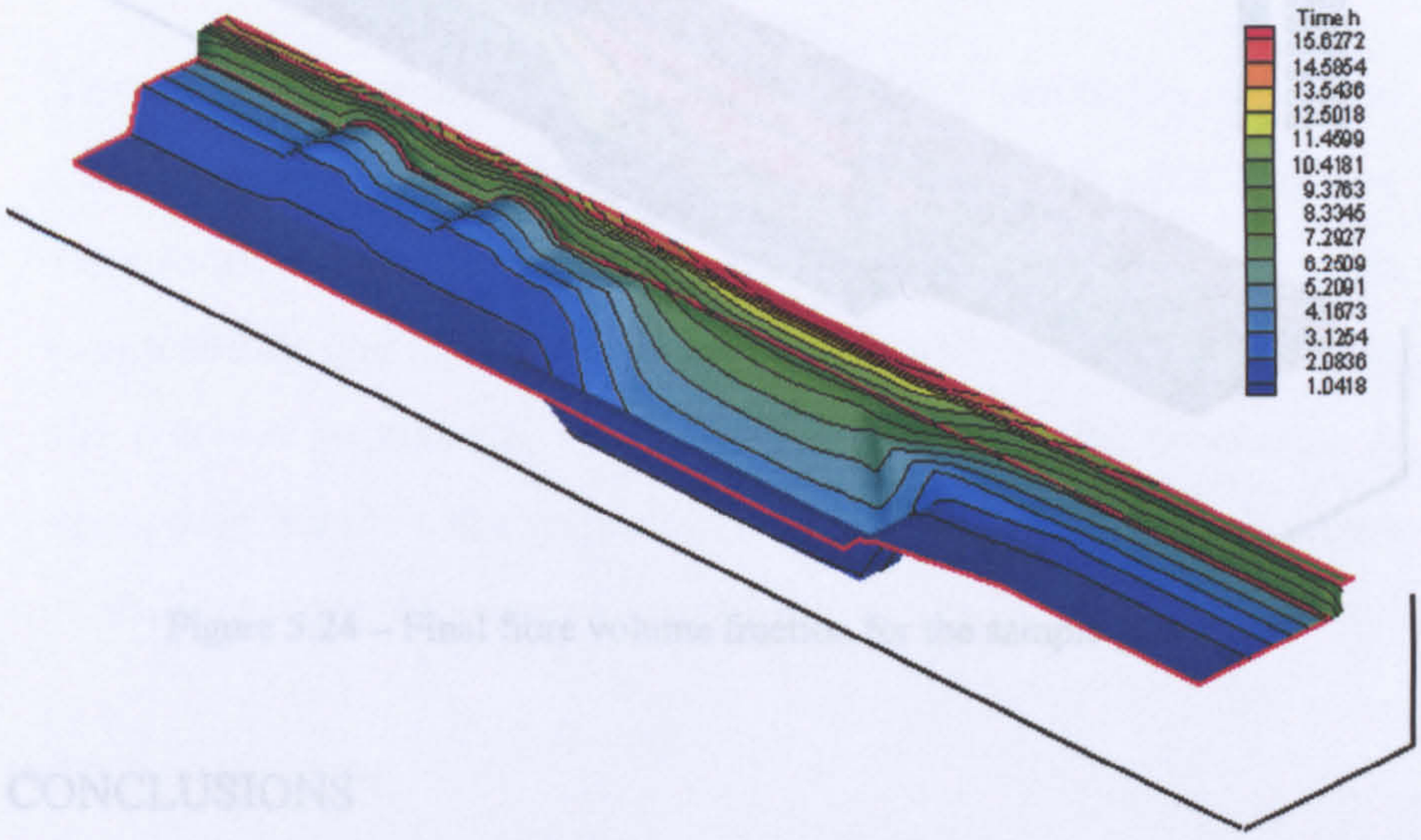

Figure 5.22 – Final fill time for a trailer consisting of a constant number of FGE layers (no DM)

Using the LIMS-VI software it is not only possible to calculate fill times in complex components but also their mass, through a correct estimate of the final panel thickness (Figure 5.23), and mechanical properties from final fibre volume fractions (Figure 5.24).

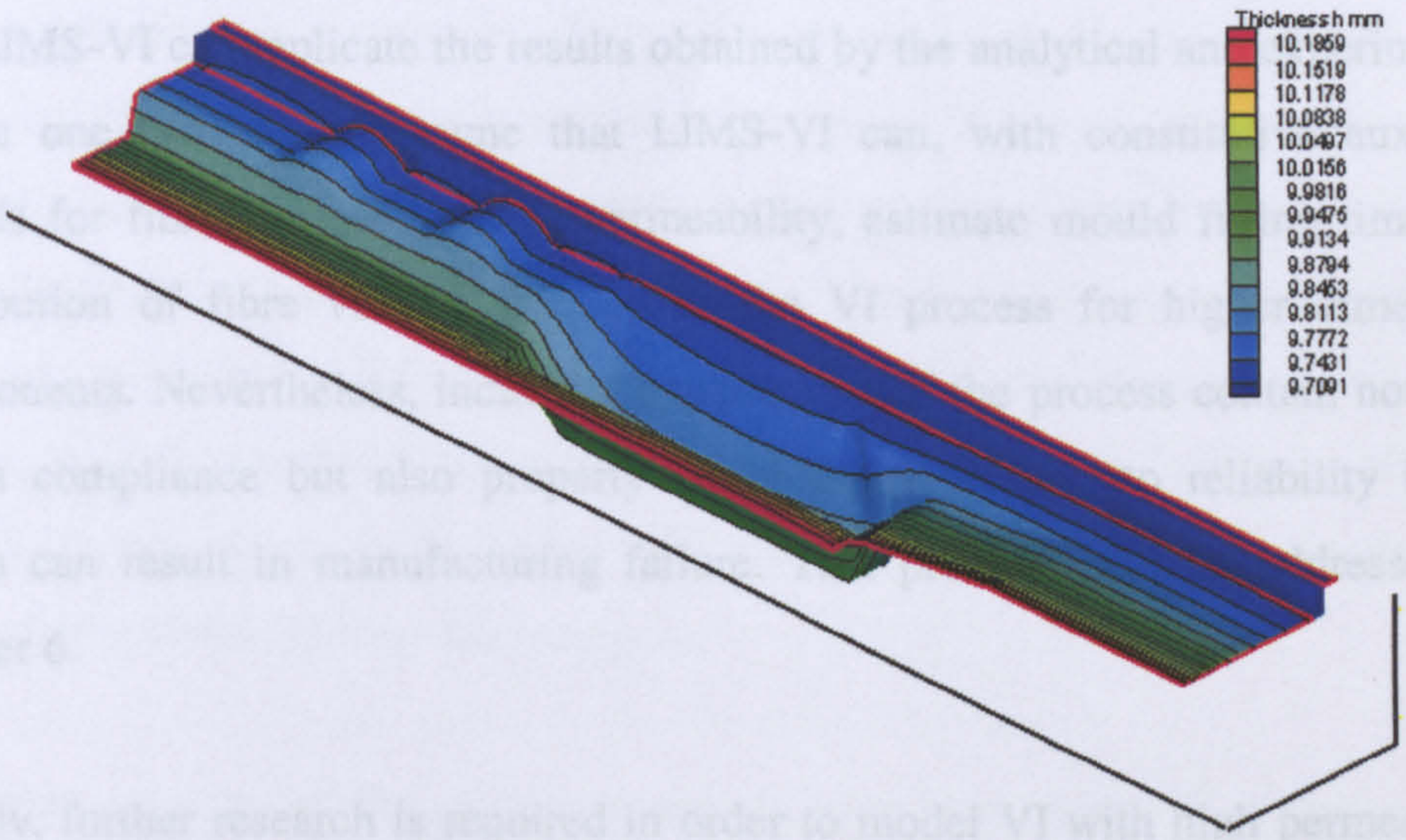

Figure 5.23 – Final thickness distribution in a VI simulation of a composite semi-trailer infusion

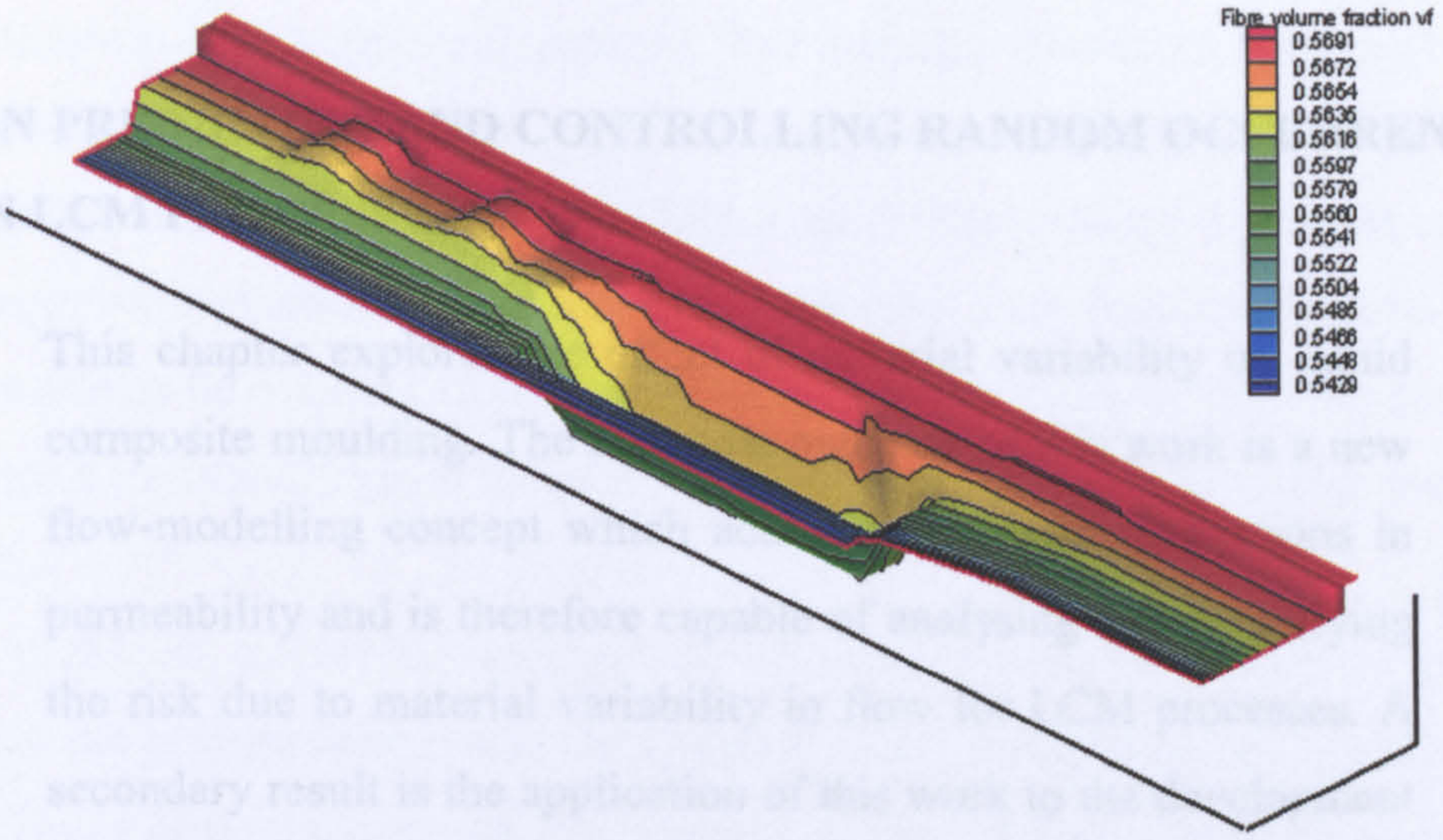

Figure 5.24 – Final fibre volume fraction for the sample geometry

5.6 CONCLUSIONS

A new numerical approach was developed for VI employing the liquid injection moulding simulation (LIMS) software and its scripting capability in LBASIC. A comparison with 1D analytical based prediction of pressure was established. Such a comparison applies also to fill time and properties such as permeability and thickness, since all of these are pressure dependent. The results of the experimental study were shown to substantiate both the necessity of understanding VI's differences and the results of the modelling. By establishing that LIMS-VI can replicate the results obtained by the analytical and experimental results one can safely assume that LIMS-VI can, with constitutive auxiliary models for fibre compaction and permeability, estimate mould filling time and distribution of fibre volume fraction in the VI process for higher dimension components. Nevertheless, industrial applications of the process contain not only media compliance but also property variability – leading to reliability issues which can result in manufacturing failure. This problem will be addressed by chapter 6.

Clearly, further research is required in order to model VI with high permeability media. Some concepts of how this can be achieved are discussed in chapter 7.

6 ON PREDICTING AND CONTROLLING RANDOM OCCURRENCES IN LCM PROCESSES.

This chapter explores the effect of material variability on liquid composite moulding. The foremost outcome of this work is a new flow-modelling concept which accounts for natural variations in permeability and is therefore capable of analysing and quantifying the risk due to material variability in flow for LCM processes. A secondary result is the application of this work to the development of on-line control tools as a way of improving industrial reliability.

6.1 INTRODUCTION

Modelling real flow through porous media is statistical in essence. As is commonly accepted and was shown in chapter 3, compaction properties of textile reinforcements vary. It is also known that permeability exhibits a statistical nature, although these and other sources of injection risk are not normally taken into account. This chapter will discuss how these and other variations can be addressed through simulation. The approach followed is based on the Monte-Carlo method which is described in detail but, insofar as this work is concerned, can be outlined as a method which involves the repeated simulation of the same case with different statistically generated properties. The main outcomes are the probabilities of specific flow occurrences such as final filling points, times and expected deviations from the ideal scenarios. These are used to characterize the efficiency of different filling strategies and applied to the concept of real flow control. It is shown that ideal simulations of flow can overlook filling problems and, while sensible strategies can be used to avoid them, some might also result in longer filling times then are necessary.

Variations in permeability of reinforcements have been observed experimentally by several researchers. These are expected to promote differences in fill time, flowfront perturbations, and incomplete mould filling. The same can be said for fibre angle or surface density of textiles for example. Nevertheless, these properties are normally averaged in standard simulations, involving a

simplification of the physical process. For industry however, failures due to natural variations can be critical, especially in large series of components, or when each component is associated with a high cost. While sensible strategies can be used to prevent problems, they are often associated with operator expertise and can sometimes be overlooked in the design stages. The ability to quantify possible flow errors statistically could therefore be used as a manufacturing-design tool.

Some problems cannot be designed-out. Computer assisted design of control schemes can only be done if one can understand and simulate natural variations in flow. The global objective of this chapter is then to examine some scenarios where flow modelling, monitoring and control can be used to advantage to address some of the real-world difficulties.

6.2 LITERATURE REVIEW

6.2.1 The influence of race tracking and draping on permeability

Most background literature on statistical variations in flow deals with the problem of race tracking (RT). Simply put, it is not possible to ensure that the cutting of textile reinforcements or their placement in moulds is perfect (although there are techniques to avoid race-tracking by pinching reinforcements around the edges of the mould). This fact gives rise to unpredictable channels around the edges of the mould leading to variations in flow patterns. Flow must therefore be controlled in order to achieve consistent production and prevent filling problems. One can break down the problem into four main issues:

1. Experimental characterization of race tracking channels.
2. Modelling the effect of race tracking channels on flow.
3. Development of control strategies to circumvent flow variations.
4. Implementation of monitoring and control hardware.

The literature combines the first two by focussing on the development of models to reproduce experimental flow disturbances. The objective is to obtain an equivalent permeability value which represents open channel flow as flow through porous media. Once this is known one can then model race tracking in standard

Darcy flow FE/CV packages. The literature identifies two relevant parameters for this study, the bulk permeability of the reinforcement and the equivalent Darcy permeability of the open channel. The first is simply modelled through Equation (6.1).

$$K_{Bulk} = \phi \cdot \mu \cdot \left(\frac{dP}{dt}\right)^{-1} \cdot \left(\frac{Q}{A}\right)^{2} \tag{6.1}$$

The second parameter requires significant flow modelling. In 1997 Hammami *et al* compare two possible race tracking models: circular channel flow (Poiseuille flow) and a derivation of Navier-Stokes for an infinite planar gap. While they conclude that the models are appropriate for some cases, their work shows dissimilar results for the retrofit Darcy simulations of experiments and the predicted values in both approaches. They point out that the reason for this can be the perturbation induced by transverse flow into the preform but the work by Bickerton *et al* (1999) using a Stokes flow on a rectangular channel is able to approximate the experiments appropriately, especially in terms of flow front shape.

These channel models are implemented enabling efficient, automated detection and control of real cases, by optimizing the number of sensors, and designing adequate control actions to steer flow fronts towards desired scenarios. Several approaches have been proposed for flow front data acquisition, from optimization of point sensor number and location through genetic algorithms (Mathur *et al,* 1999) further developed and implemented in LIMS through the streamlined inteligent RTM processing SLIC routine (Hsiao *et al*, 2002) to image acquisition in Nielsen *et al* (2002). Clearly image acquisition is not adequate for RTM because of transparent mould requirements. Nevertheless, for the same reason, it is compatible with the VI set-up (with limitations, e.g. opaque cores).

Table 6.1 shows the gap values which are considered in Devillard *et al* (2003). Note that equal probabilities are assigned to the different gap magnitudes and the modelling approach consists of running a full factorial array of possible combinations of gaps magnitudes on all available edges.

Table 6.1 – Race tracking (RT) intensity vs. gap magnitude. Devillard *et al* (2003)

Description	Gap (mm)
Very low RT (almost unavoidable)	0.02
Low RT	0.10
Medium RT	0.50
Strong RT	1.00
Very strong RT	1.60

A number of other factors can also influence permeability in flow through porous media. For instance, experimental work by Rudd *et al* (1996), Smith *et al* (1997) explores the effect of textile draping on the permeability tensor and mechanical properties of resulting laminates. As with most results found in the literature, these present a degree of scatter. However, the statistical nature of flow or mechanical properties is not explored since work focussed on the fundamentals of average behaviour. Rudd *et al* (1995), Lai *et al* (*1999*) and Long *et al* (2002) are examples of modelling approaches for draping, and of the draping effects on permeability, again, not investigating the nature of statistical variations as a possible origin of flow disturbance.

However, one must acknowledge that there is a significant understanding of race-tracking and draped permeability. The remaining issue is that real reinforcements present property variations of a statistical nature due, for example, to handling or textile manufacturing influence in architecture and orientation. These variability issues (and the locations where they typically occur) are illustrated in Figure 6.1.

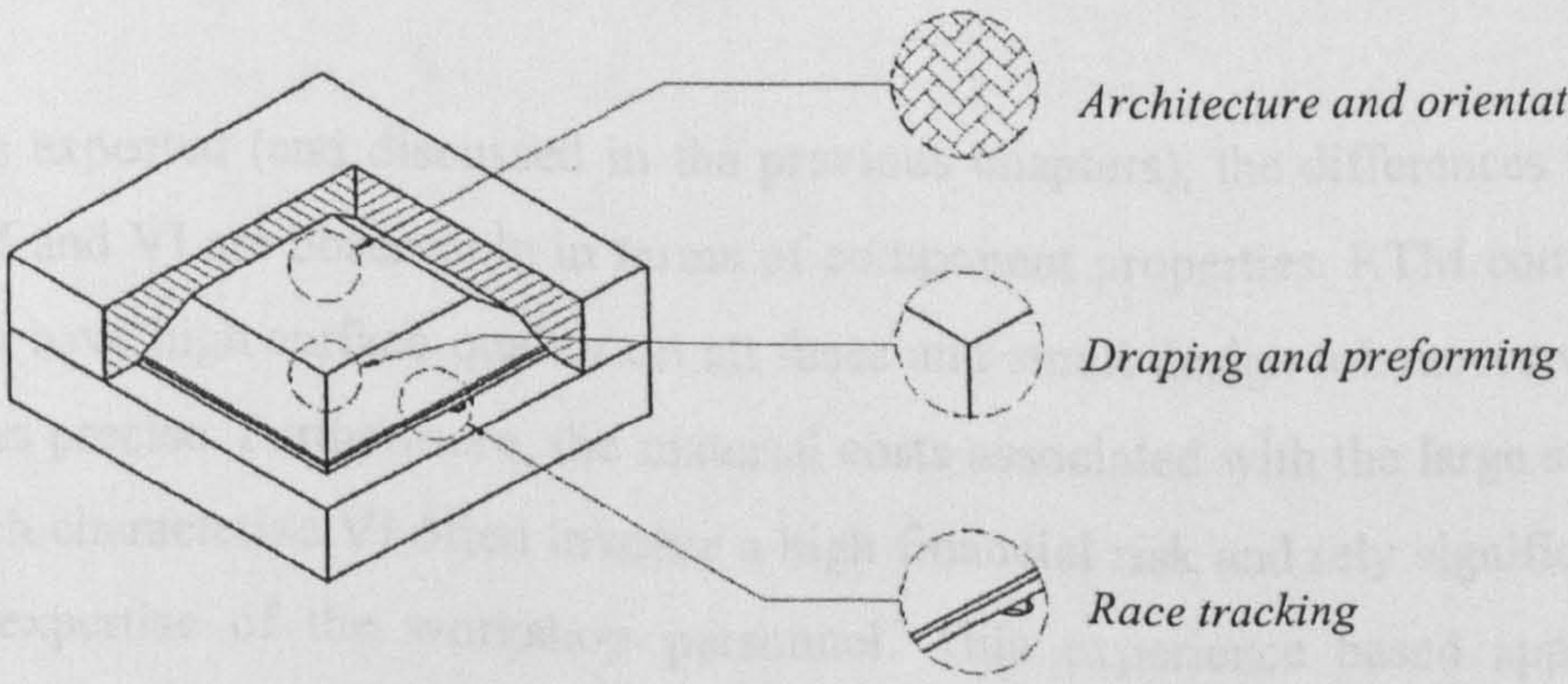

Figure 6.1 – Locations where different types of flow variability can originate

Note that in the present modelling literature the first two factors are deterministic: models of textile mechanics are used to determine nominal fibre orientation and fibre volume fraction values as a function of idealized textile architecture and mould geometry. This is not the case in recent race tracking studies where the stochastic nature of channel formation is integrated in the analysis. Nevertheless, recent experimental work has shown that local permeability is also of a statistical nature. This is discussed in the next section. Note also that the work presented here will not discuss the evaluation of published control strategies but will address techniques to virtually design and test control strategies – not the strategies themselves but a method of developing and testing strategies.

6.2.2 Permeability variation

As Gauvin *et al* (1996) summarise, while simulation software is extremely useful for flow design and optimization, the input parameters are crucial to their accuracy. From these, permeability is extremely difficult to characterize and reported permeability values for the same materials can present significant discrepancies. They highlight that flow rate and pressure, the nature of the fluid and cavity stiffness can affect the results strongly. In VI however, one can control or model these factors, the most complex being the mould and reinforcement compliance issue which chapter 2 explores. The same authors also point out the importance of reinforcement manufacturing and handling in their listing of possible causes for flow variability. Clearly, unlike the previous factors, it is not possible to control these. Thus, it becomes impossible to insure repeatability.

As is expected (and discussed in the previous chapters), the differences between RTM and VI are observable in terms of component properties. RTM components often have high surface quality on all faces and small design tolerances while VI is less precise. Furthermore, the material costs associated with the large structures which characterize VI often involve a high financial risk and rely significantly on the expertise of the workshop personnel. This experience based approach is sometimes complemented with flow modelling, under the assumption that compliance of the medium can be ignored. Not only are the output properties of these processes different, they are directly influenced by preform properties and

mould/gate design. Due to its flow dependent cavity thickness, VI may be subject to a higher degree of flow variability than that observed in RTM.

One significant source of property variations is reinforcement permeability, which, as Bickerton *et al* (1999), Pan *et al* (2000) and Hoes *et al* (2002) propose, is not a constant value but follows a statistical distribution. Consequently, flow in VI, as well as RTM, does not follow exactly the ideal case but presents variations due to the statistical nature of the flow properties in the preform. These references are currently the main source of statistical permeability characterization data and their results are summarized in Table 6.2.

Table 6.2 – Statistical permeability data by Bickerton *et al* (1999), Pan *et al* (2000) and Hoes *et al* (2002). Permeability data and key to the materials used

Bickerton *et al* (1999)

Matl.	v_f %	Orient.	Mean m^2	Median m^2	σ / mean %
B1	5.9	-	2.12×10^{-8}	-	17.9
	17.6	-	2.67×10^{-9}	-	8.6
	29.3	-	7.11×10^{-10}	-	11.4
B2	8.3	-	4.19×10^{-9}	-	5.8
	16.5	-	1.21×10^{-9}	-	3.7
	24.8	-	5.63×10^{-10}	-	5.7

Pan *et al* (2000)

Matl.	v_f %	Orient.	Mean m^2	Median m^2	σ / mean %
P1	-	-	2.96×10^{-10}	2.97×10^{-10}	6.1
P2	-	-	1.30×10^{-10}	1.27×10^{-10}	13.1

Hoes *et al* (2002)

Matl.	v_f %	Orient.	Mean m^2	Median m^2	σ / mean %
H1	-	Kx	1.43×10^{-10}	-	21.0
	-	Ky	1.79×10^{-10}	-	22.2
	-	$\ln(K_x/K_y)$	0.1 -		σ = 0.13
H2	-	x	1.23×10^{-11}	-	14.1
	-	y	2.62×10^{-11}	-	21.7
	-	$\ln(K_x/K_y)$	0.32 -	-	σ = 0.08
H3	-	x	1.49×10^{-10}	-	23.9
	-	y	1.34×10^{-10}	-	12.1
	-	$\ln(K_x/K_y)$	-0.06 -	-	σ = 0.11
H4	-	x	1.32×10^{-10}	-	8.70
	-	y	2.02×10^{-10}	-	9.90
	-	$\ln(K_x/K_y)$	0.19 -	-	σ = 0.01

Code	Type	Material	Manuf.	Ref.	No. of tests
B1	Random Mat	Glass	-	-	-
B2	Scotchbrite	-	-	-	-
P1	Knitted	Glass	CCP	COFAB A118	30
P2	Woven	Glass	PPG	HWE HTX-180	30
H1	Plain Woven	Glass	Syncoglas	R 420	86
H2	Twill Woven	Glass	Syncoglas	RE 144/255	87
H3	Basket Woven	Glass + PVC coating	Helioscreen	Natte 2115	86
H4	Basket Woven - Stiched layers	Glass + PVC coating	Helioscreen	Natte 2115	28

Note that variability in RTM is only dependent on effective permeability and porosity of the reinforcement while variability in VI depends also on compaction properties. As was discussed in chapter 3, these properties are also not constant and the hypothesis that they follow normal distributions in terms of local textile density cannot be disproved. This chapter, in line with the available references (Bickerton *et al* (1999), Pan *et al* (2000) and Hoes *et al* (2002)) also assumes that permeability follows a normal distribution. The evidence substantiating this assumption is not conclusive and requires further investigation and statistical

demonstration: the only demonstration provided in these references is that, in most cases, the resulting histograms appear to follow a Gaussian curve. The statistical analysis reported by Pan *et al* (2000) concludes that the probability distributions of permeability of their textiles followed normal distributions. This is claimed through the positive results of the Kolmogorov-Smirnov (K-S) test on the results from 30 repeats on each material. These tests were positive for both data sets. Nevertheless, the Kolmogorov-Smirnov test is an inaccurate test since it requires that the probability density function (PDF) be predetermined (not estimated from the data). To test a data set against a normal distribution without specifying the parameters, the Lilliefors test (mentioned in Chapter 3) should be used instead (The Mathworks (2002)). In all cases (Bickerton *et al* (1999), Pan *et al* (2000) and Hoes *et al* (2002)) the authors show that the results depend on textile architecture, and, according to the work by Hoes *et al* (2002), layer nesting for oriented fibre textiles.

6.2.3 The Monte-Carlo method

This chapter presents a novel approach to flow modelling through porous media in that it suggests the incorporation of statistical behaviour in what are normally considered constant material properties (which, as was shown, might be an inappropriate assumption (Table 6.2)). The effect of statistically distributed flow properties is studied here through the implementation of a Monte-Carlo method. The method was originally developed to model neutron diffusion at Los Alamos in the 1940s (Kalos *et al,* 1986) and has since been adapted to a host of physical problems. One definition of the method is that it is a technique which makes deliberate use of random numbers in a calculation which has the structure of a stochastic process. This refers to a sequence of states whose evolution is determined by random events (Kalos *et al*, 1986). In the present context Monte-Carlo is therefore a method of studying the effect of statistical variations in permeability, porosity, superficial density or compaction on the statistical outcome (and risk) of manufacturing process and strategy. The application of this technique to model flow through porous media (and flow through compliant porous media) is believed to be novel at the time of writing.

6.3 ON NATURAL VARIABILITY AND LCM FLOW MODELLING

Having established the relevant state of the art, this and the following sections will discuss the areas where the present work has contributed to the field, focussing on the stochastic study of the effects of permeability and compaction variability on flow in LCM. Useful process models should reflect these variations by predicting the distribution in possible outcomes from any moulding process. To model the effects of permeability and compaction variations on flow, predicted or measured distributions in properties must be incorporated in LCM simulations. In the present work, this is achieved by Monte-Carlo FE simulation which involves solving the same geometric problem a significant number of times insuring, each time, that the model contains different element properties (permeability and compaction). This is achieved by generating properties, by random selection from the relevant inverse PDF, thereby resulting in them being normally distributed across a significant number of elements replicating experimental measurements and making all resulting models different and non-ideal. Figure 6.2 shows this element property determination procedure. The algorithm used to produce the inverse PDF from the base normal distribution parameters was a mini-max approximation by rational functions which is then refined using Halley's rational method to achieve full machine precision. The procedure (derived from work by Peter J. Acklam (2000)) is shown in Appendix 6.C.2 in the LTQNORM function listing.

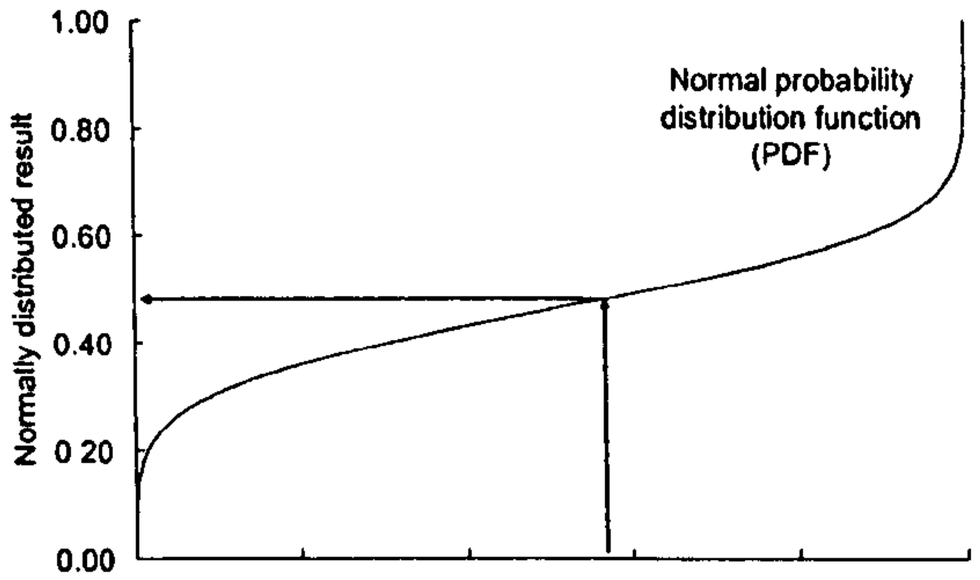

Figure 6.2 – Element property determination procedure: normally distributed properties are obtained as a function of a randomly generated number ranging from zero to one and of the experimental PDF

This procedure is repeated for all elements within the model: each will have a different permeability tensor and/or compaction properties, but permeabilities over a large number of analyses conform to the experimental normal distribution. The assignment procedure is illustrated in Figure 6.3.

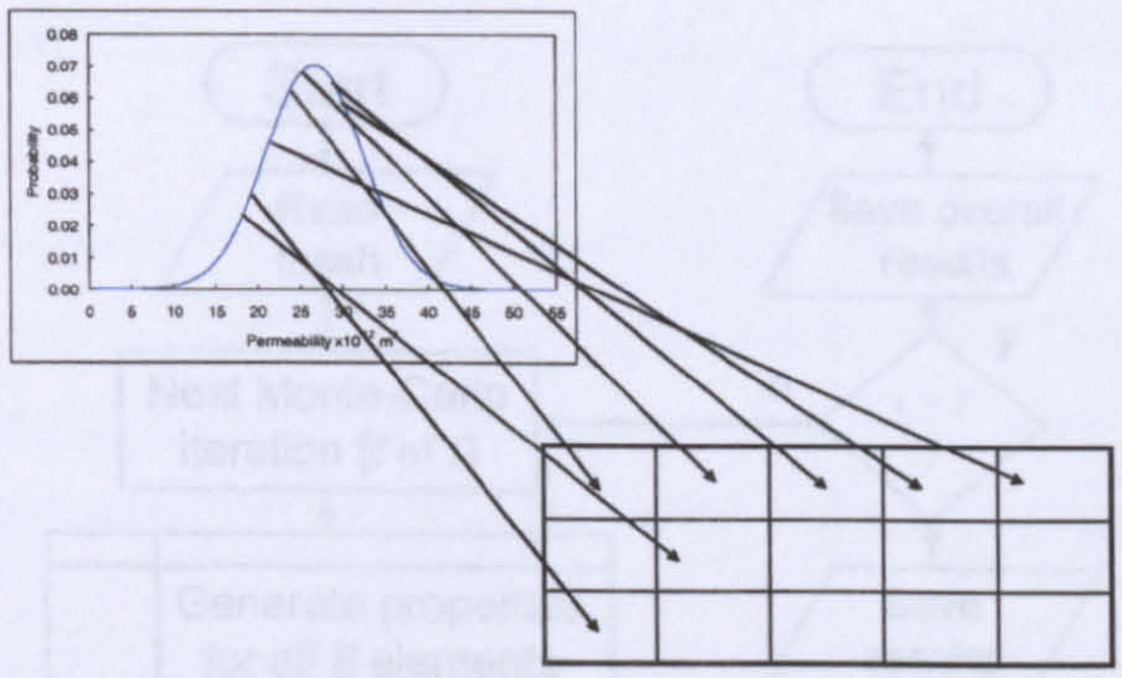

Figure 6.3 – Random assignment of normally distributed permeability to an FE/CV mesh

Input files for these simulations are generated automatically by in-house software (Appendix 6.A). These provide the range of filling patterns that might be expected, and also fill time and last point to fill (guiding gate and vent locations). From this, the likelihood of success for any combination of materials and injection strategy could be determined. To illustrate this, a number of simulations were done for a rectangular plate flow case, locating injection gates at the corners. Figure 6.4 shows four possible filling scenarios, modelled using the Monte-Carlo method. The results represent RTM flow with isotropic permeability data based on the experimental values for material H2 in the *y* direction (Table 6.2).

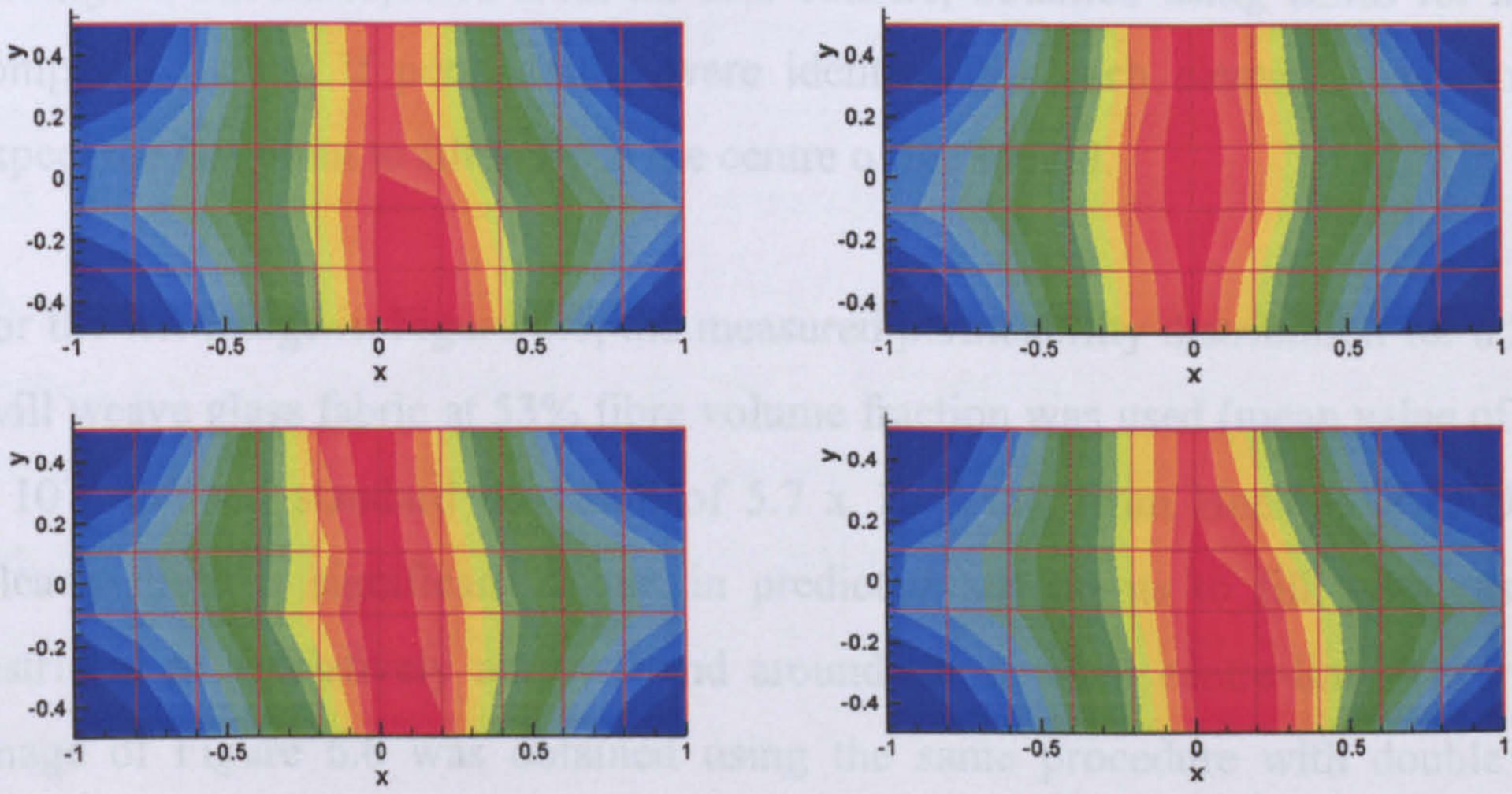

Figure 6.4 – Isochrones for four possible filling scenarios on a rectangular plate filling case, injection at the corners (50 element mesh). Time progression represented by blue-to-red evolution of the isochrones assuming constant porosity

Note that the ideal case would result in a symmetric flow pattern. Figure 6.5 shows the Monte-Carlo algorithm which was implemented.

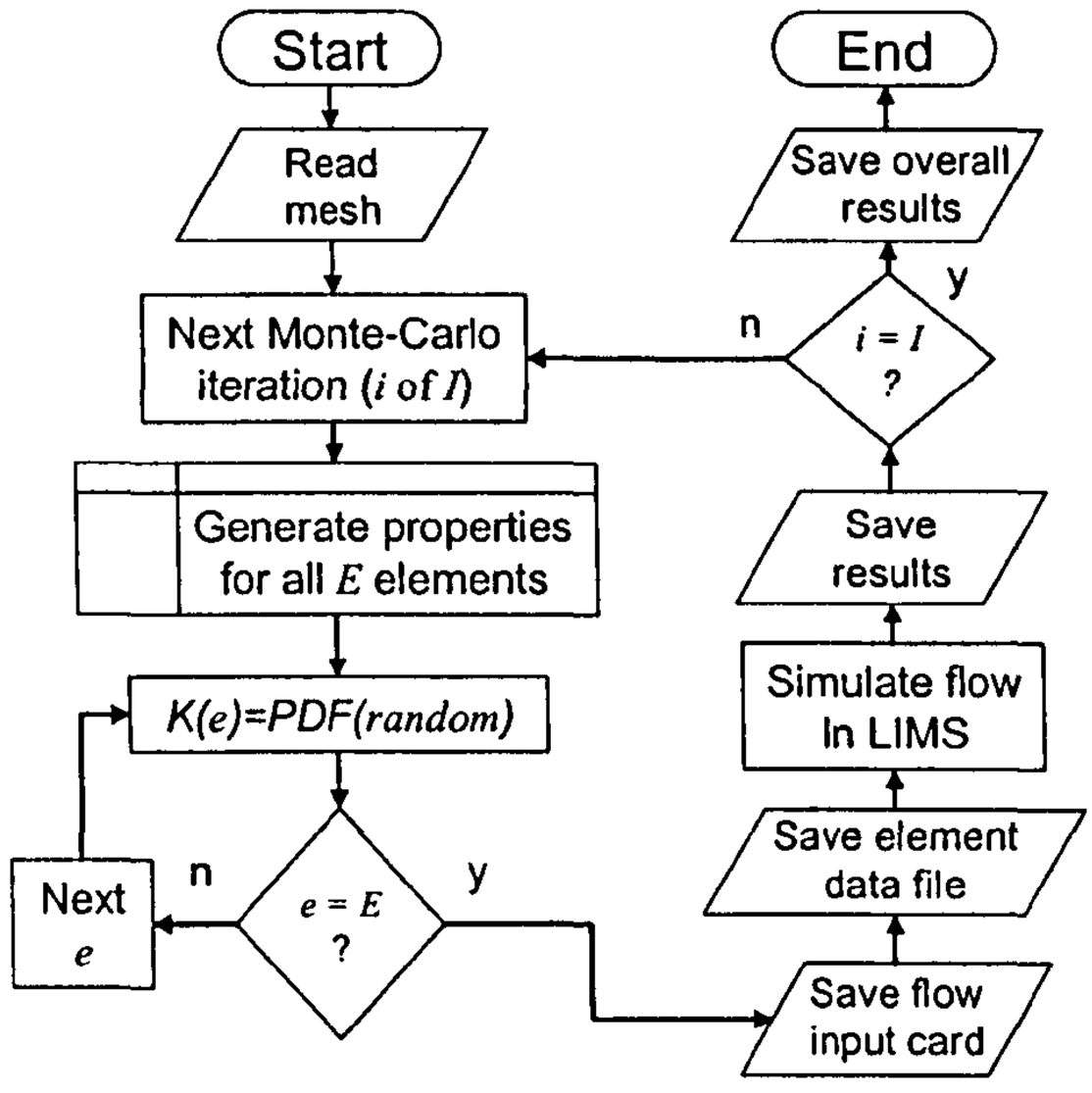

Figure 6.5 – Monte-Carlo algorithm proposed in this chapter. e and E represent the current and total number of elements and i and I the current and total number of iterations

6.4 SIMULATION OF REAL-LIFE (VARIABILITY) IN LCM FLOW

Figure 6.6 illustrates predicted locations for the last point to be filled in a rectangular mould injected from all four corners, obtained using LIMS for non-compliant media. If permeability were identical for each element, one would expect the last point to fill to be in the centre of the mould.

For the left image in Figure 6.6, the measured permeability distribution for a 2x2 twill weave glass fabric at 53% fibre volume fraction was used (mean value of 2.6 x 10^{-11} m^2 and standard deviation of 5.7 x 10^{-12} m^2, from Hoes *et al* (2002)). Clearly there is significant scatter in predicted last points to fill, with results restricted to a relatively narrow band around the vertical centre-line. The right image of Figure 6.6 was obtained using the same procedure with double the standard deviation used for the left image.

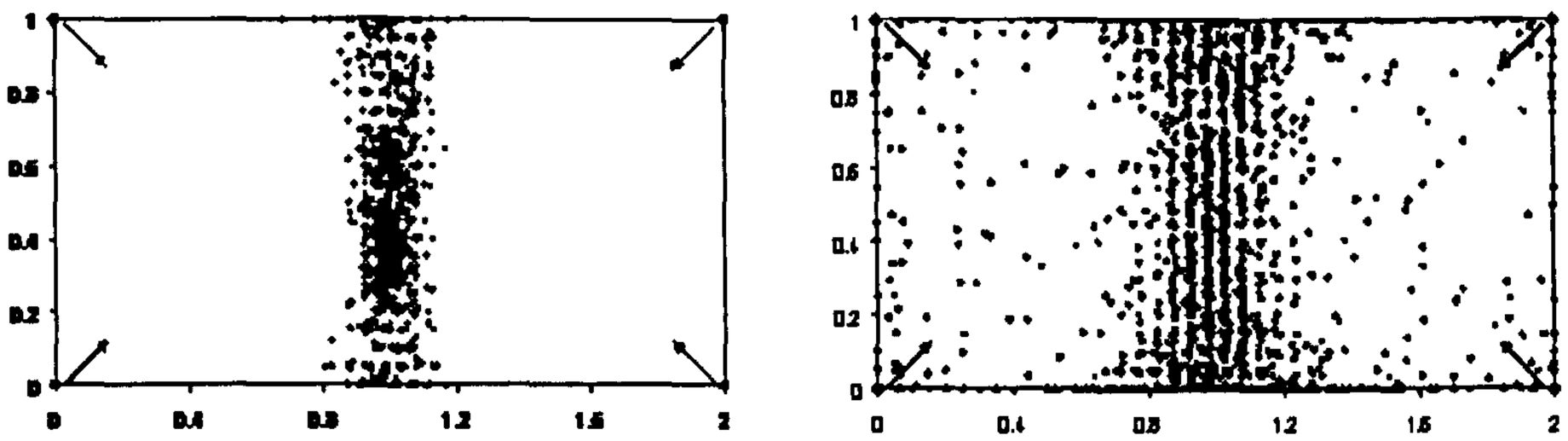

Figure 6.6 – Final points filled in a Monte-Carlo study with 5 000 RTM simulations. Four gate injection scheme (corners). Permeability data from Hoes et al (2002). Left) Standard deviation equal to the reference and right) Standard deviation doubled. Points outside central band are the result of numerical instability due to high variation of properties

Unlike the previous non-compliant case, where the only parameter in the Monte-Carlo study was permeability, there are a number of variables changing concurrently in flow through compliant media. The inclusion of a compliant porous medium requires the systematic variation of at least two of these parameters: surface density and Kozeny constant. All others (fibre volume fraction, thickness, and permeability) can be determined using the auxiliary models discussed in chapter 2 (Equations (2.11) and (2.13)). Accordingly, local values of thickness and fibre volume fraction are a direct function of an assumed surface density distribution.

Figure 6.7 shows a single Monte-Carlo result obtained for flow through a hypothetical compliant medium. The parameters used to generate this porous medium model were obtained from a combination of different experimental data and contains assumptions on most properties: the surface density distribution ($\mu_{\rho surface} = 8.43\ kg \cdot m^{-2}$ and $\sigma_{\rho surface} = 0.47\ kg \cdot m^{-2}$, where μ and σ represent the average and standard deviation) was based on experimental density measurements obtained during the compaction characterization work (chapter 3) for the FGE 117 material. Permeability, while linked to surface density through compaction and permeability models, was also varied through the introduction of a normally distributed Kozeny constant: $\mu_k = 7.18 \times 10^{-11}\ m^2$ and $\sigma_k = 4.36 \times 10^{-12}\ m^2$. These values were chosen in order to have the same permeability distribution as the H2 material described in Hoes *et al* (2002) at a compaction pressure of 100 kPa and assumes a decrease in standard deviation of permeability with increased

compaction pressure (which is only partly substantiated by the work by Bickerton *et al* (1999) on E-glass random mat). The resulting hypothetical material is therefore a combination of compaction and density properties of the FGE reinforcement and the statistical distribution of permeability published by Hoes *et al*.

Using this methodology, the 2D LIMS VI model was used to study a line gate arrangement using a compliant shell element mesh consisting of 800 elements and 861 nodes. The resulting variable permeability and fibre volume fraction and are shown in Figure 6.7. As can be observed, properties are location dependent while simultaneously representing the expected reinforcement variability.

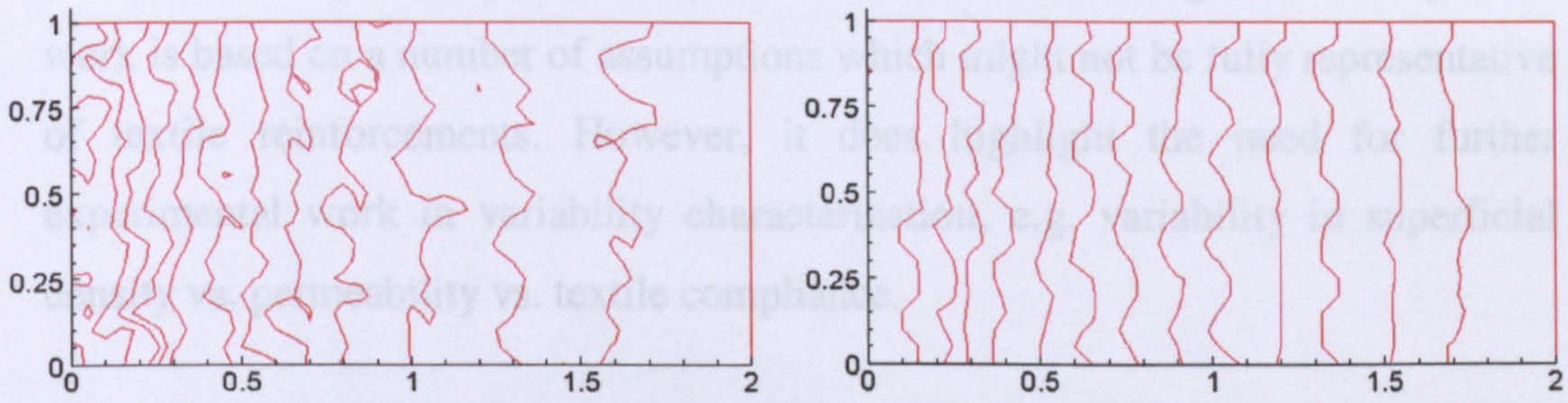

Figure 6.7 – Left) Evolution of permeability. Iso-K lines: 7.75 x 10^{-11} m^2 to 2.2 x 10^{-11} m^2 in 12 divisions. Right) Iso-v_f lines: 40% to 55% in 16 divisions. Note that flow evolves from left (inlet) to right (outlet) and that the mould is full.

Along with permeability and fibre volume fraction, panel thickness is also location dependent. The thickness of this panel is shown in Figure 6.8. The remaining issues concern the number of simulations that one requires for statistical validity and the experimental validation required to substantiate the compaction-permeability relation. The Monte-Carlo method contains techniques to assess the minimum number of trials for a certain confidence interval. In reality, these techniques are best suited for the analysis of simple variables (e.g. how many times should one toss a coin to insure with a certain confidence interval that we understand the behaviour of the entire population). However, the complexity of multivariate systems such as the analysis of flow in VI with complex moulds is not describable by typical algebraic forms found in classical Monte-Carlo. The current confidence assessment methods for complex cases involve techniques such as bootstrapping or analysis of standard error of mean.

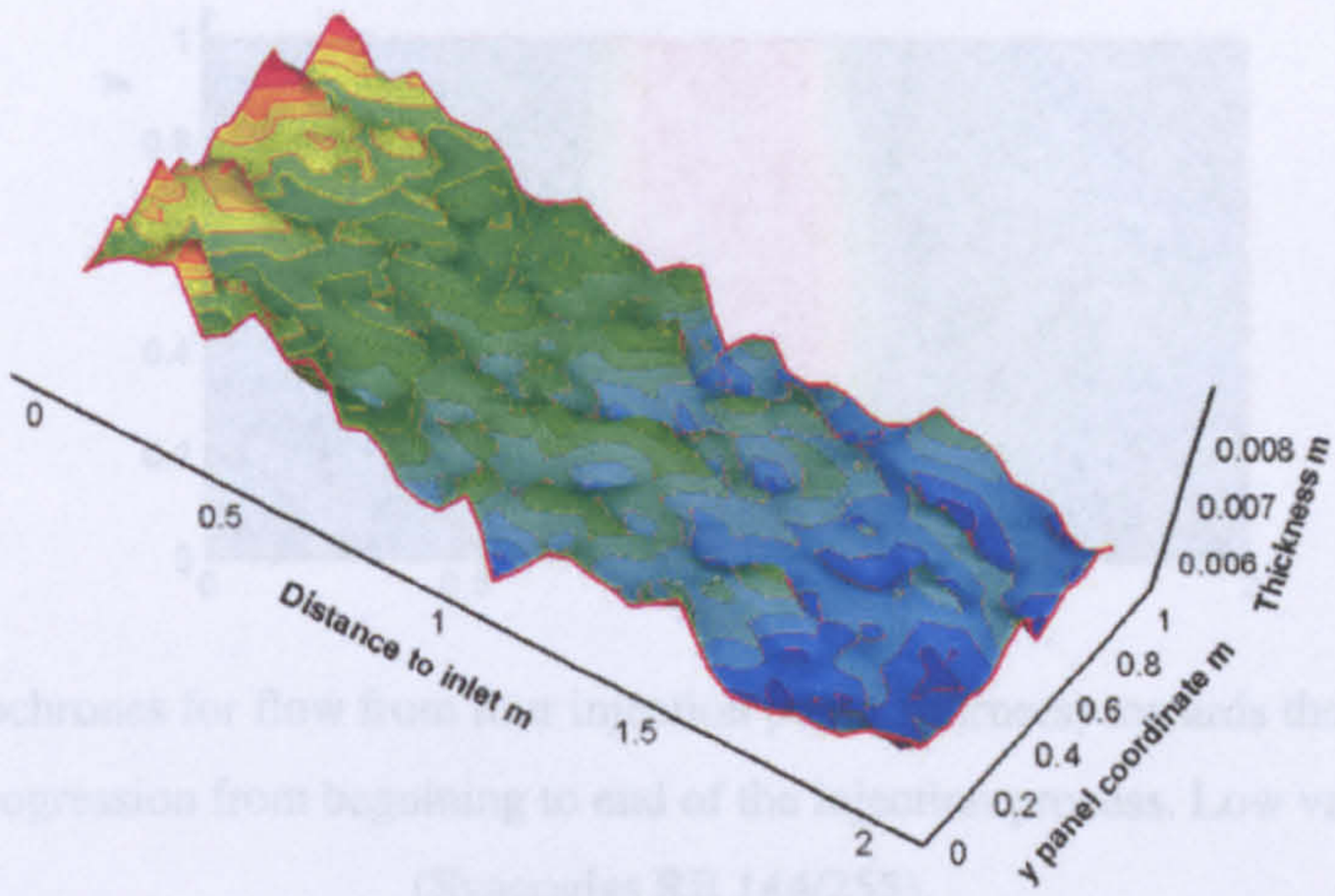

Figure 6.8 – 3D Thickness distribution (x150). Iso-h lines: 8.5 mm to 5.5 mm. Injection from left side ($x = 0$) to right ($x = 2$).

As for the compaction-permeability relation, it is acknowledged that the present work is based on a number of assumptions which might not be fully representative of textile reinforcements. However, it does highlight the need for further experimental work in variability characterization, e.g. variability in superficial density vs. permeability vs. textile compliance.

Having demonstrated the ability to model flow through a naturally variable compliant porous medium, the remaining examples discuss the studies performed on the simpler non-compliant cases.

6.5 GATING STRATEGY ROBUSTNESS

6.5.1 Point gate schemes

The Monte-Carlo method is not only relevant for the generation of variable samples for simulation but, more importantly to the analysis of the statistical outcome of a process. Figure 6.9 represents a quasi-ideal result for the Syncoglas RE 144/255 described in Table 6.2 on an 861 node 800 shell-element mesh.

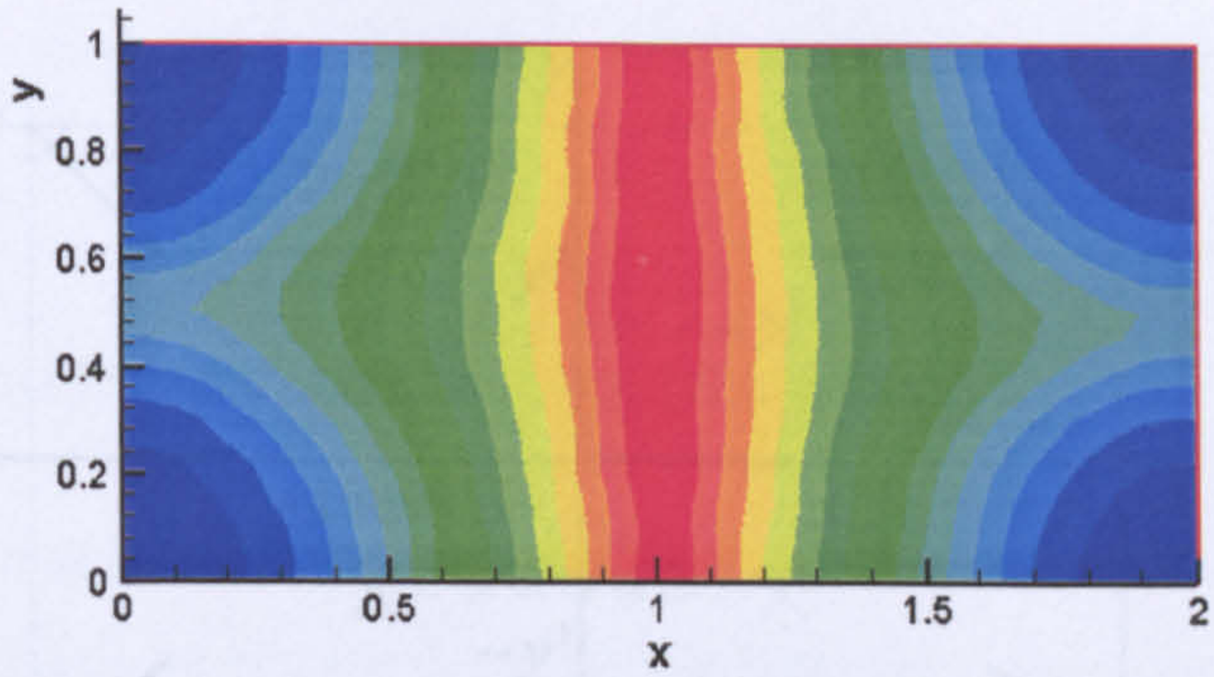

Figure 6.9 - Isochrones for flow from four injection points (corners) towards the center. Blue to red represents progression from beguining to end of the injection process. Low variability example (Syncoglas RE 144/255).

This flow case was studied by batch-running 15,000 simulations, summarizing each as to their final filling position (via cubic interpolation of nodal fill times) which then combined in a frequency map (Figure 6.10).

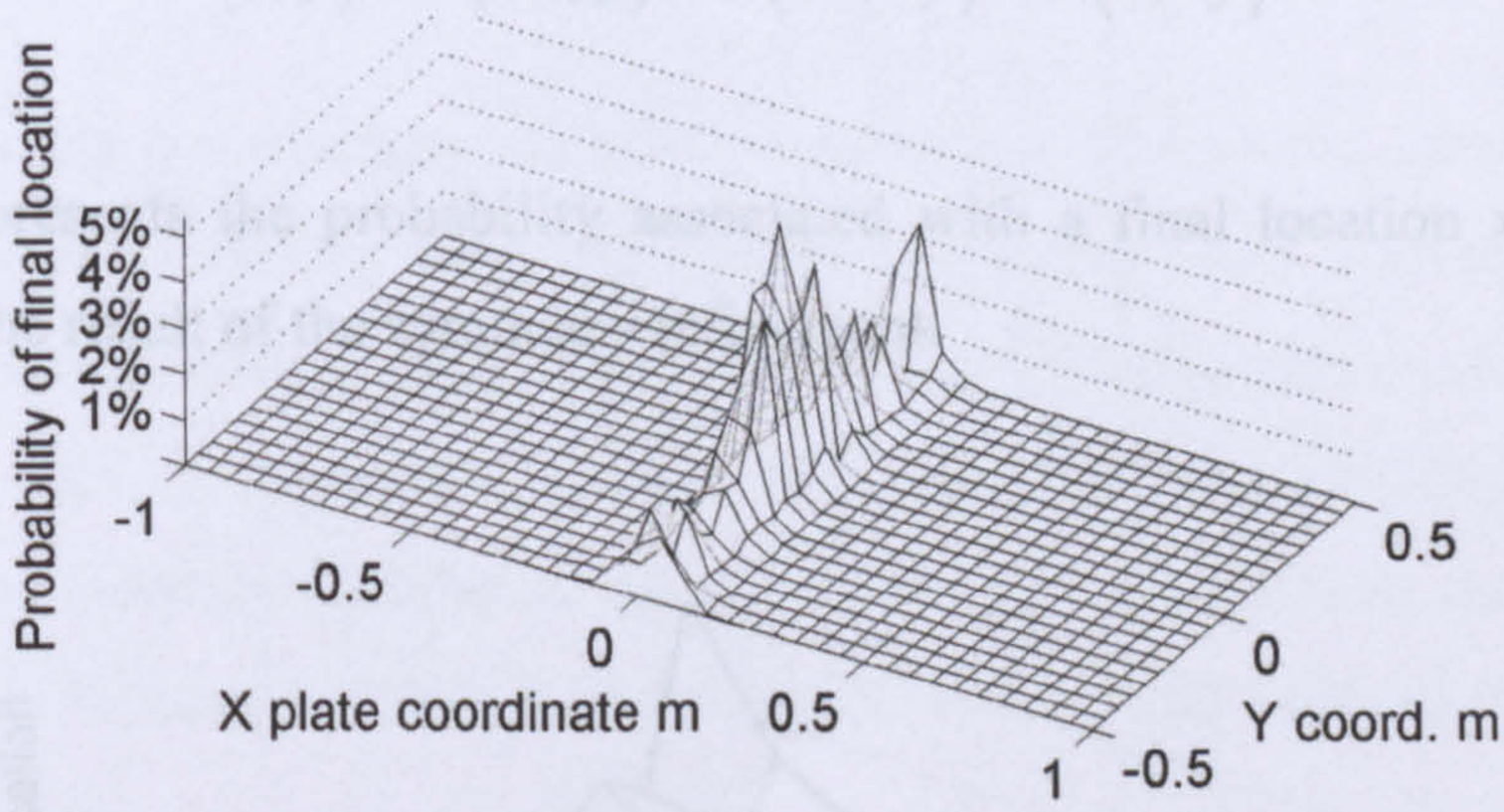

Figure 6.10 – Probability of final location from 15,000 simulations with Syncoglas RE 144/255.

The run-time for this 800 element RTM case was 12 hours, representing approximately three seconds for each complete simulation cycle. This was achieved on a PC system with an Intel Pentium 4™ processor running at 1.4 GHz. Due to symmetry, one may refine this result by combining the results of the four quadrants, as shown in Figure 6.11.

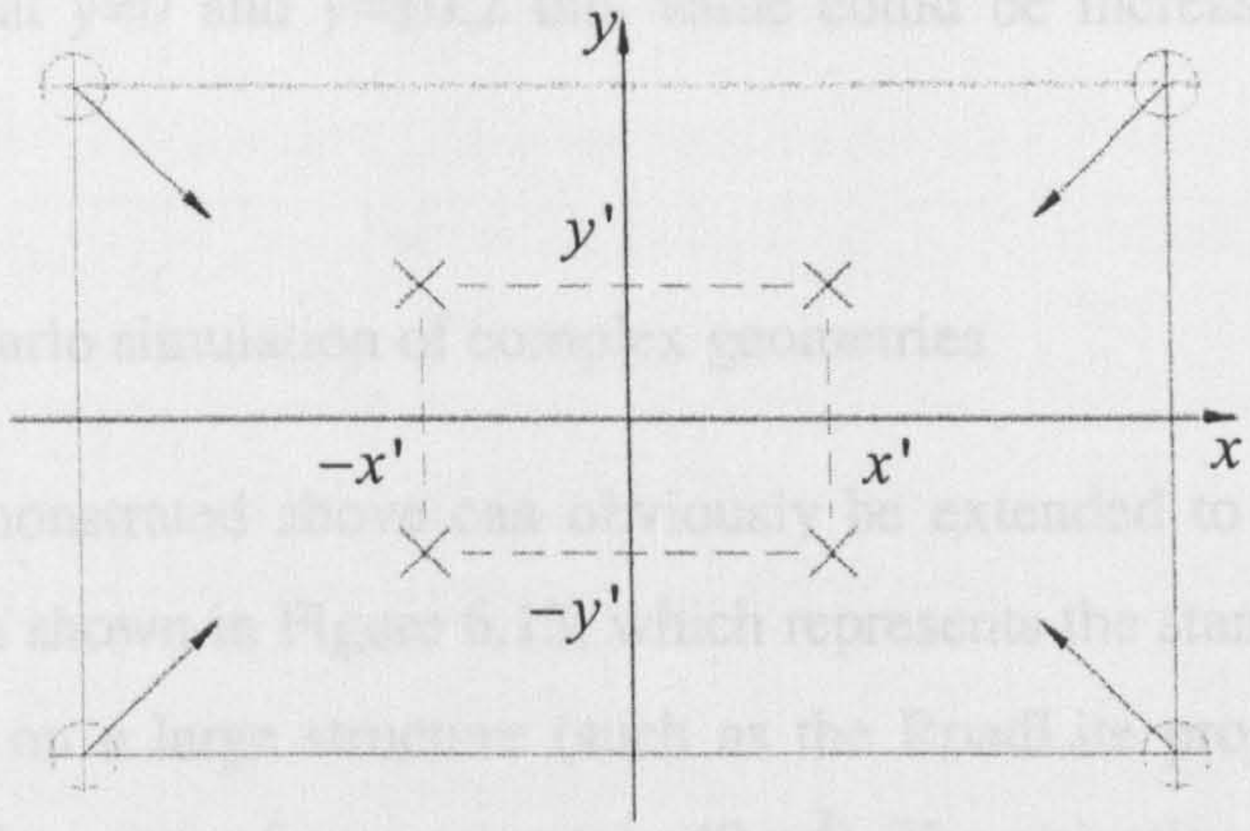

Figure 6.11 – All else remaining constant the probability of final location presents both x and y symmetry

That is:

$$P(x,y) = P(-x,y) = P(-x,-y) = P(x,-y) \tag{6.2}$$

Where P represents the probability associated with a final location x,y. Figure 6.12 shows the result of the symmetry refinement:

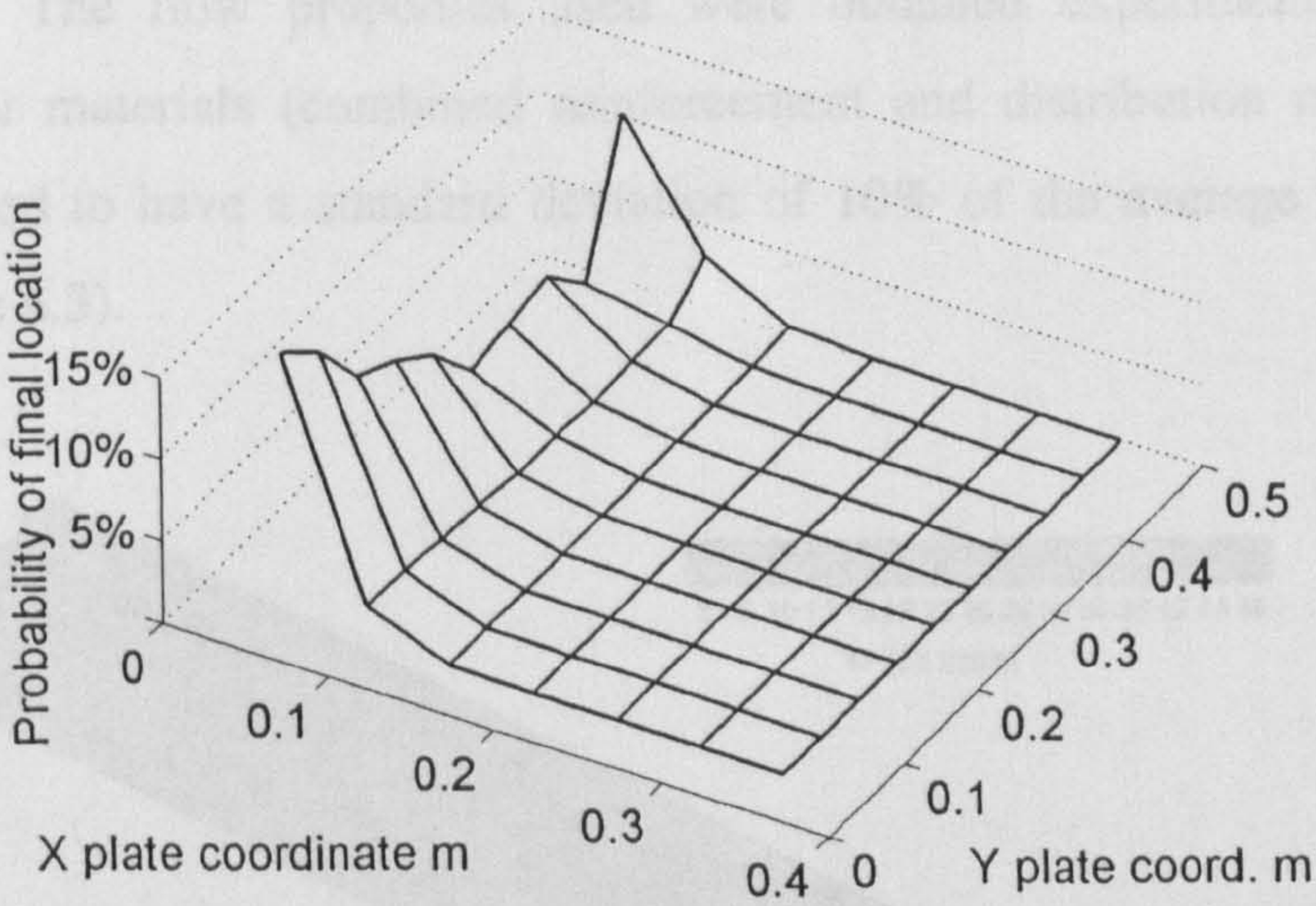

Figure 6.12 – Probability of final location on a quadrant of the four gate simulation.

From this study one can show how, for this material, locating a single vent at the centre of the mould results a final filling point at less than 55 mm from the vent for 18% of the cases. Similarly one can show that if three vents are located along

the central line at $y=0$ and $y=\pm 0.2$ this value could be increased to more than 40%.

6.5.2 Monte-Carlo simulation of complex geometries

The studies demonstrated above can obviously be extended to complex shapes. One such case is shown in Figure 6.13, which represents the standard deviation of nodal fill times on a large structure (such as the RoadLite project demonstrator which has a surface area of approximately 40 m^2). The objective of this analysis is to illustrate complex flow-geometry interactions which lead to localized variability issues. By identifying these problem areas actions can be taken either by altering the geometrical design or by introducing point gates or vents which add an active control capability. Note that the example shown is of flow through non-compliant media.

These results are the summary of 2,000 simulations. The model uses sequential line gate opening, starting from the central (symmetry line) outwards through three more line gates which are opened conditionally (if all nodes on the gate have been filled. The flow properties used were obtained experimentally for the demonstrator materials (combined reinforcement and distribution medium) and were assumed to have a standard deviation of 10% of the average permeability value (Table 6.3).

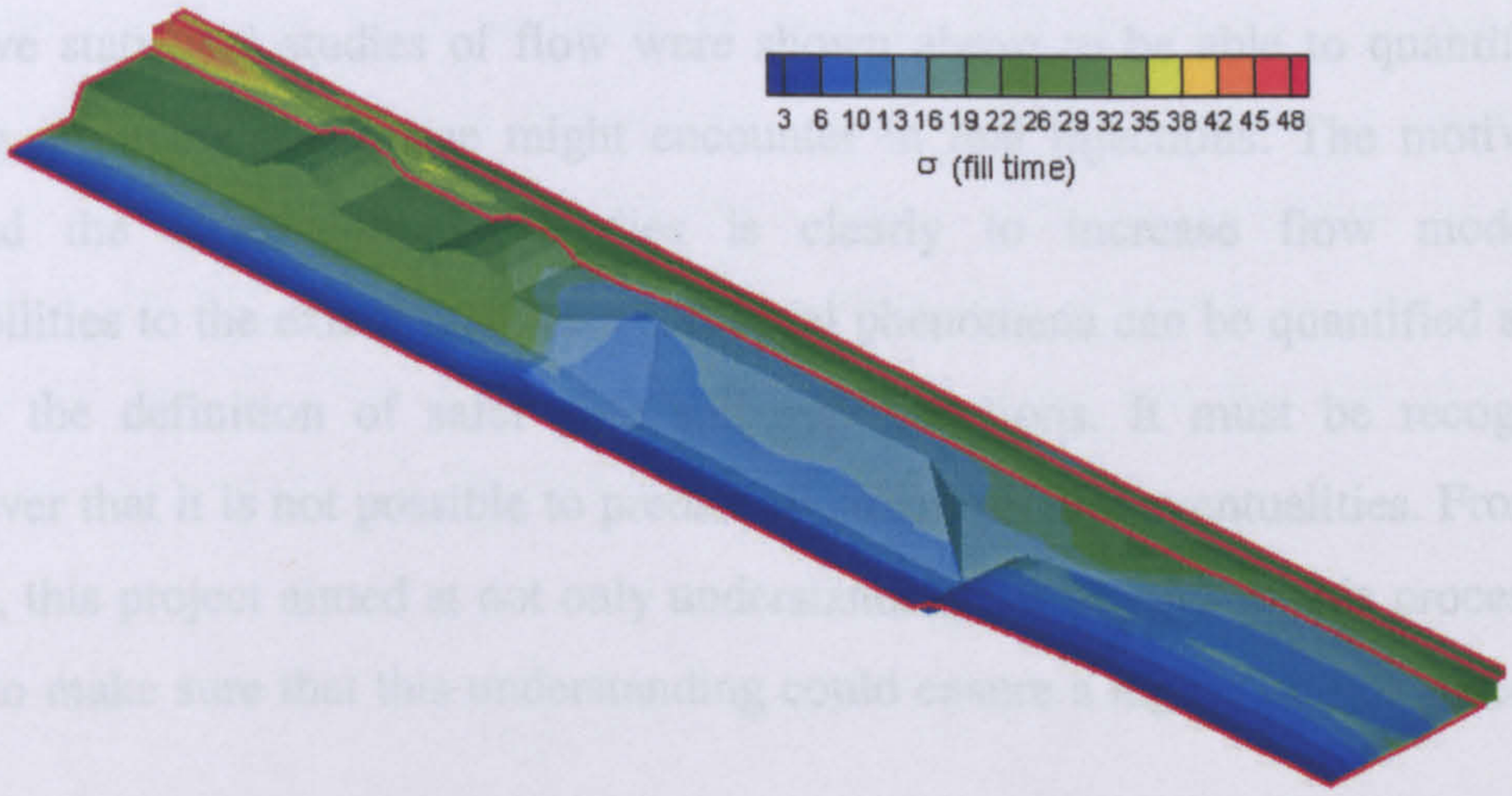

Figure 6.13 – Standard deviation of fill time on a complex mould geometry. Injection from bottom left edge. Driving pressure $\Delta P = 0.9$ bar, resin viscosity $\mu = 120$ mPa.s

Table 6.3 – Material properties for reinforcement in Figure 6.13

Material	No. of layers	Permeability data m^2			Thickness mm	Porosity -
		Kx	*Ky*	σ / K	*h*	ϕ
DM	1					
FGE117	14	$2.7 \cdot 10^{-10}\ m^2$	$1.5 \cdot 10^{-10}\ m^2$	10%	12.6	50%

A subsequent Monte-Carlo study looked into the distribution of final filling times (Figure 6.14) .

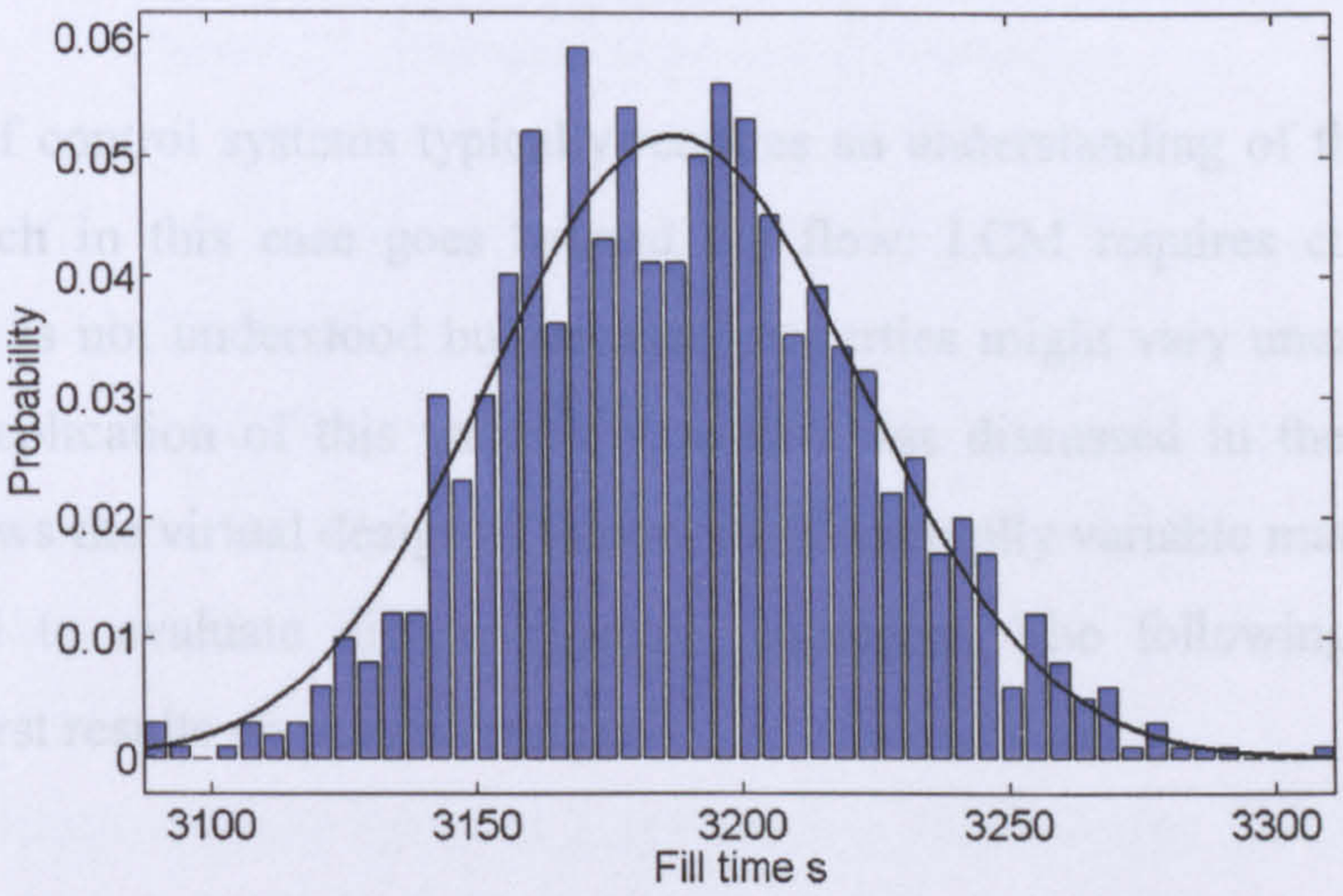

Figure 6.14 – Monte-Carlo result for fill time distribution for the case represented in Figure 6.13

6.6 PROCESS CONTROL

Passive statistical studies of flow were shown above to be able to quantify the filling problems which one might encounter in real injections. The motivation behind the aforementioned studies is clearly to increase flow modelling capabilities to the extent that these statistical phenomena can be quantified and to guide the definition of safer gate and vent locations. It must be recognized however that it is not possible to predict all situations and eventualities. From the onset, this project aimed at not only understanding the physics of this process but also to make sure that this understanding could ensure a higher rate of success in VI.

The modelling or "forecasting tool" was therefore developed with the intent of allowing integration in an automated control system which would actively ensure that the ideal flow patterns were followed. Conceptually an active control system can use the flow models to compare the actual flow patterns to the ideal, forecast the effect of different control actions on the subsequent flow pattern and, opting for the one which better reproduces the ideal situation, act on the mould to steer flow. This can be achieved through the variation of any flow parameter: opening or closing auxiliary gates, changing resin viscosity, altering inlet and outlet pressures or changing local permeabilities. Clearly some of these parameters are simpler to influence than others.

The design of control systems typically requires an understanding of the control problem which in this case goes beyond the flow: LCM requires control not because flow is not understood but because properties might vary unexpectedly. Hence, the replication of this variability, which was discussed in the previous sections, allows the virtual design of control tools: naturally variable materials can be simulated to evaluate different control strategies. The following sections present the first results on process control.

6.6.1 Virtual control algorithm

One can also apply the Monte-Carlo method in the computer assisted development of active control systems. The control concept employed in this example uses flow front positions to analyze different control actions: the effectiveness of an action is assessed by computing the difference in saturation between the ideal and the controlled cases. This is done by comparing the nodal saturation in the ideal scenario sat^{ideal} with that obtained in the real-life simulation sat^{real}. This effectiveness is assessed by the cost function shown in Equation (6.3), where n is the total number of nodes.

$$F^2 = \sum_{i=1}^{n} \left[\left(sat^{ideal}{}_i - sat^{real}{}_i \right)^2 \cdot CV_i^2 \right] \tag{6.3}$$

This is illustrated in Figure 6.15.

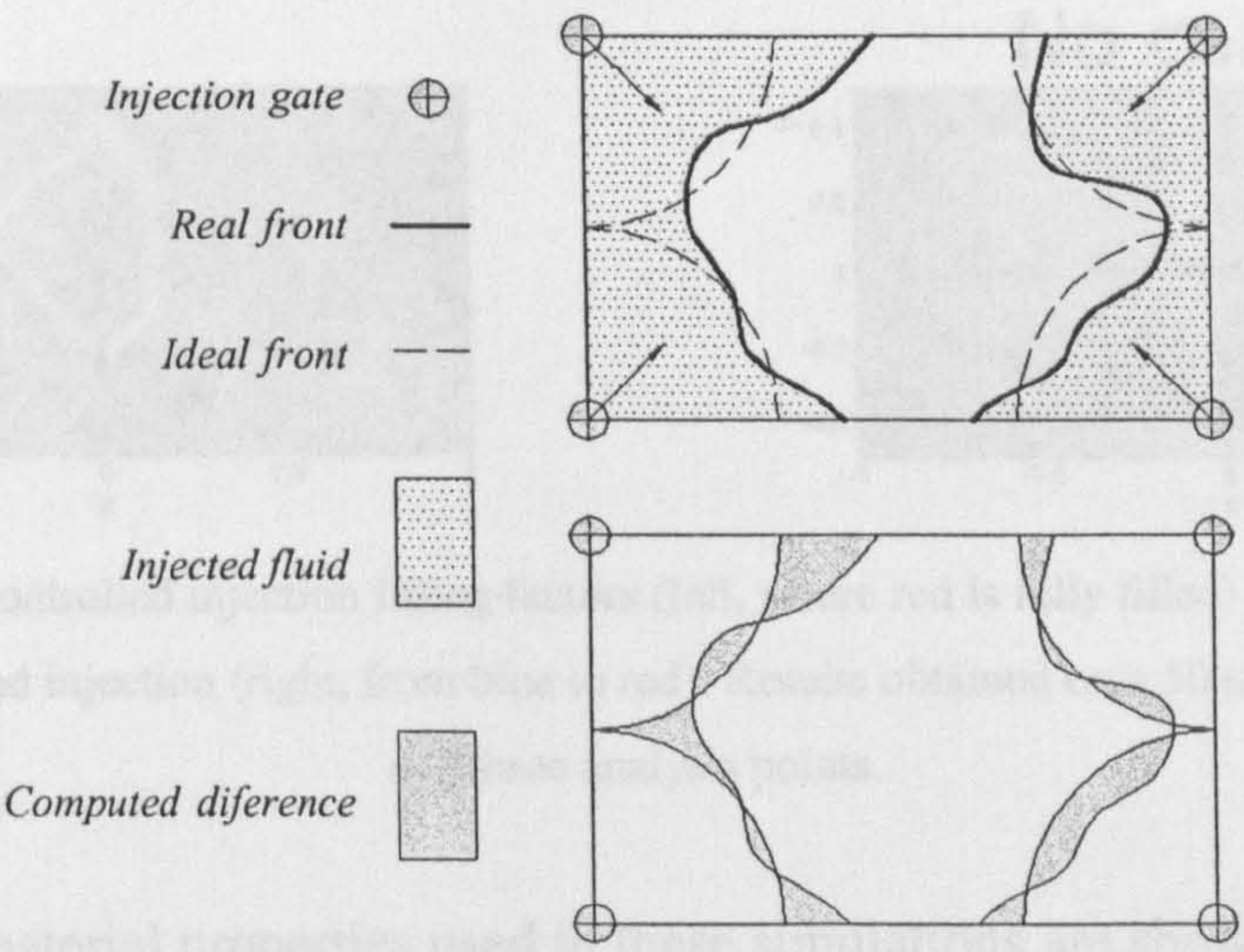

Figure 6.15 – Illustration of the control cost function.

Subsequently, the control action which leads to the closest result to the ideal scenario is activated until the next control step phase is reached. Note that this simple approach to control can be expanded to, for example, training neural networks to recognize patterns and uniquely quantify the statistical effectiveness of each approach.

Figure 6.16 illustrates one result of a typical five stage virtual on-line control strategy showing the potential benefits of flow front steering through variable inlet pressure at different injection ports. The example control code developed in this study is presented in Appendix 6.A and the relevant sub-procedures are contained in Appendix 6.B. It involves a five step analysis procedure: the mould is allowed to fill one fifth of the total number of nodes. At this point the simulation is stopped and the control algorithm implements a number of control alternatives – in this case changing the inlet pressure at the corner nodes to either 1 bar or 0.3 bar. The total number of control alternatives is therefore $4^2 = 16$ cases. Once all control simulations are completed and the database contains the predicted flow fronts for all 16 alternatives, the cost function analyzes the performance of each one, choosing the one which is closest to the ideal scenario. That action is then implemented and the algorithm runs the flow simulation – filling another fifth of the mould. At that point the control actions are re-evaluated.

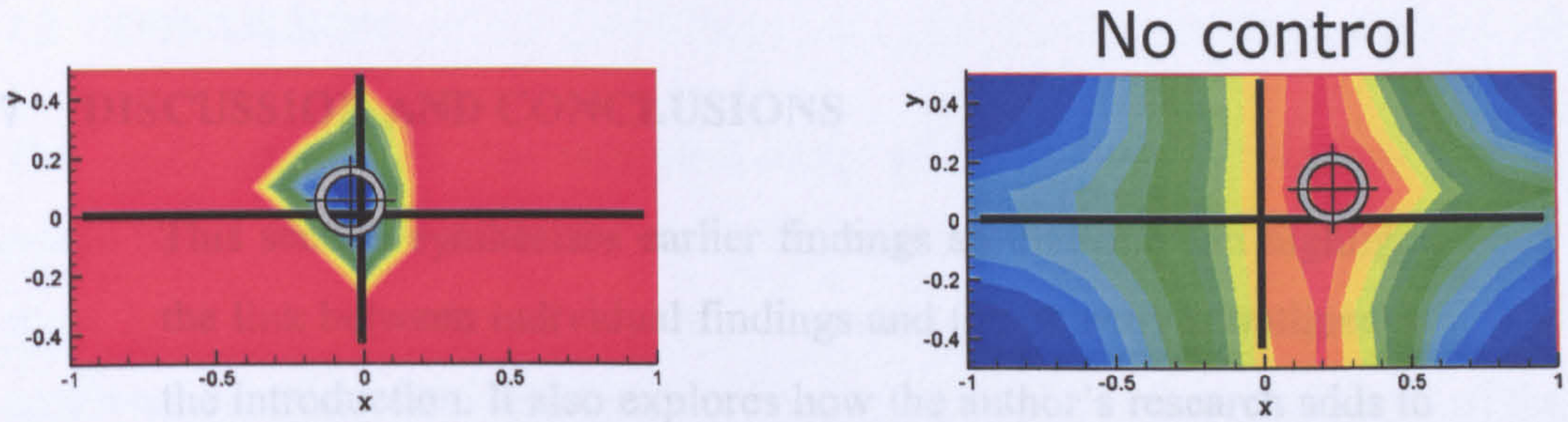

Figure 6.16 – Controlled injection filling factors (left, where red is fully filled) vs. isochrones of the non-controlled injection (right, from blue to red). Results obtained on a 50 shell-element mesh and three analysis points.

The relevant material properties used in these simulations are shown in Table 6.4.

Table 6.4 – Material data used in the control example

Material	Permeability data m^2 Ky	% σ / K	Fibre volume v_f
RE 144/255 (H2)	$26.2 \cdot 10^{-10}$	21.70%	50%

6.7 CONCLUSIONS

This chapter discusses the developments on flow modelling of LCM processes which were achieved by performing a stochastic analysis on reinforcement parameters. This was done using the Monte-Carlo method which was described and the technique was demonstrated for both compliant and non-compliant porous media. The chapter also proposes a technique to develop control techniques and, while presenting a simple example the technique can be used to experiment and develop more complex control approaches as well as quantifying the effect of different numbers of control steps or additional control gates.

With models such as the one proposed, it is foreseeable that new LCM control and optimisation tools could be deployed industrially. The full impact of the statistical distribution of permeability and compaction on LCM techniques still requires an in-depth study but the introduction of Monte-Carlo techniques within virtual experimentation / process development could have vast potential.

7 DISCUSSION AND CONCLUSIONS

This section synthesises earlier findings so that one can highlight the link between individual findings and the objectives outlined in the introduction. It also explores how the author's research adds to the field and what remains to be done.

7.1 INTRODUCTION

The main driving force behind this work lies in the development of composite materials as environmentally friendly alternatives to conventional materials for the transportation industry. Open mould manufacturing processes, which have typically been the source of large composite structures, raise environmental impact issues. Therefore, establishing composites as a viable environmental alternative requires closed moulding techniques, of which VI is the most practical for large structures. Hence, the RoadLite programme, in which this work is integrated, aimed to prove VI in composite road transportation technology. This has, in three years, produced two demonstrators: the first ever fully integrated single-shot flat bed semi-trailers.

The present work focuses on the analysis, development and validation of models for flow through compliant porous media. In this effort, the required textile compliance studies resulted in advances in experimental characterization methods and, in combination with flow models, provided quantitative guidelines for VI. Nevertheless, the industrial nature of the project highlighted variability of real flow as a major issue in large scale production. To address this problem a novel statistical flow modelling approach was developed and attention was directed to flow control system design. Time constraints have however implied that a full implementation of the control techniques was not achieved. That work is being continued.

7.2 DISCUSSION

This work begins with the analytical study of flow through compliant porous media based on the identification of a unified model for this case. It goes on to show how such a model is vital when one intends to optimise gate and vent positions, mass and final dimensions of a component. Nevertheless, in light of the same model, it demonstrates that flow front geometry is the same for both compliant and non-compliant porous media, implying that the ratio of local fill times in the two cases is a constant for a given flow scenario.

The fact that this model requires knowledge of the compliance of the porous material led to experimental and modelling studies on the mechanics of textiles. As was shown in chapter 3, it is possible to extend previous compaction work and formulate a single-parameter model for all reinforcement architectures. The resulting single parameter model was then used in parametric studies that provided guidelines for VI. The chapter continues with the exploration of several factors on this novel model – all of which reflect problems which might be found in VI moulding. In VI a mould goes through an initial dry compaction phase which can either be followed by a load cycle, if a leak is detected, or relaxation at constant load while the evacuated textiles await injection. Once resin is injected and there is a saturation of the reinforcement, a load dependent expansion occurs as local fluid pressures increase. Finally, depending on the flow control techniques used, one can also have to study cases where gates are closed or inlet pressures are changed. By changing fluid pressure, these actions lead to saturated compaction cycles. In order to reflect these issues, the influence of hysteresis, relaxation at constant load compaction, saturation, expansion and number of layers was studied. This data is required in order to perform the necessary validation studies.

That was done in the ensuing experimental characterization section (chapter 4). This part of the study looked into thickness variation, fill time and pressure field as the three main forms of detecting the influence of compliant porous media on flow. The model was shown to agree well with the results but, as was highlighted,

variability is a dominating factor in these processes, thereby launching the issue of statistical modelling of flow.

However, before this could be done, it was necessary to develop the flow model into a usable 2D modelling tool capable of analysing. That work was done by the author at the University of Delaware and involved the adaptation of the liquid injection moulding simulation (LIMS) software to flow through compliant media. The comparison between the resulting software and the 1D analytical study results (which had already been experimentally validated) showed the this LIMS-VI application can, with constitutive auxiliary models for fibre compaction and permeability, estimate mould filling time and distribution of fibre volume fraction in the VI process for higher dimension components.

Finally, the problem of statistical variability in flow was addressed through further adaptation of the FE/CV model of flow through compliant media. This novel technique, based on the Monte-Carlo method, was used to show that fill time and flow front variations can be modelled and studied statistically. This allows the quantification of possible filling problems in mass production scenarios. Unlike the non-compliant cases where permeability is the only variable, compliant media require further variation of surface density and compaction properties which was also shown. The mass production issue was developed further by showing how these naturally variable models can be used to study the implementation of control tools. Control was only addressed virtually and in its simplest possible form but this work highlights the potential for more complex control tool development for all forms of LCM.

7.3 FUTURE WORK AND RECOMMENDATIONS

The polynomial approximation used to characterize the fluid pressure field in chapter 3 is useful but not exact (with highest error at an α near zero). Better approximations can be achieved through higher order polynomials or other methods with the downside of increasing the number of parameters in the solution. However, future research could uncover solutions or different methods of approximating the fluid pressure field.

As described in chapter 3 the maximum compaction pressure used in this study differed from that which was used in other tests found in the literature. Furthermore, it is acknowledged that this pressure value affects the resulting fitting parameters in the model. The current results should therefore be complemented with other studies at higher compaction pressures to eliminate the possibility that compaction pressure affects the master curve coefficients. That is not possible with the current state of testing but is highly relevant in proving the master curve conjecture.

The Monte-Carlo modelling of real life flow through compliant media requires adequate knowledge of the statistical distribution of parameters. Yet, while the analysis of the statistical distribution of compaction results showed that the hypothesis of normal distribution of parameters v_{f0} and B cannot be disproved it is still pertinent to follow up this study with a larger numbers of observations. Furthermore, due to the fundamentally empirical nature of the power-law model one cannot yet explain the compliance behaviour of textile architectures, only highlight that there is a general behaviour (as shown by the master curve). As this work highlights, the importance of compliance in composites manufacturing processes merits continued research.

As mentioned, the low driving pressure available in the VI process implies that most industrial applications use a distribution medium to enhance flow. In fact, it is commonly acknowledged that the distribution medium dominates flow (e.g. Ragondet *et al,* 2002). Moreover, within limits, in-plane flow in the reinforcement is negligible (Section 5.2.3) but one should note that compliance also affects flow in distribution media. In light of this, the present work continues to be applicable if one can study combined compliant media.

As described in chapter 5 the influence of the element shape factor in flow results leads to model complexity problems because it implies large numbers of elements. Several alternatives will be suggested to overcome this problem, the most promising of all is the nodal through-thickness saturation method. This method can potentially reduce the lead-lag problem in 3D complex structures to 2.5D,

eliminating the aforementioned element number issue. Nevertheless, one needs to develop benchmarking simulations and experimental validation work to validate this approach. Furthermore, this links with the lead-lag work by Ragondet *et al* (2004) which must be integrated in a full model of VI.

Figure 7.1 illustrates the approach that can be taken at the current stage of evolution of the code, which assumes a non-compliant reinforcement.

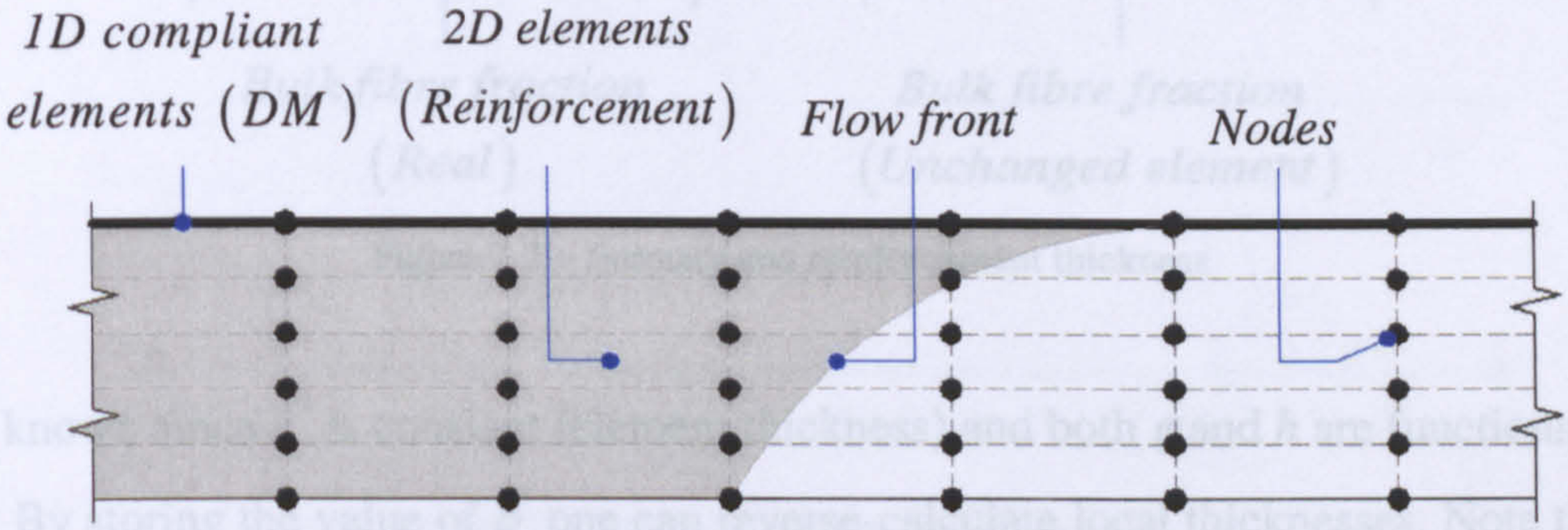

Figure 7.1 – Finite element concept for simulation of VI with distribution media

There are however three possible alternatives (1.a. and b., and 2) to this approach. By order of increasing implementation complexity (and industrial suitability):

1. Combining compliant shell elements (DM) with solid elements (reinforcement) and:
    a. Varying reinforcement porosity to replicate that of the compacted porous volume.
    b. Changing thickness by re-meshing the reinforcement.
2. Combining shell elements and a scalar saturation function to simulate through-thickness flow.

In the first (alternative 1a)) reinforcement compliance is incorporated in the value of porosity. Figure 7.2 illustrates this: the available porous volume on the real element (left) is duplicated on the unchanged element (right) by adjusting porosity, where

$$\phi^* = \frac{\phi \cdot h}{h^*} \tag{7.1}$$

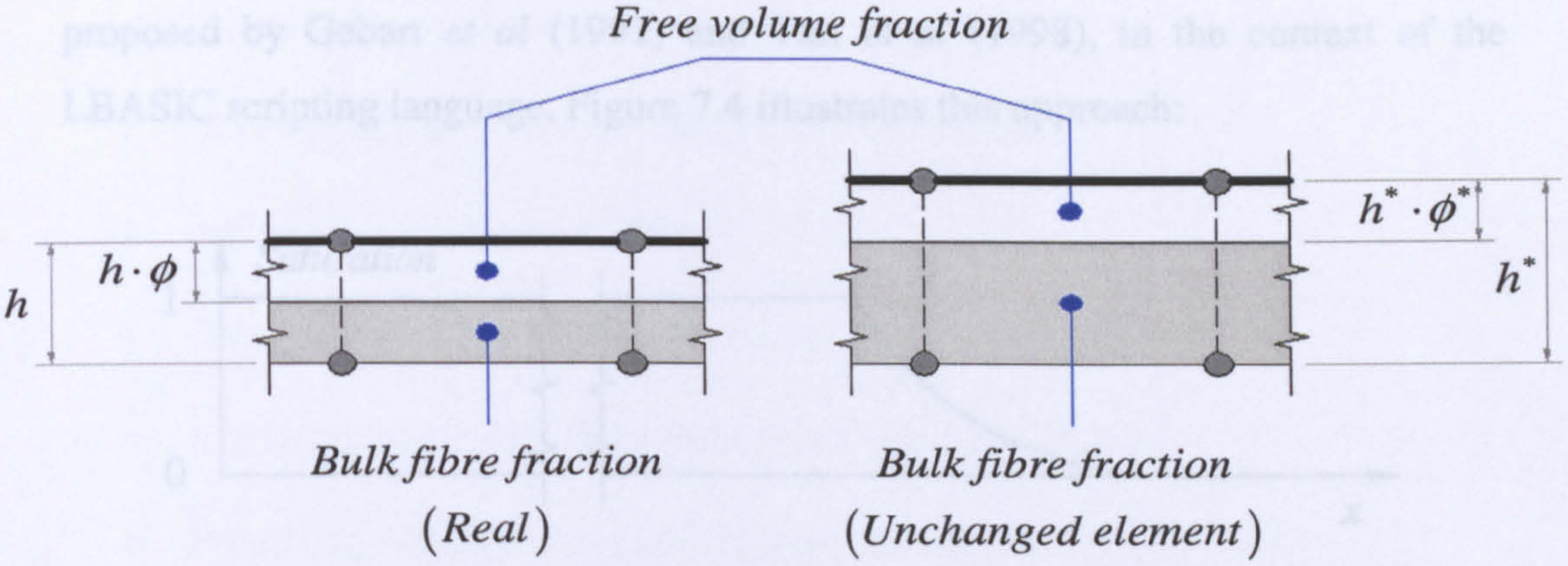

Figure 7.2 – Porosity and reinforcement thickness

is known since h^* is constant (element thickness) and both ϕ and h are functions of P. By storing the value of ϕ^* one can reverse-calculate local thicknesses. Note that permeability is necessarily the same in both cases. One advantage that this method might present is the direct calculation of lead–lag distances, even without knowledge of the final thickness. On the other hand, it involves a 3D flow solution that, as discussed in section 5.2.3, leads to high numbers of elements and can therefore be slow. The concept of combining compliant DM elements with variable nodal positions in the mesh (alternative 1b)) is directly achievable in the flow simulation software. The example in Figure 7.3 shows the simplest possible case – a 2D cross-section with one layer of shell elements through the thickness:

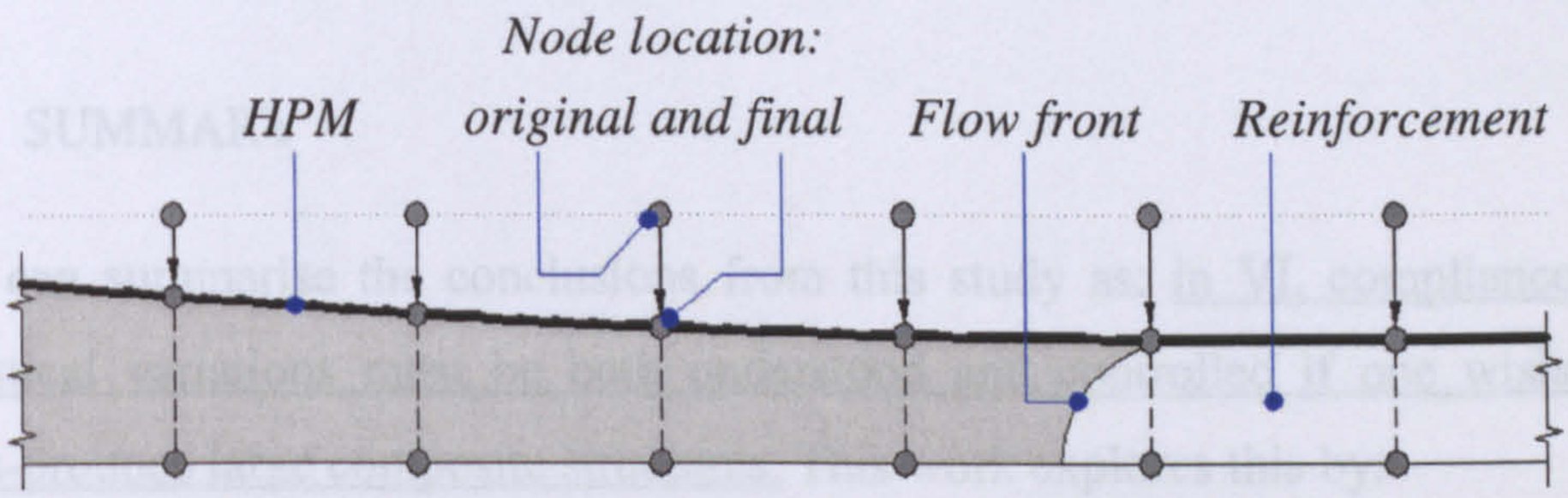

Figure 7.3 – Nodal coordinates and reinforcement thickness. DM is modelled using 1D elements while the reinforcement uses 2D shells

However, the added complexity associated with additional element layers and 3D geometries can easily render this approach impractical. In addition, highly

compliant materials could easily present shape factor problems, reducing the accuracy of the flow model. In order to eliminate the use of 3D elements a third approach is necessary. One can suggest the scalar saturation term method, as was proposed by Gebart *et al* (1991) and Tari *et al* (1998), in the context of the LBASIC scripting language. Figure 7.4 illustrates this approach:

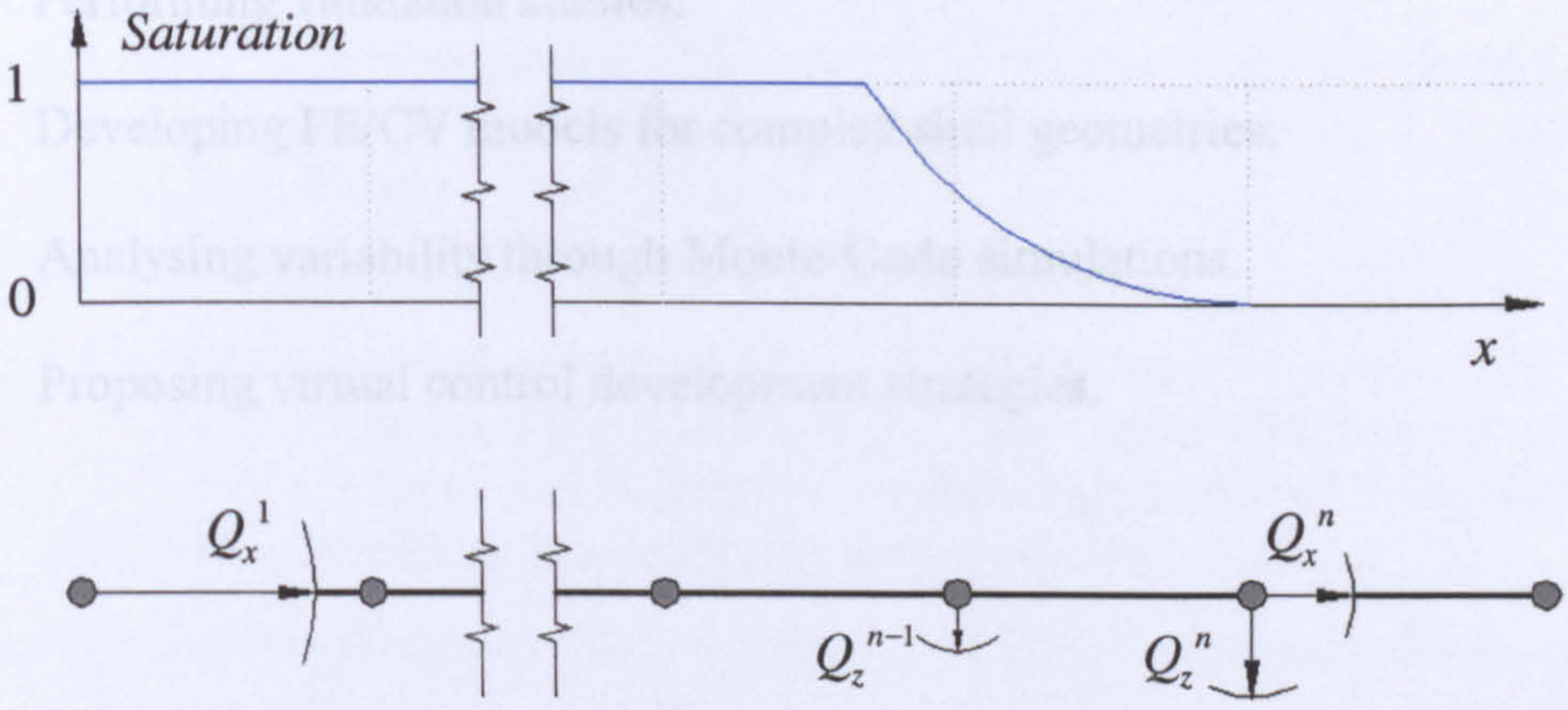

Figure 7.4 – 1D saturation vs. nodal flow rates

Here, the sum of the in-plane flow rates Q_x and the through thickness sink terms Q_z must equal the flow rate at the inlet gate:

$$\sum_{i=1}^{n} Q_x^{\,i} + \sum_{i=1}^{n} Q_z^{\,i} = 0 \tag{7.2}$$

Finally, thickness can be calculated from both through thickness and control volume saturation terms.

7.4 SUMMARY

One can summarise the conclusions from this study as: in VI, compliance and statistical variations must be both understood and controlled if one wishes to mass-produce large composite structures. This work explores this by:

- Identifying a unified analytical base for flow through compliant media.
- Modelling flow through compliant porous media analytically to build a benchmarking and parametric framework.

- Studying the compliance of textile reinforcements both experimentally and in terms of empirical model development.
- Discussing compliance statistically.
- Developing parametric guidelines for the process.
- Performing validation studies.
- Developing FE/CV models for complex shell geometries.
- Analysing variability through Monte-Carlo simulations.
- Proposing virtual control development strategies.

LIST OF FIGURES

LIST OF TABLES

REFERENCES

ACKLAM, P.J. (2000) LTQNORM *Lower tail quartile for standard normal distribution.* The MathWorks online database. www.mathworks.com.

ADVANI, S.G.; BRUSCHKE, M.V. (1994). *Resin transfer moulding phenomena in polymeric composites. In* Flow and Rheology in Polymer Composites Engineering, Elsevier, Amsterdam. 465-515.

ADVANI, S.G., AND SIMACEK, P, (1999). *Modelling and Simulation of Flow, Heat Transfer and Cure in Resin Transfer Moulding For Aerospace Structures. Ed.* Kruckenberg, T. and Paton, R., Kluwer Academic Publishers, Netherlands, 225-281.

ANDERSON, E.; BAI, Z.; BISCHOF, C.; BLACKFORD, S.; J. DEMMEL; J. DONGARRA; J. DU CROZ; A. GREENBAUM; S. HAMMARLING; A. MCKENNEY; D. SORENSEN (1999). *Lapack users guide. 3rd Edition.* http://www.netlib.org/lapack/lug/lapack_lug.html.

ANDERSSON, H. M. (2003). *Visualization of composites manufacturing.* PhD thesis. Leulea University of Technology

ANDERSSON, H.M., LUNDSTROM T.S., GEBART, B.R. AND LANGSTROM R. (2002) *Flow enhancing layers in the vacuum infusion process.* Polymer composites 23 (5): 895-901.

ANDERSSON, H.M., LUNDSTROM T.S. AND GEBART, B.R. (2003 a). *Numerical model for vacuum infusion manufacturing of polymer composites.* Polymer composites 13 (2-3): 383-394.

ANDERSSON, H.M., LUNDSTROM T.S., GEBART, B.R., SYNNERGREN, P. (2003 b). *Application of Digital Speckle Photography To Measure Thickness Variations in the Vacuum Infusion Process.* Polymer composites 24 (3): 448-455.

BICKERTON, S. AND ADVANI, S.G. (1999). *Characterization and Modeling of Race-tracking in Liquid Composite Molding Processes.* Composites Science and Technology, 59 (15): 2215-2229.

BINDING, D.M., K. FISHER, R.S. JONES (2000). *Compression of thermosetting fabric materials.* Composites: Part A, 31: 1323-1330.

BIOT, M.A. (1941). *General theory of three dimensional consolidation.* J. of Applied Physics, 12: 155-164.

BRUSCHKE, M. V. AND ADVANI, S. G. (1993). *Flow of Generalized Newtonian Fluids Across a Periodic Array of Cylinders.* J. Of Rheology, 37: 479-498.

BRUSCHKE, M. V. AND ADVANI, S. G., (1990). *A finite element/control volume approach to mould filling in anisotropic media*. Polymer Composites, 11: 398-405.

CALADO, V.M.A.; ADVANI, S.G. (1996) *Effective average permeability of multi-layer preforms in resin transfer moulding*. Composites Science and Technology, 56: 519-531.

CHEN, B. AND CHOU, T.-W. (1999). *Compaction of Woven-Fabric Preforms in Liquid Composite Moulding Processes: Single-Layer Deformation*. Composites Science and Technology, 59: 1519-1526.

CHEN, B. AND CHOU, T.-W. (1999). *Compaction of Woven-Fabric Preforms in Liquid Composite Moulding Processes: Nesting and Multi-Layer Deformation*. Composites Science and Technology, 59:1519-1526.

CHUNG, T. J. (2002). *Computational Fluid Dynamics.* Cambridge University Press, U.K.: 218-239 and 491-508.

CONOVER, W. J. (1980). *Practical Nonparametric Statistics*. New York, Wiley and Sons.

CORDEN, T.J.; RUDD, C.D. (1997) *Permeability measurements and modelling techniques for vacuum infusion*. Proc. of the international conference on composite materials - ICAC '97, 4-5 September 1997, Glasgow, UK: 230-242.

DAVÉ, R., (1990). *A unified approach to modelling rein flow during composite processing.* J. of Composite Materials, 24: 22-41.

DE BOER, R., (2000). *Theory of porous media: highlights in historical development and current state.* Berlin; Springer.

DEVILLARD M.; HSIAO K-T.; GOKCE A.; ADVANI S.G. (2003) *On-Line Characterization of Bulk Permeability and Race-Tracking During the Filling Stage in Resin Transfer Molding Process.* Journal of Composite Materials, 37 (17): 1525-1541.

GAUVIN, R., TROCHU, F., LEMENN, Y., AND DIALLO, L. (1996). *Permeability Measurement and Flow Simulation Through Fiber Reinforcement.* Polymer Composites, 17 (1): 34-42.

GEBART, B. R. (1992). *Permeability of unidirectional reinforcements for RTM.* J. Of Composite Materials, 26(8): 1101-1133.

GRIMSLEY, B. W., PASCAL HUBERT, XIAOLAN SONG, ROBERTO J. CANO, ALFRED C. LOOS, R. BYRON PIPES. (2001) *Flow and compaction during the vacuum assisted resin transfer moulding process*. International SAMPE Technical Conference, 33: 140-153.

GUTOWSKI T.G., Z. CAI, J. KINGERY AND S.J. WINEMAN, (1986). *Resin Flow/Fiber Deformation Experiments*. Sampe Quarterly; 17(4): 54-58.

GUTOWSKI T.G., Z. CAI, S. BAUER, D. BOUCHER, J. KINGERY AND S.J. WINEMAN, (1987). *Consolidation experiments for laminate composites*. J. Of Composite Materials, 21: 560-668.

GUTOWSKI, T.G. AND DILLON, G. (1987) *The Elastic Deformation of Fiber Bundles. In* Advanced Composites Manufacturing, ed. T.G. Gutowski, John Willey and sons, Inc., 138-139.

GUTOWSKI, T.G., T. MORIGAKI, AND Z. CAI, (1987). *The Consolidation of Laminate Composites*. J. Of Composite Materials, 21:172-188.

HAMMAMI, A. AND GEBART, B.R., (1998). *Experimental investigation of the vacuum infusion moulding process. Proc.* of the Eighth European Conference on Composite Materials ECCM8, Naples; 577-585.

HAMMAMI A., GAUVIN R. AND TROCHU F. (1998) *Modelling the edge effect in liquid composites molding*. Composites: Part A, 29 (5-6): 603-609.

HAMMAMI, A. AND GEBART, B.R., (2000). *Analysis of the vacuum infusion moulding process*. Polymer Composites, 21(1): 28-40.

HAN, K., JIANG, S., ZHANG, C. AND WANG, B., (2000). *Flow modelling and simulation of SCRIMP for composites manufacturing*. Composites: Part A, 31: 79–86.

HOES, K., DINESCU, D., VANHEULE, M., SOL, H., PARNAS, R., BELOV, E. AND LOMOV, S. (2002) *Statistical distribution of permeability values of different porous materials. Proc.* of the Tenth European Conference on Composite Materials (ECCM10) June 3-7, 2002, Brugges, Belgium.

HSE (2003) *Assessing and controlling styrene levels during contact moulding of fibre-reinforced plastic (FRP) products*. Plastics processing sheet 14. HSE - Health and Safety Executive, London.

HSIAO, K.-T., MATHUR, R., S.G. ADVANI, J.W. GILESPIE, JR., B.K. FINK. (2000) *A closed form solution for flow during the Vacuum Assisted Resin Transfer Moulding Process.* J. Manufacturing Science and Engineering, 122: 463-475.

HSIAO, K.-T., DEVILLARD, M. AND ADVANI, S.G. (2002). *Streamlined Intelligent RTM Processing: From Design to Automation*. Proc. of 47th International SAMPE Symposium and Exhibition, 47: 454–465.

KANG, M.K., LEE, W.I. AND HAHN, H.T., (2000). *Formation of microvoids during the resin transfer moulding process.* Composites Science and Technology, 60: 2427-2434.

KANG, M.K., W.I. LEE AND H.T. HAHN, (2001). *Analysis of the vacuum bag resin transfer moulding process*. Composites: Part A, 32: 1535-1560.

KEYNOTE (2002) *Road Haulage Market Report 2002* Seventeenth Edition Ed. Lynsey Barker

KUEH, S.R.M., PARNAS, R.S., AND ADVANI, S.G., 2002, *Methodology for using long-period gratings and mould-filling simulations to minimize the intrusiveness of flow sensors in liquid composite moulding*. Composites Science and Technology, 62 (2): 311-327.

LAI, C.-L. AND YOUNG, W.-B. (1999) *The Effects of Preforming Induced Variable Permeabilities on the RTM Molding Flow*. Polymer Composites, 20 (2): 225-239.

LAWRENCE, HSIAO, DON, SIMACEK, ESTRADA, SOZER, STADTFELD AND ADVANI (2002) *An approach to couple mold design and on-line control to manufacture complex composite parts by resin transfer molding.* Composites: Part A, 33: 981–990.

LOOS, A.C.; MACRAE, J.D. (1996). *A process simulation model for the manufacture of a blade-stiffened panel by the resin film infusion process*. Composites Science and Technology, 56: 273-289.

LOOS, A.C. (2001) *Low-cost fabrication of advanced polymeric composites by resin infusion processes*. Advanced Composite Materials, 10 (2-3): 99–106.

LIN, H.H., RANGANATHAN, S. AND ADVANI S.G., (1994). *Consolidation of continuous-fiber systems. In* Flow and Rheology in Polymer Composites Manufacturing, ed. S.G. Advani, Elsevier Science: 325-358.

LONG, A.C., SOUTER, B.J., ROBITAILLE, F. AND RUDD, C.D. (2002) *Effects of fibre architecture on reinforcement fabric deformation*. Plastics Rubber and Composites, 31(2): 87-97.

MARCO METHOD, (1950). U.S. Patent Office, Pat No. 2495640.

MATHUR, R., ADVANI, S.G. AND FINK, B.K. (2000). *A Sensitivity-based Gate Location Algorithm for Optimal Mould Filling During the Resin Transfer Moulding Process*, Advances in Computational Engineering and Sciences, 1: 138-144.

MATHUR, R., ADVANI, S.G. AND FINK, B.K. (1999). *Use of Genetic Algorithms to Optimize Gate and Vent Locations for the RTM Process*. Polymer Composites, 20(2): 167-178.

MATHUR, R.; HEIDER, D.; HOFFMANN, C.; GILLESPIE, J.W.; ADVANI, S.G.; FINK, B. K. (2001). *Flow front measurements and model validation in the vacuum assisted resin transfer moulding process*. Polymer Composites, 22(4), 477-490.

MODI, D., ŠIMÁČEK, P., ADVANI, S. (2002*). Numerical issues in mould filling simulations of liquid composites processing. Proc.* 10th US-Japan conference on composite materials, 16-18th September 2002, Stanford University, CA, USA.

NIELSEN, D.R., R. PITCHUMANI (2002). *Closed-loop flow control in resin transfer molding using real-time numerical process simulations*. Composites Science and Technology, 62: 283–298.

NIXON, J. A (2000) *Vacuum infusion: cost-effective closed mould processing to meet the challenges of the styrene issue. In.* Integrated Design and Manufacture Using Fibre-Reinforced Polymeric Composites, pp. 125-139. Eds. Owen, Mike J.; Middleton, Victor; Jones, I. Arthur. Woodhead Publishing, Cambridge, UK.

PARNAS, R.S. AND PHELAN, F.R., (1991). *The effect of heterogeneous porous media on mould filling in resin transfer moulding*. Sampe quarterly; January 1991: 53-60.

PAN, R., LIANG, Z., ZHANG, C., AND WANG P. (2000) *Statistical Characterization of Fiber Permeability for Composite Manufacturing*. Polymer Composites, 21 (6): 996-1006.

PARNAS, R.S., SALEM, A.J., SADIQ, T.A.K., WANG, H.-P. AND ADVANI, S.G., (1994). *The interaction between micro- and macro-scopic flow in RTM preforms*. Composite Structures, 27: 93-107.

PILLAI, K.M., L, C.L. TUCKERA,*, F.R. PHELAN. (2001) *Numerical simulation of injection/compression liquid composite moulding. Part 2: preform compression*. Composites: Part A, 32: 207–220.

K. M. PILLAI AND S. G. ADVANI. (1998). *A Model for Unsaturated Flow in Woven Fiber Preforms during Mold Filling in Resin Transfer Molding*. J. Comp. Mat., 32:1753-1783.

K. M. PILLAI AND S. G. ADVANI. (1998). *A Numerical Simulation of Unsaturated Flow in Woven Fiber Preforms during Resin Transfer Molding Process*, Polymer Composites, 19:71-80.

RAGONDET, A., CORREIA N.C., ROBITAILLE, F., LONG, A. C., AND RUDD, C.D. (2002) *Experimental Investigation And Modelling Of The Vacuum Infusion Process*. Proc. of ECCM 10 June 3-7, 2002, Brugges, Belgium.

RAGONDET, A., (2004) *Low cost manufacturing of large transportation structures*. PhD Thesis. University of Nottingham.

ROBITAILLE, F. AND GAUVIN, R. (1998). *Compaction of Textile Reinforcements for Composites Manufacturing: I - Review of Experimental Results*. Polymer Composites, 19(5): 543-557.

ROBITAILLE, F. AND GAUVIN, R. (1998). *Compaction of textile reinforcements for composites manufacturing. II: Compaction and relaxation of dry and H_2O saturated woven reinforcements*. Polymer Composites, 19(2): 198-216.

ROBITAILLE, F. AND GAUVIN, R., (1998). *Compaction of Textile Reinforcements for Composites Manufacturing: III - Reorganization of the Fibre Network in Woven*. Polymer Composites, 20(1): 48-61.

RUDD, C. D.; KENDALL, K. N.; LONG, A. C. (1997) *Liquid molding technology: resin transfer moulding, structural reaction injection moulding and related processing techniques*. Woodhead, Cambridge, UK.

RUDD, C.D., LONG, A.C., MCGEEHIN, P. AND SMITH, P. (1996). In-*plane permeability for simulation of liquid composite moulding of complex shapes*. Polymer Composites, 17(1): 52-59.

RUDD, C.D., LONG, A.C., MCGEEHIN, P., CUCINELLA, F., AND BULMER, L.J. (1995) *Processing and mechanical properties of bi-directional preforms for liquid composite moulding*. Composite Manufacturing, 6: 211-219.

SAYRE, J. R. and LOOS, A. C. 2003 *Resin Infusion of Triaxially Braided Preforms With Through-the-Thickness Reinforcement*. Polymer Composites. 24 (2) 229-236.

SAUNDERS, R.A. (1997) *Compression and microstructure of glass fibre fabrics in the processing of polymer composites*. PhD. Thesis. U. of Surrey.

SCHEIDEGGER, ADRIAN E., (1974). *The physics of flow through porous media.* 3rd ed. Toronto: University of Toronto Press.

SEEMANN, W.H. (1990). *Plastic transfer molding techniques for the production of fiber reinforced plastic structures* U.S. Patent Office, Pat No. 4902215.

SEEMANN, W.H. (1991). *Plastic transfer molding apparatus for the production of fiber reinforced plastic structures*. United States Patent 5,052,906 .

SEEMANN, W.H. (1995). *Unitary vacuum bag for forming fiber reinforced composite articles and process for making same*. United States Patent 5,439,635 .

SHOJAEI, A., GHAFFARIAN, S.R. AND KARIMIAN, S.M.H. (2003) *Modeling and simulation approaches in the resin transfer molding process: A review.* Polymer Composites, 24 (4): 525-544.

SIMACEK, P., LEDERMANN, C., AND ADVANI, S.G. (2001). *Fast Three Dimensional Numerical Simulation of Isothermal Mould Filling for Liquid Composite Moulding Processes. Proc.* of the American Society for Composites Sixteenth Technical Conference, September 9-12.

SLAUGHTER (2003). *Method for making composite structures.* United States Patent 6,630,095.

SMITH, P., RUDD, C. D., AND LONG, A. C. (1997). *The effect of shear deformation on the processing and mechanical properties of aligned reinforcements.* Composites Science and Technology 57: 327-344.

TARI, M. J., IMBERT, J.-P., LIN, M.Y., LAVINE, A.S. AND HAHN, H.T. (1998). A*nalysis of resin transfer molding with high permeability layers*. J. of Manufacturing Science and Engineering 120: 609-616.

THE MATHWORKS (2002). *Matlab function reference.* 1(A – E): 2.11-2.17.

US DOE (2000). *Technology Roadmap for the 21st Century Truck Program.* US Department of Energy

WYK, C. M. VAN (1948). *Note on the compressibility of wool.* J. of the Textile Institute, 39, 285-291.

WALSH (2003). *Apparatus and method for selectively distributing and controlling a means for impregnation of fibrous articles*. United States Patent 6,586,054.

WILLIAMS, C., SUMMERSCALES, J. AND GROVE, S., (1996). *Resin infusion under flexible tooling (RIFT): A review*. Composites: Part A, 27A: 517-524.

WILLIAMS, C.D., GROVE, S.M. AND SUMEMERSCALES J.. The compression response of fibre-reinforced plastic plates during manufacture by the resin infusion under flexible tooling method. Composites: Part A 29A (1998) 111-114

YOUNG, W. B., HAN, K., FONG, L.H., LEE, L.J. AND LIOU, M.J. (1991). Flow simulation in molds with preplaced fibre mats. Pol. Comp. 12 (6): 391-403.

APPENDICES

APPENDIX 1.A JOURNAL PUBLICATIONS

N. C. CORREIA; F. ROBITAILLE; A.C. LONG; C.D. RUDD; P ŠIMÁČEK; S.G. ADVANI (2004*) Use Of Resin Transfer Molding Simulation To Predict Flow, Saturation And Compaction In The Vartm Process*. ASME Journal of Fluids Engineering (Accepted for publication).

N. C. CORREIA, F. ROBITAILLE, A.C. LONG, C.D. RUDD, P. ŠIMÁČEK, S.G. ADVANI (2004). *Analysis of the vacuum infusion moulding process: I. Analytical formulation*. Composites: Part A (Accepted for publication).

APPENDIX 1.B PUBLICATIONS IN CONFERENCE PROCEEDINGS

N. C. CORREIA, F. ROBITAILLE, A. C. LONG AND C. D. RUDD (2004). *Variability In Liquid Composite Moulding Techniques: Process Analysis And Control. Proc. of* The 7th International Conference on Flow Processes in Composite Materials, FPCM-7, July 7-9, 2004, Newark, Delaware, USA (Accepted).

N. C. CORREIA, F. ROBITAILLE, A. C. LONG AND C. D. RUDD (2003). *Analytical And Numerical Studies Into The Vacuum Infusion Process: In-Plane Flow In Compressible Porous Media. Proc. of* International conference on composite materials ICCM14, July 14-18, 2003 San Diego, California.

A.C. LONG, N.C. CORREIA, A. RAGONDET, F. ROBITAILLE, C.D. RUDD (2003). *Analytical And Numerical Modelling Of Vacuum Infusion. Proc. of* 24th SAMPE International Conference and Forum SAMPE Europe 2003, April 1-3, 2003, Paris, France.

N. C. CORREIA; F. ROBITAILLE; A.C. LONG; C.D. RUDD; P ŠIMÁČEK; S.G. ADVANI. (2002). *Use Of Resin Transfer Molding Simulation To Predict Flow, Saturation And Compaction In The Vartm Process. Proc. of* The ASME International Mechanical Engineering Conference and Exposition IMECE. November 17-22, 2002, New Orleans, Louisiana.

A. RAGONDET, N.C. CORREIA, F. ROBITAILLE, A. C. LONG AND C.D. RUDD (2002). *Experimental Investigation And Modelling Of The Vacuum Infusion Process. Proc. of* Tenth European Conference on Composite Materials ECCM 10 June 3-6 2002, Bruges, Belgium.

A. RAGONDET, N. C. CORREIA, F. ROBITAILLE, A.C. LONG, C.D RUDD (2002). *Experimental Investigation On Vacuum Infusion Process. Proc. of* Ninth International Conference on Fibre Reinforced Composites FRC9, 26-28 March 2002, Newcastle, UK.

N. C. CORREIA, A. RAGONDET, F. ROBITAILLE, A. C. LONG AND C. D. RUDD (2002). *Modelling The Vacuum Infusion Of Composite Materials. Proc.* of Ninth International Conference on Fibre Reinforced Composites FRC9, 26-28 March 2002, Newcastle, UK.

APPENDIX 2.A ANALYTICAL MODEL OF VI

Figure 2.4 can be mathematically interpreted as:

$$\oint_S \rho \cdot \mathbf{u} \cdot \hat{\mathbf{n}} \cdot dS + \frac{\partial}{\partial t} \cdot \int_V \rho \cdot \phi \cdot dV = 0 \tag{2.A.1}$$

Assuming that porosity presents a negligible variation within the control volume:

$$\frac{\partial}{\partial t}\left[\phi \cdot \int_V dV\right] + \left(u_o \cdot h_o - u_i \cdot h_i\right) = 0 \tag{2.A.2}$$

Integrating over the volume and changing to a differential form:

$$\frac{\partial}{\partial t}[\phi \cdot h \cdot \partial x] + \partial\left(u \cdot h\right) = 0 \tag{2.A.3}$$

Converting the porosity term:

$$\partial x \cdot \frac{\partial}{\partial t}\left[\left(1 - v_f\right) \cdot h\right] = -\partial\left(u \cdot h\right) \tag{2.A.4}$$

And noting that $v_f \cdot h$ is constant in time, one obtains:

$$\frac{\partial h}{\partial t} = -\frac{\partial\left(u \cdot h\right)}{\partial x} \tag{2.A.5}$$

APPENDIX 2.B.1 UNIFICATION OF VI MODELS IN THE LITERATURE

Gutowski *et al* (1987) propose:

$$\frac{\partial}{\partial x}\left(u\cdot\frac{\partial\xi}{\partial z}\right)+\frac{\partial}{\partial t}\left[\left(1-v_f\right)\cdot\frac{\partial\xi}{\partial z}\right]=0 \qquad (2.B.1.6)$$

Where:

$$\frac{\partial\xi}{\partial z}=\frac{v_{f_0}}{v_f} \qquad (2.B.1.7)$$

And v_0 is the initial fibre volume fraction. Rearranging,

$$\frac{\partial}{\partial x}\left(u\cdot\frac{v_0}{v_f}\right)+\frac{\partial}{\partial t}\left[\left(1-v_f\right)\cdot\frac{v_0}{v_f}\right]=0 \qquad (2.B.1.8)$$

Rearranging leads to:

$$v_{f_0}\cdot\frac{\partial}{\partial x}\left(u\cdot\frac{1}{v_f}\cdot\frac{h}{h}\right)+v_{f_0}\cdot\frac{\partial}{\partial t}\left[\left(1-v_f\right)\cdot\frac{1}{v_f}\cdot\frac{h}{h}\right]=0 \qquad (2.B.1.9)$$

Equation (2.B.1.9) can be simplified further:

$$\frac{\partial}{\partial x}\left(u\cdot\frac{\rho\cdot h}{\rho_{\text{sup}}}\right)+\frac{\partial}{\partial t}\left[\left(1-v_f\right)\cdot\frac{\rho\cdot h}{\rho_{\text{sup}}}\right]=0 \qquad (2.B.1.10)$$

Where ρ and $\rho_{surface}$ are constants and can therefore be removed from the differentials:

$$\frac{\partial}{\partial x}(u\cdot h)+\frac{\partial}{\partial t}\left[\left(1-v_f\right)\cdot h\right]=0 \qquad (2.B.1.11)$$

This, in light of Equation (2.A.4) leads to

$$\frac{\partial h}{\partial t}=-\frac{\partial}{\partial x}(u\cdot h) \qquad (2.B.1.12)$$

APPENDIX 2.B.2 UNIFICATION OF THE SCHEIDEGGER-HAN MODELS

Scheidegger and Han *et al* (2000) propose:

$$\frac{\partial\left(\phi\cdot\left(1+\kappa\right)\right)}{\partial t}=\frac{\partial u}{\delta x} \tag{2.B.2.1}$$

where the bulk compressibility κ is described in Scheidegger (1974) as:

$$\left(1+\kappa\right)=\frac{V}{V_0}=\frac{h}{h_0} \tag{2.B.2.2}$$

V represents volume and the index *0* refers to its initial value. Equation (2.B.2.2) can be written as:

$$\frac{\partial\left(\left(1-\frac{\rho_{sup}}{\rho\cdot h}\right)\cdot\frac{h}{h_0}\right)}{\partial t}=\frac{\partial u}{\partial x} \tag{2.B.2.3}$$

Simplifying the LHS:

$$\frac{1}{h_0}\frac{\partial\left(h-\frac{\rho_{sup}}{\rho}\right)}{\partial t}=\frac{\partial u}{\partial x} \tag{2.B.2.4}$$

This can then be written in a compact form as:

$$\frac{\partial h}{\partial t}=h_0\cdot\frac{\partial u}{\delta x} \tag{2.B.2.5}$$

Note that, in the development of (2.B.2.1), Scheidegger uses Gauss' theorem. This approach requires moving the time differential inside the volume integral, which is incorrect in VI since the volume is also changing with time.

APPENDIX 2.B.3 UNIFICATION OF THE MODEL BY KANG *ET AL.*

According to Kang *et al* (2001) flow in VI is given by:

$$-\frac{1}{v_f}\cdot\frac{\partial v_f}{\partial t}=\frac{\partial}{\partial x}\left(\frac{K}{\mu}\cdot\frac{\partial P}{\partial x}\right) \tag{2.B.3.1}$$

Which can be written as:

$$\frac{\rho\cdot h}{\rho_{\sup}}\cdot\frac{\partial\left(\frac{\rho_{\sup}}{\rho\cdot h}\right)}{\partial t}=\frac{\partial u}{\partial x} \tag{2.B.3.2}$$

Expanding the LHS:

$$-\frac{1}{h}\cdot\frac{\partial h}{\partial t}=\frac{\partial u}{\partial x} \tag{2.B.3.3}$$

Which becomes:

$$\frac{\partial h}{\partial t}=-h\cdot\frac{\partial u}{\partial x} \tag{2.B.3.4}$$

APPENDIX 2.C DEVELOPMENTS ON THE EXPANSION RATE DIFFERENTIAL

The expansion rate differential (LHS of Equation (2.23)) is a composite function of α, L and t. In the terms defined by Equation (2.24) the expansion rate becomes:

$$\frac{\partial(h(\alpha))}{\partial\alpha}\cdot\frac{\partial(\alpha(L))}{\partial L}\cdot\frac{\partial(L(t))}{\partial t}=-\frac{\partial h}{\partial\alpha}\cdot\frac{x}{L^2}\cdot\frac{\partial L}{\partial t} \qquad (2.C.1)$$

Due to the constant flow rate condition in 1D one can interpret the velocity of the flow front $\delta L / \delta t$ as:

$$\frac{\partial L}{\partial t}\cdot[h]_{\alpha=1}=u\cdot h \qquad (2.C.2)$$

where $[h]\alpha_{=1}$ is the thickness at the flow front. Rearranging (2.C.2):

$$\frac{\partial L}{\partial t}=\frac{u\cdot h}{[h]_{\alpha=1}}=u\cdot h^{*} \qquad (2.C.3)$$

Where h^{*} is the thickness value normalised with the thickness at the flow front. Considering (2.C.1) and (2.C.3) one can write:

$$\frac{\partial h}{\partial t}=\frac{K\cdot x\cdot h^{*}}{\mu\cdot L^2}\cdot\frac{\partial h}{\partial\alpha}\cdot\frac{\delta P}{\delta\alpha}\cdot\frac{\delta\alpha}{\delta x} \qquad (2.C.4)$$

and since

$$x\cdot\frac{\partial\alpha}{\partial x}=x\cdot\frac{1}{L}=\alpha \qquad (2.C.5)$$

One can write:

$$\frac{\partial h}{\partial t}=\frac{h^{*}\cdot\alpha\cdot K}{L^2\cdot\mu}\cdot\frac{\delta h}{\delta\alpha}\cdot\frac{\delta P}{\delta\alpha} \qquad (2.C.6)$$

Which leads to:

$$\frac{\partial h}{\partial t}=\frac{h^{*}\cdot\alpha\cdot K}{L^2\cdot\mu}\cdot\frac{\delta h}{\delta P}\cdot\left(\frac{\delta P}{\delta\alpha}\right)^2 \qquad (2.C.7)$$

Through this substitution, one converts Equation (2.23) to an ODE.

APPENDIX 3.A VISCOELASTICITY IN SATURATED EXPERIMENTS

Using a model of radial flow through isotropic porous media one can determine the contribution of squeeze-flow of Newtonian fluids to the total compaction force (Saunders, 1997):

$$P_{\text{Squeeze flow}} = \frac{\mu \cdot R^2}{8 \cdot K \cdot h} \cdot \frac{dh}{dt} \tag{3.A.1}$$

However, in experiments one observes that the contribution of squeeze flow is negligible. This is illustrated in Figure 3.A.1.

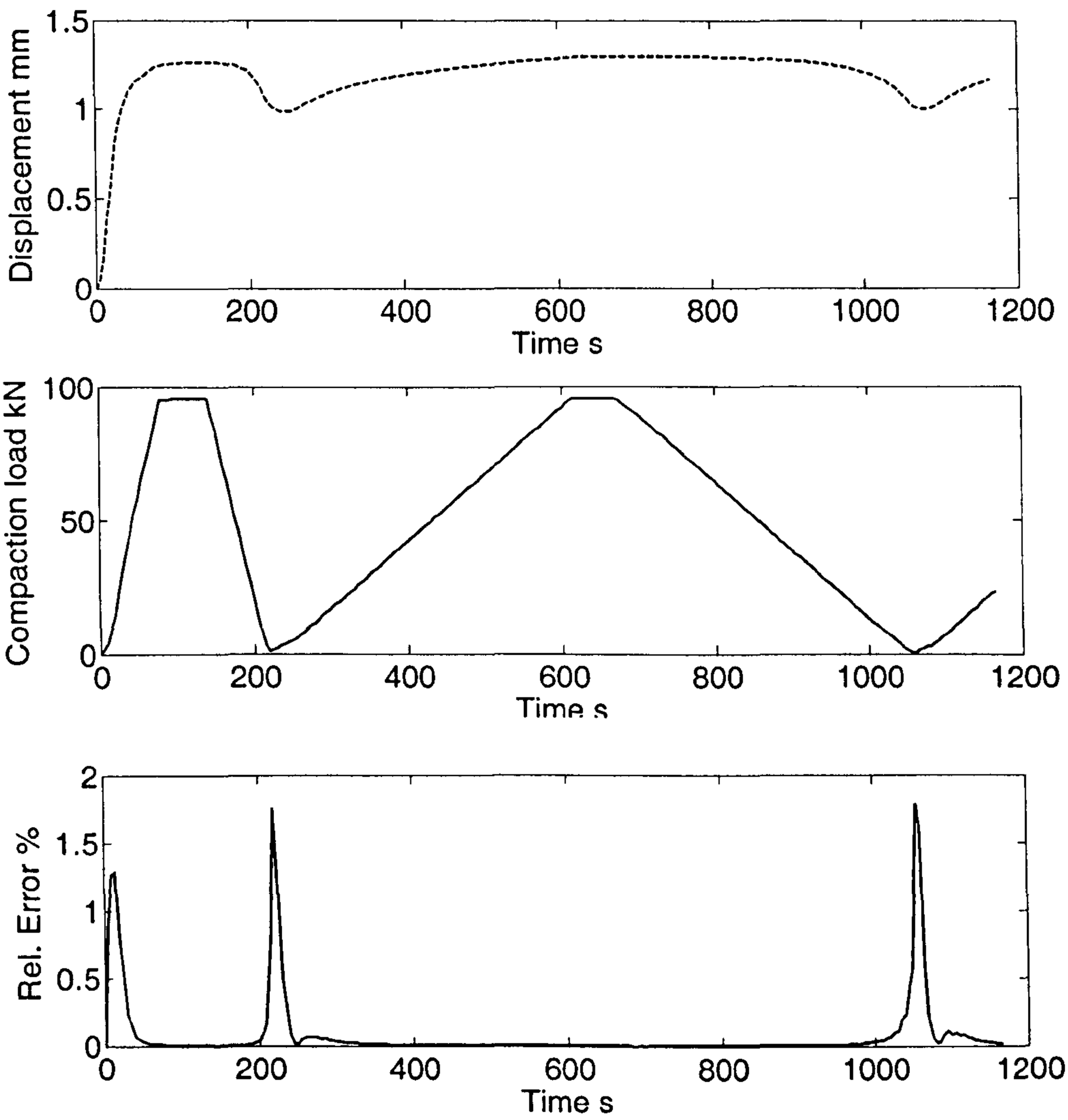

Figure 3.A.1 – Error in measured pressure due to squeeze flow. Figure illustrates that the error increases at low compaction loads (as crosshead speed is maximum) but does not reach 2% at the loading rate used

APPENDIX 3.B RIG ALIGNMENT AND STIFFNESS

The parallelism of the compaction surfaces of the rig was checked to within ±0.05 mm through the use of feeler gages ensuring that the set-up was parallel. It was thought that this level of parallelism was adequate for the experiments. Figure 3.B.1 shows the load displacement curve in a machine compliance test. Note that there is virtually no load before 40 μm, which is possibly due to the lack of exact parallelism between the compaction surfaces. Note also that, at 0.1 kN maximum load, the compaction tests are virtually free from machine compliance error.

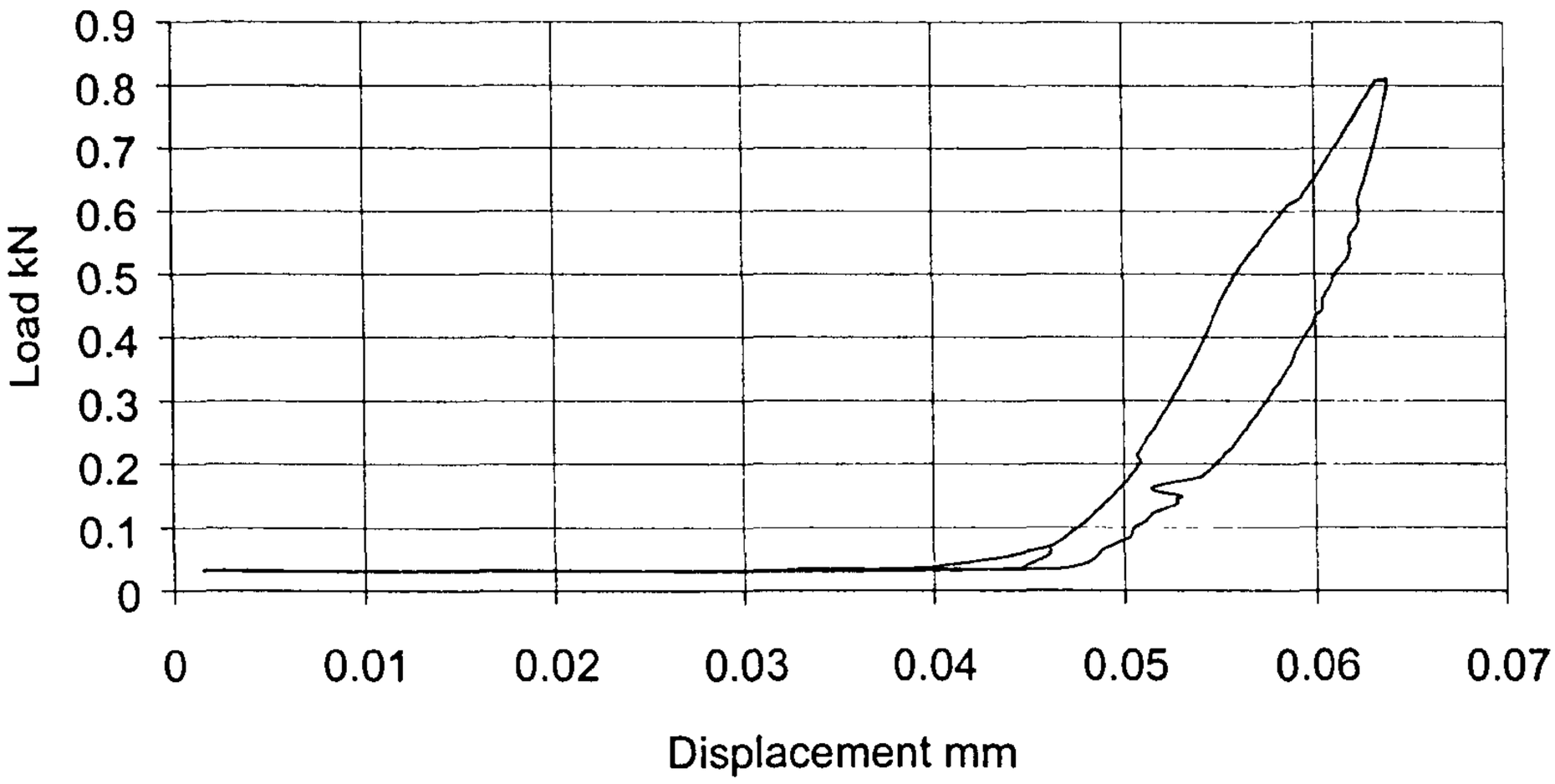

Figure 3.B.1 – Machine compliance test results. At 10 times the load applied to the reinforcements the test results show good stiffness of the setup: a maximum deflection of 65 μm at 0.8 kN

APPENDIX 3.C COMPACTION SUMMARY DATASHEETS

The following tables (3.C.1, 3.C.2, 3.C.3 and 3.C.4) present the summarized compaction data for the examined reinforcements.

Table 3.C.1 – FORMAX FGE 117 summary table

			Cycle	1		2		3	
				v_{f0}	B	v_{f0}	B	v_{f0}	B
Dry	Comp.	No. L.	3	0.201	0.089	0.332	0.045	0.350	0.041
			6	0.206	0.088	0.363	0.040	0.382	0.036
			12	0.205	0.089	0.379	0.036	0.398	0.033
			Cycle	1		2		3	
				v_{f0}	B	v_{f0}	B	v_{f0}	B
	Exp.	No. L.	3	0.409	0.028	0.409	0.028	0.435	0.023
			6	0.403	0.032	0.434	0.026	0.437	0.026
			12	0.419	0.028	0.428	0.027	0.445	0.024
			Cycle	1		2		3	
				v_{f0}	B	v_{f0}	B	v_{f0}	B
Saturated	Comp.	No. L.	3	0.129	0.128	0.333	0.046	0.413	0.027
			6	0.153	0.117	0.376	0.038	0.393	0.026
			12	0.156	0.112	0.354	0.042	0.420	0.024
			Cycle	1		2		3	
				v_{f0}	B	v_{f0}	B	v_{f0}	B
	Exp.	No. L.	3	0.456	0.018	0.467	0.017	0.495	0.014
			6	0.464	0.019	0.488	0.017	0.488	0.015
			12	0.464	0.018	0.482	0.016	0.478	0.014

Table 3.C.2 – Flemings UDUC summary table

			Cycle	1		2		3	
				v_{f0}	B	v_{f0}	B	v_{f0}	B
Dry	Comp.	No. L.	3	0.113	0.108	0.190	0.066	0.197	0.065
			6	0.110	0.114	0.206	0.062	0.217	0.059
			12	0.114	0.112	0.216	0.059	0.225	0.057
			Cycle	1		2		3	
				v_{f0}	B	v_{f0}	B	v_{f0}	B
	Exp.	No. L.	3	0.234	0.050	0.248	0.046	0.263	0.041
			6	0.243	0.049	0.265	0.043	0.264	0.044
			12	0.252	0.048	0.262	0.045	0.277	0.041
			Cycle	1		2		3	
				v_{f0}	B	v_{f0}	B	v_{f0}	B
Saturated	Comp.	No. L.	3	0.133	0.092	0.213	0.054	0.196	0.068
			6	0.127	0.101	0.215	0.058		
			12	0.145	0.091	0.217	0.059		
			Cycle	1		2		3	
				v_{f0}	B	v_{f0}	B	v_{f0}	B
	Exp.	No. L.	3	0.263	0.037	0.272	0.035		
			6	0.262	0.043	0.268	0.042		
			12	0.257	0.046	0.266	0.044		

Table 3.C.3 – Vetrotex RT600 summary table

Dry

Comp.

Cycle		1		2		3	
		v_{f0}	B	v_{f0}	B	v_{f0}	B
No. L.	3	0.035	0.150	0.059	0.107	0.063	0.102
	6	0.029	0.176	0.056	0.121	0.062	0.114
	12	0.031	0.166	0.064	0.105		

Exp.

Cycle		1		2		3	
		v_{f0}	B	v_{f0}	B	v_{f0}	B
No. L.	3	0.072	0.092	0.076	0.088	0.076	0.089
	6	0.067	0.109	0.070	0.105	0.073	0.103
	12	0.075	0.094	0.142	0.038		

Saturated

Comp.

Cycle		1		2		3	
		v_{f0}	B	v_{f0}	B	v_{f0}	B
No. L.	3	0.022	0.199	0.042	0.145		
	6	0.021	0.222	0.046	0.158		
	12	0.031	0.169	0.060	0.114		

Exp.

Cycle		1		2		3	
		v_{f0}	B	v_{f0}	B	v_{f0}	B
No. L.	3	0.060	0.117	0.064	0.105		
	6	0.062	0.132	0.064	0.130		
	12	0.074	0.097	0.076	0.096		

Table 3.C.4 – Vetrotex U750 summary table

Dry

Comp.

Cycle		1		2		3	
		v_{f0}	B	v_{f0}	B	v_{f0}	B
No. L.	3	0.175	0.086	0.306	0.041	0.321	0.038
	6	0.178	0.088	0.309	0.042	0.320	0.041
	12	0.178	0.090	0.302	0.047	0.321	0.043

Exp.

Cycle		1		2		3	
		v_{f0}	B	v_{f0}	B	v_{f0}	B
No. L.	3	0.359	0.028	0.372	0.026	0.386	0.024
	6	0.362	0.029	0.382	0.026	0.359	0.032
	12	0.347	0.037	0.436	0.017	0.000	0.000

Saturated

Comp.

Cycle		1		2		3	
		v_{f0}	B	v_{f0}	B	v_{f0}	B
No. L.	3	0.176	0.085	0.284	0.050		
	6	0.181	0.086	0.270	0.055		
	12	0.174	0.093	0.285	0.053		

Exp.

Cycle		1		2		3	
		v_{f0}	B	v_{f0}	B	v_{f0}	B
No. L.	3	0.368	0.027	0.397	0.023		
	6	0.354	0.031	0.376	0.028		
	12	0.357	0.033	0.374	0.031		

APPENDIX 3.D POLYNOMIAL FIT DATA TABLES

Table 3.D.1 – Fluid pressure field coefficients as a function of inlet and outlet pressure and compaction properties of the reinforcement.

Parameters			Coefficient
Pout	*Pin*	*vf0*	*a* Pa
0	50000	0.10	-9555
		0.15	-8186
		0.20	-7088
		0.25	-6136
	60000	0.10	-14914
		0.15	-12784
		0.20	-11072
		0.25	-9587
	70000	0.10	-22347
		0.15	-19161
		0.20	-16597
		0.25	-14370
	80000	0.10	-32936
		0.15	-28238
		0.20	-24450
		0.25	-21157
	90000	0.10	-49408
		0.15	-42302
		0.20	-36559
		0.25	-31565
10000	50000	0.10	-6466
		0.15	-5541
		0.20	-4800
		0.25	-4158
	60000	0.10	-10981
		0.15	-9416
		0.20	-8160
		0.25	-7070
	70000	0.10	-17467
		0.15	-14983
		0.20	-12986
		0.25	-11252
	80000	0.10	-26952
		0.15	-23118
		0.20	-20031
		0.25	-17348
	90000	0.10	-42020
		0.15	-35997
		0.20	-31136
		0.25	-26910

Parameters			Coefficient
Pout	*Pin*	*vf0*	*a* Pa
20000	50000	0.10	-3865
		0.15	-3314
		0.20	-2872
		0.25	-2489
	60000	0.10	-7492
		0.15	-6427
		0.20	-5572
		0.25	-4831
	70000	0.10	-12982
		0.15	-11140
		0.20	-9662
		0.25	-8378
	80000	0.10	-21304
		0.15	-18283
		0.20	-15854
		0.25	-13743
	90000	0.10	-34894
		0.15	-29910
		0.20	-25895
		0.25	-22405
30000	50000	0.10	-1837
		0.15	-1576
		0.20	-1366
		0.25	-1185
	60000	0.10	-4523
		0.15	-3881
		0.20	-3367
		0.25	-2922
	70000	0.10	-8958
		0.15	-7690
		0.20	-6674
		0.25	-5792
	80000	0.10	-16047
		0.15	-13779
		0.20	-11958
		0.25	-10376
	90000	0.10	-28071
		0.15	-24077
		0.20	-20866
		0.25	-18075

Table 3.D.2 – Fluid pressure field coefficients as a function of inlet and outlet pressure and compaction properties of the reinforcement

Parameters			Coefficient
Pout	*Pin*	*vf0*	*a* Pa
		0.10	-495
	50000	0.15	-425
		0.20	-368
		0.25	-320
		0.10	-2176
	60000	0.15	-1868
		0.20	-1621
		0.25	-1408
		0.10	-5483
40000	70000	0.15	-4709
		0.20	-4090
		0.25	-3552
		0.10	-11256
	80000	0.15	-9670
		0.20	-8399
		0.25	-7295
		0.10	-21605
	90000	0.15	-18544
		0.20	-16088
		0.25	-13955

APPENDIX 4.A COMPACTION AT THE SATURATION FRONT

Assuming that flow occurs through the thickness alone one can express the 1D flow of resin according to Darcy's law as:

$$\dot{h}_S = \left\langle \dot{h} \right\rangle = -\frac{K_S}{\mu} \cdot \frac{\Delta P}{h_S} \tag{4.A.1}$$

Where the subscripts *S* and *NS* indicate saturated and non-saturated terms shown in Figure 4.A.1.

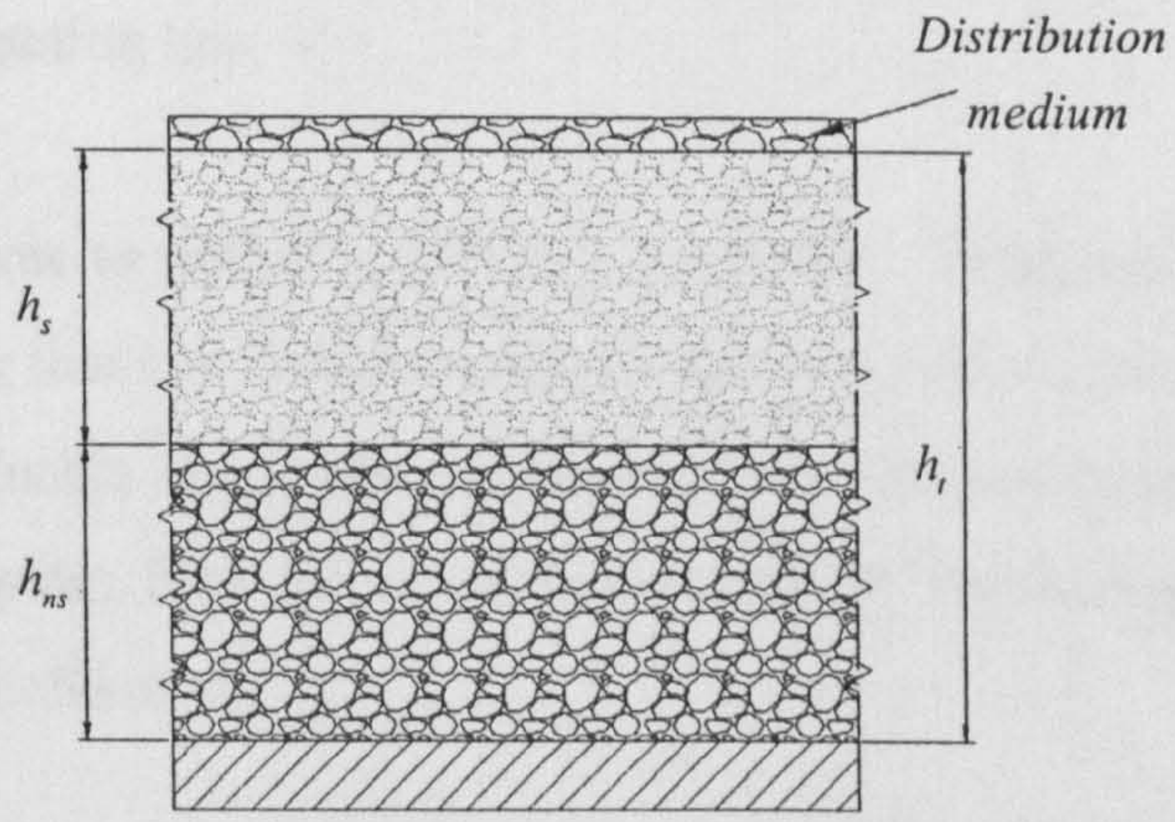

Figure 4.A.1 – 1D vertical flow saturation problem

Equation (4.A.1) can in turn be integrated to yield the saturated thickness during a time interval. Considering the pressure gradient to be constant during that interval:

$$\Delta h_{S_i} = \sqrt{-\frac{K_{NS}}{\mu} \cdot \Delta P_i \cdot \Delta t_i} \tag{4.A.2}$$

Which makes the total height saturated at time interval i in a node j equal to:

$$h_{i,j} = \sum_{n=1}^{i} \Delta h_{n,j} \tag{4.A.3}$$

And the flow rate into the element:

$$\dot{Q}_{i,j} = \left\langle \dot{h}_{i,j} \right\rangle \cdot dx \cdot dy \tag{4.A.4}$$

Where *dx* and *dy* refer to the dimensions of element *i*.

Another important issue is the definition of the term "saturation". Saturation is normally described as the fraction of free interconnected-pore volume that is filled with fluid. Due to the different compaction behavior displayed by dry and lubricated fibers, the definition of free volume must be cautious. The "real" free volume that can be occupied by resin is the volume that is defined by compacted lubricated fibers only. The "real" saturation (or S_{real}) is therefore only function of the lubricated compaction law.

It is possible however to define a different saturation. "Apparent" saturation (or S_{ap}) is the saturation that can be calculated by using as free volume the sum of the dry and wet free volumes at any given moment. This apparent saturation is, as will be shown, an important element in the calculation of the thickness in the non-saturated area. It is defined as:

$$s_{ap} = \frac{h_S \phi_S}{h_S \phi_S + h_{NS} \phi_{NS}} \tag{4.A.5}$$

Accepting that the v_f in any given moment is given by

$$v_f = \frac{A_s}{\rho} \cdot \frac{1}{h_T} \tag{4.A.6}$$

and that the total thickness (h_T) is:

$$h_T = h_S + h_{NS} \tag{4.A.7}$$

Then:

$$h_T = \frac{A_s}{\rho} \cdot \frac{1}{S_{ap} v_{f_S} + \left(1 - S_{ap}\right) v_{f_{NS}}} \tag{4.A.8}$$

Where A_s and ρ represent respectively the superficial density and density of the reinforcement, and v_f is the fibre volume fraction.

Combining Equations (4.A.3), (4.A.5), (4.A.7) and (4.A.8) one can obtain the values of s_{AP} and h_T and h_{NS} analytically. The results of this analysis are shown in Figure 4.A.2.

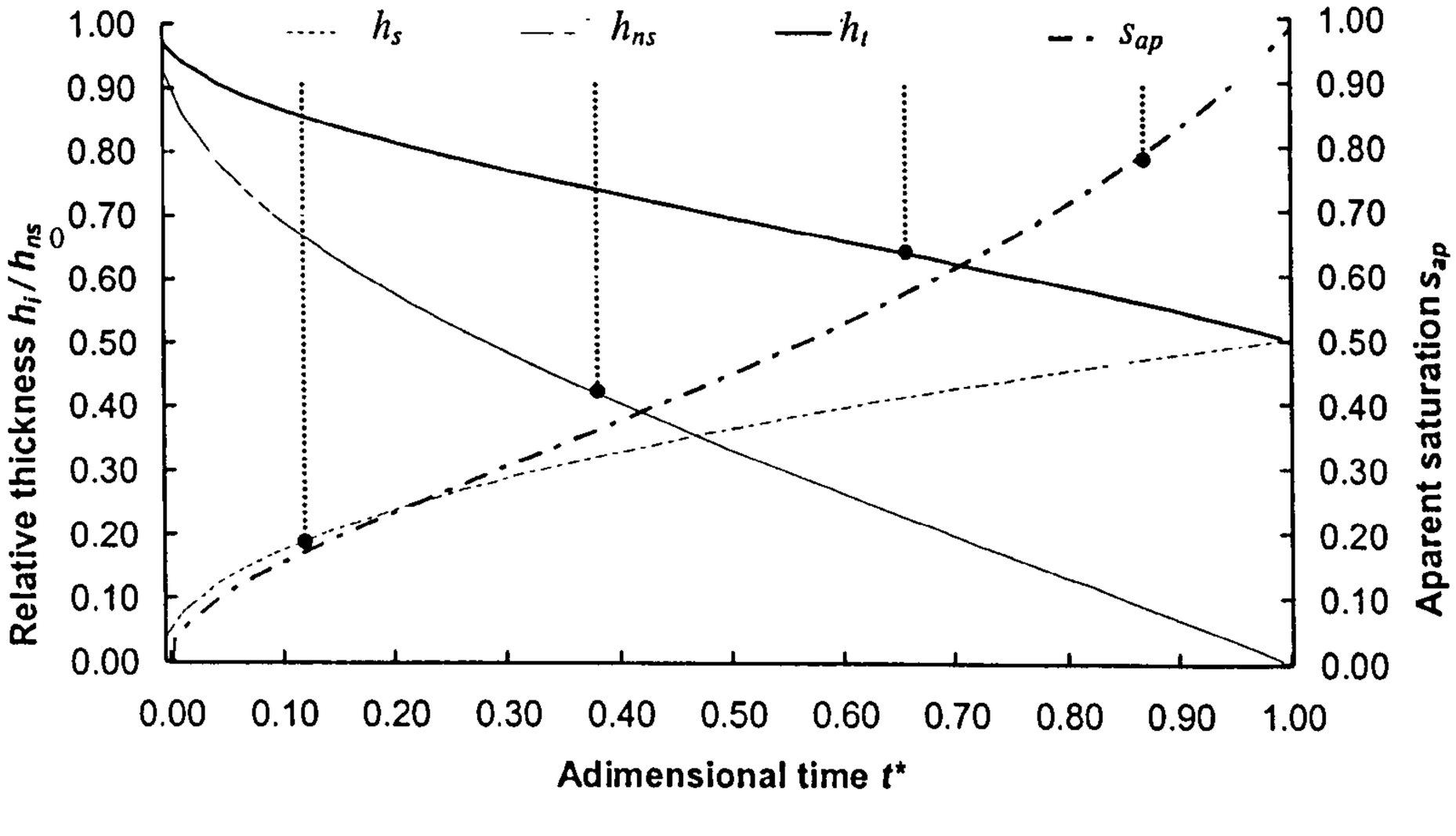

Figure 4.A.2 – Thickness in a saturating section vs. time

APPENDIX 4.B EVOLUTION OF INLET PRESSURE WITH TIME

Applying Poiseuille's law to the laminar flow in the inlet pipe system:

$$Q = -\frac{\pi D^4}{32\mu} \cdot \frac{(P_2 - P_1)}{L_{\text{Hose}}} \tag{4.B.1}$$

Where P_1 is the atmospheric pressure and P_2 is the pressure at the gate inside the mould. The equivalent permeability of the pipe can therefore be seen as:

$$K_{\text{hose}} = \frac{\pi D^4}{32\mu} \tag{4.B.2}$$

Inside the mould, flow rate is given by Darcy's law:

$$Q = -\frac{(L_{\text{inlet}} h) \cdot K_{VI}}{\phi \cdot \mu} \frac{P_3 - P_2}{\cdot L} \tag{4.B.3}$$

where P_3 is the outlet pressure and L_{inlet} is the dimension of the inlet. Recognizing that both flow rates are the same one postulates that:

$$(L_{\text{inlet}} h) \cdot \frac{K_{VI}}{\phi} \cdot \frac{P_3 - P_2}{L} = \frac{\pi D^4}{32} \cdot \frac{(P_2 - P_1)}{L_{\text{Hose}}} \tag{4.B.4}$$

It is then possible to show that pressure at the inlet is a weighted average of permeabilities, pressures and filled length:

$$\frac{(L_{\text{inlet}} h) \cdot K_{VI} \cdot \frac{P_3}{L} + \frac{\pi D^4}{32} \cdot \frac{P_1}{L_{\text{Hose}}}}{\frac{(L_{\text{inlet}} h) \cdot K_{VI}}{L} + \frac{\pi D^4}{32} \cdot \frac{1}{L_{\text{Hose}}}} = P_2 \tag{4.B.5}$$

Fill time then follows from the variable gate pressure defined in Equation(4.B.5) and Darcy's law. Considering the flow front position L equals *0* at $t=0$:

$$\frac{\phi \cdot \mu}{K_{VI} \cdot (P_1 - P_3)} \frac{L^2}{2} + \frac{32 \cdot \phi \cdot \mu \cdot L_{\text{Hose}} \cdot L_{\text{inlet}} \cdot h}{(P_1 - P_3) \cdot \pi \cdot D^4} L = t \qquad (4.B.6)$$

Combining Equations (4.B.5) and (4.B.6) one can solve this problem and model the gate pressure as a function of the inlet arrangement.

APPENDIX 5.A LBASIC LIMS-VI CODE

```
REM=============================================================================
REM                    By Nuno A.C.M. Correia, Started 16th of January 2002.
REM                    LBASIC code to model flow in Vacuum Infusion with LIMS
REM=============================================================================

REM=============================================================================
REM                              PROCEDURE VI (vacuum infusion)
REM=============================================================================

PROC        VI

  PRINT     "Reading mesh"
  READ      "FE mesh.dmp"
  PRINT     "Mesh: OK"

  PRINT     "Setting gates"
  CALL            Setting
  PRINT     "Gates: SET"

  PRINT     "Setting variables and constants"
  CALL      SetConstants
  PRINT     "Variables and constants· SET"

  PRINT     "Sorting elements"
  CALL      SortVerticalElements
  PRINT     "Sorting complete"

  PRINT     "Generating property table"
  CALL      PropertyData
  PRINT     "Property table: OK."

  PRINT     "Updating properties"
  CALL      UpdateProperties
  PRINT     "Properties: SET"

  PRINT     "Advancing flow front"
  SOLVE
  PRINT     "Flow advancement: OK."

  REM <           Begin solver
  CALL            FLOW

  SETOUTTYPE      "TPLT"
  WRITE           "VI_OUT"

ENDPROC

REM=============================================================================
```

```
REM                              INDEX OF SUB-PROCEDURES
REM
REM          1. PROCEDURE SetConstants          - Sets the global variables
REM          2. PROCEDURE PropertyData          - Create a table of material prpts V. pressure
REM             2.1. PROCEDURE TableCompletion  - Prints the state of the property data table completion
REM          3. PROCEDURE FLOW                  - Computes VI flow
REM             3.1. PROCEDURE SortVerticalElements - Computes geom. data for material property update
REM             3.2. PROCEDURE UpdateProperties - Updates material properties according to the pressure
field
REM          6. PROCEDURE Setting               - Sets the inlet scheme.
REM=============================================================================
REM=============================================================================
REM                              PROCEDURE SetConstants
REM
REM          This procedure sets the script's constants and variables.
REM          Variables and constants (f=floating point, i=integer and a=array)
REM=============================================================================

PROC          SetConstants

  DIM                 aOldPressureInNodes(sonumbernodes),          aNewPressureInNodes(sonumbernodes),
aOldNodalSinkTerms(sonumbernodes)
  DIM          aOldNodalFreeVolume(sonumbernodes),aNewNodalFreeVolume(sonumbernodes)
  DEFDBL        fPressureInElements, fPreviousTimeStep, fPreviousMoment, fMaxError, fError, fAux
  DEFINT        iElementCounter, iNodeCounter, iTypeOfElement, iAux
  DEFINT        NoOfNodes, NoOfElements

  LET           fMaxError=10
  LET           fPreviousMoment=0
  LET           fPreviousTimeStep=0
  LET           NoOfNodes=SONUMBERNODES
  LET           NoOfElements=SONUMBERELEMS

ENDPROC

REM=============================================================================
REM                              PROCEDURE PropertyData
REM          This procedure generates a number of vectors containing permeability, porosity, etc as a function of an index
(iBin)
REM                              which is the same as compaction pressure (from 1Pa to 100001 Pa)
REM=============================================================================
PROC          PropertyData


  DEFDBL                fCoeffA,fCoeffB,  fAreaDensityOfReinforcement,  fDensityOfReinforcement,
fSpecificSurfaceAreaOfFibres
  DEFDBL        fViscosity, fKozenyConstant
  DEFINT        iBin, iBinNo

  LET           fCoeffA=0.185
```

```
LET       fCoeffB=0.0965
LET       fAreaDensityOfReinforcement=12*.936                    REM kg/m2     DM
LET       fDensityOfReinforcement=2540                           REM kg/m3     RhoGlass=2540
LET       fKozenyConstant=71.8e-12
LET       fViscosity=.12
LET       iBinNo=105000                                          REM Bins are of roughly 1 Pa
DIM       aVolumeFraction(iBinNo)
DIM       aThickness(iBinNo)
DIM       aPermeabilityX(iBinNo)
DIM       aPermeabilityY(iBinNo)

FOR       iBin=1 TO iBinNo

  DEFDBL      fCompactionPressure

  LET       fCompactionPressure=iBin
  LET       aVolumeFraction(iBin)=fCoeffA*fCompactionPressure^fCoeffB
  LET       aThickness(iBin)=fAreaDensityOfReinforcement/(fDensityOfReinforcement*aVolumeFraction(iBin))
  LET       aPermeabilityX(iBin)=fKozenyConstant*(1-aVolumeFraction(iBin))^3/(aVolumeFraction(iBin))^2
  LET       aPermeabilityY(iBin)=fKozenyConstant*(1-aVolumeFraction(iBin))^3/(aVolumeFraction(iBin))^2

  CALL      TableCompletion

  ERASE     fCompactionPressure

NEXT        iBin

  ERASE     fCoeffA,fCoeffB,  fAreaDensityOfReinforcement,  fDensityOfReinforcement,
fSpecificSurfaceAreaOfFibres
  ERASE     fKozenyConstant, fViscosity, iBin, iBinNo

ENDPROC

REM=============================================================================
REM                          PROCEDURE TableCompletion
REM                  Prints the completed percentage of the data table.
REM=============================================================================

PROC        TableCompletion

IF      ((fCompactionPressure/105000*100)=((FLOOR(fCompactionPressure/105000*10))*10)) THEN

  DEFINT Completed
  LET    Completed=fCompactionPressure/105000*100
  PRINT  "Material data table ",Completed, "% completed"
  ERASE  Completed

ENDIF
```

```
ENDPROC

REM=============================================================================
REM                                PROCEDURE FLOW
REM                          Iterative flow advancement for VI
REM=============================================================================

PROC            FLOW

  DO
  REM <         Advance the flow front

 DO
 REM <          Iterate the pressure solution

   REM PRINT    "Getting pressure data for error calculation"
   REM <        Pressure data for error calculations
   FOR          iNodeCounter=1 TO NoOfNodes
     LET        aOldPressureInNodes(iNodeCounter)= GETNODALDATA(iNodeCounter, 10)
   NEXT         iNodeCounter
   REM PRINT    "Fetching pressure data: OK"

   REM <        Compute new pressure and flow rate and update properties

    REM PRINT   "Updating pressure field"
    UPDATEPQ
                REM PRINT   "UPDATEPQ: OK"

    REM PRINT   "Updating reinforcement properties"
    CALL        UpdateProperties
    REM PRINT   "Properties: SET"

   REM PRINT    "Computing error"
   REM <        Compute error in pressure solution
   LET          fError=0
   FOR          iNodeCounter=1 TO NoOfNodes
     LET        fError=fError+abs(GETNODALDATA(iNodeCounter, 10)-aOldPressureInNodes(iNodeCounter))
   NEXT         iNodeCounter
   LET          fError=fError/NoOfNodes
   REM PRINT    "Error calculation: OK. Error = ", fError

    LOOP        WHILE   (fError>fMaxError)

    SOLVE
    PRINT       "Flow calculation ",((1-SONUMBEREMPTY()/NoOfNodes)*100), "% completed"

  LOOP          WHILE   ((SONUMBERFILLED>0)and(SONUMBEREMPTY()>0))

ENDPROC

REM=============================================================================
```

```
REM                    PROCEDURE SortVerticalElements
REM        This procedure builds two vectors (aVrtclElmnts and aHrzntElmnts) which sort the elements into vertical and
"other"
REM                    so that permeability assignements can be adjusted for the element caracteristics.
REM=============================================================================

PROC            SortVerticalElements

   REM          Element counter definition
   DEFINT        iVrtclElmntsCntr, iHrzntlElmntsCntr
   REM

   REM          Boolean tests 1 and 2
   DEFINT        bTest1, bTest2
   REM

   LET          iVrtclElmntsCntr  = 1
   LET          iHrzntlElmntsCntr  = 1

   DIM          aVrtclElmnts(NoOfElements), aHrzntElmnts(NoOfElements)

     FOR        iElementCounter=1 TO NoOfElements

       REM      Tests "bTest*" check wether the y-coordinates of the first 3 nodes in an element are equal -> Vertical
wall
       LET                bTest1  =  ((1000*(GETNODALDATA(GETELEMDATA(iElementCounter,101),1)))  =
(1000*(GETNODALDATA(GETELEMDATA(iElementCounter,102),1))))
       LET                bTest2  =  ((1000*(GETNODALDATA(GETELEMDATA(iElementCounter,102),1)))  =
(1000*(GETNODALDATA(GETELEMDATA(iElementCounter,103),1))))

       IF       (bTest1=1 AND bTest2=1) THEN

         LET    aVrtclElmnts(iVrtclElmntsCntr) = iElementCounter

         REM    The following procedure is used to advance the counter "iVrtclElmntsCntr"
         REM    without leaving the old instance in memory

         DEFINT AUX
         LET    AUX = iVrtclElmntsCntr
         ERASE  iVrtclElmntsCntr
         DEFINT iVrtclElmntsCntr
         LET    iVrtclElmntsCntr = AUX+1
         ERASE  AUX

       ELSE

         LET    aHrzntElmnts(iHrzntlElmntsCntr) = iElementCounter

         REM    The following procedure is used to advance the counter "iHrzntlElmntsCntr"
         REM    without leaving the old instance in memory
```

```
    DEFINT  AUX
    LET     AUX = iHrzntlElmntsCntr
    ERASE   iHrzntlElmntsCntr
    DEFINT  iHrzntlElmntsCntr
    LET     iHrzntlElmntsCntr = AUX+1
    ERASE   AUX

  ENDIF

NEXT        iElementCounter
PRINT       "  Total number elements: ", NoOfElements
PRINT       "  Number of vertical elements: ", iVrtclElmntsCntr
PRINT       "  Number of horizontal elements: ", iHrzntlElmntsCntr
PRINT       "  Total elements (sorted): ",(iVrtclElmntsCntr+iHrzntlElmntsCntr)


ENDPROC

REM=============================================================================
REM                          PROCEDURE UpdateProperties
REM
REM          This procedure assigns material properties according to the data in the material tables
REM
REM=============================================================================


PROC            UpdateProperties

  DEFINT        iElementCounter


  FOR           iElementCounter=1 TO NoOfElements

    DEFDBL      fCompactionPressure = 0
    DEFINT      iUpdtPrprtsBin
    LET             iUpdtPrprtsBin = FLOOR(1e5-GETNODALDATA((GETELEMDATA(iElementCounter, (101))),
10))+1

    SETELEMDATA   (iElementCounter, 3,  aVolumeFraction(iUpdtPrprtsBin))
    SETELEMDATA   (iElementCounter, 2,  aThickness(iUpdtPrprtsBin))
    SETELEMDATA   (iElementCounter, 10, aPermeabilityX(iUpdtPrprtsBin))
    SETELEMDATA   (iElementCounter, 12, aPermeabilityY(iUpdtPrprtsBin))

    ERASE       fCompactionPressure, iUpdtPrprtsBin

  NEXT          iElementCounter
  ERASE         iElementCounter

ENDPROC
```

```
REM==========================================================================
====
REM                          PROCEDURE Setting (Definition of inlets)
REM==========================================================================
====


PROC Setting

  setgate 1, 1, 100000.000000

ENDPROC
```

APPENDIX 6.A MONTE-CARLO BASED VIRTUAL CONTROL CODE

```
%=============================================================================%
%                                Control code                                 %
%                                                                             %
%                        Permeability Generator  (PG)                         %
%                                and Process                                  %
%                        Control Algorithm (PCA)                              %
%=============================================================================%

function []                    =  Controlr()


%                                                                           1
%=============================================================================%

%  RELEVANT CONSTANTS

   Average                     =  26.2e-12;
   Standard_Deviation          =  2*5.68e-12;
   Thickness                   =  0.29e-3;
   Volume_Fraction             =  0 528;
   No_OF_TESTS                 =  5;
   No_OF_CONTROL_PHASES        =  5;
   GATES                       =  [1 2 3 4],
%=============================================================================%


%                                                                           1
%=============================================================================%

%  FE MODEL READER

   cd Bin, [NODAL_COORD, CONNECTIVITY_DATA]   =  MODEL_DATA;
   No_OF_ELEMENTS                 =  max(size(CONNECTIVITY_DATA));
   No_OF_NODES                    =  max(size(NODAL_COORD));

%=============================================================================%


%                                                                           1
%=============================================================================%

%  GATE SCHEME READER

   cd Bin, SCHEMES                =  GATE_SCHEMES;
%=============================================================================%
```

```
%                                                                                                    1
%=====================================================================================================%

%  IDEAL CASE DATA

   cd Bin, IDEAL_ELEM_DATA              =  GENERATE_DATA ( 1, No_OF_ELEMENTS, 0, ..
                                       Average, Thickness, Volume_Fraction);

   cd Bin, LIMSINFILE                          ( NODAL_COORD, CONNECTIVITY_DATA, IDEAL_ELEM_DATA,
No_OF_ELEMENTS );

   cd Bin, GATE_NODE_NUMBERS            =  find(GATES.*SCHEMES(1,:)>0);
   LIMS_AUTO_FILE                      ( 0, SCHEMES(1,GATES), GATE_NODE_NUMBERS);

   !lims

   cd bin, IDEAL_RESULT                 =  LIMS_RESULT (No_OF_NODES);    %(Node_Number, x, y, Time, Fill)
   IDEAL_RESULT                        =  sortrows(IDEAL_RESULT, [4 1]);

   BEGIN_INTERVAL=0;
   for i=1:1:No_OF_CONTROL_PHASES

      INTERVAL                         =  No_OF_NODES/No_OF_CONTROL_PHASES;
      CURRENT_INTERVAL                 =  BEGIN_INTERVAL+1:1:i*INTERVAL;
      IDEAL_NODES_FILLED(CURRENT_INTERVAL,1) =  IDEAL_RESULT(CURRENT_INTERVAL,1);
      IDEAL_NODES_FILLED(CURRENT_INTERVAL,2) =  IDEAL_RESULT(CURRENT_INTERVAL,5)*(i);
      BEGIN_INTERVAL                   =  max(CURRENT_INTERVAL)+1;

   end

   IDEAL_NODES_FILLED=sortrows(IDEAL_NODES_FILLED, 1);

   for i=1:1:No_OF_CONTROL_PHASES
      AUX(:,i)                         =  ((IDEAL_NODES_FILLED(:,2)<i+1).*IDEAL_NODES_FILLED(:,1)>0);
   end

   IDEAL_NODES_FILLED=AUX; %Nodes filled (rows 1/0) in each control step (columns). Equal to fill factor at each
step.
   clear AUX;

   copyfile ('AutoK.txt', 'ideal.txt')
%=====================================================================================================%


%                                                                                                    1
%=====================================================================================================%

%  TEST CYCLE

   for TEST_COUNTER                    =  1:1:No_OF_TESTS
```

TEST_COUNTER

```
%                                                                                                                    2
%====================================================================================================================%

% REALISTIC DATA GENERATOR

  cd Bin, ELEM_DATA                 =  GENERATE_DATA ( TEST_COUNTER, ...
                                       No_OF_ELEMENTS, Standard_Deviation, ...
                                       Average, Thickness, Volume_Fraction);

%====================================================================================================================%



 %                                                                                                                   2
%====================================================================================================================%

% LIMS INPUT FILE WRITER

  cd Bin, LIMSINFILE  ( NODAL_COORD, CONNECTIVITY_DATA, ELEM_DATA, No_OF_ELEMENTS )
  copyfile   ('AutoK.txt', 'real.txt')
  FILE_NAME                         =  ['Results\T#',num2str(TEST_COUNTER),'.txt'];
  copyfile   ('AutoK.txt', FILE_NAME)

  %                                                                                                                  2
  %==================================================================================================================%



  %                                                                                                                  2
  %==================================================================================================================%

  % RUN THE FIRST PHASE FOR THE "REAL" CASE (ALL GATES FULLY OPEN)

    cd Bin, GATE_NODE_NUMBERS               =  find(GATES.*SCHEMES(1,:)>0),% first gate scheme is all gates
open
    LIMS_AUTO_FILE( 0 , SCHEMES(1,GATES),  GATE_NODE_NUMBERS);
    !lims
    FILE_NAME                       =  ['Results\Sample#',num2str(TEST_COUNTER),'_No_control.tec'];
    copyfile   ('out.tec', FILE_NAME)

    cd Bin, GATE_NODE_NUMBERS               =  find(GATES.*SCHEMES(1,:)>0);% first gate scheme is all gates
open
    LIMS_AUTO_FILE(                 (No_OF_NODES-floor(No_OF_NODES/(No_OF_CONTROL_PHASES+1))),
SCHEMES(1,GATES),  GATE_NODE_NUMBERS);

    !lims

    cd bin, REAL_RESULT             =  LIMS_RESULT (No_OF_NODES);
```

```
    REAL_FILLED_NODES_OLD                    =    find((REAL_RESULT(:,1).*(REAL_RESULT(:,5)>0)>0))
%Nodes with fill factors larger than zero
    FILL_FACTORS                  =  (REAL_RESULT(:,1).*(REAL_RESULT(:,5))>0).*REAL_RESULT(:,5);
    Disagreement                                                    =      sum((IDEAL_NODES_FILLED(:,1)-
FILL_FACTORS).*(IDEAL_NODES_FILLED(:,1)...
                                -FILL_FACTORS));

    FILE_NAME                    =  ['Results\Phase#1Sample#',num2str(TEST_COUNTER),'.tec'];
    copyfile                       ('out.tec', FILE_NAME, 'ascii');
```

```
%=========================================================================%

  %                                                                      2
%=========================================================================%

  %  CONTROL CYCLE

    for CONTROL_PHASE_COUNTER          = 1:1:No_OF_CONTROL_PHASES

      copyfile ('ideal.txt', 'AutoK.txt'); % All control models use the "ideal" case for simulations since real data is not
known

    %                                                                      3
%=========================================================================%

    %  GATE CYCLE

      for GATE_CYCLE_COUNTER           =1:1:max(size(SCHEMES))


      %                                                                    4
%=========================================================================%

      %  RUN CONTROL PHASE m FOR GATE SCHEME n IN THE "IDEAL" CASE WITH REAL CASE FILL
FACTORS

        cd Bin, GATE_NODE_NUMBERS          = find(GATES.*SCHEMES(GATE_CYCLE_COUNTER,:)>0);
        LIMS_AUTO_FILE(                                                    (No_OF_NODES-
floor(No_OF_NODES*(CONTROL_PHASE_COUNTER+1)/(No_OF_CONTROL_PHASES+1))), ...
                  SCHEMES(GATE_CYCLE_COUNTER,GATES),  REAL_FILLED_NODES_OLD);

        !lims

        cd bin, REAL_RESULT              =  LIMS_RESULT (No_OF_NODES);
        REAL_FILLED_NODES                  =  find((REAL_RESULT(:,1).*(REAL_RESULT(:,5)>0)>0));
```

```
        FILL_FACTORS                                                    =
(REAL_RESULT(:,1).*(REAL_RESULT(:,5))>0).*REAL_RESULT(:,5);
        AREA_ERROR(GATE_CYCLE_COUNTER, 1)       =  GATE_CYCLE_COUNTER;
        AREA_ERROR(GATE_CYCLE_COUNTER,    2)                    =          sum((
IDEAL_NODES_FILLED(:,CONTROL_PHASE_COUNTER)-FILL_FACTORS)...
                                        .*(IDEAL_NODES_FILLED(:,CONTROL_PHASE_COUNTER)-
FILL_FACTORS));

      %
%=============================================================================%

      %                                                                  4
%=============================================================================%

      %  FILE BACKUP

        FILE_NAME                                                       =
['Results\Phase',num2str(CONTROL_PHASE_COUNTER+1),'\SCHM#',...
                                num2str(GATE_CYCLE_COUNTER),'T#',num2str(TEST_COUNTER),'.tec'];
        copyfile                        ('out.tec', FILE_NAME, 'ascii');


%=============================================================================%

    end %4

%=============================================================================%


    AREA_ERROR=sortrows(AREA_ERROR,2);
    GATE_SEQUENCE(TEST_COUNTER, CONTROL_PHASE_COUNTER) = AREA_ERROR(1,1)

    cd Bin, GATE_NODE_NUMBERS           = find(GATES.*SCHEMES(AREA_ERROR(1,1),:)>0);
    LIMS_AUTO_FILE( (No_OF_NODES-floor(No_OF_NODES/No_OF_CONTROL_PHASES)), ...
            SCHEMES(AREA_ERROR(1,1),GATES),...
            REAL_FILLED_NODES_OLD);

    copyfile ('real.txt', 'AutoK txt')
    !lims

    FILE_NAME               = ['Results\Phase#',num2str(CONTROL_PHASE_COUNTER+1),...
                        'Sample#',num2str(TEST_COUNTER),'.tec'];
    copyfile                ('out.tec', FILE_NAME, 'ascii');

    cd bin, REAL_RESULT             = LIMS_RESULT (No_OF_NODES);
    REAL_FILLED_NODES_OLD               = find((REAL_RESULT(:,1).*(REAL_RESULT(:,5)>0)>0));
    FILL_FACTORS                = (REAL_RESULT(:,1).*(REAL_RESULT(:,5))>0).*REAL_RESULT(:,5);
```

```
clear AREA_ERROR

%                                                                                                    2
%=====================================================================================================%

%   RESULT READER

   cd Bin
   RESULTS (TEST_COUNTER, :)          =   ANALYSE_OUTPUT (No_OF_NODES, TEST_COUNTER);

%=====================================================================================================%
```

```
  end %3

%=====================================================================================================%


end %2
%=====================================================================================================%


%=====================================================================================================%
%   SAVING RELEVANT OUTPUTS
  RESULTS                            =   sortrows(RESULTS,[ 3 2 ]);
  %Rows are sorted by fill time in order to determine which simulation took the longest to fill.

  cd Results
     save Results.txt RESULTS -ascii;
        %RESULTS(X, Y, FILL.TIME, TEST.COUNTER,LAST.NODE.NUMBER)
  cd ..

  %plot (RESULTS(:,1), RESULTS(:,2), '.')
%=====================================================================================================%

GATE_SEQUENCE
```

APPENDIX 6.B AUXILIARY FUNCTIONS IN APP. 6.A

6.B.1 Function ANALYSE_OUTPUT

```
function [ RESULTS ] = ANALYSE_OUTPUT(No_OF_NODES, TEST_COUNTER)
% This function analyses the LIMS output, storing the time step results in a matrix (RESULTS)

  cd ..
  [x, y, z, p, Time, Fill]          =  textread('out.tec','%f %f %f %s %f %f','headerlines',3);
  Time                              =  Time(1:1:No_OF_NODES);
  Fill                              =  Fill(1:1:No_OF_NODES);
  x                                 =  x(1:1:No_OF_NODES);
  y                                 =  y(1:1:No_OF_NODES);

  % Formation of a regular grid with the same dimensions as the FE mesh model.
  [xi,yi]                           =  meshgrid((min(x)):((max(x)-min(x))/300).(max(x)),...
                                       (min(y)):((max(y)-min(y))/300):(max(y)));

  % Generation of the interpolated surface of the fill time on the mesh grid
  Ti                                =  griddata(x,y,Time,xi,yi, 'cubic');

  %Finding the index of the highest fill time value (last point filled)
  INDEX                             =  find (Ti==max(max(Ti)));

  RESULTS(1)                        =  xi(INDEX);
  RESULTS(2)                        =  yi(INDEX);
  RESULTS(3)                        =  Ti(INDEX);
  RESULTS(4)                        =  TEST_COUNTER;

  %RESULTS(X, Y, FILL.TIME, TEST.COUNTER,LAST.NODE.NUMBER)
```

6.B.2 Function LTQNORM

% This solution of the inverse cumulative normal distribution was obtained in the Math Works database and is an implementation of Halley's rational method.

```
function z = LTQNORM(p)
%LTQNORM Lower tail quantile for standard normal distribution.

% Coefficients in rational approximations.
a = [ -3.969683028665376e+01  2.209460984245205e+02 ...
    -2.759285104469687e+02  1.383577518672690e+02 ...
    -3.066479806614716e+01  2.506628277459239e+00 ];
b = [ -5.447609879822406e+01  1.615858368580409e+02 ...
    -1.556989798598866e+02  6.680131188771972e+01 ...
    -1.328068155288572e+01 ];
c = [ -7.784894002430293e-03 -3.223964580411365e-01 ...
    -2.400758277161838e+00 -2.549732539343734e+00 ...
     4.374664141464968e+00  2.938163982698783e+00 ];
d = [  7.784695709041462e-03  3.224671290700398e-01 ...
     2.445134137142996e+00  3.754408661907416e+00 ];

% Define break-points.
plow  = 0.02425;
phigh = 1 - plow;

% Initialize output array.
z = zeros(size(p));

% Rational approximation for central region:
k = plow <= p & p <= phigh;
if any(k(:))
  q = p(k) - 0.5;
  r = q.*q;
  z(k) = (((((a(1)*r+a(2)).*r+a(3)).*r+a(4)).*r+a(5)).*r+a(6)).*q ./ ...
       (((((b(1)*r+b(2)).*r+b(3)).*r+b(4)).*r+b(5)).*r+1);
end

% Rational approximation for lower region:
k = 0 < p & p < plow;
if any(k(:))
  q  = sqrt(-2*log(p(k)));
  z(k) = (((((c(1)*q+c(2)).*q+c(3)).*q+c(4)).*q+c(5)).*q+c(6)) ./ ...
       ((((d(1)*q+d(2)).*q+d(3)).*q+d(4)).*q+1);
end

% Rational approximation for upper region:
k = phigh < p & p < 1;
if any(k(.))
  q  = sqrt(-2*log(1-p(k)));
  z(k) = -(((((c(1)*q+c(2)).*q+c(3)).*q+c(4)).*q+c(5)).*q+c(6)) ./ ...
       ((((d(1)*q+d(2)).*q+d(3)).*q+d(4)).*q+1);
```

```
end

% Case when P = 0:
z(p == 0) = -Inf;

% Case when P = 1:
z(p == 1) = Inf;

% Cases when output will be NaN:
k = p < 0 | p > 1 | isnan(p);
if any(k(:))
  z(k) = NaN;
end

% The relative error of the approximation has absolute value less
% than 1.15e-9.  One iteration of Halley's rational method (third
% order) gives full machine precision.
k = 0 < p & p < 1;
if any(k(:))
  e = 0.5*erfc(-z(k)/sqrt(2)) - p(k);          % error
  u = e * sqrt(2*pi) .* exp(z(k).^2/2);        % f(z)/df(z)
%   z(k) = z(k) - u;                           % Newton's method
  z(k) = z(k) - u /( 1 + z(k).*u/2 );          % Halley's method
end
```

6.B.3 Function GATE_SCHEMES

```
function [ SCHEMES ]          =          GATE_SCHEMES( )
%Truth table array of pressures at the corner nodes on a rectangular plate

SCHEMES                       =
          [100000   100000   100000   100000
          100000    100000   100000   30000
          100000    100000   30000    100000
          100000    100000   30000    30000
          100000    30000    100000   100000
          100000    30000    100000   30000
          100000    30000    30000    100000
          100000    30000    30000    30000
          30000     100000   100000   100000
          30000     100000   100000   30000
          30000     100000   30000    100000
          30000     100000   30000    30000
          30000     30000    100000   100000
          30000     30000    100000   30000
          30000     30000    30000    100000
          30000     30000    30000    30000
          ];
cd..
```

6.B.4 Function GENERATE_DATA

```
function [ ELEM_DATA ]    =    GENERATE_DATA (TEST_COUNTER, No_OF_ELEMENTS, ...
                               Standard_Deviation, Average, Thickness, Volume_Fraction);

  FILE_NAME               =    ['ELEM_DATA',num2str(TEST_COUNTER),'.txt'];

  for i                   =    1:1:No_OF_ELEMENTS

      x                   =    rand;
      Kx (i)              =    Standard_Deviation*(NORMINV(x))+Average;
      y                   =    rand;
      Ky (i)              =    Standard_Deviation*(NORMINV(x))+Average;
      aThickness(i)       =    Thickness;
      aVolume_Fraction(i) =    Volume_Fraction;

  end

    ELEM_DATA             =    aThickness';
    ELEM_DATA(:,2)        =    aVolume_Fraction';
    ELEM_DATA(:,3)        =    Kx';
    ELEM_DATA(:,4)        =    Ky';

    cd ../results
    FILE_NAME             =    ['ELEM_DATA',num2str(TEST_COUNTER),'.txt'];
    save                       (FILE_NAME, 'ELEM_DATA', '-ascii');
  cd ..
```

6.B.5 Function LIMS_AUTO_FILE

```
function [ ]        =        LIMS_AUTO_FILE ( No_OF_NODES_TO_BE_LEFT_EMPTY, ...
                             GATE_SCHEME,  FILLED_NODE_NUMBERS)

 cd ..
 fid                =        fopen('Auto.lb', 'w' );

 fprintf   (fid,'PROC AUTO\n\nREAD "AutoK.txt", "dmp"\nCALL DEFINE_GATES\nCALL FILL');
 fprintf   (fid,'\n\nDO\n  SOLVE\nLOOP WHILE ...
           (SONUMBEREMPTY()>%d)', No_OF_NODES_TO_BE_LEFT_EMPTY);
 fprintf   (fid,'\n\nSETOUTTYPE "tplt"\nWRITE "out"\n\nENDPROC\n\nPROC DEFINE_GATES\n');
 fprintf   (fid,'SETGATE 1, 1, %d\nSETGATE 2, 1, ...
           %d\nSETGATE 3, 1, %d\nSETGATE 4, 1, %d\n', GATE_SCHEME);
 fprintf   (fid,'ENDPROC\n\nPROC FILL\n');
 fprintf   (fid,'SETFILLFACTOR %d,1\n', FILLED_NODE_NUMBERS);
 fprintf   (fid,'ENDPROC');

 fclose     (fid);
```

6.B.6 Function LIMS_RESULT

```
function [ RESULTS ] = LIMS_RESULT( No_OF_NODES )

  cd ..
  [x, y, z, p, Time, Fill]        =  textread('out.tec','%f %f %f %s %f %f','headerlines',3);

  RESULTS(1:1:No_OF_NODES,1)      =  (1:1:No_OF_NODES)';
  RESULTS(:,2)                    =  x(1:1:No_OF_NODES);
  RESULTS(:,3)                    =  y(1:1:No_OF_NODES);
  RESULTS(:,4)                    =  Time(1:1:No_OF_NODES);
  RESULTS(:,5)                    =  Fill(1:1:No_OF_NODES);
```

6.B.7 Function LIMSINFILE

```
function [  ] = LIMSINFILE( NODAL_COORD, CONNECTIVITY_DATA, ELEM_DATA, No_OF_ELEMENTS )

cd ..
fid                     =  fopen('AutoK txt', 'w' );

fprintf                 (fid,'Number    of      nodes   :       66      \nIndex   x       y
        z \n==================================================  \n');
fprintf                 (fid,'\t %g \t %g \t %g \t% g\n', NODAL_COORD);
fprintf                 (fid,'Number    of      elements  :     50 \nIndex NNOD    N1      N2
        N3      (N4)    (N5)    (N6)    (N7)    (N8)    h       Vf      Kxx     Kxy
        Kyy     Kzz     Kzx     Kyz
\n==========================================================================
==========================================================================
=\n');

        for i=1:1:No_OF_ELEMENTS
                fprintf     (fid,'\t%d\t%d\t%d\t%d\t%d\t%d\t', CONNECTIVITY_DATA(i,1), ...
                            CONNECTIVITY_DATA(i,2), CONNECTIVITY_DATA (i,3), ...
                            CONNECTIVITY_DATA(i,4), CONNECTIVITY_DATA(i,5), ...
                            CONNECTIVITY_DATA(i,6));
                fprintf     (fid,'%g\t%g\t%6.3E\t0\t%6.3E\n', ELEM_DATA(i,1),  ...
                            ELEM_DATA(i,2), ELEM_DATA(i,3), ELEM_DATA(i,4));
         end
end

fprintf         (fid,'Resin     Viscosity  model    NEWTON \nViscosity       :       0.12\n');
fclose          (fid);
```

6.B.8 Function MODEL_DATA

function [NODAL_COORD, CONNECTIVITY_DATA] = MODEL_DATA

```
NODAL_COORD          =        [
                              1          -1          -0.5        0
                              ... Nodal coordinates are inputted here. .
                              66         -0.4        0.3         0
                              ];

CONNECTIVITY_DATA    =        [
                              1          4          12          13          40          38
                              ... connectivity data is inputted here...
                              50         4          65          64          63          66
                              ];

NODAL_COORD=NODAL_COORD';

cd ..
```